Soft Matter and Molecular Biophysics Group

Department of Applied Physics

Faculty of Physics

Doctoral Thesis, 2011

DESIGN AND DEVELOPMENT OF SPECIFIC NANOSTRUCTURED SYSTEMS BASED ON BIOCOMPATIBLE MATERIALS

Natalia Hassan López

Facultad de Física-Campus Vida

15782 Santiago de Compostela

D. Juan M. Ruso Beiras, Profesor Titular del Departamento de Física Aplicada de la Universidad de Santiago de Compostela,

INFORMA:

Que el trabajo de investigación titulado: "***Design and Development of Specific Nanostructured System Based on Biocompatibles Materials***" que presenta la alumna Natalia Andrea Hassan López ha sido tutorado bajo mi dirección dentro del grupo "Materia Blanda y Biofísica Molecular" de la Universidad de Santiago de Compostela y reúne los requisitos de calidad y rigor científicos necesarios para optar al Grado de Doctor en Ciencias Físicas.

Para que así conste a los efectos oportunos.

Santiago de Compostela, septiembre de 2011

Juan Manuel Ruso Beiras

To my parents

Acknowledgments

It not easy to leave home and leave family, but I am very sure that It was the most comfortable and rewarding experience in my life. I am very grateful to have met very special people in this magic city, Santiago de Compostela.

Firstly I would like to thank to my supervisor Juan Ruso who was the most important person in this thesis. He gave me the scientific support and I appreciate all his contributions of time, ideas, and funding my PhD experience productive and comfortable. The joy and enthusiasm he has for his research was contagious and motivational for me. Thank you Juan for trust me and give me this opportunity to live the most important experience in my life.

I also want to thank all the group members of Soft Matter and Molecular Biophysic group that I have worked, Ángel Piñeiro, Pedro Vazquez, Paula Messina and Valeria Verdinelli.

During this work I have had the pleasure to work with Victor Morris, Patrick Gunning and Julia Maldonado-Valderrama in the Institute of Food Research (Norwich-UK). For this reason I would like to thanks these persons for this incredible opportunity to learn, deepen my knowledge and for everything you contributed to my stay.

I wish to express my sincere thanks to Josué Juarez, one of the most important friend-labmate during these years, for his patient, enthusiasm and immense knowledge: Thank you for all “Wua yu sei”!. Also, I wish to thanks to all wonderful people, my special friends of the faculty: Irais Bautista, Elena Blanco, Paula Toimil, Miguel Morales, Antonio Topete, Alejandra Flores, Ceila Fong. All of you were a support and were very important part of my life these years.

Last but not the least, I would like to thank my family: My father Hector Hassan, my mother Viviana López, my middle sister Marjorie Hassan and my youngest sister Belén Hassan for their unconditional love and their immense support in all my decisions. These years have not been easy for us far from home, but I am very grateful for their patient, I love you so much.

Abstract

The challenges and applications in the nanomaterials research domain are numerous: medicine, energy, biosensing devices, technology. This motivated us to address in this study new design strategies and concepts to develop new biofunctional materials to achieve bio- and hemocompatibility.

This thesis is divided in three main parts. The first part has been focused on the self-assembled of surfactants and drugs where has been found to depend on several factors, such as hydrophobic chain length and type, temperature, the nature of contraion, etc. As well as we have studied the effect of mixing alkanes and perfluoroalkanes and a new idea of "self-assembled" drugs based in the combination of one or more drugs. We have focused on how the principal experimental parameters are determined and how these data can be evaluated to obtain relevant information of the interaction. Different techniques have contributed to a deeper understanding of interactions between proteins and surfactants/drugs. The complexation between serum proteins and these different surfactants and drugs has been analyzed at different conditions. We have analyzed conformational changes as a function of different external agents and as well as the stability of the complexes and the stability of the complexes besides. Then, we designed optimal templates that manage the formation of biocompatible materials. For this purpose we used reverse microemulsions and proteins. We have determined structural properties (shape, size, stability) as a function of different external parameters. In addition, this characterization has been realized with experimental and dynamic molecular simulations. Both of them allowed us to optimize the design process of templates with specific purposes. The final part of this thesis is devoted to prepare the materials with structures not studied in details currently; with the purpose to obtain stable materials and with biocompatibility properties. The last step was to evaluate the adsorption of proteins and drugs, characterized in the first part, in specific conditions.

The structure of this thesis has been presented distributing the work in four different chapters based on homogeneity and steps to reach the aim. Each chapter has been structured by a brief introduction where the subject is exposed as well as some important facts or descriptions of concepts or techniques. The relevant aspects of the research are exposed and finally the publications that have been obtained are appended.

List of Papers

I. **On the Self-assembly of a highly selective benzothiazole-based TIM inhibitor in aqueous solution.**
Natalia Hassan, M. Pilar Gárate, Tania Sandoval, Luis Espinoza, Ángel Piñeiro, Juan M. Ruso.
Langmuir 26(22) (2010) 16681–16689.

II. **Self-assembling drugs: A new therapeutic strategy**
Natalia Hassan, Juan M. Ruso, Alfredo González-Pérez.
Soft Matter 7 (2011) 5194-5199.

III. **Hydrogenated/fluorinated catanionic surfactants as potential templates for nanostructure design.**
Natalia Hassan, Juan M. Ruso, Ángel Piñeiro.
Langmuir 27 (2011) 9719–9728.

IV. **Assessment of interactions between four proteins and benzothiazol derivates by DSC and CD.**
Natalia Hassan, Pedro V. Verdes, Juan M. Ruso.
J. Chem. Thermodynamics 43 (2011) 399–404.

V. **Mechanisms of fibrinogen-acebutolol Interactions: Insights from DSC; CD and LS.**
Natalia Hassan, Juan M. Ruso, P. Somasundaran.
Colloids and Surfaces B: Biointerfaces 82 (2011) 581–587.

VI. **Surface characterization and AFM imaging of mixed fibrinogen-surfactant films**.
Natalia Hassan, Julia Maldonado-Valderrama, A. Patrick Gunning, Victor J. Morris, Juan M. Ruso.
J. Phys. Chem. B 2011, 115 (19), 6304–6311.

VII. **Investigating the effect of an arterial hypertension drug on the structural properties of plasma protein**.
Natalia Hassan, Julia Maldonado-Valderrama, A. Patrick Gunning, V.J. Morris, Juan M. Ruso.
Colloids and Surfaces B: Biointerfaces 87 (2011) 489–497.

VIII. **Fibrinogen Stability Under Surfactants Interactions**.
Natalia Hassan, Leandro R.S. Barbosa, Rosangela Itri, Juan M. Ruso.
Journal of Colloid and Interface Science 362 (2011) 118–12.

IX. **Rheological properties of ovalbumin hydrogels as affected by surfactants addition**.
Natalia Hassan, Paula Messina, Veronica I. Dodero, Juan M. Ruso.
International Journal of Biological Macromolecules 48 (2011) 495–500.

X. **Mimicking Natural Fibrous Structures of Opals by Means of a Microemulsion-Mediated Hydrothermal Method.**
Natalia Hassan, Valeria Verdinelli, Juan M. Ruso, Paula Messina.
Langmuir 27 (2011) 8905–8912.

Contents

Chapter 1: Introduction 17

1. Introduction 19

1.1 Aim 20

Chapter 2: Methods 23

2. Methods 25

2.1 Introduction 25

2.2 Conductivity 25

2.3 Density and ultrasound velocity 27

2.4 Surface tensión 28

2.5 Langmuir-Blodgett films 29

2.6 Circular dichroism 30

2.7 UV-visible spectroscopy 31

2.8 Fluorescence 33

2.9 Ligth scattering 34

2.10 Differential scanning calorimeter (DSC) 35

2.11 Electron microscopy techniques 37

2.12 Atomic force microscopy (AFM) 39

Chapter 3: Theoretical Aspects 43

3.1 Self-assembly of Surfactants 45

3.1.1 Introduction 45

3.1.2 Factors affecting the critical micellar concentration 48

3.1.3. The hydrophobic group 48

3.1.4 Hydrophilic group 49

3.1.5 Effect of counterions 49

3.1.6 Effect of additives 49

3.1.7 Temperature effect 50

List of papers including in this section 51

3.2 Protein-Ligand Interactions 52

3.2.1 Introduction 52

3.2.2 Protein structure 52

3.2.3 Protein-Ligand Interactions 54

3.2.4 Stabilization of protein structure 58

3.2.5 Thermodynamic binding 59

3.2.6 Ligand binding and folding equilibrium 62

List of papers including in this section 64

3.3 Hydrogels 65

3.3.1 Introduction 65

3.2.2 Hydrogels structure 66

3.2.3 Hydrogels characterization 69

3.3.4 Theoretical aspects 70

3.3.5 Response to an oscilating shear field 70

3.4 Synthesis of Nanomaterials 76

3.4.1 Introduction 76

3.4.2 Synthesis by organic molecules used as templates 76

3.4.3 Synthesis by molecular self-assembly:

Liquid crystals and cooperative organization 77

3.4.4 Synthesis spatially restricted: Foams, and microemulsions 78

Chapter 4: Results and Discussions 81

4.1 Published Articles: Relevant Aspects 83

4.2 Articles preparing for publications 167

Chapter 5: Concluding Remarks 187

Bibliography 191

Resumen 201

Chapter 1:

INTRODUCTION

1. Introduction

Amphihilic compounds, that is, those that have distinct hydrophilic and lipophilic parts, are used in most branches of industry and are ubiquitous in biological systems. They range from low molecules weight substances (like surfactants and lipids) to macromolecules (comprising synthetic graft and block polymers) and biomacromolecules (like proteins, lipopolysaccharides, and nuclei acids)[1-3]. Amphiphilic molecules self-organize both in bulk solution and at interfaces. Low-molecular-weight amphiphilic compounds, mainly constituted of surfactants and polar lipids, have been thoroughly investigated extensively and are well understood both with respect to their bulk self-assembly and surface modifying ability. The study of high molecular weight amphiphilic molecules is much more recent. Regarding the effect that these compounds have on their interactions with biomacromolecules it has been proposed that the amphiphilic behavior of these molecules play an essential role for attachment at the polipepetide chain, leading to their high efficiency[4].

Proteins are not only the building devices of life, but also rule life. They play a variety of roles in life processes: they are structural proteins (viral coat proteins, epidermal keratin); catalytic proteins (enzymes); transport and storage proteins (haemoglobin, myoglobin); regulatory proteins (hormones); and proteins of the immune system and the immunoglobulin superfamily. Much biotechnological, medical and drug delivery system aims to predict their behavior on the basis of the set of molecules involved, mainly proteins and amphiphilic molecules, specifically drugs. Understanding the interactions between these molecules is therefore crucial to such efforts. Although many thousands of interactions are known, precise molecular details are available for only tiny fraction of them. The difficulties that are involved in experimentally determining atomic structure for interacting proteins make predictive methods essential for progress. Structural details can ultimately turn abstract system representations into models that more accurately reflect biological reality[5].

Proteins undergo changes in their natural state by the action of ligands, which after their adsorption onto the protein can control the hydrophobic-hydrophilic character of protein surface. Understanding protein-ligand interactions is central to discovery new medicines, and, when the ligand is a drug, these interactions are central to drug delivery to benefit human health. Essential for high biological activity are a good geometric fit and a high degree of complementary of hydrophobic and polar parts of both entities, the binding site of the protein and the ligand.

On the other hand, the synthesis of nanoparticles and nanoporous materials is a recent branch of the nanotechnology. Increasingly, colloidal chemists are contributing to the biomimetic synthesis of inorganic nanostructures with dimensional, morphological and architectural specificity by using organized self-assemblies of surfactants as nanostructured reaction media or templates. A large variety of methods have been proposed to synthesize nanoparticles, among them the use of microemulsions enables the control of particles size, as well as protein hydrogels as a templates. Also these bio-inspired templates can offer a fast, general, inexpensive and environmental friendly procedure for the synthesis of nanostructured materials[6-8]. The reduction of such materials at the nanometer scale offers a number of outstanding optical and mechanical properties, including electrical, magnetic, thermal, chemical and biomedical properties.

1.1 Aim

Recent advances in nanotechnology or hybrid nanomaterial have triggered the enthusiasm for these complexes and systems. For this purpose the main aim of this thesis is to design biocompatible materials for different applications, specifically drug delivery. Firstly, we have characterized the self-assembly of surfactant and drugs, and its interaction with proteins such as mioglobin, lysozyme, ovalbumin and fibrinogen. Finally, we have prepared nanomaterials to adsorb drugs and we studied its interaction with proteins. In the compilation of this thesis an attempt has been made to give appropriate recognition to the current interest in normal and emergency applications of these systems, by discussing such aspects as newer systems, unusual approaches and highly used techniques including information about the physical principles and effectiveness of selected techniques. For this reason it has been focused on the experimental point of view.

The specific aims are:

1. First Aim: Study and characterization of different amphiphilic molecules (BTS, acebutolol, propranolol, C_8HONa, C_8FONa, $C_{12}HONa$, dicloxacillin, CTAB) estimating the critical micellar concentration including the thermodynamics properties of micellization, as a function of temperature, concentration, and also salt concentration. As well as the characterization of mixtures of heterogeneous molecules (dicloxacillin-CTAB, $C8F^-$-CTA^+) which self-assemble in aqueous solutions and to propose a new idea of self-assembled drug based on the combination of two or more drugs.
   Study of protein-drug interaction, structural analysis of complex formed. Influence of concentration, temperature and environment. Interaction protein-drug by fluorescence, RAMAN spectroscopy, UV-Vis, differential scanning calorimeter (DSC).
   Characterization of complex protein-drug by dynamic light scattering (DLS), circular dichroism (CD), RMN, Transmission Electron Microscopy (TEM), SAXS. Achieving this objective will know the interactions between the most important proteins and drugs selected. Also will be characterized the structures of the complex formed as well as conformational changes in the protein induced by drugs. This knowledge will design the subsequent study:

2. Second aim: Structural and energetic characterization of the templates obtained by different strategies: A) Fibrinogen hydrogels B) reverse microemulsions of aerosol OT (dioctyl sodium sulfosuccinates), phase diagrams of template (cubic, lamellar, hexagonal) depending on the length of the alkyl chain (4-16), electric charge (pH 3,2) and temperature range (15-45°C) with measures of electrical conductivity, Differential Scanning Calorimeter (DSC), Transmission Electron Microscopy (TEM).

   Study of colloidal stability of the systems by processing data from dynamic light scattering (hydrodynamic radius). Study dynamic surface tension in different media and temperatures. Structural analysis of the systems by TEM and rheology.

   Study of the AOT microemulsion / oil phase / water as a function of temperature, different oil phases (hexane, n-heptane, cyclohexane), pH, ionic strength.

   Characterize by dynamic molecular simulations the behavior of certain samples of elements of the templates at diverse concentrations and temperatures. Achieving this goal will be able to determine the structure, chemical stability and functionality of the templates based on specific use.

3. Third aim: Preparation of mesoporous materials, adsorption of active principles and study of the delivery from the material. Design and characterization of the pores of the ceramic material (TEOS, SiO_2). Determine the number, size, shape, distribution, connectivity and possible functionalization of their walls, depending upon the drug and the ceramic material is to be used (both pure and mixtures in various proportions) based on nitrogen adsorption measurements and SAXS, SEM, TEM, IR.

Chapter 2:

METHODS

2. Methods

2.1 Introduction

There is a wide range of methods available to characterization of different colloidal particles. To establish these methods it is necessary to take into account some considerations, that is, it is possible to define the following groups:

- Physical Chemistry Characterization
- Electrical and spectroscopic properties
- Size and shape distributions
- Concentrated solutions: Ordering and structural organization

To study the physicochemical properties of soft materials it is possible to use several techniques, which in the case of surfactant molecules, can provide us information related with self-aggregation partnerships, energy, interactions between aggregates, interactions with surrounding media or stability.

2.2 Conductivity

Conductivity is a physical property using for studying ionic solutions. The conductivities have been extensively used mainly for determining the critical micelle concentration (cmc) of ionic surfactants, at which the concentration dependence of each conductivity breaks. Along the definition of cmc by Philips in which the cmc is considerate as the concentration at which the slope of the plot of a physical property of the solution against concentration is changing most rapidly. The conductivity allows us to determining ionic constants of aggregates such as equilibrium constant, degree of counterion dissociation of micelles and aggregation number.

The conductivity of a solution depends on the transport of charges. Species with a small hydrodynamic radius conduct better than larger ones since they can move fast. Ions of higher charge usually attract more water, resulting in a larger hydrodynamic radius. For ionic species

at low concentrations, the conductivity is linearly dependent of concentration.

For measuring the electrical conductivity it is necessary to know the electric resistance R of a specific volume in the solution using a potentiometer display. The most common is the *Wheatstone bridge*, which it is used to measure an unknown electrical component.

For determining the electrical conductivity it is common to use a platinum cell. This cell is made up of two parallel plates and between of them the solution is situated. The quantity that is measured is the resistance situated between the parallel plates and taking into account the geometry of the cell, that is, the distance between plates (L) and the surface of the plates (S), the conductivity can be obtained by the following:

$$R = \frac{1}{\kappa}\frac{L}{S} \tag{2.1}$$

where κ is the conductivity of the solution between the plates.

Due to the fact that is not easy to specify the dimensions of the parallel plates, it is necessary to consider that the proportion between R and $1/\kappa$ is constant:

$$R = k\frac{1}{\kappa} \tag{2.2}$$

where k is the cell constant obtained for a reference solution.

In surfactants solutions a break in the conductivity versus concentration curve can be found at cmc, indicating a charge in structure. The degree of counterion binding, β, is defined as the number of counterions close to a micelle divided with the aggregation number of that micelle, and can be determined from $\beta = 1 - \alpha$. The degree of ionization of the micelles, α, can roughly estimated from the ratio of the slopes above and below the cmc.

2.3 Density and ultrasound velocity

Density and ultrasound velocity measurements may be used for determining the critical micellar concentration of amphiphilic molecules.

The apparent molal volume (V_ϕ) is a classical and well defined thermodynamic quantity that can be obtained from density measurement using the following equation:

$$V_\phi = \frac{M}{\rho} - \frac{10^3(\rho-\rho_0)}{m\rho\rho_0} \tag{2.3}$$

where M is the molecular weight of the solute, ρ the density of the solution, m the molality and ρ_0 the density of pure solvent.

Generally it is accepted that the solutions of surfactants in the premicellar region behave as singly dispersed systems and they may be described by the Debye-Hückel limiting law equation:

$$V_{\phi=}V_\phi^0 + A_\upsilon m^{1/2} + B_\upsilon m + \cdots \tag{2.4}$$

Where V_ϕ^0 is the value of apparent molal volume at infinite dilution, A_υ is the Debye-Hückel limiting law coefficient and B_υ is an adjustable parameter related to a pair interaction, and equivalent to the second virial coefficient which measures the deviation from the limiting law due to the non-electrostatic solute-solute interactions.

Density and ultrasound velocity measurements can be combined to calculate adiabatic compressibilities using the Laplace equation:

$$\kappa_S = -\frac{1}{V}\left(\frac{\partial V}{\partial P}\right)_S = \frac{10^{-3}}{\rho u^2} \tag{2.5}$$

where V, P and s refer to volume, pressure and entropy, respectively. κ_s is the adiabatic compressibility coefficient, expressed in Pa^{-1} when the ultrasound velocity u is expressed in $cm\,s^{-1}$ and the density in $g\,cm^{-3}$. The isoentropic apparent molal compressibility, K_ϕ, can be calculated from ultrasound measurements:

$$K_\phi = \frac{10^3(\kappa_s - \kappa_s^0)}{m\rho_0} + \kappa_s^0 V_\phi \tag{2.6}$$

where κ_s and κ_s^0 are the isentropic coefficients of compressibility of the solution and solvent, respectively.

Apparent molal volume at infinite dilution consists of two contributions: the intrinsic volume of the solute molecule and that of the hydration shell. In contrast, apparent molal compressibility data, at infinite dilution, provide insight into the compressibility of the hydration layer around the solute molecule, since the solute intrinsic compressibility is assumed to be zero.

2.4 Surface Tension

The surface tension is most easily illustrated for a liquid-gas interface. In the bulk of the fluid, the net force acting on a molecule averages to zero over time scales larger than the relaxation time of the molecular neighborhood. At the surface, the net force does not vanish. To increase the surface area, one needs to perform work to transfer the molecules from the bulk toward the surface. The work needed to increase the surface area by small quantity dA is proportional to dA:

$$dW = \sigma dA \tag{2.7}$$

The positive-definite coefficient σ is called the surface tension.

However this relationship is the case for a pure material. Whenever another species are present (such as amphiphilic molecules) the distribution becomes important as this control the details of the intermolecular forces in the interfacial region.

Because surface tension manifests itself in various effects, it offers a number of paths to its measurement. Some of the most used methods are: capillary rise, pendant drop, du Nouy ring or Wilhelmy plate method[9]. Which method is optimum depends upon the nature of the liquid being measured, the conditions under which its tension is to be measured, and the stability of its surface when it is deformed.

Since the surface tension depends on the amount of adsorbed molecules, it is interesting to obtain a relationship between the surface tension and the concentration solution.

2.5 Langmuir-Blodgett films

Monolayer is one molecule thick layer of insoluble substances (such as amphiphilic compounds) spread onto a supporting liquid subphase.

In studying the solubility of the adsorbed species, it is necessary to point out two categories: insoluble and soluble surfaces layer. With facts in mind, Langmuir layer is a monolayer formed by a substance that is insoluble in the liquid subphase are labeled, and Gibss layer constitute the monolayer formed by a substance soluble I the bulk but adsorbed preferentially at the interface.

The surface pressure of a monolayer film is defined as the difference between the surface tension of the pure supporting liquid (γ_0) and that of the liquid with an adsorbed film (γ):

$$\pi = \gamma_0 - \gamma$$

The surface pressure represents an expanding pressure exerted by the monolayer acting against the (contracting) surface tension of the pure liquid substrate. For that reason it is possible to construct a pressure-area ($\pi - A$) curve for a monolayer. Experimentally, this study may be done by the classical Langmuir though spreading the adsorbed material (as a dilute

solution in a volatile solvent) onto liquid substrate[10]. The surface pressure is usually measured using the Wilhemly plate (a thin plate that is used to measure equilibrium surface or interfacial tension at an air-liquid or liquid-liquid interface). In this method, the plate is oriented perpendicular to the interface, and the force exerted on it is measured.

Monolayer films exhibit characteristics that may be equated to the solid, liquid and gaseous states of matter. These equivalent states are roughly defined as:

- Condensed solid films, which are essentially incompressible and densely packed. The molecules have little mobility and are preferentially oriented perpendicular to the surface
- Expanded films, roughly equivalent to the liquid state, in which the monolayer is relatively densely packed but is much more compressible than condensed films.
- Molecular orientation is still approximately perpendicular to the surface, but the compounds are less rigidly packed.
- Gaseous films, in which the molecules are relatively far apart and have significant surface mobility for acting independently.

Insoluble film monolayer films, formed by a substance that is insoluble in the liquid subphase, may be transferred to solid substrates. This method is commonly referred to as the Langmuir-Blodgett technique. The molecular density at the air-water interface is manipulated with moveable barriers in a Langmuir-Blodgett through. A monolayer can be transferred to a flat solid support, as e.g. a hydrophilic silicon substrate is hydrophilic, the headgroup of the monolayer will oriented towards to the solid surface, whereas the hydrophobic alkyl chains are exposed to the air. During the transfer, the surface pressure of the monolayer is kept constant by automatically compressing the film by the barrier to account for the material loss. It is important the effect of transfer speed of a monolayer to a substrate. At high transfer speeds the quality of the transferred monolayer will largely be dominated by hydrodynamics: the underlying water layer has to be removed from the monolayer in contact with the solid surface. At low transfer speeds, the monolayer quality after transfer will be increasingly dominated by molecular interaction between the monolayer and the solid surface.

2.6 Circular Dichroism

Circular Dichroism (CD) measures the interaction of circularly polarized light with molecules. Circularly polarized light comes in left- and right-handed forms, rather like screw threads.

These forms interact equally with non-chiral chromophores, but differently when the chromophore has a right- or left-handed form. The result is a small difference in the extinction coefficients for left- and right-polarized light, which varies with wavelength.

CD spectra in the far-UV region (170-260 nm) provide important information about protein secondary structure. In proteins, the chiral arrangement of peptide bonds in secondary structures such as α-helix and β-sheets leads to characteristic CD spectra at UV wavelengths. Alteration of the relative orientations, due to conformational or structural variations, causes changes in the CD spectrum.

CD is reported in units of absorbance or ellipticity. Each of these can be normalized for molar concentration of the sample. To calculate molar ellipticity, the sample concentration (g/L), cell pathlength (cm), and the molecular weight (g/mol) must be known. If the sample is a protein, the main residual weight (average molecular weight of the amino acids it contains) is used in place of the molecular weight, essentially treating the protein as a solution of amino acids.

Molar ellipticity is determinate as follows:

$$[\theta]_l = \frac{\theta_l M_r}{ncl} \tag{2.8}$$

Where c is the protein concentration, l is the path length of the cell, $[\theta]_l$ is the measured ellipticity at a wavelength λ, is the molecular mass of the protein, and n is the number of residues.

2.7 UV-visible spectroscopy

UV-visible spectroscopy (*UV-Vis*) provides information about the structure, formulation, and stability of the materials in solution. Absorption spectra are produced when ions or molecules absorb electromagnetic radiation in the ultraviolet or visible regions. The intensity of the absorption is proportional to the number, type and location of color absorbing structures in the molecule.

The conventional or single-beam spectrophotometer contains two source lamps, a deuterium lamp and tungsten lamp. Polychromatic light from the source is focused on the entrance slit of a monochromator, which selectively transmits a narrow band of spectrum. This light then passes through the sample area to the detector. The absorbance of a sample is determined by measuring the intensity of light reaching the detector without the sample (the blank) and comparing it with the intensity of light reaching the detector after passing through the sample[11].

When the light passes through or is reflected from a sample, the amount of light absorbed is the difference between the incident radiation (I_0) and the transmitted radiation (I). The amount of light absorbed is expressed as either transmittance or absorbance. Transmittance usually is given in terms of a fraction of 1 or as a percentage and is defined as follows:

$$T = \frac{I}{I_0} \quad or \ \ \%T = (I/I_0) \times 100 \tag{2.9}$$

Absorbance is defined as follows:

$$A = -logT \tag{2.10}$$

For most applications, absorbance values are used to determine many physicochemical characteristics of compounds and thus can provide information as to identify of a particular compound. For example the absorbance spectra of proteins result largely from the presence of the aromatic amino acids tryptophan, tyrosine and phenylalanine. A protein at room temperature has a specific tertiary structure or conformation that in turn creates a specific electronic environment for the aromatic amino acids. If the protein is heated it will, at certain temperature, unfold or melt and lose the structure. In this process, the electronic environment of the aromatic amino acids changes, which in turn results in spectral changes or shifts. However, the observed absorbance is always significantly less than expected because their electronic environment. When a molecule is heated, the hydrogen bonds break, the double helix unwinds, and the absorbance increases.

2.8 Fluorescence

Fluorescence is the process by which electronically excited molecules decay to the ground state via the emission of a photon without any change in spin multiplicity. Emission is detected by spectrofluorometers and occurs at longer wavelengths than the corresponding absorbance band. The quantum yield of fluorescence emission is defined as the ratio of photons emitted through the fluorescence to the number of photons absorbed.

Changes in intensity and wavelength reflect the influence of local environment on emission.

The quenching of fluorescence is known to occur by two process, namely collisional (dynamic) quenching and/or formation of a complex between the quencher and fluorophore (static quenching)[12]. The fluorescence quenching data were analyzed according to the Stern-Volmer equation:

$$F_0/F = 1 + K_{sv}[Q] \tag{2.11}$$

where F_0 and F are the fluorescence peak intensities of the fluorophore in the absence and presence of quencher. Collisional quenching can determine the accessibility of fluorophores in proteins via the Stern-Volmer analysis. When the drug molecules bind independently to a set of equivalent sites on a protein, the equilibrium between free and bound molecules is given by the equation:

$$\log\left(\frac{F_0-F}{F}\right) = \log K + n\log[Q] \tag{2.12}$$

where F_0, F, are the stady-state fluorescence intensities in the absence and presence of quencher; K and n are the binding constant and the number of binding sites, respectively.

2.9 Light Scattering

Dynamic Light Scattering (*DLS*) is also known as *Photon Correlation Spectroscopy*. This technique is one of the most important methods used to determine the size of particles. When a beam of light passes through a colloidal dispersion, the particles or droplets scatter some of the light in all directions. When the particles are very small compared with the wavelength of the light, the intensity of the scattered light is uniform in all directions (*Rayleigh scattering*); for larger particles (above approximately 250 nm), the intensity is angle dependent (*Mie scattering*).

If the light is coherent and monochromatic, as from a laser, it is possible to observe time-dependent fluctuations in the scattered intensity using a suitable detector such as a photomultiplier capable of operating in photon counting mode. These fluctuations arise from the fact that the particles are small enough to undergo random thermal (Brownian) motion and the distance between them is therefore constantly varying. Constructive and destructive interference of light scattered by neighboring particles within the illuminated zone gives rise to the intensity fluctuation can therefore yield the diffusion coefficient of the particles from which, via the Stokes-Einstein equation, knowing the viscosity of the medium, the hydrodynamic radius or diameter of the particles can be calculated.

The time dependence of the intensity fluctuation is most commonly analysed using a digital correlator. This device determines the intensity autocorrelation function which can be described as the ensemble average of the product of the signal with a delayed version of itself as a function of the delay time. The signal in this case is the number of photons counted in one sampling interval. At short delay times, correlation is high and, over time as particles diffuse, correlation diminishes to zero and the exponential decay of the correlation function is characteristic of the diffusion coefficient of the particles. Data are typically collected over a delay range of 100 ns to several seconds depending upon the particle size and viscosity of the medium.

Analysis of the autocorrelation function in terms of particle size distribution is done by numerically fitting the data with calculations based on assumed distributions. A truly monodisperse sample would give rise to a single exponential decay to which fitting a calculated particle size distribution is relatively straightforward. The autocorrelation function decays exponentially as follows:

$$g(\tau_c) = \exp\left(-\tau_c D_s q^2\right) \tag{2.13}$$

where τ_c is termed the correlation delay time, D_s is the self-diffusion coefficient of the particle, and q is the scattering vector defined as the vector difference between the wave propagation vector of the incident and the scattered beam, both of length $2\pi/\lambda$:

$$q = \frac{4\pi}{\lambda}\sin\left(\frac{\theta}{2}\right) \tag{2.14}$$

where λ is the wavelength of the scattered radiation in the medium.

To give the hydrodynamic radius of the particle the Stokes-Einstein relationship is used:

$$R_h = \frac{k_B T}{6\pi\eta_0 D_s} \tag{2.15}$$

where η_0 is the viscosity of the continuous phase.

In practice, polydisperse samples give rise to a series of exponentials and several quite complex schemes are devised for the fitting process.

2.10 Differential Scanning Calorimeter (DSC)

Differential scanning calorimeter (DSC) is an experimental techniques widely used in the study of binary and multicomponent systems containing substances of different classes, as a salt (surfactants), metals, oxides, organic compounds, liquid crystals, etc. including methods available to the biophysical chemist for the study of macromolecules conformation and thermal transitions might be affected by ligand binding. Thermal transition (melting) temperatures (for samples in solution, solid or mixed phases, e.g. suspensions) and enthalpies

are often determined and used to draw the limits of existence of the different phases. A phase transition in a two-component system is often characterized by a single transition temperature and a transition enthalpy, which is done by mechanical analogy with a transition in pure individual substance[13-16].

The advantages of calorimetric techniques arise because they are based on direct measurements of intrinsic thermal properties of the samples and usually non-invasive and require no chemical modifications or extrinsic probes. Furthermore, with careful analysis and interpretation, calorimetric experiments can directly provide fundamental thermodynamic information about the processes involved.

In a DSC experiment a sample is heated at constant rate in the calorimeter cell alongside and identical reference cell containing the blank. Differences in heat energy uptake between the sample and reference cells required to maintain equal temperature, correspond to differences in apparent heat capacity, and it is these differences in heat capacity that give direct information about the energetic of thermally induced processes in the sample.

From DSC experiment is obtained a thermogram showing the excess heat capacity (C_p sample minus reference) as a function of temperature. For the case of simple globular proteins the thermogram comprises three regions: pre-transition baseline, the endothermic unfolding transition, and post-transition baseline (Fig.2.1).

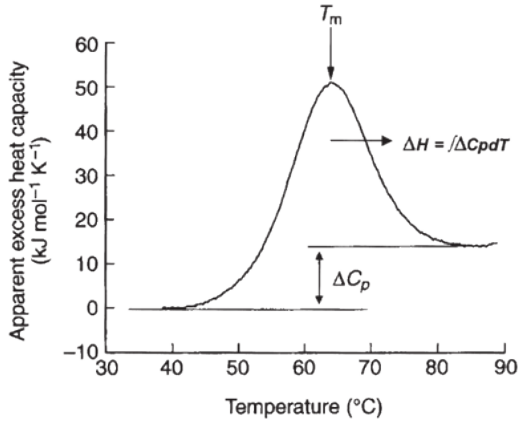

Figure 2.1: Typical thermogram of DSC measurements.

The heat capacity (or specific heat) of any substance reflects the ability of the substance to absorb heat energy without increase in temperature, and this central to DSC measurements

and to the fundamental underlying thermodynamics. The absolute enthalpies (H) and entropies (S) may be derived by the heat capacity, (fundamental properties from which all thermodynamic quantities are derived). Changes in enthalpy and entropy (ΔH and ΔS) as a system changes from one state to another ($A \rightarrow B$) at constant temperature follow directly from the integral definitions:

$$\Delta H = H_B - H_A = \int_0^T \Delta \mathrm{C_p}\, dT + \Delta H(0) \tag{2.16}$$

$$\Delta S = S_B - S_A = \int_0^T (\Delta C_p/\mathrm{T})\ \mathrm{dT} \tag{2.17}$$

where $\Delta C_p = C_{p,B} - C_{p,A}$ is the heat capacity difference between states A and B at given temperature. $\Delta H(0)$ is the ground state enthalpy difference between A and B at absolute zero.

The Calorimeter enthalpy (ΔH_{cal}) is the total integrated area under the thermogram peak which, after appropriate baseline correction, represents the total heat energy uptake by the sample undergoing the transition. The van't Hoff enthalpy (ΔH_{VH}) is an independent estimate of the enthalpy of the transition, based on an assumed model for the process. Here one simply uses the area under the C_p peak at any temperature, divided by the total area, as a measure of the fraction or extent of unfolding that has occurred at that temperature. The relationship between ΔH_{cal} and ΔH_{VH} can sometimes provide insights not accessible from ΔH_{cal} alone, for example, if a protein is composed of two identical domains which unfold independently with the same T_m and ΔH_{cal}, the ratio $\Delta H_{cal}/\Delta H_{VH}$ will be 2.0, while it would be 1.0 if the protein had only a single domain. If, on the other hand, the protein dimerized and the dimer underwent only a single coupled transition then $\Delta H_{cal}/\Delta H_{VH}$ ratio will be 0.5. It is clear from this that the calorimetric heat ΔH_{cal} refers to heat change per mole while ΔH_{VH} is heat change per unfolding unit (called cooperative unit). Thus the ratio $\Delta H_{cal}/\Delta H_{VH}$ can, in simple cases, be thought of as the number of cooperative units per mole[17].

2.11 Electron Microscopy techniques

Electron microscopy is an important viewing technique to examine biological materials (such

as organisms and cells), a variety of large molecules, medical biopsy samples, metals and crystalline structures, and the characteristics of various surfaces. It can be defined as a specialized field of science that employs the electron microscope as a tool and uses a beam of electrons to form an image of a specimen.

Electron microscopy is operated in the vacuum and focuses the electron beam and magnifies images with help of electromagnetic lenses. It has much higher magnification or resolving power than normal light microscope, due to increasing the velocity of electrons results in a shorter wavelength and increased resolving power.

The two basic types of electron microscopes are the scanning electron microscope and the transmission electron microscope. The relatively high magnification range of both basic types of electron microscopy allows investigators to detect in specimens much greater detail than those examined by light microscopy.[18]

The Transmission Electron Microscopy (TEM) projects electrons through an ultrathin slice of the specimen and produces a two dimensional image. The sample is bombarded by a highly focused beam of single-energy electrons. The electrons are accelerated by an electric potential and focused by electromagnetic lenses onto the sample. The beam has enough energy for the electrons to be transmitted through the sample. The transmitted beam contains information about electron density, phase and periodicity; this beam is used to form an image.

The scanning electron microscope reveals information about the sample, for example, external morphology, chemical composition, and crystalline structure and orientation of materials making up the sample. The electrons interact with the sample within a few nanometers to several microns of the surface, depending on beam parameters and sample type. Electrons are emitted from the sample primarily as either backscattered electrons or secondary electrons. Secondary electrons are the most common signal used for investigations of surface morphology, which provides one of the main signals for image formation in the scanning electron microscopy. Electrons of low energy (up to 50 eV) may be ejected from the specimen; these are secondary electrons. Once these electrons escape from the sample surface, they are typically detected by a photomultiplier detector. The SEM image formed is the result of the intensity of the secondary electron emission from the sample at each x,y data point during the rastering of the electron beam across the surface

Some energy from the beam electrons is transferred to the conduction band electrons in the sample, providing enough energy for their scape from the sample surface as secondary electrons. Since these electrons travel farther into the sample than the secondary electrons, they can emerge from the sample at a much larger distance away from the impact of the incident beam which makes their spatial distribution larger.

This occurs in a vacuum environment ranging from 10^{-4} to 10^{-10} Torr. The electrons are guides to the sample by a series of electromagnetic lenses in the electron column. The resolution and depth of field of the image are determined by the beam current and the final spot size, which are adjusted with one or more condenser lenses and the final, probe-forming objective lenses. The lenses are also used to shape the beam to minimize the effects of spherical aberration, chromatic aberration, diffraction, and stigmatism.

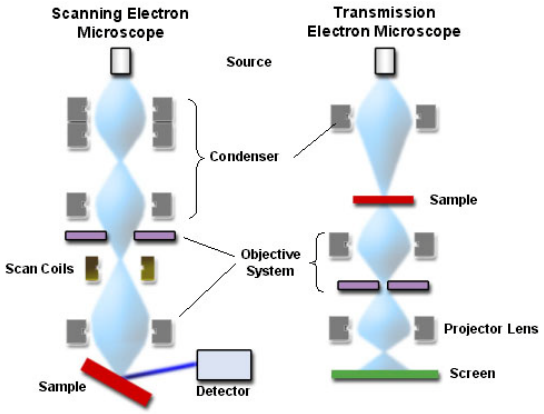

Figure 2.2: Scheme of Scanning Electron Microscope (SEM) and Transmission Electron Microscope (TEM).

2.12 Atomic Force Microscopy (AFM)

The AFM is a powerful new tool that consists of scanning a sharp tip on the end of a flexible cantilever across a sample surface while maintaining a small, constant force. The main difference between these types of microscopy and the AFM is, as the name suggests, interactive forces between the sample and the tip. The force most commonly associates with atomic force microscopy is an interatomic force called the van der Waals force. This technique has the advantage of imaging almost any type of surface, including surfactants, polymers, ceramics, and biological samples either resolution at an atomic scale.

AFM technique mainly uses a laser beam deflection system, where a beam is reflected from the back of the reflective AFM lever and onto a position-sensitive detector. The tips typically have an end radius of 2 nm to 20 nm, depending on tip type and are microfabricated from Si or Si_3N_4.

It is known that the AFM technique is based on the forces between the tip and sample, but this force is not measured directly. The force is calculated by maintaining a constant cantilever deflection; the force between the tip and the sample remains constant, and is calculated from Hook's law, which is given by:

$$F = -kx \tag{2.18}$$

where F is the force, k is the spring constant, and x is the cantilever deflection. A plot of the laser deflection versus tip position on the sample surface provides the resolution of the hills and valleys that constitute the topography of the surface. A scheme can be seen in Figure 2.3:

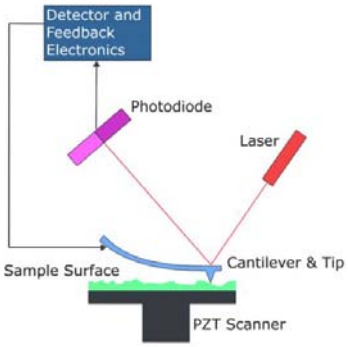

Figure 2.3: A deflection AFM. The cantilever deflection is detected by a reflected laser beam and photodiode. The tip is integrated with the cantilever. The substrate is moved in the xyz directions by a piezoelectric scanner. A feedback loop controls the rate of z movement.

In AFM, different modes of operation are applicable to specific application requirements: *Contact mode*, *Non-Contact mode* and *Tapping mode*. The two most commonly used modes of operation are *Contact Mode AFM* and *Tapping Mode AFM*, which are conducted in air or liquid environments.

Contact Mode consists of raster-scanning the probe or sample while monitoring the change in cantilever deflection with the split photodiode detector. A feedback loop maintains a constant cantilever deflection by vertically moving the scanner at each (x,y) data point is stored by the computer to form the topographic image of the sample surface. This feedback loop maintains a constant force during imaging.

Tapping Mode depends on the detection of amplitude of a driven cantilever oscillation; the cantilever is driven to oscillate close to its resonance frequency (~300 kHz) and lightly "tapping" the tip on the surface during the scanning. The laser reflection method is used to detect the root-mean-square (RMS) amplitude of the cantilever oscillation. A feedback loop maintains constant amplitude by moving the scanner vertically at every (x,y) data point. By maintaining constant oscillation amplitude a constant tip-sample interaction is maintained during imagining.

The advantage of Tapping Mode over contact mode is that it eliminates the lateral, shear forces present in contact mode. This enables Tapping Mode to image soft, fragile, and adhesive surfaces without damaging them, which can be a drawback of contact mode AFM.

Chapter 3:

THEORETICAL ASPECTS

3.1 Self-Assembly of Surfactants

3.1.1 Introduction

Surfactants are characterized by the presence of two moieties in the same molecule, one polar and other nonpolar. The polar group may carry a positive or negative charge or both of them, giving rise to cationic, anionic or zwitterionic surfactants respectively, or may contain ethylene oxide chains or sugar or saccharide-type groups, as in the case of nonionic surfactants[19]. The nonpolar part of the molecule is generally a hydrocarbon chain or may consist of a fluorocarbon chain, aromatic rings, etc. The most significant characteristic of this type of amphiphile is the tendency to adsorb very strongly at the interface between air and water; in doing so, the hydrophobic part of the molecule can escape from the aqueous environment whilst the hydrophilic head group can remain immersed in water. Such substances are said to be strongly surface-active because they lower the surface (or interfacial) tension, γ [20]

As surfactant is added to water, the molecules dissolve. In most cases, an increase in temperature aids this process but this is not universally true. In solution, the polar head groups are hydrated, they can take part in the H-bonding structure of water. The hydrophobic tails, on the other hand, cannot do this and we can visualize a discontinuity in the structure of the water around these tails. This has been referred to as a “cage” and cited as the origin of the “hydrophobic effect”[21], which is related with the fact that the contact between water molecules and hydrocarbon or fluorocarbon chains are minimized and the entropy of the system is increased. Furthermore, there is an additional enthalpic term associated to the van der Waals clustering of the chains.

The formation of micelles is an aggregation process which often occurs at about the same surfactant concentration. These are structures in which the hydrophobic portions of the surfactant molecule associate together to form regions from which the solvent, water is excluded. The hydrophilic head groups remain on the outer surface to maximize their interaction with the water and the oppositely charged ions (called counterions). A significant fraction of the counterions remain strongly bound to the head groups so that the lateral

repulsive force between those groups is greatly reduced. The precise structure of the micelle depends upon the temperature and the concentration but also on the details of the molecular structure: size of head group, length and number of hydrocarbon chains, presence of branches, double bonds or aromatic rings, etc[22].

At low temperatures, the solubility is low with surfactant molecules in equilibrium with the surfactant solution. There is a critical point known as the *Krafft* point, and at temperatures higher than the value at this point (the Krafft temperature) the solubility appears to increase rapidly and the solution phase consists of surfactant aggregates or micelles, as well as single molecules. Below the Krafft temperature, micelles are not formed. The concentration at which micelles are produced is known as the critical micelle concentration (*cmc*). The latter varies with temperature about the Krafft temperature. The *cmc* is marked by quite sharp changes in slope when various transport and equilibrium properties (like electrical conductivity and surface tension) are plotted against concentration.

The shape of micelle produced in aqueous media is of importance in determining various properties of surfactant solution. Changes in temperature, concentration of surfactant, additives in the liquid phase, and structural groups in the surfactant may all cause change in the size, shape, and aggregation number of the micelle, with the structure varying from spherical through rod- or dislike to lamellar in shape (Fig.3.1.1).

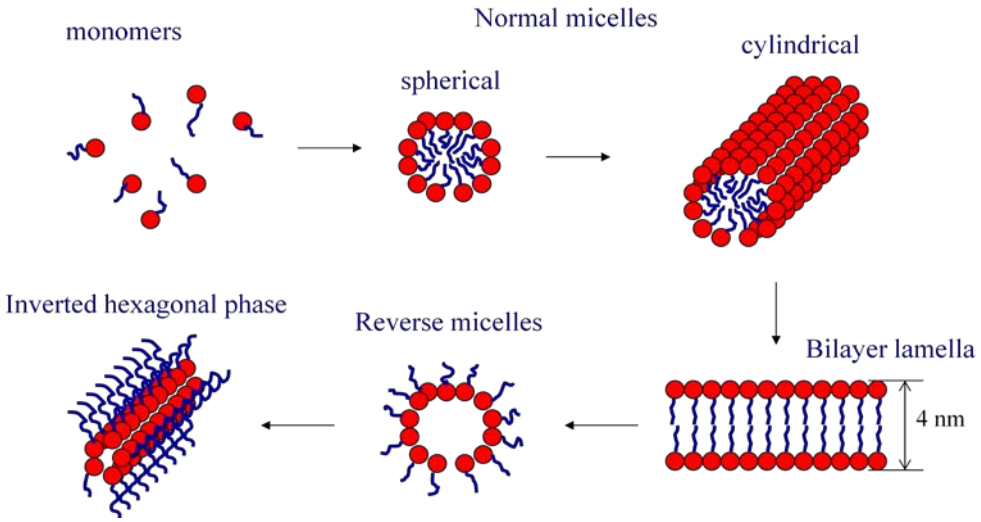

Figure 3.1.1: Different structures of surfactants increasing the concentration.

A theory of micellar structure, based upon the geometry of various micellar shapes and the space occupied by the hydrophilic and hydrophobic groups of the surfactant molecules, has been developed by Israelachvili, Mitchell and Ninham (1976, 1977). The volume V_H occupied by the hydrophobic groups in the micellar core, the length of the hydrophobic group in the core l_c, and the cross-sectional area a_0 occupied by the hydrophilic group at the micelle-solution interface are used to calculate a packing parameter, which determines the shape of the micelle:

$$P = \frac{V_H}{l_c a_0} \tag{3.1.1}$$

where $V_H = 27.4 + 26.9n\ \text{Å}^3$, n is the number of carbon atoms of the chain embedded in the micellar core (the total number of carbon atoms in the chain, or one less); $l_c \leq 1.5 + 1.265n\ \text{Å}^3$, depending upon the extension of the chain. For saturated, straight chains, l_c may be 80% of the fully extended chain[22]. Amphiphilic molecule tends to aggregate into: monomers, spherical micelles ($0 < P \leq 1/3$), cylindrical micelles ($1/3 \leq P \leq 1/2$), vesicles ($P \leq 1$), lamellae ($P \approx 1$), and inverse (reversed) micelles ($P > 1$).

The shape of a micelle, as mentioned earlier, is related to its size. The size usually expressed in terms of an aggregation number. From geometric considerations, the aggregations numbers N_{agg} of micelles in aqueous media should increase rapidly with increase in the length of the hydrophobic group l_c of the surfactant molecules, and decrease with increase in the cross-sectional area of the hydrophilic group a_0 or the volume of the hydrophobic group V_H. For example, in a spherical micelle in aqueous media, the surface area:

$$N_{agg} = 4\pi(l_c + \Delta)^2/a_0 \tag{3.1.2}$$

where Δ is the added length of the radius of the sphere due to the hydrophilic group. Similarly, the volume of the hydrophobic core:

$$N_{agg} = \frac{4}{3}\pi(l_c)^3/V_H \tag{3.1.3}$$

An increase in the temperature appears to cause a small decrease in the aggregation number in aqueous medium of ionics, presumably because a_0 is increased due to thermal agitation. If small amounts of hydrocarbons or long-chain polar compounds are added to an aqueous solution of a surfactant above its *cmc*, these normally water-insoluble materials may be solubilized in the micelles. This solubilization generally causes an increase in the aggregation number of the micelle, and as the amount of material solubilized by the micelle increases, the aggregation continues to increase until the solubilization limit is reached.

3.1.2 Factors affecting the critical micellar concentration

Among of factors known affect the cmc in aqueous solution, such as the structure of surfactants, the presence of added electrolyte in solution, the presence in solution of various organic compounds, the presence of a second liquid phase, and the temperature of the solution.

Among of factors which affect the cmc in aqueous solution, the structure of surfactants, the presence of added electrolyte in solution, the presence in solution of various organic compounds, the presence of a second liquid phase, and the temperature of the solution have the greater impact on it.

In general, the cmc in aqueous media decreases as the hydrophobic character of the surfactant increases.

3.1.3 The Hydrophobic Group

An increase in the length of the hydrocarbon chain in the unbranched portion of the chain decreases the cmc. Generally, used rule for ionic surfactants is that the cmc is halved by the addition of one methylene group to a straight-chain hydrophobic group attached to a single terminal hydrophilic group. When the hydrophobic group is branched, the carbon atomos on the branches appear to have about one-half the effect of carbon atoms on a straight chain. When carbon-carbon double bonds are present in the hydrophobic chain, the cmc is generally higher than that of the corresponding saturated compound, with the cis isomer generally having a higher cmc than the trans isomer. Similarly, introduction of polar groups such as –O- or –OH- into the chain normally increases the cmc in aqueous medium at room temperature.

3.1.4 Hydrophilic Group

In aqueous medium, ionic surfactant have much higher cmc than nonionic surfactants containing equivalent hydrophobic groups. This is due to electrostatic repulsion between the head groups of the neighboring surfactant monomers within the micelles. Zwitterionics appear to have slightly smaller cmc than ionics with the same number of carbon atoms in the hydrophobic group.

Surfactants containing more than one hydrophilic group in the molecule show larger cmc than those with one hydrophilic group and the equivalent hydrophobic group.

For a given chain length, variation of the actual ionic headgroup present on the surfactant can markedly affect the cmc. The cmc in alkyl ionic surfactants follows the order: aminium salts > carboxylates > sulfonates > sulfates[23].

3.1.5 Effect of Counterions

The critical micellar concentration in aqueous solution reflects the degree of binding of the counterions to the micelle. Increased binding of the counterion, in aqueous systems, causes a decrease in the cmc of the surfactant. The extent of adsorption of counterios depends also on the properties of the counterions. For example, an increase in the valency, as well as in the polarizability of the counterions, decreases the cmc. An increase in the hydrated radius, on the other hand, increases the cmc. For a given hydrophobic chain and anionic head group, such as dodecylsulfates, the cmc decreases in the order: $Li^+ > Na^+ > K^+ > Cs^+ > Mg^{2+} > Ca^{2+}$. For cationic series, dodecyltrimethyl ammonium, for example, the cmc decreases as: $F^- > Cl^- > Br^- > I^-$[19].

3.1.6 Effect of additives

The electrolyte effect is more pronounced for anionic and cationic than zwitterionic surfactants and more pronounced for zwitterionics than nonionics. This effect consist of in aqueous solution the presence of electrolyte causes a decrease in the cmc of most surfactants. The dependence of cmc on electrolyte level can be described using the following equation:

$$\log cmc = -A \log C_e + B \tag{3.1.4}$$

where A and B are constants and C_e is the total concentration of the counterions. Zwitterionics and nonionics exhibit less dependence on electrolyte levels than ionics surfactants, and the corresponding relation is given by:

$$\log cmc = -K\, C_s + constant \tag{3.1.5}$$

where K is a constant for a particular surfactant-electrolyte system at a given temperature and C_s is the salt concentration.

Addition of an oppositely charged surfactant in small amounts to a given ionic surfactant can also result in a significant decrease in the cmc[24]. Note, however, that addition of equimolar amounts of oppositely charged surfactants can result in precipitation and the region of homogeneus solution is restricted to very low total concentrations.

3.1.7 Temperature effect

The process of micellization itself is dependent on temperature in a complex way. Ionics surfactants typically exhibit a minimum in cmc with increase in temperature. This behavior is a consequence of the decrease in hydrophobicity of the surfactant molecules, an initial decrease in the cmc with the temperature. The increase in temperature causes a decrease in the hydration of the hydrophilic head group, favoring micelles formation. At the same time the increase in temperature causes a breakdown in the structured water molecules surrounding the hydrophobic alkyl chains, disfavoring the micellization process and the cmc increasing with temperature. The U-shaped curve observed is the outcome of the interplay of these two effects and was observed for different ionic and nonionic surfactants[25]. The effect of counterions is even more relevant on the minimum due to their different hydration capabilities. It was postulated that the cmc of ionic surfactants should follow the Hofmeinster series[26,27].

List of papers included in this section

- On the Self-Assembly of a Highly Selective Benzothiazole-Based TIM Inhibitor in Aqueous Solution.

- Self-assembling drugs: A new therapeutic strategy.

- Hydrogenated/fluorinated catanionic surfactants as potential templates for nanostructure design.

3.2 Protein-Ligand Interactions

3.2.1 Introduction

For decades, researches focused their attention on functions and characteristics of proteins and protein surfactants mixtures based on their widespread applications (purification of receptors in their active forms, solubilization of enzymes lipoprotein, SDS-PAGE, isolation of hydrophobic proteins, drug delivery, or cosmetic industry). The recent flurry of research activity in biomedical, bioelectronics, or molecular templating of these system claims for substantial progress in determining the physical principles that underlie these phenomena.

Proteins are structures with a great importance. Many medical, health and biological projects and advances are concerned with these materials. The stability and functionality of proteins are strongly dependent on the medium properties.

3.2.2 Protein structure

Proteins are linear sequences of amino acids linked together by peptide bonds. In solutions contain a mixture of different types of chemical groups, such as non-polar, polar and electrical charged. For this reason it is possible to characterize a typical protein as an amphoteric molecule and it is not surprising that most small amphiphilic molecules will interact strongly with proteins.

Protein structures contain four levels of complexity: primary, secondary, tertiary and, sometimes but not always, quaternary. Each level has its own characteristics, and all levels are related to each other and depend on each other, together creating an extremely complex network. The primary structure (Fig.3.2A) is built up by the linear sequence of amino acids as joined together by peptide bonds (and includes any disulfide bond). The peptide bond is a chemical, covalent bond formed between the α-amino group of one amino acid and the α-carboxyl group of another. Disulfide bonds are often present in extracellular proteins, but are rarely found in intracellular proteins. These are primarily disulfide bonds between cysteine residues that are adjacent in space but not in the linear amino acid sequence. Amino acid compositions vary enormously from protein to protein. Except in certain special cases, the various amino acids are distributed apparently randomly along the polypeptide chain. All

properties of a protein are derived from the primary structure, the linear sequence. They may be classified into three main types: fibrous, globular and disorderer.

The secondary structure in a protein is the regular folding of regions of the polypeptide chain. The two most common types of protein fold are the α-helix (Fig.3.2B) and the β-sheet (Fig.3.2C). In the rod-like α-helix, the amino acids arrange themselves in a regular helical conformation. The β-sheet structure is a pleated sheet composed of β-strands in parallel or antiparallel arrangement depending on whether they run in the same direction or in opposite directions, respectively. β-pleated sheets are always slightly curved and, if several polypeptides are involved, the sheet can close up to form a β-barrel. Regions of the polypeptide chain that are not in a regular secondary structure are said to have a coil or loop conformation. The secondary structure elements fold into structural units, called domains, which comprise the tertiary structure.

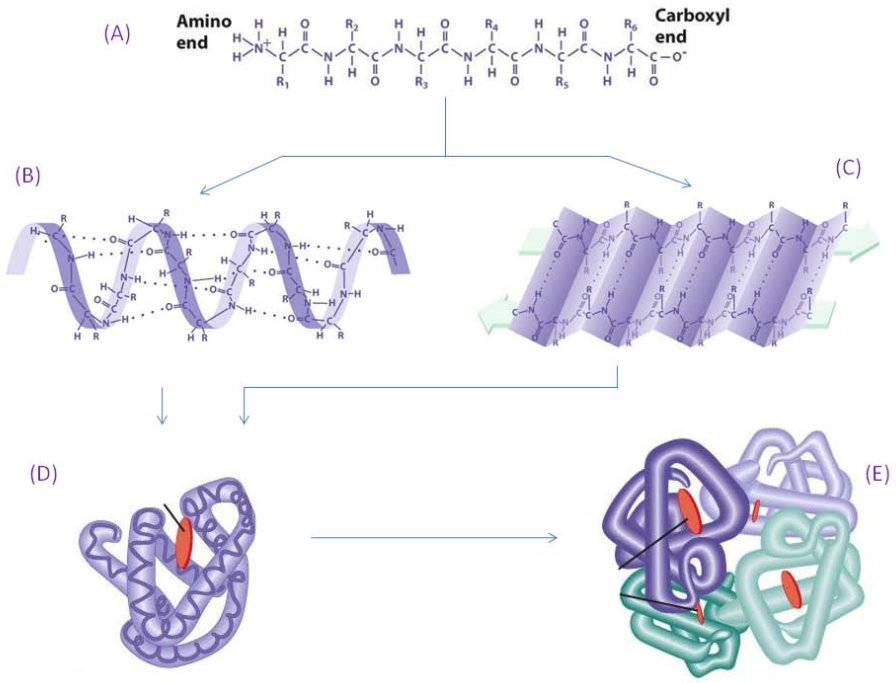

Figure 3.2: Protein structure (A) primary structure. Secondary structure: (B) α-helix (C) β-sheets. (D) Tertiary structure. (E) Quaternary structure.

Tertiary structure refers to the spatial arrangement of amino acids that are far apart in the linear sequence as well as those residues that are adjacent (Fig.3.2D). This structure is maintained by four types of interaction between side chain groups of amino acids residues: hydrogen bonding, ionic interaction between oppositely charged group, hydrophobic interactions and disulfide cross-linkages.

Proteins containing more than one polypeptide subunits exhibit quaternary structure, referring their arrangement in space (Fig.3.2E).

3.2.3 Protein-Ligand interactions

The interaction of small molecules (surfactants, drug molecules and denaturants) with macromolecules with specific receptors sites on surfaces of supramolecular organizations of biological systems in one of the extensively studied phenomena in recent biochemical research as it plays a role in a vast range of vital biochemical phenomena. As mentioned above, proteins are formed by a mixture of amino acids in unique combinations. The different nonpolar, polar and charged properties of the amino acids lead to complex interactions that determine the proteins' secondary, tertiary and quaternary structure. Due to the hydrophobic and hydrophilic properties of amino acids, a protein exhibits a dualism that makes small amphiphilic molecules interact with proteins.

The native structure is the three-dimensional arrangement of the functional protein when it is located in its natural environment. Changes in the environment, e.g., a rise in temperature, variation of pH or addition of denaturants, may cause denaturation of the protein. When a protein is denaturated, the characteristic three-dimensional arrangement is disrupted (the protein unfolds), and, consequently its biological function is lost.

Proteins interact strongly with oppositely charged surfactants in aqueous solution due to a hydrophobic attraction between the surfactant tail and hydrophobic region on the surface and in the interior of the protein, as well as an electrostatic attraction between the headgroup of the surfactant and the protein (amphiphilic molecules)[28]. Many pharmacologically active compounds are amphiphilic molecules, and exhibit the same behavior as traditional surfactants, i.e., they tend to self-associate to form micelles when dispersed in aqueous solutions[29].

Much of biotechnological, medical and drug delivery systems aims to predict their behavior on the basis of the set of molecules involved, mainly proteins and drugs. Understanding the interactions between these molecules is therefore crucial to such efforts. Although many thousands of interactions are known, precise molecular details are available for only a tiny fraction of them. The difficulties that are involved in experimentally determining atomic structure for interacting proteins make predictive methods essential for progress. Structural details can ultimately turn abstract system representations into models that more accurately reflect biological reality[5].

Understanding protein-ligand interaction is central, for example, to drug design and discovery of new medicines to benefit human health, and as well as, stabilizers functions in natural systems like in processed food used to stabilize emulsions, and as stabilizers for inorganic particles in paints or photographic films. A high level of steric complementary between the protein and the ligand is described by the lock-and-key paradigm and a high degree of complementary of hydrophobic and polar parts of both entities, namely, the binding site of the protein and the ligand. There is usually high complementary of the surface properties between the protein and the ligand. Lipophilic parts of the ligands are most frequently found to be in contact with lipophilic part of the protein. Polar groups are usually paired with suitable polar protein groups to form hydrogen bonds or ionic interactions. The experimentally determined hydrogen bond geometries display a fairly small scatter-in other words, the hydrogen bond geometry is strongly preserved. With very few exceptions, there are not repulsive interactions between the ligand and the protein. Direct interactions between the protein and the ligand are very important for binding, and these binds in an energetically favorable conformation[30]. The most important direct interactions are hydrogen bonds, ionic interactions, hydrophobic interactions, cation-π interactions and metal complexation. Therefore, in the ligand design process one has to ensure that polar functional groups, either of the protein or the ligand, will find suitable counterparts if they become buried upon ligand binding.

Amphipatic molecules such as surfactants interact with proteins and to alter their structure, physico-chemical and rheological properties. Therefore, understanding of interaction between the surfactants and proteins in the bulk and the interface, formation of protein-surfactant complexes and displacement of protein molecules from the interface by surfactant molecules is important from scientific as well as practical viewpoints. With anionic surfactants, the interaction is predominantly electrostatic, and exist different models that explain how anionic surfactant interact with proteins. Compared to the anionics, cationic surfactants weakly

interact with the proteins as a consequence of smaller relevance of electrostatic interactions at the pH of interest. However, the binding isotherms of both types of surfactants have been found to be similar. The surfactant ions bind to groups of opposite charge on the protein and hydrophobic interactions between the aliphatic chains of the surfactants and the non polar protein surface regions that are adjacent to charged sites occurs (Fig. 3.3). These initial interactions cause the protein unfold, which result in the exposure of more binding sites, and, as the surfactant concentration is increased, binding becomes cooperative, and ultimately saturation occurs[31]. Compared ionics, nonionic surfactants bind weakly to the proteins due to the absence of electrostatic interactions, thus making micelle formation in bulk more favourable.

The pH has also an effect on the net charge of the protein, which depends on its isoelectric point (pI). Below pI (when the net charge in aqueous solution is zero), the protein has a positive net charge, and interactions with anionic surfactants generally results in precipitation of the complexes, owing to neutralization of the charges. Above pI, the negatively charged protein forms stable soluble complexes. To a first approximation, protein solubility in water increases with the proportion of polar and charged groups, and decreases with increasing molecular weight. Most protein show a minimum in solubility at the isoelectric point where electrostatic interactions are minimal[19].

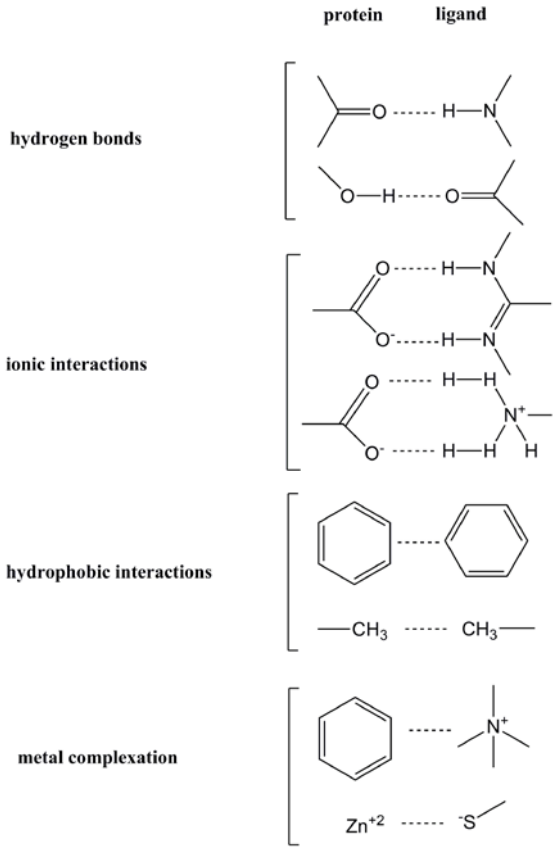

Figure 3.3: Typical non-bonded interactions found in protein-ligand complexes.

However, this short characterization is only a part of the story: ligand and binding site flexibility, distortion energies, desolvation effects, entropy, molecular electrostatic field complementary, and other effects are often qually important.

Thus, the interpretations of data in the extensive literature on the unfolding of proteins in aqueous solution by amphiphilic molecules (drugs) have been recently analyzed [32,33]. During the 2000s improved methods were revised for improving assumptions associated with incomplete equilibrium constants, contradict model-free interpretation of the data and misuse of the Van't Hoff relation is really common. In addition, the notion that proteins are simply three-dimensional, compact objects has been questioned: while proteins need to keep their specific

native fold structure thermally stable, the native fold displays the ability to perform large amplitude conformational changes that allow proper function.

Unfolding transition can be monitored by different techniques. Indeed, the possibility that proteins may be characterized by fractal geometry rather than as a compact three-dimensional object appeared in a variety of measurement. New techniques such as “Dip Pen Nanolitography” have been extended to protein arrays with features as small as 45 nm. The ability to identify small molecule ligands for any protein of interest has far-reaching implications, both for the elucidating of protein function and for the development of novel pharmaceuticals[34].

3.2.4 Stabilization of Protein structure

Thermodynamically, as a first approximation, the denaturation process can be considered as a transition between the two macroscopic states: The native state (N) and a denaturated state (D):

$$N \rightleftharpoons U \tag{3.2.1}$$

The equilibrium between the native and denatured state is defined by:

$$K_0 = [U]/[N] \tag{3.2.2}$$

where K_0 is the unfolding equilibrium constant for the protein in absence of ligand.

Free energies and other thermodynamic parameters are relative quantities that depend on an arbitrary choice of reference or standard state. It turns out that the equilibrium constant (K_0) for any process is related to the standard Gibbs free energy change:

$$\Delta G^0 = -RTln(K_0) = \Delta H^0 - T\Delta S^0 \tag{3.2.3}$$

where R correspond to the universal gas constant and T is the absolute temperature. The Gibbs energy is dependent on temperature. Is important to know that this equation involve the equilibrium between the native and denatured state regardless of the possible presence of intermediate states. ΔH^0 and ΔS^0 are strongly temperature-dependent so that the free-energy change is better written as:

$$\Delta G^0 = \Delta H_R^0 - T\Delta S_R^0 + \Delta C_P \left\{(T - T_R) - T \ln\left(\frac{T}{T_R}\right)\right\} \quad (3.2.4)$$

where the subscript R indicates the value of ΔH^0 and ΔS^0 at a reference temperature, T_R, and ΔC_P is the heat-capacity change.

The result of significant ΔC_P is that the free energy is not a linear function of temperature. Rather, it shows significant downward curvature and has a maximum value at some temperature, often near physiological. If T_R is equal to the midpoint for thermal denaturation, T_m, then ΔG^0 is equal to zero and ΔS^0 is just $\Delta H^0/T_m$. Thus the equation can be rewritten as:

$$\Delta G^0 = \Delta H_m \left(1 - \frac{T}{T_m}\right) + \Delta C_P \left\{(T - T_m) - T \ln\left(\frac{T}{T_m}\right)\right\} \quad (3.2.5)$$

where ΔH_m is the value of ΔH^0 at T_m.

3.2.5 Thermodynamic of binding

Application of Le Chatelier's principle, or simple equilibrium considerations, shows that if any ligand (small molecule or other protein or macromolecule) binds preferentially to the folded or native form of the protein, then this will stabilize the folded state, and unfolding of the protein will become progressively less favourable as ligand concentration increases. Conversely, ligands that bind preferentially to the unfolded protein will destabilize the fold and will encourage unfolding.

The binding of a ligand (L) to a single site on a protein (N) is defined by the equilibrium:

$$N + L \rightleftharpoons PL \tag{3.2.6}$$

with an association constant:

$$K = [N][L]/[NL] \tag{3.2.7}$$

The binding of surfactants to proteins can be treated as a multiple-equilibrium phenomenon which can be written in terms of the native protein (N), the surfactant (S) and the complexes (NS_n):

$$N + S \rightleftharpoons NS_1 \tag{3.2.8}$$

$$NS_1 + S \rightleftharpoons NS_2 \tag{3.2.9}$$

$$NS_{n-1} \rightleftharpoons NS_n \tag{3.2.10}$$

where n is the maximum number of sites available on the protein. For such multiple equilibria, if the equilibrium constants K for all the steps are identical, then,

$$K^n = \frac{[NS_n]}{[N][S]^n} \tag{3.2.11}$$

The number of surfactant molecules bound per protein molecule, υ, is given by:

$$\nu = \frac{n[SL_n]}{[S]+[NS_n]} = \frac{n(K[S])^n}{1+(KS)^n} \tag{3.2.12}$$

More realistically, however, ligand binding to one site may lead to an increase or decrease in the affinities of the other sites, that is, there may be positive or negative cooperativity. This is allowed by empirically by introducing a cooperativity coefficient n'. The general expression for v then becomes:

$$\upsilon = \frac{n(K[S])^{n'}}{1+(K[L])^{n'}} \tag{3.2.13}$$

In positively cooperative binding $n' > 1$. A value of n' less than one represents negatively cooperative binding, the binding of one ligands weakens the binding of subsequent ligands. If n' is equal to one there is no cooperativity.

Interesting differences occurs in the binding isotherms for ionic and nonionic surfactant. The binding of charged surfactant molecules to protein can be predict in two distinct stages. Initially, the surfactant ligand binds to specific sires of the protein surface. One expect an electrostatic interactions formed between the charged group of the ionic surfactants and the opposite charged amino acid residues of the protein, together with a hydrophobic interaction between the aliphatic chains of the surfactant and the nonpolar regions on the protein surface that are adjacent to charged sites [35]. In the second stage of binding by anionic surfactants, the protein unfolds to expose its hydrophobic interior and hence further potential binding sites. In this nonspecific cooperative binding region the main driving force is the hydrophobic interaction between the surfactant tails and the nonpolar residues of the unfolded protein[36]. Nonionic surfactants exhibit nonspecific hydrophobic protein-surfactant interactions near the *cmc*, but specific binding does not occur except in certain special cases[37,38].

The number of ligand molecules capable of binding to a single protein molecule is large, and the binding isotherms take the form of plots of the average number of bounds ligands per protein molecule as a function of the concentration of unbound ligand molecules in aqueous solution.

3.2.6 Ligand binding and folding equilibrium

For the simplest case in which a ligand molecule (L) binds specifically to a single site on the native folded protein (N) the equilibria apply is represented by the equation (3.2.6) and with its dissociation constant associated (eq.3.2.7). The unfolding process is represented by the equation (3.2.1) with its respectively unfolding equilibrium constant (eq.3.2.2).

In general the effective unfolding equilibrium constant (K_{unf}) is given by the ratio of the total concentrations of unfolded to folded species:

$$K_{unf} = [U]/([N] + [NL]) = K_0/\{1 + ([L]/K)\} \approx K_0 K/[L] \qquad (3.2.14)$$

where the final approximate form applies only at high free ligand concentration ($[L] > K$). In this case K_{unf} decreases and the folded form become more stable with increasing ligand concentration. This can be expressed alternatively in free energy terms:

$$\Delta G_{unf} = -RT \ln\left(K_{unf}\right) = \Delta G_{unf,0} + RT \ln(1 + [L]/K)$$
$$\approx \Delta G_{unf,0} + \Delta G_{diss,N} + RT \ln[L] \qquad ([L] \gg K) \qquad (3.2.15)$$

where $\Delta G_{unf,0}$ is the unfolding free energy of the unliganded protein, and $\Delta G_{diss,N} = -RT \ln K$ is the standard Gibbs free energy for dissociation of the ligand from its binding site of the native protein. The approximate form again applies only at high ligand concentrations.

The same approach can be applied to situations where ligand binds only to the unfolded protein:

$$U + L \rightleftharpoons UL \qquad (3.2.16)$$

$$K_U = [U][L]/[UL] \qquad (3.2.17)$$

for which:

$$K_{unf} = [U] + [UL]/(N) = K_0\big(1 + ([L]/K_U)\big) \approx K_0[L]/K_U \qquad (3.2.18)$$

and:

$$\Delta G_{unf} = -RT\ln\big(K_{unf}\big) = \Delta G_{unf,0} - RT\ln(1 + [L]/K_U)$$

$$\approx \Delta G_{unf,0} - \Delta G_{diss,U} - RT\ln[L] \qquad (for\ high\ [L]) \qquad (3.2.19)$$

This illustrates the destabilizing effect of a reduction in unfolding free energy as ligand binds to the unfolded polypeptide.

List of papers including in this section

- Assessment of interactions between four proteins and benzothiazole derivatives by DSC and CD.
- Mechanisms of fibrinogen-acebutolol Interactions: Insights from DSC; CD and LS.
- Surface characterization and AFM imaging of mixed fibrinogen-surfactant films.
- Fibrinogen stability under surfactant interaction
- Investigating the effect of an arterial hypertension drug on the structural properties of plasma protein

3.3 Hydrogels

3.3.1 Introduction

Hydrogels are cross-linked 3-D networks containing covalent bonds (produced by the reaction of one or more comonomers), physical cross-links (due to chain entanglements), hydrogen bonds, strong van der Waals interactions, and crystallite associations (bringing two or more macromolecular chains) [39]. These structures have been recently attracted much interest in the biomaterials sector because of their ability to entrap large quantities of water or biological fluids. This high water content mimics the natural environment, which gives them excellent biocompatibility while the three-dimensional network provides mechanical support. Recently the ability of proteins and peptides to self-assemble into ordered supramolecular architecture on the meso to macroscopic length scales has attracted considerable attention in the development of novel biomaterials due to their potential biocompatibility and biodegradability. Consequently they have found a wide range of applications in the medical, pharmaceutical and biomaterials sectors (drug delivery, materials for artificial organs) [40-42].

The hydrogels properties can be modulated by varying the synthetic factors, such as vessel, reaction time, reaction temperature, monomer type, type of crosslinker, monomer concentration, and type and amount of initiator. Based on different aspects of hydrogels their classification may be based on the source:

- Natural, synthetic gels or hybrid hydrogels: composed of synthetic and natural molecules.
- Nature of the crosslinking: covalent or physical gels
- Nature of the network: homopolymer networks, copolymer networks, interpenetrating networks or double networks.
- Physical structure: homogeneous (optically transparent) microporous, and macroporous hydrogels
- On their fate in an organism: degradable and nondegradable hydrogels.

There are three classes of molecules that can be used to produce hydrogels: polymers, peptides and proteins. Polymers have been used extensively to create hydrogels; however many are not adhesive to cells. Consequently, recent efforts have focused on modifying the material to induce biocompatibility for tissue engineering application [43-46].

3.3.2 Hydrogels Structure

Based on the nature of the crosslinking force, hydrogels can be categorized as chemical (covalent) or physical gels. In chemical hydrogels the network of chemical links joining different chains can be obtained by cross-linking bulk polymers or polymers in solution. Due to the covalent crosslinks, chemically crosslinked hydrogels generally have high mechanical strength. On the other hand, the chemical reactions required to form crosslinks might potentially affect the structure and biological activity of encapsulated pharmaceuticals. Moreover, chemical crosslinking often requires crosslinking reagents or catalysts that are toxic towards cells [47-48]. Physical hydrogels chains are held together by non-permanent interactions, such as ionic interactions, hydrophobic interactions, hydrogen bonds and specific biomimetic interactions [49-52] (Figure 3.3.1). These interactions can be disrupted by changes in the environment, such as temperature, pH, ionic strength, presence of specific solutes, and stress; consequently, the formation of physical hydrogels may be reversible.

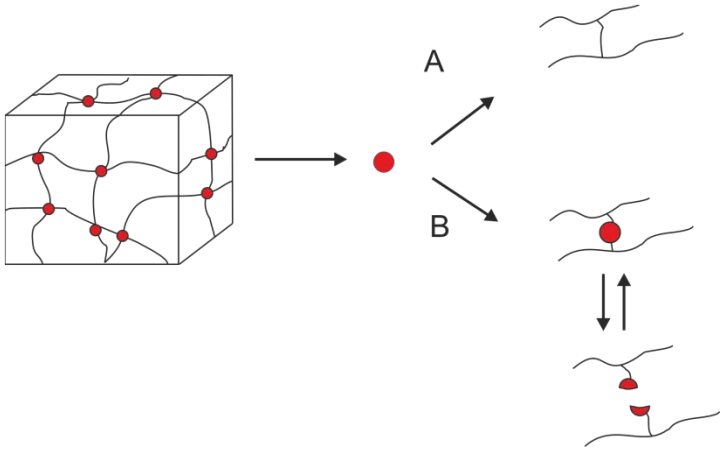

Figure 3.3.1: Schematic representation of: A) Chemical and B) Physical crosslinked hydrogels.

The properties of both chemically and physically crosslinked hydrogels can often be controlled by a wide variety of parameters, such as the number of crosslinks, the chemical structure of the polymer main chain and the water content [53]. In both cases, the density of cross-links is crucial in determining the properties and applications of the gels, as it is responsible for the swelling behavior and therefore for the combine solid-like and liquid-like characteristics [54].

The swelling capacity of a hydrogels can be determined by the amount of space inside the hydrogels network available to accommodate water. Hydrogels can also be classified as

neutral, anionic, or cationic depending on the charges of the building blocks (Fig. 3.3.2). Non-ionic hydrogels swell in aqueous medium solely due to water-polymer interaction. Cationic and anionic hydrogels swelling are dependent on the pH of the aqueous medium. At low pH cationic hydrogels display superior swelling due to their chain dissociation; the same for anionic hydrogels, at higher pH dissociate more, and hence exhibit superior swelling in neutral to basic solutions.

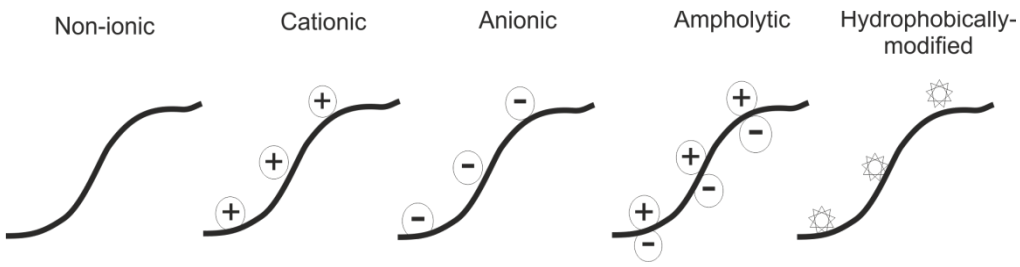

Figure 3.3.2: Different Hydrogels structures.

Interestingly, a large number of biopolymers possess property to self-structure upon temperature variation. Two different types of temperature sensitive materials can be distinguished: upper critical solution temperature and lower critical solution temperature materials. In the first case, the gelation of many biopolymers is induced by the reversible temperature-sensitive formation of intermolecular hydrogen bonds. The second class, at low temperatures, a homogeneous solution is obtained. Upon heating, aggregation of the hydrophobic groups occurs, inducing phase separation and hydrogel formation. The endothermal gelation is driven by an entropy change. In contrast with the increase in order during the aggregation of the hydrophobic segments, the entropy increase during the hydrogel formation. This is due to the large amount of water molecules released by the hydrophobic part of the polymer[55]. Gelation thus occurs spontaneously upon heating because the entropy ($T\Delta S$) compensates for the unfavorable enthalpy (ΔH).

For example, the gelation of methylcellulose (MC) is mainly induced by intermolecular, hydrophobic interactions. Consequently, these macromolecules are fully hydrated at low temperatures. Upon heating, gradual dehydration occurs, resulting in a viscosity increase. Near the transition temperature, polymer-polymer interactions are dominant and result in the formation of a polymer network[56]. It was demonstrated that MC is a promising candidate material to be applied as brain cell support, including the treatment of multiple-site injuries,

and in combination with hydroxyapatite, cellulose shows potential to be applied for bone tissue engineering [57].

Protein gels that form *in-vivo* are of profound physiological importance. The human body is approximately 65% water by mass and much of that water is contained in tissues throughout the body [58]. For example, even though dermal layers are approximately 70% water, skin is flexible enough to permit a large range of motions and also elastic enough to support the underlying tissues and fluids [59]. Another important example is the blood clot, which, despite its high water content, is strong enough to support haemostasis at an injury site while also facilitating tissue repair [60]. Both of these tissues have an underlying microscopic network of interconnected protein fibers that form through the self-assembly of collagen and fibrin respectively

Proteins are essentially polymers of amino acids and are known to form β-sheets-rich fibrils (nanometers in width and micrometer in length) that also further self-organize and entangle to form three-dimensional hydrogels under appropriate conditions. It is through that the fibrillar network is stabilized by intermolecular and/or intramolecular hydrogen bonding, electrostatic interactions and hydrophobics effects.

A typical example of a protein motif used in synthesis of hybrid hydrogels or protein-based hydrogels is the coiled-coil. Coiled-coils have been found in over two hundred native proteins [61]. Structurally the coiled-coil is a supercoil formed by two or more strands of α-helices, will be used as an example to demonstrate the potential for the design of well-organized hydrogel structures. The primary sequence of a typical coiled-coil is composed of 7-residues repeats, designed as heptads (Figure 3.3.3, left panel). The amino acid residues in a heptad are conventionally denoted as “a, b, c, d, e, f, g”. Hydrophobic residues at positions “a” and “d” form an inter-helical hydrophobic core, providing a stabilizing interface between the helices. Charged residues at positions “e” and “g” form electrostatic interactions, which contribute to coiled-coil stability and mediate specific association among helices.

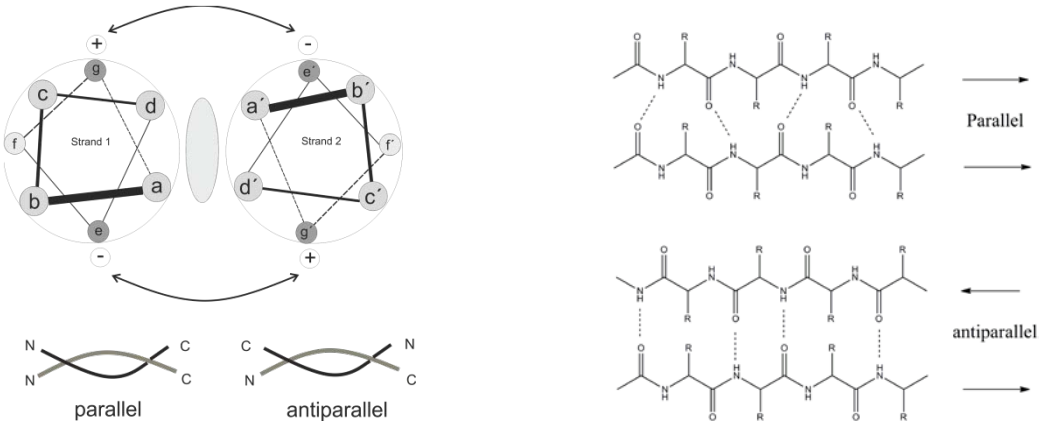

Figure 3.3.3: Left panel: helical wheel diagram of a two stranded coiled-coil. Right panel: β-sheets structure motif.

β-sheets are important structural elements in proteins. β-strands are aligned adjacent to each other and are stabilized by hydrogen bonds between the carbonyl oxygen of an amino acid in one strand and the backbone nitrogen of a second amino acid in another strand (Figure 3.3.3, right panel). The strands (at least two, but frequently more) can arrange in parallel or antiparallel fashion to form the β-sheets.

3.3.3 Hydrogels Characterization

Hydrogels can be described in a rheological way. Rheology is the science of flow and deformation of matter, deformation (shear strains and shear rate) that occurs when a material is subjected to a stress (force). The relationship between stress and deformation is a property of the material. Therefore, it can be define “Rheology” as the study of stress-deformation relationship.

The stress (force per unit area) can be applied in various ways: as a compression, as a tension, or as a shearing process. In compression and tension, dilute dispersions behave very much like simple liquids, especially if the particles are rigid and/or incomprenssible. Only in highly concentrated dispersions does one encounter unusual behavior under tension, while under compression most condensed materials (solid or liquid) behave rather similarly

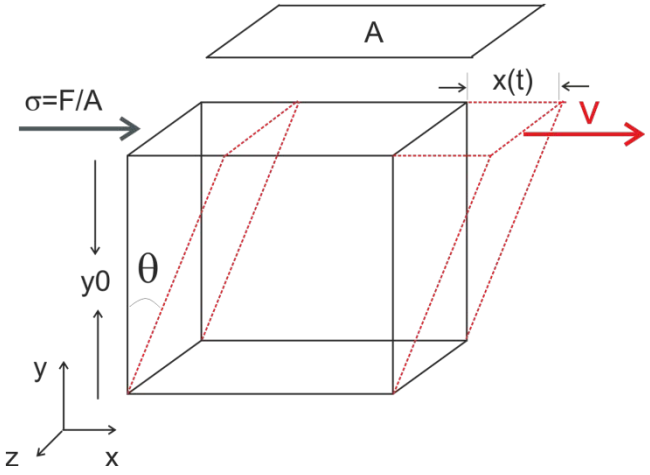

Strain, $\gamma = \frac{x(t)}{y0}$ Strain rate, $\dot{\gamma} = \frac{V}{y0}\frac{d\,x(t)}{d\,t}$ Viscosity, $\eta = \frac{\tau}{\dot{\gamma}}$

Figure 3.3.4: Scheme of application of a shearing stress to a material, produces a strain, $\gamma = \tan\theta$

3.3.4 Theorical aspects

Dynamics tests allow analyze the viscoelastic response of a material. These tests, also called "oscillatory test", consists on to apply a shear stress or shear strain that is varied sinusoidal over time while is during the test.

Oscillatory or dynamic test consists basically undergo to the material to a periodic deformation, which usually it is a simple sinusoidal shear that could be generated moving forward and backward to the top plate, consisting of deforming a material positioned between two parallel plates to move linearly the upper plate at given distance.

3.3.5 Response to an oscillating shear field

The shear strain applied to the material can be expressed as a function of time according to:

$$\gamma = \gamma^0 \sin \omega t \tag{3.3.1}$$

where γ is the shear strain, γ^0 is the maximum amplitude of the strain corresponding to simple harmonic motion, ω is the frequency and t is the time applied in the test.

The shear rate is also a periodic function:

$$\dot{\gamma} = \frac{(d\gamma)}{(dt)} = \gamma^0 \omega \cos(\omega t) = \dot{\gamma}^0 \cos(\omega t) \tag{3.3.2}$$

A material subjected to small sinusoidal strain, that guarantees a linear viscoelastic answer, responds after a certain number of cycles with a shear stress that also follows a sinusoidal function with respect to the time at the same frequency but with an amplitude characteristic of the nature of such material.

Hook's law describes ideal mechanical behavior using a constitutive equation in which stress and strain are related through a constant. If the material behaves as an ideal solid, the response is purely elastic and therefore the shear strain depends linearly as:

$$\sigma = G\gamma \tag{3.3.3}$$

where G is the ridigity modulus, and therefore the shear strain waves and shear stress will be in phase:

$$\sigma = G\gamma^0 \sin \omega t \tag{3.3.4}$$

Newton formulated a similar proposal concerning properties of liquids. If the material was a viscous ideal fluid, it will fulfill the Newton's law:

$$\sigma = \eta[(d\gamma)/(dt)] \tag{3.3.5}$$

This law assumes that a force (or resistance) is proportional to a velocity (of movement). The coefficient of proportionality, η, is called *viscosity* (or coefficient of viscosity)

And taking into account the expression (3.3.2), the wave corresponding to the shear stress would be out of phase in 90° with respect to shear strain wave:

$$\sigma = \eta\dot{\gamma}^0 \cos(\omega t) = \sigma^0 \cos(\omega t) = \sigma^0 \sin(\omega t + 90) \tag{3.3.6}$$

Both models (Hook and Newton models) represent properties of many materials and work well describing their behavior with considerably high degree of accuracy. However, there are numerous other real materials which are not described by above mentioned Hook and Newton laws. Rheology relies on the idea that non-Newtonian and non-Hookean materials exist in reality. Such materials are said to be visco-elastic and they may be intrinsically solids or liquids, depending on which of the two characteristics is dominant. A viscoelastic material shows an intermediate behavior between pure viscous and pure elastic ones, hence the shear stress displays a phase angle between 0° and 90° respect to the shear strain (Fig.3.3.5). The shear stress can be expressed mathematically as:

$$\sigma = \sigma^0 \sin(\omega t + \delta) \tag{3.3.7}$$

where σ^0 is the maximum amplitude corresponding to the shear stress and δ is the phase angle related to the deformation.

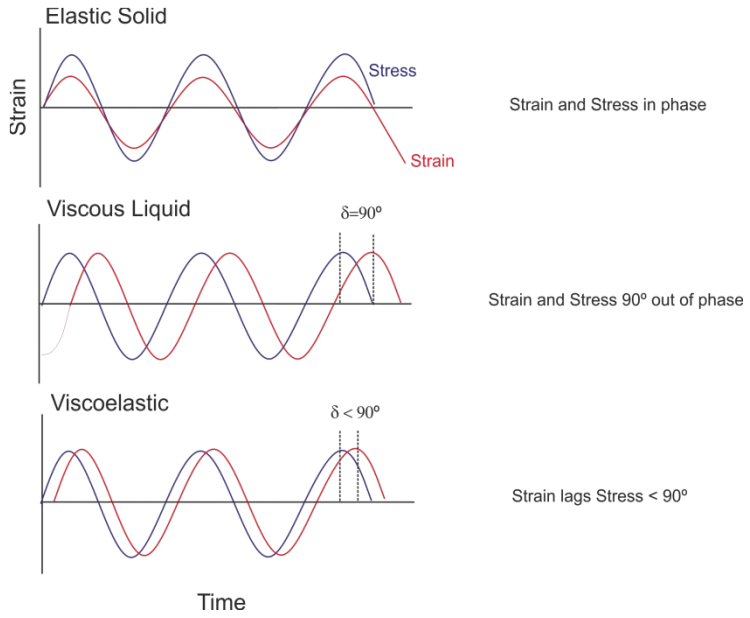

Fig.3.3.5: Elastic solid, viscous liquid and viscoelastic behavior of hydrogels.

If the expression (3.3.7) is developed trigonometrically we have:

$$\sigma = \sigma^0(\sin \omega t \cos \delta + \sin \delta \cos \omega t) \tag{3.3.8}$$

An analysis of the expression (3.3.8) suggests that the wave related to the shear stress can be decomposed in two waves of the same frequency, a phase corresponding to the shear strain wave ($\sin \omega t$) and another one with a phase angle of 90° ($\cos \omega t$). Thus, (3.3.8) can be displays as follows:

$$\sigma = \sigma' + \sigma'' = \sigma'^0 \sin \omega t + \sigma''^0 \cos \omega t \tag{3.3.9}$$

From the comparison between (8) and (9) it can deduce that:

$$\sigma'^0 = \sigma^0 \cos\delta \tag{3.3.10}$$

$$\sigma''^0 = \sigma^0 \sin\delta \tag{3.3.11}$$

This decomposition allows the definition of two dynamic modulus:

$$G' = (\sigma'^0/\gamma^0) = (\sigma^0/\gamma^0)\cos\delta \tag{3.3.12}$$

$$G'' = (\sigma''^0/\gamma^0) = (\sigma^0/\gamma^0)\sin\delta \tag{3.3.13}$$

G'y G'' are called storage modulus and loss modulus respectively., and in general depends on the frequency. G'represents a modulus that measures the ratio of the *in-phase* stress and G'' measures the ratio of the stress to the strain which is 90° out of phase.

An oscillating measurement at frequency ω corresponds to a transient measurement over time $t = 1/\omega$ and the result obtained gives two pieces of information: the ratio of the amplitudes of stress to strain (σ^0/γ^0) and the phase angle, δ, or alternatively the values of $G'$and G''

The expressions (3.3.12) and (3.3.13) suggest that G' and G'' can be analyzed as an alternative representation in terms of a complex modulus, G^*, which trigonometric form would be:

$$G^* = (\sigma^0/\gamma^0)\cos\delta + i(\sigma^0/\gamma^0)\sin\delta = G' + iG'' \tag{3.3.14}$$

The complex modulus G^* would be:

$$|G^*| = (G'^2 + G''^2)^{1/2} = \sigma^0/\gamma^0 \tag{3.3.15}$$

On the other hand from (3.3.12) and (3.3.13) it can be deduced that:

$$\tan \delta = (G'' / G') \tag{3.3.16}$$

The tangent of phase angle, also called loss tangent, is a dynamic viscoelastic function, generally frequency dependent, which indicates the ratio of viscous and elastic components displayed by the material. Thus, the loss tangent value indicates that under these conditions the materials responds with viscous and elastic component of the same value. That is, as one would expect a phase angle of 45^{o} means that a superiority of the elastic component does not exist on the viscous component and viceversa.

Another form to analyze the dynamic results, consist of defining a material function called dynamic viscosity. This methodology tends to be more comfortable for viscoelastics materials with predominantly fluid character. The dynamic viscosity is defined as a function of the stress component respect to the shear strain, σ^0. It is related to the viscous component of the viscoelastic behavior, G''.

$$\eta = \sigma^0 / \gamma^0 = G'' \tag{3.3.17}$$

3.4 Synthesis of Nanomaterials

3.4.1 Introduction

The synthesis of nanoparticles and nanoporous materials is recent branch of the nanotechnology that grows in complexity and number of applications. The high specific areas obtained, together with the effect of confinement, give rise to nanostructures having properties which differ from those shown by conventional materials. Due to advances in this field, new challenges are appearing. One of the most attention has received in recent years is the control of the solid structures at different scales [62-64], producing new properties that can be controlled by changing the synthesis conditions.

Different approaches ranging from physical to chemical methods have been exploited for the controlled fabrication of well-defined inorganic structures. Increasingly, colloidal chemists are contributing to the biomimetic synthesis of inorganic nanostructures with dimensional, morphological, and architectural specificity by using organized self-assemblies of surfactants as nanostructured reaction media or templates. It has been necessary to develop new synthetic techniques based on weak interactions due to precise control of the organization of the solid. In addition, it has been used biomimetic techniques, inorganic precursors and biomaterials. Exist different ways to synthesize templates: by organic molecules, molecular self-assembly, copolymers, liquid crystals, cooperative organization, microemulsions, foams, etc.

3.4.2 Synthesis by organic molecules used as templates:

This synthesis is based on the use of organic molecules as templates to direct the formation of solids around it. The templates are characterized by preserving its original shape and size during the synthesis of nano-structured material. The removal of the templates is a common step in the preparation of materials with controlled porosity [1,65-66]. Organic compounds must present different requirements to be used as a template: i) chemical stability ii) specific interaction with the precursor of the solid and iii) finalized the synthesis, the possibility to be removed.

Among the materials prepared using organic templates include zeolites, which are microporous crystalline aluminosilicates (pore size below 2 nm) widely used in catalysis, separation, adsorption and ion exchange [67].

This synthesis strategy using templates proved extremely useful and versatile. Also, is important to know that not only conventional organic molecules has been used as templates, additionally supramolecular structures[68], dendrimers[69], polymers[70], colloidal suspensions of nano-particles[71], latex spheres[72], and even biological materials such as, DNA[73] or viruses[74].

3.4.3 Synthesis by molecular self-assembly: Liquid crystals and cooperative organization.

This synthesis differs from the previous one because organic molecules are not kept in shape and size of the nanostructured solid during the synthesis. The structures prepared by self-assembling molecules are generally larger than those obtained with organic templates, due to these organic molecules are amphiphilic, i.e. consist of a hydrophilic and hydrophobic part, and self-assemble in micelles with different geometries. The synthesis using molecular self-assembly system to produce around nanometer scales, resulting mesoporous materials. The large size of the mesoporous (2-50nm) facilitates access to the interior of solid reagents allowing to process bulky molecules that cannot access the interior of solids with smaller pores, such as zeolites. By controlling the synthesis conditions, for example, the concentration of surfactant, it is possible to prepare solids with mesopores sorted structures: hexagonal (MCM-41), cubic (MCM-48) or lamellar (MCM-50). The acronym MCM corresponds to *Mobile Composition of Mater* (Fig.4.1).

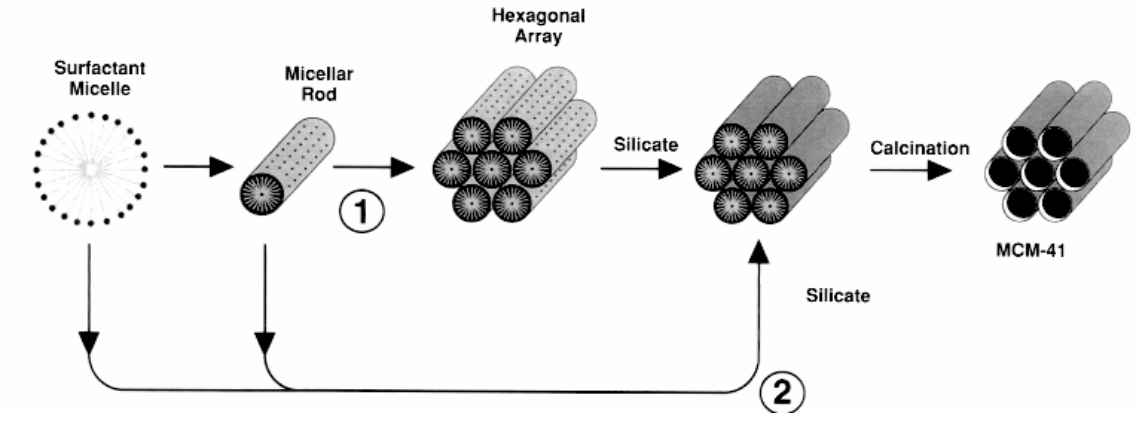

Figure 4.1: Scheme of possible mechanistic pathways for the formations of MCM-41: 1) Liquid crystal phase initiated and 2) Silicate anion initiated.

Most work on ordered mesoporous solids are based on silica, but in important to know that recent years have also been described to synthesis of mesoporous oxides of titanium, aluminum, zirconium, niobium, tin, iron and manganese and so on[75]. The main reason to use silica in the construction of materials with controlled porosity is due to silica alkoxides are hydrolyzed slowly allowing its proper interaction with surfactant molecules. On the other hand, some metal oxides are less stable to the removal of the surfactant, causing the collapse of the structure.

3.4.4 Synthesis spatially restricted: foams, and microemulsions

It is possible to control the final shape and size of the solid by using techniques that restrict the space where the synthesis takes place, achieving, in combination with the synthesis strategies described above, precise control of the structure of solids from the molecular to macroscopic level. This is the ultimate goal of building solid, it combines emergent properties of various dimensions.

Surfactant molecules have for a long time been employed in stabilizing finely dispersed matter since they have, due to their amphiphilic character, the tendency to adsorb at hydrophilic/hydrophobic interfaces such as water/air, water/oil or water/(hydrophobic) solid and oil/(hydrophilic) solid. In many inorganic or organic (colloidal) particle preparation routes, different types of surfactants have been added to stabilize the formed particles sterically o electrostatically against (irreversible) aggregation (and, if applicable, coalescence) processes. Apart from their stabilishing properties, surfactants have progressively gained more attention because they may self-assemble under certain conditions in binary and ternary systems of surfactant(s), water and/or oil into thermodynamically stable nano-heterogeneous systems, with a variety of different morphologies. These self-assembled systems can in principle be used as a kind of micro or better nanoreactor to separate and control nucleation and growth processes and as a template to direct growth and to control the morphology of the forming solid phase. Over the last two to three decades our knowledge of self-assembles surfactants systems has increased dramatically and a number of these systems have thoroughly investigated for advances materials synthesis[76-78].

The formation and morphological control of colloidal assemblies during a microemulsion-mediated hydrothermal synthesis is a complex process which depends on the particular combination of all the relevant microemulsion parameters. The effect of various factors on the final particle size is actually system specific, including the rate and the order of reactants addition[79].

Microemulsions are thermodynamically-stable complex fluids composed of water and oil domains that are separated by a surfactant monolayer which reduces unfavourable oil-water contact[80-81]. The topology of the oil and water domains can vary, depending on the composition and temperature[82]. Distinct, nanometer-size, surfactant-coated water droplets are maintained dispersed in the apolar solvent at low volume fractions of water; this system is called a reverse micellar phase or a water-in-oil microemulsion. Both the mesoporosity of the solid as well as

the size of the microspheres can be modified by varying the dimensions of the surfactant concentration, the nature of the organic phase and the synthesis conditions (temperature, pH, etc.).

Despite the versatility of using molecular or supramolecular templates for the preparation of materials with controlled porosity, this synthetic strategy requires the use of organic templates and inorganic precursors compatible in terms of interaction and stability to pH, temperature, solvent and salt concentration.

On the other hand, the elimination of the template molecule is a complex step, because during this process may deteriorate the porosity of the solid, especially in certain metal oxides. To avoid these drawbacks, it is possible to use organic mold, often described as rigid molds. After removing the mold, nanomaterials can be used directly or further modified to improve their properties. This technique is possible to obtain very homogeneous nanomaterials with different sizes (determined by the dimensions of the pores) and forms (depending on the architecture of the solid used as a template). This would have been able to prepare nanoparticles and nanowires of different metals into mesoporous silica by reduction of metal precursors[83]. Following this procedure, have been prepared, a variety of solid with controlled porosity[84].

Chapter 4:

RESULTS AND DISCUSSION

4. Results and Discussions

In this chapter we expose and discuss the obtained results. Early results have been published, we include the corresponding articles. Other studies, with both quantitative and qualitative results, have been done recently but the results have not yet been published so we include the data and analysis in the present form.

4.1 Published articles

4.1.1 Relevant Aspects of published articles.

- **Self-Assembly of Surfactants**

I. On the self-assembly of a highly selective benzothiazole-based TIM inhibitor in aqueous solution.

Benzothiazole derivates are selective and high affinity inhibitors of different triosephosphate isomerases (TIM) including Tripanozome cruzi (Tc) and Tripanosome brucei (Tb) TIMs from Trypanosoma cruzi (TcTIM), the parasite that causes Chagas disease that affects 18 million people in American Continent. Effective treatments for trypanosomiasis are still challenge with one of the benzothiazole derivate, 3-(2-Benzothiazolylthio)-propanesulfonic acid (BTS). It has been shown that premature aggregation of amphiphilic molecules below the corresponding critical aggregation concentration induced by presence of macromolecules is possible. These findings, together with our own interest in drug self-assembly, drug-protein interaction and even TcTIM (the actual target of BTS), encouraged us to perform this comprehensive study of BTS self-assembly as a function of its concentration, temperature and also salt concentration.

II. Hydrogenated/fluorinated catanionic surfactants as potential templates for nanostructure design.

Catanionic surfactants are chemical species consisting of an amphiphilic anionic and an amphiphilic cationic molecule. Mixtures of heterogeneous molecules which self-assemble in aqueous solution represent an interesting alternative for the design of nanoparticles due to its higher flexibility when compared to systems based on homogeneous molecules.

A combined experimental/computational study involving density, sound velocity, and dynamic light scattering measurements, together with transmission and scanning electron, as well as confocal laser microscopy images, and molecular dynamics simulations of equimolar mixtures of these two surfactants at several concentrations and at room temperature was performed for this aim.

III. Self Assembly drugs: A new therapeutic strategy.

Here we define a new strategy namely “self assembled drugs” as a self assembled structure (spherical or worm-like micelles, vesicles or liquid crystals) that is formed uniquely by drugs that combined assemble in such structures. All the individual compounds should display a therapeutic effect by themselves and resulting self-assembled structure display at the same time the role of support vector. Many drugs display amphiphilic properties thus they can be combined with hydrotropic drugs to form different kind of self-assembled structure, “self-assembled drugs”. By combination of hexadecyltrimethylammonium bromide (CTAB) and dicloxacillin (DC) resulting in the formation of worm-like micelles. Both drugs display well known therapeutic activity. The experimental techniques and theoretical background are now well established making them easy to characterize under different conditions. In this case we investigated this system using density and sound velocity, dynamic light scattering and cryo-electron microscopy (Cryo-TEM) and UV.

We expect our work to encourage the scientific community to investigate new self-assebled drugs and their advantages over more conventional strategies in drug delivery.

- **Protein-Ligand Interactions**

IV. Assessment of Interaction between four proteins and benzothiazole derivates by DSC and CD.

The interaction of small molecules with macromolecules of biological systems and with specific receptors sites on supramolecular organizations is one of the most extensively studied phenomena in biophysical research. Benzothiazoles have been reported to possess potent anticancer properties due to their structural similarity with naturally occurring purines as they can easily interact with biomolecules of the living systems.
The interaction of this drug with different proteins is attractive due to possible conformational changes or unfolding transitions induced by BTS. In order to understand the thermal stability of the lysozyme, ovalbumin, myoglobin and fibrinogen and the effect of BTS concentration we have carried out differential scanning calorimetric studies. Circular dichroism (CD) spectroscopy has been also employed to determine the effect of BTS on the secondary structure content. Measurements by DSC have yielded information regarding transition temperature (T_m), calorimetric enthalpy (ΔH), van't Hoff enthalpy (ΔH_V).

V. Mechanism of fibrinogen-acebutolol interactions: Insights from DSC, CD and LS.

Many pharmacologically active compounds are amphiphilic molecules and many of these drugs exhibit the same behavior as traditional surfactants, i.e., they tend to self-associate to form micelles usually with a small aggregation number. This phenomenon is very important for their application, particularly for their effects upon membrans or pharmaceutical formulations. Previously have been investigated the complexation of different proteins with amphiphilic ligands (surfactants, lipids and drugs) using physicochemical methods. From these results is possible to obtain a thermodynamic picture of the nature of the protein-amphiphilic interaction. A very important prescribed drug for hypertension treatment is acebutolol, a beta-selective betablocker that exhibits, as many b-adrenoceptor blocking agents, a range of pharmacological effects which arise as a result of modification of the cell membrane. One of the routes of administration of acebutolol is intravenous, where immediately delivered to the bloodstream to interact with plasma proteins as fibrinogen (who major function is to form fibrin clots). In this paper was investigated the nature of the interactions of acebutolol with fibrinogen using differential scanning calorimetry, dynamic light scattering and circular dichroism.

VI. Surface Characterization and AFM imaging of mixed fibrinogen-surfactant films.

Is well known that the behavior of proteins at interfaces is important to numerous phenomena in biology and biochemistry where adsorption occurs onto biomaterial surfaces. Due to the strong amphipatic nature of proteins, they tend to adsorb at the fluid interfaces, lowering the interfacial tension. In addition also is well known that many small amphiphilic molecules bind strongly to proteins to form protein-surfactant complexes and as a consequent can stabilize the interface through different mechanism.

Hydrogenated and fluorinated surfactants can act as stabilizer at low surfactant concentration or as a denaturant of proteins at high surfactant concentration. Details of the specific interactions occurring between proteins and fluorinated surfactants are still unknown. Fibrinogen is considered to be a major inhibitor of lung surfactants' function at the lining layer of alveoli, and also one of the most relevant protein that adsorb onto biomaterial surface. This article study the adsorption behavior of fibrinogen in presence of hydrogenated and fluorinated surfactant at the air-water interface using surface techniques including surface tension, surface dilatational rheology, and atomic force microscopy (AFM).

VII. **Investigating the effect of an arterial hypertension drug on the structural properties of plasma protein**.

Protein-drugs molecule interactions have been extensively studied by a variety of experimental methods. Because of their peculiar self-assembly behavior, their properties have evolved from being of a purely scientific interest to become a key concept in nano and biotechnological applications, such as drug delivery, sensors, and catalysts.

Propranolol is a β-adrenergic blocking agent. It is the most prescribed drug in treating hypertension; it is also applied to manage chronic stable angina. Previous studies on β -adrenoceptor blocking agents have shown that their pharmacological effects arise as a result of modification of the cell membrane. Due to the importance of fibrinogen in a several function of the body we have investigated the effect of propranolol with this plasma protein using different experimental techniques such as differential scanning calorimeter (DSC), dynamic light scattering (DLS), circular dichroism (CD), surface tension and atomic force microscopy (AFM). Such characterization may provide crucial information towards the design of drugs with optimal performance.

VIII. Fibrinogen stability under surfactants interactions.

Contemporary studies have been centered on the use of fibrinogen for nonviral vector delivery, scaffolds, and biocompatibility studies. Despite the very interesting applications of this protein, its interaction with small molecules as surfactants has not been exploited yet. We have focused our research on the stability, possible conformational changes and interactions between fibrinogen and hydrogenate/fluorinated surfactants with a view of better understanding the mechanism that are responsible for the adsorption of amphiphile molecules to biopolymers.

These surfactants allow us to compare the differences between hydrocarbon and fluorocarbon surfactants with the same chain alkyl chain with those where the hydrocarbon chain is 1.5 times longer than the fluorocarbon chain. We made use of differential scanning calorimetry (to get insight into thermodynamic parameters), absorbance spectroscopy, and circular dichroism, as well as small-angle X-ray scattering (to have information on protein conformational changes). A proposal of this work could be of interest for applications in biomaterial science where devices should be created with improved hemocompatibility.

- **Hydrogels**

IX. Rheological properties of ovalbumin hydrogels as affected by surfactants addition.

Hydrogels are three-dimensional networks of crosslinked hydrophilic polymers, which are able to retain considerable amounts of water. The ability to form a gel is an important function of proteins in food systems. Most food protein gels are formed by denaturation, aggregation, and gelation during heating process. The aggregation of globular proteins is regulated by many factors such as covalent bonding, electrostatic interactions, hydrogen bonding, hydrophobic interactions, and van der Waals forces. If external conditions are changed, the protein in solution may unfold and expose interior hydrophobic regions and sulfydryl groups to the solvent. The partially denaturated proteins can aggregate and, under appropriate conditions, produce a macroscopically continuous three-dimensional gel network that entraps and restricts the motion of the solvent. Nowadays, interaction of protein with surfactants has been is of great importance in the fields of industrial, specifically interactions of ovalbumin with surfactant has been a hotspot these days. Concerning the interest of the industry in ovalbumin hydrogels range from emulsifying activity (it is higher at acid pH) or drug delivery systems.

We have investigated the effect of sodium perfluorooctanote, sodium octanoate, and sodium dodecanoate, on the properties and structure of the ovalbumin gels with the purpose of analyze how the presence of fluorine atoms in the alkyl chain affects the gel structure. The physicochemical properties of these samples were evaluated by using rheological measurements that are easy to conduct, especially in high concentration range proteins.

X. Mimicking Natural Fibrous Structures of Opals by Means of a Microemulsion-Mediated Hydrothermal Method.

The synthesis of new materials made of particles, rods and wires with dimensions in the nanoscale is among the most active areas of research in science due to the unique properties of these materials compared to conventional materials made from micron sized particles. Metal oxides including silica represent a large class of inorganic materials that find many scientific and technological applications. For example, silicon-based nanomaterials are of the great interest because of their potential applications in constructing electronic and optoelectronic nanodevices.

We have designed a simple and controllable route for the synthesis of opals-CT materials with unusual fibrous microstructures similar to those existed in the nature, using a bottom-up microemulsion droplet system as chemical microreactor. The microcrystalline structure of opals and consequently their optoelectronic properties are a result of a particular combination of all the relevant microemulsion parameter, hydrothermal treatment time, and calcinations temperature.

Langmuir
Article
pubs.acs.org/Langmuir

On the Self-Assembly of a Highly Selective Benzothiazole-Based TIM Inhibitor in Aqueous Solution

Natalia Hassan,[†] M. Pilar Gárate,[‡] Tania Sandoval,[‡] Luis Espinoza,[‡] Ángel Piñeiro,*[,†] and Juan M. Ruso*[,†]

[†]*Soft Matter and Molecular Biophysics Group, Department of Applied Physics, University of Santiago de Compostela, Campus Vida s/n, 15782, Santiago de Compostela, Spain, and* [‡]*Departamento de Ingeniería Química y Ambiental, Universidad Técnica Federico Santa María, Av. Vicuña Mackenna 3939, Santiago, Chile*

Received April 26, 2010. Revised Manuscript Received September 17, 2010

Benzothiazole is a common scaffold on which many bioactive structures, including protein inhibitors and biosensors, are based. The potential self-aggregation of such molecules to form nanoparticles is relevant for a number of practical applications. 3-(2-Benzothiazolylthio)-propanesulfonic acid (BTS) has been reported as a powerful and selective inhibitor of triosephosphate isomerase from *Trypanosoma cruzi*, the parasite that causes the Chagas' disease. Electrical conductivity, sound velocity, density, and nuclear magnetic resonance experiments as a function of temperature and of NaCl concentration have been performed in the present work to provide a comprehensive physicochemical description of this compound in aqueous solution. Molecular dynamics simulations of the same system were also performed to characterize the structure and dynamic behavior of the corresponding aggregates at several concentrations of BTS.

1. Introduction

Natural and artificially designed amphiphilic molecules are widely employed in multiple industries—diagnosis tools, drug development, cosmetics, paints, or food processing—as well as in consumer products. For this reason their study changed from being originally considered as a branch of fundamental science to be essential in nano and biotechnology applied research. For applications in drug delivery, previous reports revealed that nanoparticles with different sizes and structures would bind to different tissues and organs. Their thermal and mechanical stabilities are interesting issues that should be considered to increase their blood circulation time, thus contributing to reduce side effects. Molecular architecture is a key factor in the design of self-assembling systems for nanoparticle preparation.[1] Structural information of the aggregates, like the packing parameter, directly related with the amphiphile molecule structure and with its hydrophilic/hydrophobic balance, as well as thermodynamic properties as a function of temperature and of the concentration of the molecule itself or of any cosolute, represent the keystone of the proper analysis that should be done on new molecules with biomedical applications.[2−4]

A number of pharmaceutical targets are susceptible to being inhibited by amphiphilic molecules with one or more aromatic nuclei.[5] Previous studies have focused on the self-assembly properties of the benzothiazole ring.[6] Benzothiazole derivatives have been widely employed in both therapeutic treatments and diagnosis including amyloid-β markers and dyes to sense protein conformational changes in living cells.[7] It has been demonstrated that a series of benzothiazoles substitutes are selective and high affinity inhibitors of different triosephosphate isomerases (TIM) including *Tripanosome cruzi* (Tc) and *Tripanosome brucei* (Tb) TIMs. These tripanosomes are flagellated protozoa responsible for American and African tripanosomiasis, parasitic sicknesses currently considered as emerging infectious diseases[8] that eventually end in patient death. In spite of their prevalence in endemic regions and of their increasing propagation over the whole world,[9] effective treatments for trypanosomiasis are still a challenge. 3-(2-Benzothiazolylthio)-propanesulfonic acid (BTS; see Figure 1) is one of the recently developed species-selective TIM inhibitors proposed to treat tripanosomiasis.[10,11] Although the structure of the complex formed by only one BTS molecule and TcTIM was crystallized, with the ligand located at the interface between the two enzyme subunits, kinetic and thermodynamic studies showed that at least two BTS molecules per enzyme are needed for inactivation.[12] On the other hand, it has been shown that premature aggregation of amphiphilic molecules below the

*Corresponding authors. E-mail: Angel.Pineiro@usc.es; JuanM.Ruso@usc.es. Tel.: +34 981 563 100. Fax: +34 981 520 676.

(1) (a) Cheng, L.; Cao, D. *Langmuir* **2009**, *25*, 2749 2756. (b) Ariga, K.; Hill, J. P.; Lee, M. V.; Vinu, A.; Charvet, R.; Acharya, S. *Sci.Technol. Adv. Mater.* **2008**, *9*, 14109 14109. (c) Klok, H. A.; Lecommandoux, S. *Adv. Mater.* **2001**, *13*, 1217 1229. (d) Davis, J. T.; Spada, G. P. *Chem. Soc. Rev.* **2007**, *36*, 296 313.

(2) Israelachvili, J. N.; Mitchell, D. J.; Ninham, B. W. *J. Chem. Soc., Faraday Trans. 2* **1976**, *72*, 1525 1567.

(3) Farias, T.; de Menorval, L. C.; Zajac, J.; Rivera, A. *Colloid Surf. A* **2009**, *345*, 51 57.

(4) Kopecka, B.; Fazekas, T.; Kaclik, P.; Kopecky, F. *Tenside, Surfactants, Deterg.* **2009**, *46*, 169 174.

(5) Schreier, S.; Malheiros, S. V. P.; Paula, E. *Biochim. Biophys. Acta* **2000**, *1508*, 210 234.

(6) (a) Roulia, M.; Vassiliadis, A. A. *Microporous Mesoporous Mater.* **2009**, *122*, 13 19. (b) Kuroda, S. *Adv. Colloid Interface Sci.* **2004**, *111*, 181 209. (c) Sovenyhazy, K. M.; Bordelon, J. A.; Petty, J. T. *Nucleic Acids Res.* **2003**, *31*, 2561 2569.

(7) (a) Henriksen, G.; Hauser, A. I.; Westwell, A. D.; Yousefi, B. H.; Schwaiger, M.; Drzezga, A.; Wester, H.-J. *J. Med. Chem.* **2007**, *50*, 1087 1089. (b) Mathis, C A.; Wang, Y.; Holt, D. P.; Huang, G.-F.; Debnath, M. L.; Klunk, W. E. *J. Med. Chem.* **2003**, *46*, 237 243. (c) Toutchkine, A.; Kraynov, V.; Hahn, K. *J. Am. Chem. Soc.* **2003**, *125*, 4132 4145.

(8) Jones, K E.; Patel, N. G.; Levy, M. A.; Storeygard, A.; Balk, D.; Gittleman, J. L.; Daszak, P. *Nature* **2008**, *451*, 990 993.

(9) Schmunis, G. A. *ISBT Sci. Ser.* **2007**, *2*, 6 11.

(10) Briceño-Leon, R. *Cad. Saúde Pública, Rio de Janeiro* **2009**, *25*(Sup1), 71 82.

(11) Téllez-Valencia, A.; Ávila-Ríos, S.; Pérez-Montfort, R.; Rodríguez-Romero, A.; Gómez-Puyou, M. T.; López-Calahorra, F.; Gómez-Puyou., A. *Biochem. Biophys. Res. Commun.* **2002**, *295*, 958 963.

(12) Téllez-Valencia, V.; Olivares-Illana, A.; Hernández-Snatoyo, R.; Pérez-Montfort, M.; Costas, A.; Rodríguez-Romero, F.; López-Calahorra, M. T.; Gómez-Puyou, A; Gómez-Puyou, J. *Mol. Biol.* **2004**, *341*, 1355 1356.

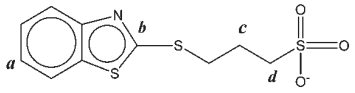

Figure 1. BTS molecule two-dimensional structure. The a−d labels correspond to the groups considered in the NMR analysis.

corresponding critical aggregation concentration induced by the presence of macromolecules is possible.[13] These findings, together with our own interest in drug self-assembly,[14] drug−protein interaction,[15,16] and even TcTIM (the actual target of BTS),[17] encouraged us to perform the present comprehensive study of BTS self-assembly as a function of its concentration, temperature, and also salt concentration. The potential effect of pH changes was not considered in the present work since it is not expected to be serious due to the relatively low pK_a value of BTS (~1.2) when compared to the pH of most representative biological environments (~3 in the stomach, ~5 in the small intestine and ~7.4 in blood). The results are expected to provide useful information for potential pharmaceutical developments based on BTS and, in general, with benzothiazole as a common scaffold.

2. Methods

2.1. Materials. BTS (>97% purity) was purchased from Aldrich Lancaster. All measurements except NMR were performed using distilled water with conductivity below 3 μS cm^{-1} as a solvent. The solutions were prepared at 298.15 K as indicated in the following section. For nuclear magnetic resonance experiments, deuterated water (> 99.99% purity) purchased from Sigma-Aldrich G.A was used as the solvent. The pH of BTS solutions was 5.5.

2.2. Experimental Methods. Conductivities were measured using a Kyoto Electronics conductometer model CM-117 with a K-121 cell type. The cell constant was determined using KCl solutions following the procedure suggested by Monk.[18] All measurements were performed in a PolyScience model PS9105 thermostatted water bath, at the required constant temperature within ±0.05 K. Conductivity isotherms were obtained by continuous dilution of a concentrated sample, prepared by weight. The expected duration of the dynamics processes varies from 10^{-8} to 10^{-2} s, i.e., between typical aggregate−solvent exchange time of amphiphilic molecules and typical fusion time of the corresponding aggregates. Thus, the equilibrium is guaranteed a few seconds after dilution.[19]

Ultrasound velocities and densities were continuous, simultaneous and automatically measured using a DSA 5000 Anton Paar density and sound velocity analyzer. This equipment possesses a new generation vibrating tube for density measurements and a stainless-steel cell connected to a sound velocity analyzer with resolution ±10^{-6} g cm^{-3} and 10^{-2} m s^{-1}, respectively. Both speed of sounds and densities are extremely sensitive to temperature, so this was controlled to within ±10^{-3} K through a Peltier device incorporated in the equipment. Each sample was measured three times, and standard deviations were found to be 10^{-6} g cm^{-3} and 10^{-2} m s^{-1}, respectively. The temperature range was from 288.15 to 318.15 K and the NaCl concentrations from 0.00 to 0.20 mol kg^{-1}.

The samples for NMR experiments were prepared directly in the spectrometer tubes, by adding solvent and BTS using micropipets to achieve the desired concentration. Three concentrations (50, 160 and 270 × 10^{-3} mol kg^{-1}) of BTS pure water solutions as well as in the presence of 0.05, 0.10, and 0.20 mol kg^{-1} of NaCl were employed for these experiments. The spectra were recorded at 400.132 MHz, 300 K and 1 bar, using a Bruker AVANCE 400 Digital NMR spectrometer containing an inverse detection probe of type BBI 5 mm 1H-BB, with gradient units Z-GRD Z8202/0253. Diffusion-ordered spectroscopy (DOSY) experiments, based on pulse-field gradient spin−echo ^{1}H NMR, were performed to determine the diffusion coefficient of each species in the sample. The signal of residual water in the solvent was taken as the reference. The diffusion coefficients are calculated by using the Stejskal−Tanner equation

$$A = A_0 \exp\left[-Dg^2\gamma^2\delta^2\left(\Delta - \frac{\delta}{3}\right)\right]$$

where A is the intensity of the signal, A_0 is the intensity of the initial (highest) signal, D is the self-diffusion coefficient, g is the gradient force, γ is the gyromagnetic ratio, δ is the time step of the gradient, and Δ is the diffusion time. All experiments were carried out using a LED sequence (ledbpgp2s pulprog) obtained and optimized from the library of standard parameters from Bruker. For our samples, A_0 was set to 36106812.514, using the residual water signal 4.67 ppm as a reference. γ was set to 2.675197 × 10^4 G^{-1} s^{-1} for ^{1}H, g ranged from 2% to 98%, δ was set to 2 ms, and Δ was set to 200 ms. Using these parameters, the spectrometer generated a DOSY spectrum in which the signals can be seen with ppm on the horizontal axis and the value of log D on the vertical axis.

2.3. Molecular Dynamics Simulations. Three random mixtures consisting of ~6500 waters and 20, 40, or 60 BTS molecules with their corresponding counterions (Na^+ cations) were introduced in cubic boxes of edge length 6 nm. Then, an energy minimization of the system using the steepest descent method was carried out. Trajectories of 50 ns at 298 K and 1 bar were performed for each of the three systems using the GROMACS package[20] version 4.0.5. The GROMOS96 (53a6) force field[21] with partial charges, bond lengths, angles, and proper and improper dihedral parameters obtained by using both the engine and the building blocks repository available at the Automated Topology Builder (ATB) server [http://compbio.chemistry.uq.edu.au/atb/], was employed to model BTS. The simple point charge (SPC) model[22] was utilized for water molecules. Three dimensional periodic boundary conditions were used for all of the trajectories. Water + ions on the one hand and BTS molecules on the other hand were separately coupled to a Nose−Hoover thermostat with a common period of 0.1 ps.[23] The pressure was isotropically controlled by using a Parrinello−Rahman barostat[24] with a coupling constant of 0.5 ps and considering a isothermal compressibility of 4.5 × 10^{-5} bar^{-1}. Long range electrostatic interactions were calculated using the particle mesh Ewald method[25]

(13) Jiang, Y. B.; Wang, X. J. Direct Evidence for β-Cyclodextrin-Induced Aggregation of Ionic Surfactant Below Critical Micelle Concentration. *Appl. Spectrosc.* **1994**, *48*, 1428 1431.
(14) Ruso, J. M.; Attwood, D.; Taboada, P.; Suárez, M. J.; Sarmiento, F.; Mosquera, V. *J. Chem. Eng. Data* **1999**, *44*, 941 943.
(15) (a) Taboada, P.; Attwood, D.; Ruso, J. M.; García, M.; Mosquera, V. *Phys. Chem. Chem. Phys.* **2000**, *2*, 5175 5179. (b) Ruso, J. M.; Taboada, P.; Martinez-Landeira, P.; Prieto, G.; Sarmiento, F. *J. Phys. Chem. B* **2001**, *105*, 2644 2648.
(16) Ruso, J. M.; Deo, N.; Somasundaran, P. *Langmuir* **2004**, *20*, 8988 8991.
(17) Diaz-Vergara, N.; Piñeiro, A. *J. Phys. Chem. B* **2008**, *112*(11), 3529 3539.
(18) Monk, B. *Electrolytic Dissociation*; Academic Press: London, 1961.
(19) Smit, K.; Essenlink, P. A. J.; Hilbers, N. M.; van Os, L. M. A.; Rupert, I.; Szeleifer *Langmuir* **1993**, *9*, 9 11.
(20) Berendsen, H. J. C.; van der Spoel, D.; van Drunen, R. *Comput. Phys. Commun.* **1995**, *91*, 43 56. (b) Lindahl, E.; Hess, B.; van der Spoel, D. *J. Mol. Model.* **2001**, *7*, 306 317. (c) van der Spoel, D.; Lindahl, E.; Hess, B.; Groenhof, G.; Mark, A. E.; Berendsen, H. J. C. *J. Comput. Chem.* **2005**, *26*, 1701 1718.
(21) Oostenbrink, C.; Villa, A.; Mark, A. E.; van Gunsteren, W. F. *J. Comput. Chem.* **2004**, *25*, 1656 1676.
(22) Berendsen, H. J. C.; Postma, J. P. M.; van Gunsteren, Hermans, J. Interaction models for Water in Relation to Protein Hydration. *Intermolecular Forces*; Pullman, B., Ed.; D. Reidel Publ. Co.: Holland, 1981.
(23) (a) Nosé, S. *Mol. Phys.* **1984**, *52*, 255 268. (b) Hoover, W. G. *Phys. Rew. A* **1985**, *31*, 1965 1975.
(24) (a) Parrinello, M.; Rahman, A. *J. Appl. Phys.* **1981**, *52*, 7182 7190. (b) Nosé, S.; Klein, M. L. *Mol. Phys.* **1983**, *50*, 1055 1076.
(25) (a) Darden, T.; York, D.; Petersen, L. *J. Chem. Phys.* **1993**, *98*, 10089 10092. (b) Essmann, U.; Perera, L.; Berkowitz, M. L.; Darden, T.; Lee, H.; Pedersen, L. G. *J. Chem. Phys.* **1995**, *103*, 8577 8593.

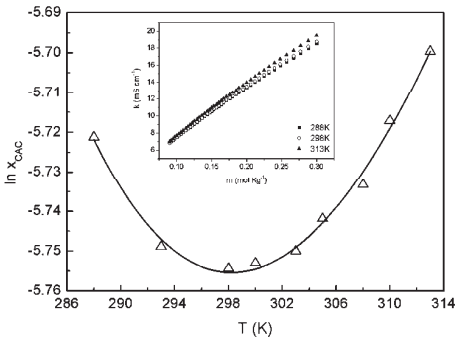

Figure 2. Natural logarithm of the critical aggregation concentration as a function of temperature. The solid line corresponds to the fit of experimental data to eq 1.

with a real-space cutoff of 1.2 nm, a 0.15 nm spaced grid, and fifth-order B-spline interpolation. Random initial velocities were assigned to the systems from a Maxwell−Boltzmann distribution at 298 K. The equations of motion were integrated using the leapfrog method[26] with a time step of 2 fs. Bond lengths and angles in water were constrained using the SETTLE algorithm,[27] and the LINCS algorithm[28] was used to constrain bond lengths within the surfactant molecules. During the MD simulations, coordinates of every particle in the simulation systems were stored every 10 ps for further analysis.

3. Results and Discussion

3.1. Electrical Conductivity Measurements. For the studied temperature range (288−318 K) the electrical conductivity concentration dependence shows a monotonic increase with a slight gradual decrease in slope, as expected for self-assembly processes[29a] (see Figure S1 in the Supporting Information). Critical aggregation concentration (CAC) values were calculated by fitting the experimental isotherms to the nonlinear function obtained by direct integration of a Boltzmann-type sigmoid function.[29b] The CACs obtained by this method as a function of temperature show the typical U-shaped behavior observed for the critical micelle concentration (CMC) of surfactant molecules. For those systems, the CMC decrease with temperature increase, like that observed in Figure 2 at $T <$ 298 K, is typically explained by the net rupture of structured water surrounding the hydrophobic tails, thus promoting micellization.[30a] The opposite trend at higher temperatures (Figure 2) is typically due to the dominant effect coming from the dehydration of the charged head groups accompanied by the subsequent electrostatic repulsion.[30b] Thermodynamic parameters corresponding to the aggregation process can be obtained by analyzing the CAC dependence on temperature. The Rodriguez model[31] was employed to describe this behavior

Table 1. Standard Molar Isobaric Heat Capacities, $\Delta C^0_{P,m}$ (J mol^{-1} K^{-1}), Enthalpies, ΔH^0_m (J mol^{-1}), Entropies ΔS^0_m (J mol^{-1} K^{-1}), and Free Energies of Aggregation, ΔG^0_m (J mol^{-1}), at Different Temperatures (K)

T	$\Delta C^0_{P,m}$	ΔH^0_m	ΔS^0_m	ΔG^0_m
288.15	−495.74	17293	92.3	−9305.3
293.15	−531.89	14178	81.5	−9739.7
298.15	−568.04	11244	71.6	−10122.6
303.15	−604.18	8490	62.5	−10457.7
308.15	−640.33	5918	54.0	−10748.9
313.15	−676.48	3526	46.3	−10999.8
318.15	−712.63	1315	39.3	−11213.9
323.15	−748.78	−715	33.0	−11394.7
328.15	−784.93	−2565	27.3	−11545.5

in the present work

$$\ln x_{CAC} = \ln x^*_{CAC}\left\{1+\beta_1 T^*\left[\frac{1}{2-\beta}\left(\frac{T^*}{T}-2-\frac{\beta_0-2}{\beta_1 T^*}\right)+\frac{1}{2-\beta^*}\left(1+\frac{\beta_0-2}{\beta_1 T^*}\right)\right]\right\}+\frac{\Delta C^{0*}_{P,m}}{(2-\beta)R}\left(1-\frac{T^*}{T}-\ln\frac{T}{T^*}\right)+\frac{\alpha}{(2-\beta)R}\left(\frac{T^{*2}-T^2}{2T}+T^*\ln\frac{T}{T^*}\right) \quad (1)$$

where the degree of ionization dependence on temperature, $\beta = \beta_0 + \beta_1 T$ (0.8 and −0.0005 for β_0 and β_1, respectively) and the standard change in isobaric molar heat capacity, $\Delta C^0_{P,m} = \Delta C^{0*}_{P,m} + \alpha(T - T^*)$, are explicitly considered. $\ln x^*_{CAC}$ and T^* correspond to the minimum. Figure 2 shows the fair fit of eq 1 to experimental data. Results obtained from the fitting were 298.2 K, −5.75, −568.37 J mol^{-1} K^{-1}, and 0.87 for T^*, $\ln x^*_{CAC}$, $\Delta C^{0*}_{P,m}$, and α/R respectively. The standard enthalpic and entropic changes due to aggregates formation at the minimum are given by

$$\Delta H^{0*}_m = RT^{*2}\beta_1 \ln x^*_{CAC} \quad (2)$$

$$\Delta S^{0*}_m = \frac{\Delta H^{0*}_m}{T^*}\left(2+\frac{\beta_0-2}{\beta_1 T^*}\right) \quad (3)$$

The dependence of the thermodynamic functions on temperature is obtained from the following expressions:

$$\Delta H^0_m = \Delta H^{0*}_m + \Delta C^{0*}_{P,m}(T-T^*) + (\alpha/2)(T-T^*)^2 \quad (4)$$

$$\Delta S^0_m = \Delta S^{0*}_m + \Delta C^{0*}_{P,m}\ln(T/T^*) + \alpha\{T - T^* - T^*\ln(T/T^*)\} \quad (5)$$

and the standard Gibbs energy of aggregates formation is given by

$$\Delta G^0_m = \Delta H^0_m - T\Delta S^0_m = (2-\beta)RT\ln x_{CAC} \quad (6)$$

where the right side of the equation can be obtained from both the charged phase separation model[32,33] which provides a good approximation for relative comparison if the aggregation number

(26) Hockney, R. W.; Eastwood, J. W. *Computer Simulation Using Particles*, 1st ed.; Adam Hilger: Bristol, 1988.
(27) Miyamoto, S.; Kollman, P. A. *J. Comput. Chem.* **1992**, *13*, 952 962.
(28) Hess, B.; Bekker, H.; Berendsen, H. J. C.; Fraaije, J. G. E. M. *J. Comput. Chem.* **1997**, *18*, 1463 1472.
(29) (a) Moroi, Y. *Micelles: Theoretical and Applied Aspects*; Plenum: New York, 1992.(b) Blanco, E; González-Pérez, A.; Ruso, J. M.; Pedrido, R.; Prieto, G.; Sarmiento, F. *J. Colloid Interface Sci.* **2005**, *288*, 247 260.
(30) (a) González-Pérez, A.; Ruso, J. M.; Romero, M. J.; Blanco, E.; Prieto, G.; Sarmiento, F. *Chem. Phys.* **2005**, *313*, 245 259. (b) Zielinski, R. *J. Colloid Interface Sci.* **2001**, *235*, 201 209.
(31) Rodríguez, J. R.; González-Pérez, A.; Del Castillo, J. L.; Czapkiewicz, J. *J. Colloid Interface Sci.* **2002**, *250*, 438 443.
(32) Mukerjee, P.; Korematsu, K.; Okawauchi, M.; Sugihara, G. *J. Phys. Chem.* **1985**, *89*, 5308 5312.
(33) Shinoda, K.; Hutchinson, E. *J. Phys. Chem.* **1962**, *66*, 577 582.

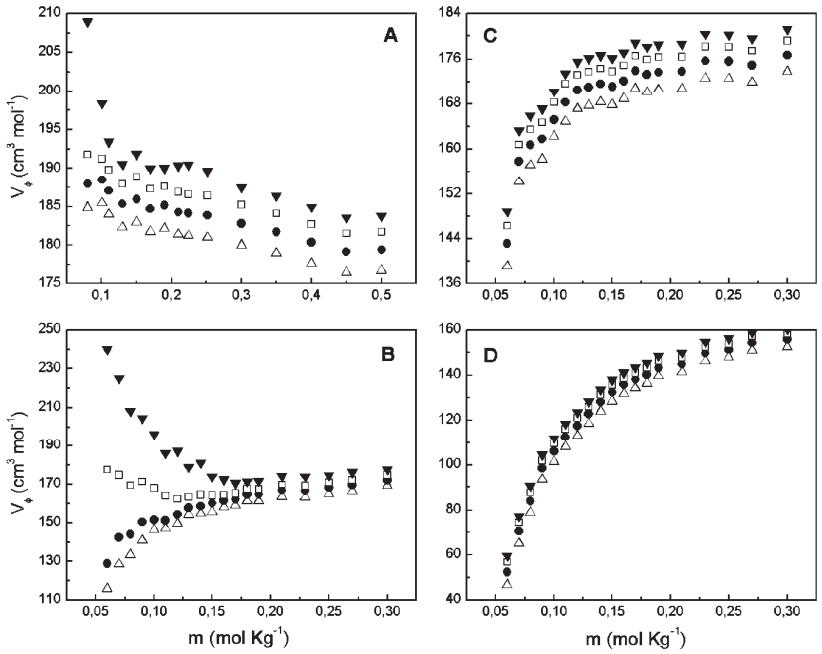

Figure 3. - Apparent molar volumes, V_ϕ, as a function of concentration, m, for different temperatures: (△) 288.15, (●) 298.15, (□) 308.15, and (▼) 318.15 K; and NaCl concentrations: (A) 0.00, (B) 0.05, (C) 0.10, and (D) 0.20 mol kg^{-1}.

is large enough and the mass action model.[34] Heat capacity, enthalpy, entropy, and standard free energy data corresponding to the aggregation process are listed in Table 1. ΔH_m^0 and ΔS_m^0 are quite sensitive to temperature. ΔH_m^0 values indicate that the BTS aggregation is increasingly more exothermic at higher temperatures. Positive values of ΔH_m^0 have been attributed to the release of structured water from the hydration layers around the hydrophobic parts of the molecules[35] during the aggregate formation. Such dehydration becomes increasingly negligible with the partial breakdown of the water structure as the temperature increases and the aggregation becomes primarily an enthalpic process. Negative ΔH_m^0 values suggest the importance of London-dispersion interactions as the major force for aggregation.[36] However, ΔS_m^0 decreased with temperature and remained positive. It has often been found that this kind of aggregation is entropic driven at low temperatures for ionic surfactants whereas enthalpic contributions become more important at high temperatures.[38−40] The above-mentioned higher order of water molecules around hydrocarbon chains at lower temperatures could explain this. Strictly speaking, as the temperature increases the hydrogen bonds between water molecules diminished and therefore less energy was required to break up the water cluster.[37] This fact has been observed not only for many typical surfactants but also for amphiphilic drugs with an aromatic ring like penicillins[39] and betablockers.[40] However, our results show that entropy dominates the aggregation process for the temperature range under study.

3.2. Density and Apparent Molar Volume Measurements. From density measurements, apparent molar volumes can be calculated using the following equation:

$$V_\phi = \frac{10^3(\rho_0 - \rho)}{m\rho\rho_0} + \frac{M}{\rho} \quad (7)$$

where ρ is the density of the mixture at a given concentration, ρ_0 is the density of pure water, M is the molecular weight of the surfactant, and m is the molality of the solution. Figure 3 shows plots of V_ϕ versus BTS molality at different temperatures and electrolyte concentrations (for clarity, some of the isotherms are shown in the Supporting Information, Figure S2). These plots provide a general overview of the BTS aggregation process. At low concentrations the volumes are strongly dependent on both temperature and electrolyte concentration. This region is characteristic of the monomeric state, showing a significant variation of V_ϕ. The value of the slope in this region presents positive and also negative values depending on the temperature and salt concentration. Negative values are usually considered as a manifestation of the solvophobicity of surfactant molecules and thus account for the solvophobic effect. The solute−solvent interactions cannot be overlooked even in dilute solutions as is done in Debye−Hückel limiting law. Two opposing effects of solvophobicity and charge interactions contribute considerably in determining the sign and

(34) Rusanov, A. I. *Adv. Colloid Interface Sci.* **1993**, *45*, 1 15.
(35) Kresheck, G. C. *Water, A Comprehensive Treatise*; Plenum: New York, 1975.
(36) Nusselder, J. J. H.; Engberts, J. B. F. N. *J. Colloid Interface Sci.* **1992**, *148*, 353 361.
(37) Mehta, S. K.; Bhasin, K. K.; Chauhan, R.; Dham, S. *Colloids Surf. A* **2005**, *255*, 153 157.
(38) Ruso, J. M.; Fontán, J. L.; Prieto, G.; Sarmiento, F. *J. Chem. Phys.* **2003**, *118*, 5964 5970.
(39) Taboada, P.; Attwood, D.; García, M.; Jones, M. N.; Ruso, J. M.; Mosquera, V.; Sarmiento, F. *J. Colloid Interface Sci.* **2000**, *221*, 242 245.
(40) Ruso, J. M.; Attwood, D.; Rey, C.; Taboada, P.; Mosquera, V.; Sarmiento, F. *J. Phys. Chem. B* **1999**, *103*, 7092 7096.

order of the slope. The positive value implies that interactions between the charged species overcome the nonpolar−nonpolar and nonpolar−polar interactions. The change of the slope from negative to positive values indicates strong electrostatic interactions.[41] Similar changes have also been observed for phenothiazine drugs at different pH values.[42] As observed in Figure 3, the apparent molar volumes became constant at high surfactant concentrations. That limits the values that can be taken as the apparent molar volume of a monomer in the aggregate. The concentration dependence of the apparent molar values is generally considered to reflect solute−solute interactions other than the long-range Debye−Hückel type. The apparent molar volumes of this compound change systematically with temperature in the range under study. A vertical translation to higher volumes with temperature is usual. Such behavior was already observed in previous studies for amphiphilic drugs.[43]

Assuming that the additivity rule for the apparent molar volumes and adiabatic compression of the ions in the system stands

$$nV_\phi = n_f V_f + n_c V_c + n_m V_m \quad (8)$$

where V_m is the apparent molar volume of the micelles in the system and n is the total number of BTS moles. n_f, n_c, and n_m are the numbers of moles of free monomers, free counterions, and micelles respectively. Since the studied salt is a 1:1 electrolyte, according the pseudophase separation model below the CAC

$$m_f = m_c = m \quad (9)$$

and above CAC:

$$m_f = \mathrm{CAC} \qquad m_c = \mathrm{CAC} + \beta(m - \mathrm{CAC})$$
$$m_m = (m - \mathrm{CAC})/N_{agg} \quad (10)$$

where N_{agg} is the aggregation number, β is the degree of ionization of micelles, and m_f, m_c, m_m, and m are concentration (molality) of free monomers, free counterions, micelles, and the total concentration, respectively.

Dividing eq 8 by the mass of the solvent (in kg) and taking into account relations 9 and 10 the following set of equations is obtained:

$$V_\phi = (V_f + V_c) \qquad m \le \mathrm{CAC}$$
$$V_\phi = \left(\frac{V_m}{N_{agg}} + \beta V_c\right) - \left(\frac{V_m}{N_{agg}} + (\beta - 1)V_c - V_f\right)\frac{\mathrm{CAC}}{m} \qquad m \ge \mathrm{CAC} \quad (11)$$

Linear fitting of V_ϕ vs $1/m$ in the concentration range above CAC (CAC/$m \le 1$ region) allows us to obtain the value of the apparent molar volume, V_ϕ^{CAC} (intercept + slope), of the surfactant at the CAC, and the change in the apparent molar volume upon aggregation, ΔV_ϕ^{CAC} (slope). The results are collected in Table 2. It is worth to mention that the ΔV_ϕ^{CAC} values of isotherms at different temperatures change from positive, in water, to negative in the presence of salt (Figure S3, Supporting Information). De Lisi et al.[44] attributed the negative slopes observed for ΔV_ϕ^{CAC} of sodium octyl, decyl and dodecyl sulphates in water vs T in the range 298 to 403 K at different pressures to the expansibility of the surfactant in the micellar state being smaller than that in the aqueous phase. Attwood et al.[45] found this decrease with temperature for chlorpromazine an effect which has been attributed to the dehydration of the ionic headgroup. These authors compared their results with those of previous works, finding that negative ΔV_ϕ^{CAC} values are due to micelle formation of lower

Table 2. Apparent Molar Volumes at the CAC, V_ϕ^{CAC} ($cm^3\ mol^{-1}$), Apparent Molar Volume Changes upon Aggregation, ΔV_ϕ^{CAC} ($cm^3\ mol^{-1}$), Isentropic Apparent Molar Adiabatic Compressibilities at the CAC, K_ϕ^{CAC} ($cm^3\ Pa^{-1}\ mol^{-1}$), and Isentropic Apparent Molar Adiabatic Compressibilities upon Aggregation, ΔK_ϕ^{CAC}, of BTS at Different Temperatures (K) and NaCl Concentrations (mol kg^{-1})

T	V_ϕ^{CAC}	ΔV_ϕ^{CAC}	$K_\phi^{CAC}\cdot 10^8$	$\Delta K_\phi^{CAC}\cdot 10^9$
		0.00 NaCl		
283.15	174.05	2.71	0.130	−5.69
288.15	175.55	2.76	0.664	−4.84
293.15	176.90	2.81	1.135	−4.18
298.15	178.14	2.85	1.556	−3.70
303.15	179.30	2.90	1.933	−3.27
308.15	180.39	2.94	2.275	−2.91
313.15	181.42	2.98	2.582	−2.65
318.15	182.32	3.11	2.873	−2.16
323.15	183.56	4.09	3.039	−0.77
		0.05 NaCl		
288.15	173.76	−1.39	0.108	−7.51
298.15	177.64	−1.37	1.243	−6.71
308.15	179.96	−1.32	2.003	−5.78
318.15	182.01	−1.27	2.623	−5.06
		0.10 NaCl		
288.15	170.43	−3.48	0.188	−11.51
298.15	173.00	−3.38	1.312	−10.48
308.15	175.35	−3.32	1.898	−8.78
318.15	180.09	−3.23	2.676	−7.93
		0.20 NaCl		
288.15	153.07	−7.32	−0.480	−19.21
298.15	155.81	−7.12	0.513	−16.92
308.15	158.09	−6.96	1.266	−15.29
318.15	160.51	−6.89	1.915	−14.24

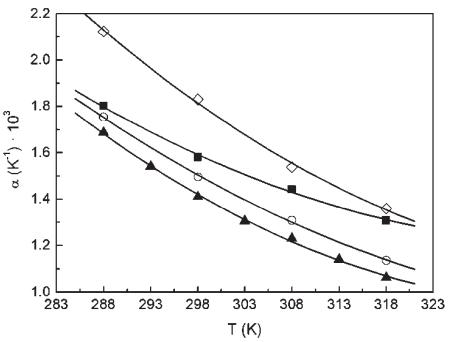

Figure 4. Apparent thermal expansion coefficients, α, as a function of temperature for different NaCl concentrations: (▲) 0.00, (○) 0.05, (■) 0.10, and (◇) 0.20 mol kg^{-1}.

(41) Mehta, S. K.; Sharma, S.; Joshi, I. M. *Colloids Surf. A* **2002**, *196*, 259 267.
(42) Cheema, M. A.; Siddiq, M.; Barbosa, S.; Tabeada, P.; Mosquera, V. *J. Chem. Eng. Data* **2008**, *53*, 368 373.
(43) Ruso, J. M.; González-Pérez, A.; Prieto, G.; Sarmiento, F. *Colloid Surf. B* **2004**, *33*, 165 175.
(44) de Lisi, R.; Milioto, S.; Muretore, N. *Langmuir* **2001**, *17*, 8078 8085.
(45) Attwood, V.; Mosquera, C.; Rey, M.; García *J. Colloid Interface Sci.* **1991**, *147*, 316 320.

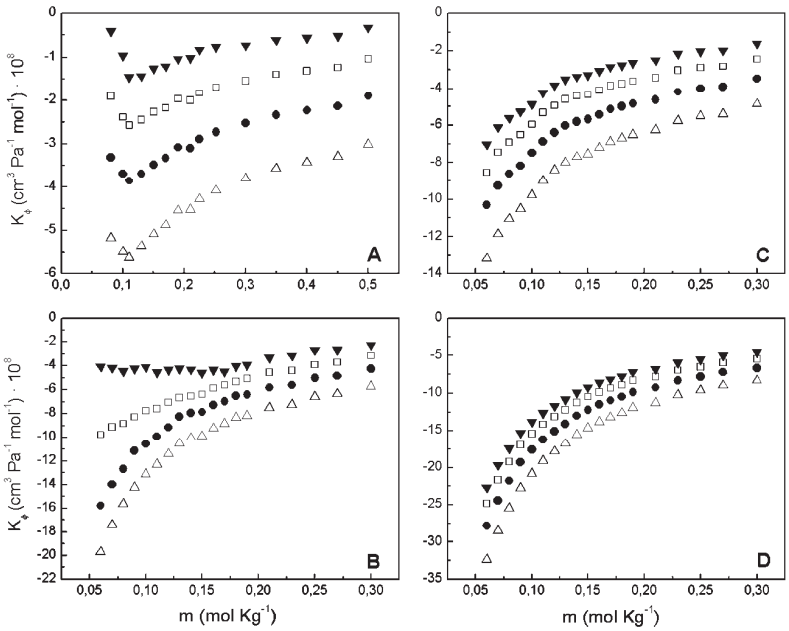

Figure 5. Isentropic apparent molar compressibilities, K_ϕ, as a function of concentration, m, for different temperatures: (△) 288.15, (●) 298.15, (□) 308.15, and (▼) 318.15 K; and NaCl concentrations: (A) 0.00, (B) 0.05, (C) 0.10, and (D) 0.20 mol kg^{-1}.

aggregation numbers. On the other hand, the positive slope observed in the absence of salt could be related to a larger ionization degree and to a better ability to form hydrogen-bonding interactions. Classical surfactants exhibit large positive ΔV_ϕ^{CAC} values due to the release of structured water in the hydration shell of the monomers upon micelle formation, allowing more structural flexibility and, consequently, larger volume available per monomer within the aggregate compared to that in solution.[46] However, ΔV_ϕ^{CAC} values found for BTS are significantly lower than those of classical surfactants. Such small increase in free space of drug molecules during the transition to the micelle state could be a consequence of the BTS stacked arrangement already observed for tricyclic compounds,[47] or simply due to the rigidity of this molecule, undertaking small geometrical changes upon aggregation. It has been reported that apparent thermal expansion coefficients provide information about solute−solute interactions.[48] This property can be calculated from the temperature dependence of the apparent molar volume at constant pressure and number of the solute moles, by using the following expression:

$$\alpha = \left(\frac{1}{V_\phi}\right)\left(\frac{\partial V_\phi}{\partial T}\right)_{p,n_i} \qquad (12)$$

Apparent thermal expansion coefficients (α) of BTS solutions in water and three different concentrations of NaCl (0.05, 0.1, and 0.2 mol kg^{-1}) as a function of T are plotted in Figure 4. The obtained values, with negative slope, are comparable to those found for inorganic salts such as ammonium chloride, ammonium acetate, or ammonium propionate. In general, different α profiles as a function of the concentration indicate a significant dependence on structural features, such as electrical charge, size, type of ion, as well as the relative proportions of the hydrophilic or hydrophobic parts of the molecule.[49] It has been shown that higher α values for the free molecules are related with their stronger hydration compared with that of the monomers in micelles. Accordingly, from the present results the lower values of this parameter at high BTS concentrations (over CAC) indicate a lower hydration of BTS in the aggregated form. The role of salt concentration is also assessed in Figure 4. The higher α values in the presence of salt suggest a higher hydration of BTS molecules when increasing the salt concentration.

Table 3. Hydrodynamic Radii (nm) of Aggregates at Different BTS and NaCl Concentrations (mol kg^{-1})

	[NaCl]:			
[BTS]	0.00	0.05	0.10	0.20
0.050	0.60	0.71	0.77	0.99
0.160	0.90	1.18	1.36	1.81
0.270	1.31	1.67	1.87	2.42

3.3. Sound Velocity and Compressibilities. Using the Laplace equation, density and ultrasound velocity measurements were combined to calculate adiabatic compressibilities

$$\beta' = -\frac{1}{V}\left(\frac{\partial V}{\partial P}\right)_S = \frac{10^{-3}}{\rho u^2} \qquad (13)$$

(46) Zielinski, R.; Ikeda, S.; Nomura, H.; Kato, S. *J. Chem. Soc. Faraday Trans. I* **1988**, *84*, 151 163.
(47) Attwood, D.; Waight, R.; Blundell, R.; Bloor, D.; Thevand, A.; Boitard, E.; Dubès, J. P.; Tachoire, H. *Magn. Reson. Chem.* **1994**, *32*, 468 472.
(48) (a) Rudan-Tasic, D.; Klofutar, C. *Monatch. Chem.* **1998**, *129*, 1245 1257. (b) Idqbal, M.; Verrall, R. E. *Can. J. Chem.* **1989**, *67*, 727 734.
(49) Klofutar, C.; Horvat, J.; Rudan-Tasič, D. *Acta Chim. Slov.* **2006**, *53*, 274 283.

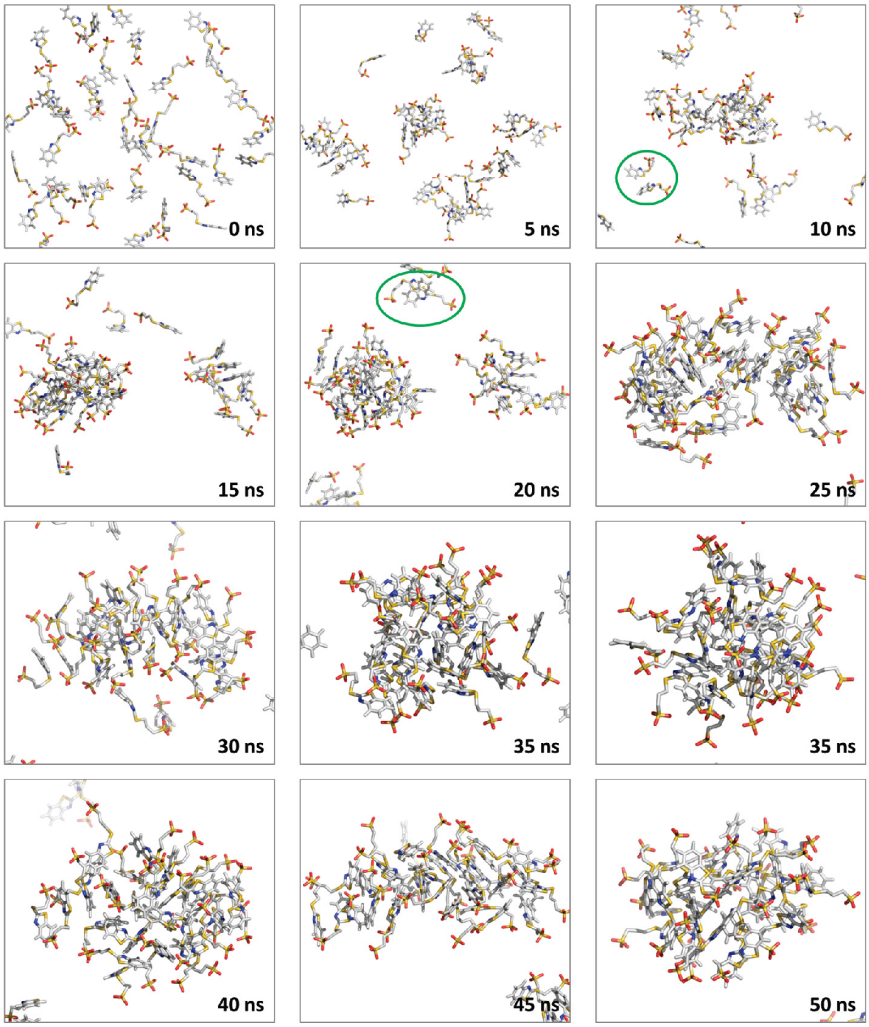

Figure 6. Snapshots taken from a molecular dynamics trajectory for a system with 40 BTS molecules (in sticks representation) and 6513 waters (not shown). The simulation times are indicated in the right lower corner of each image. Two different views are shown for the aggregate at 35 ns. Dimeric structures with the aromatic rings stacked are green-encircled in the snapshots at 10 and 20 ns.

where V, P, and S refer to volume, pressure, and entropy, respectively. β' is the adiabatic compressibility coefficient, expressed in Pa^{-1} when ultrasound velocities u are expressed in cm s^{-1} and densities ρ in g cm^{-3}. Apparent molar isentropic adiabatic compressibilities, K_ϕ, can be calculated from ultrasound measurements

$$K_\phi = \frac{10^3(\beta' - \beta_0')}{m\rho_0} + \beta_0' V_\phi \qquad (14)$$

where β' and β_0' are the isentropic compressibility coefficients of the solution and solvent, respectively. Figure 5 shows plots of K_ϕ vs BTS molality at different temperatures and electrolyte concentrations. Following a procedure similar to that previously explained (eqs 8−11) but substituting V_ϕ, V_m, V_f, and V_c for K_ϕ, K_m, K_f, and K_c, respectively, experimental values for K_ϕ^{CAC} (apparent molar adiabatic compressibility at the CAC) and ΔK_ϕ^{CAC} (apparent molar adiabatic compressibility upon aggregation) can be calculated from linear fittings of K_ϕ vs $1/m$. The values obtained for the systems under study are listed in Table 2. Moreover, since the solute intrinsic compressibility is assumed to be zero, apparent molar compressibility data at infinite dilution provide insight into the compressibility of the hydration layer around the solute molecule. The more negative the solute compressibility the stronger the hydration. Upon aggregation, the hydration of the hydrophobic groups of amphiphilic molecules vanishes and the compressibility of the aggregate by itself becomes the dominant factor. Previous studies of K_ϕ have

shown that this quantity is large and negative for ionic compounds in water, intermediate and positive for mainly hydrophobic solutes, and small and negative for uncharged hydrophilic solutes.[50] When the aggregate is formed, the released water molecules that were in the vicinity of the hydrophobic part of the molecule become bulk water. The water molecules around the hydrophobic part are highly structured, having a rather low compressibility compared to the bulk water. The values calculated for K_ϕ^{CAC} increase linearly with temperature. Meanwhile, those obtained for the absolute values of ΔK_ϕ^{CAC} decrease with T. Previous studies have reported positive ΔK_ϕ^{CAC} values for drugs[51] which were attributed to the predominant role of the decrease in hydrophobic hydration in the association process. The negative values obtained in the present work suggest that the aggregation process of BTS could be related to a different event, probably to steric interactions. In contrast with the temperature dependence, K_ϕ^{CAC} mostly decreases and the absolute values of ΔK_ϕ^{CAC} increases with salt concentration. An earlier study[52] on the influence of NaCl on SDS micelles showed no measurable change in the compressibility-concentration plot gradients above the CMC upon electrolyte addition (0 to 1 mol dm^{-3} NaCl). Although the author of that work concluded that the compressibility of SDS micelles was not affected by the presence of electrolyte, it should be noted that these data, in fact, predict a slight decrease. The same pattern has been found for propanolol and acebutolol.[49] The variation of ΔK_ϕ^{CAC} with electrolyte concentration shown in the present study could be attributed to a decrease in the intramicellar repulsion due to the shielding of the ionic environment or, alternatively, to the increase in the BTS aggregation due to the well-known salting-out effect.[53]

3.4. Nuclear Magnetic Resonance Measurements. BTS self-association has been investigated by high-resolution NMR spectroscopy. The chemical shifts of four selected molecular positions (see Figure 1) were measured from ^{1}H NMR spectra of BTS solutions at concentrations well below and above the CAC. The examination of the magnitude and sign of chemical shift changes upon aggregation, $\Delta\delta$, ($\Delta\delta = \delta_{aggregate} - \delta_{monomer}$), calculated for each position, provides insight into the possible molecular ordering of the aggregates. Upfield shifts indicate that protons are transferred to a less polar environment[54] while downfield shifts indicate stronger interactions with water molecules. The alkyl chain proton chemical shifts in typical spherical aggregates drop in synchrony with a decrease in the packing parameter and in the proton screening on moving outward from the core to the aggregate surface.[55] In the case of BTS, all protons show pronounced upfield shifts upon aggregation, obtaining similar values for all the electrolyte concentration under study: $\Delta\delta$ = 0.23, 0.03, 0.06, and 0.07 for protons a, b, c, and d, respectively (see Table S1 in Supporting Information). The greatest change corresponds to the protons of the aromatic ring system which results from the association to form micelle-like cores. The proton environment of the side-chains was less affected by the association process.

Diffusion ordered 2D NMR (DOSY) spectra of BTS at several concentrations were analyzed. As an example, the ^{1}H NMR and 2D DOSY spectrum of BTS in water (0.0 NaCl) at a concentration of 0.160 mol kg^{-1} are showed in Figure S4 (Supporting Information).

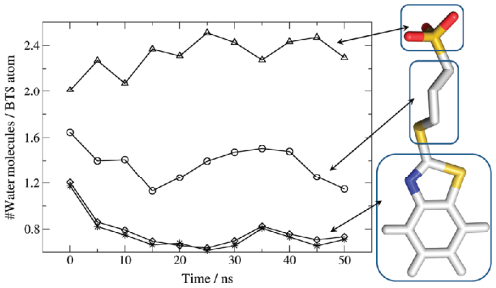

Figure 7. Number of water molecules per atom at less than 4 Å of each of the three groups indicated on the right of the plot, as a function of the simulation time. For the aromatic rings the calculations were performed considering only the heavy atoms (◇) and both the heavy atoms and the hydrogens (*).

It is noteworthy that all signals appear at a single diffusion coefficient with no evidence of polydispersity. Slower core than outer covering diffusion values have been reported. However, DOSY spectra show the whole BTS molecule diffusing in the same way for different concentrations (0.050, 0.160, and 0.270 mol kg^{-1}) both in the absence and in the presence of electrolyte at 0.05, 0.10, and 0.20 NaCl mol kg^{-1}. Using the Stokes−Einstein equation, $D = kT/6\pi\eta R$, where η is the viscosity of D_2O (1.0511 cP at 300 K), which assumes perfectly spherical and noninteracting aggregates hydrodynamic radii were obtained (Table 3).

3.5. Molecular Dynamics Simulations. 50 ns long computational molecular dynamics simulations, following the protocol described in the Methods section, were performed for simulation boxes with 20, 40, and 60 BTS molecules. The snapshots shown in Figure 6 illustrate both the self-aggregation process observed during the first 25 ns, and the typical behavior of the resulting nanoparticles from 25 to 50 ns. The aggregation time scale is larger than that observed for surfactants with aliphatic chains, and the aggregates are less tight than standard micelles. The hydration level per atom for three segments of the BTS molecule, namely the two rings, the ionic head and the linker joining both is shown in Figure 7. It is clear that, during the trajectory, both the propane linker and the aromatic rings tend to lose the contact with water molecules, in contrast with the sulfonic headgroup that tends to increase its hydration. This is in agreement with the NMR and thermodynamic results obtained at 298 K. Moreover, it is clear from the snapshots that the aromatic rings are oriented toward the core of the structure but they do not exhibit the clear stacking pattern previously observed for other structures based on molecules with aromatic rings. This might be due to the charge of the propanesulfonic groups that would be too close to each other in such structures, producing an important electrostatic repulsion. The latter explanation is supported by the structure of several dimers with stacked rings seen throughout the trajectory, where the charged groups appear oriented toward opposite sides with the BTS molecules in both parallel and antiparallel orientation (see the green-encircled dimers in the snapshots at 10 and 20 ns, respectively). The aggregate diameter estimated from the simulations varies between 2.5 and 3.0 nm while the typical aggregation number of the observed nanoparticles ranges from 28 to 32 BTS molecules.

4. Conclusions

The present work provides experimental and theoretical evidence of the BTS self-aggregation. Such an association process

(50) Ruso, J. M.; González-Pérez, A.; Prieto, G.; Sarmiento, F. *Colloid Surf. B* **2004**, *33*, 165 175.
(51) Taboada, P.; Attwood, D.; Ruso, J. M.; García, M.; Mosquera, V. *Langmuir* **2001**, *17*, 173 177.
(52) Shigerehara, K. *Bull. Chem. Soc. Jpn.* **1966**, *39*, 2332 2335.
(53) Long, F. A.; McDevit, W. F. *Chem. Rev.* **1952**, *51*, 119 169.
(54) Bijma, K.; Engberts, J. B. F. N. *Langmuir* **1997**, *13*, 4843 4849.
(55) Yoshino, A.; Yoshida, T.; Okabayashi, H.; Kamaya, H.; Ueda, I. *J. Colloid Interface Sci.* **1998**, *198*, 319 322.

seems to be entropically driven, as indicated by the thermodynamic analysis. The logarithm of the CAC as a function of temperature is U-shaped, in agreement with most amphiphilic drugs. The aggregate formation in absence of salt is related to a likely larger ionization degree and a better ability to form hydrogen bonds. Nevertheless in the presence of salt the higher degree of salt ions binding on the aggregate surface reduces the repulsive interaction between head groups, thus promoting the aggregates growth. In addition, apparent coefficients of expansibility as well as compressibilities indicate that the aggregation process tends to decrease the intramicellar repulsion, in the presence of salt, due to the shield of the ionic interaction. This process could be explained by the presence of steric interactions producing negatives apparent molar adiabatic compressibility values. Based on the similarities of our volumetric results with other drugs molecules, a BTS arrangement with the aromatic rings toward the core of the structure upon aggregation has been proposed. This fact is supported by the analysis of NMR spectra and molecular dynamics simulations. The size of the self-associated nanoparticles was estimated to be about 2.5−3.0 nm with an aggregation number of ~30 BTS molecules. On the whole, this work provides comprehensive information of BTS solution properties, helping to increase our understanding of its self-assembly process as well as the structure of the resulting aggregates. The present results are expected to be useful as a reference for the study of other benzothiazole-based molecules.

Acknowledgment. Authors thank Dirección Xeral de Promoción Científica e Tecnológica do Sistema Universitario de Galicia for financial support. Á.P. thanks "Xunta de Galicia" for his "Isidro Parga Pondal" research position. We are grateful to the "Centro de Supercomputación de Galicia" (CESGA) for computing time and for their excellent services.

Supporting Information Available: Figures S1−S5 and Table S1. This material is available free of charge via the Internet at http://pubs.acs.org.

Soft Matter

Dynamic Article Links

Cite this: *Soft Matter*, 2011, **7**, 5194

www.rsc.org/softmatter

PAPER

Self-assembling drugs: A new therapeutic strategy†

Natalia Hassan,[a] Juan M. Ruso[a] and Alfredo González-Pérez*[b]

Received 22nd December 2010, Accepted 31st March 2011
DOI: 10.1039/c0sm01529f

In the current work we proposed the new idea of "self-assembled drug" based on the combination of two or more drugs. As model system we used hexadecyldimethylammonium bromide: dicloxacilin at room temperature. The two drugs are well known for their therapeutic effect and together form worm-like micelles with the combined therapeutic effect of both individual compounds. The system was investigated using, density and sound velocity, dynamic light scattering and cryo- electron microscopy (cryo-TEM) and UV for a complete physicochemical and stability characterization.

Introduction

Spontaneously self-assembled bilayer vesicles or cylindrical micelles can be optimized to transport therapeutic molecules, ranging from small insoluble molecules to larger macromolecules like therapeutic proteins or oligonucleotides. Different structures have been seen as a suitable support for drug delivery, for example as a vector that transports insoluble drugs to be delivered in order to display a specific therapeutic effect.

Here we define a new strategy namely "self-assembled drug" as a self-assembled structure (spherical or worm-like micelles, vesicles or liquid crystals) that is formed uniquely by drugs that combined assemble in such structures. All the individual compounds should display a therapeutic effect by themselves and the resulting self-assembled structure display at the same time the role of support or vector. Many drugs display amphiphilic properties thus they can be combined with hydrotropic drugs[1] to form different kind of self-assembled structures, "self-assembled drugs".

Many authors have focused their investigations on the possibilities of incorporating an active drug substance as one of the surfactants in the catanionic complexes. The purpose of this idea is to prolongate the release rate of the drug with the aim of increasing the bioavailability of the drug compound.[2–4] The self-assembled drugs will display advantages over the current methodologies based in the combination of drugs and vectors.

As far as we know this strategy has received very little attention. However the potential is outstanding due to the possibility to apply therapies of combined drugs with optimal formulation were the self-assembled drug is at the same time the vector. This methodology could be very useful for many insoluble drugs that are small molecules with hydrotropic character optimal to form different kind self-assembled structures in combination with amphiphilic drugs. Parameters like stability, permeability can be easily controlled and the characterization performed using well stabilized techniques. The optimization of the necessary amount of therapeutic compounds avoiding the inclusion of additional supports that plays the role of vectors like in liposomes, made this strategy very interesting from the economical point of view and easy to upscale due to the intrinsic nature of the self-assembled process that do not require additional energy to be prepared.

In the current work we prepared a self-assembled drug by combination of hexadeciltrimethylammonium bromide (CTAB) and dicloxacilin (DC) resulting in the formation of worm-like micelles. Both drugs display well known therapeutic activity. CTAB is widely used due to its germicidal activity and DC is a well known penicillin with biocide activity that belongs to the group of benzyl penicillins.[5–10] Both CTAB and DC have the ability to self-assemble alone and combined to form worm like micelles. As worm like micelles have been investigated for years and the properties and applications have been recently summarized in different reviews.[11] Additionally worm-like micelles can be stabilized by using different approaches, for example *via* polymerization induced by hydrotropic salts.[12] The experimental techniques and theoretical background are now well established making them easy to characterize under different conditions. Additionally worm-like micelles have been used to give effective elongated pharmacokinetics.

Experimental

Materials and sample preparation

Hexadecyltrimethylammonium bromide, CTAB and sodium dicloxacillin monohydrate ([3-(2,6-dichlorophenyl)-5-methyl-4-isoxazolyl] penicillin) was obtained from Sigma-Aldrich Co. and

[a]*Soft Matter and Molecular Biophysics Group, Department of Applied Physics, University of Santiago de Compostela, Campus Sur s/n, 15782 Santiago de Compostela, Spain*
[b]*Membrane Biophysics Group, Niels Bohr Institute, University of Copenhagen, Blegdamsvej 17, 2100 Copenhagen, Denmark. E-mail: gonzalez@nbi.ku.dk; alfredogp@gmail.com; Web: http://www.gonzalez-perez.sitew.com/*

† Electronic supplementary information (ESI) available. See DOI: 10.1039/c0sm01529f

was well characterized by surface tension to be used as received. All solutions were made up by weight at room temperature using a METTLER AT20 balance with a precision of 0.001 mg; the water was treated with a Millipore Q system. The experiments were carried out at 25 °C. The samples have been prepared by mixing different volumes form two stock solutions of CTAB and CD in water.

Density and sound velocity

Densities and sound velocities were continuously, simultaneously, and automatically measured using a commercial density and sound velocity measurement apparatus (Anton-Paar DSA 5000 densimeter and sound velocity analyzer). Both speed of sound and density are extremely sensitive to temperature, which was therefore kept constant within $\pm 10^{-2}$ K using the Peltier method. The repeatability of the density and sound velocity measurements was better than $\pm 5 \times 10^{-6}$ g cm^{-3} and $\pm 10^{-2}$ m s^{-1}, respectively.

UV-vis

Difference spectra were measured using a Beckman spectrophotometer (model DU 640) which operates in the UV–visible region of the electromagnetic spectrum wavelength. All measurements were made in carefully matched quartz cuvettes (50 µL capacity). For absorbance difference spectra, just two cells were used. The first microcuvette contained only water and was used as a blank reference; meanwhile the other was filled with the corresponding DC or DC plus CTAB solutions. The microcuvettes were filled and placed in the same orientation for all the tests. The evolution of the systems was characterized for a fortnight. Samples have been analyzed at a fixed temperature of 25 °C.

Dynamic light scattering

Dynamic light scattering measurements were made at 298 ± 0.1 K and at a scattering angle of 90°. Time correlation was analysed by an ALV-5000 (ALV-GmbH) instrument with vertically polarized incident light of wavelength λ = 488 nm, supplied by a CW diode-pumped Nd; YAG solid-state laser supplied by Coherent. Inc. and operated at 400mW. Solutions were clarified as described above.

In dynamic light scattering a time correlation function (TCF) of the scattering intensity is measured that is formed by an autocorrelator from the scattering intensities measured at a certain starting time i(0) and at a very short time interval t later. In mormalized form the TCF is given by

$$g_2(t) = \frac{\langle i(0)i(t)\rangle}{\langle i(\infty)\rangle} \quad (1)$$

where i(∞) is the scattering intensity at very low delay times. For theoretical evaluations mostly the electric field time correlation function id used $g_1(t)$, which is related to the intensity TCF $g_2(t)$ by the Siegert relationship

$$g_2(t) = 1 + |g_1(t)|^2 \quad (2)$$

Monodisperse spherical particles show a single-exponential decay in $g_1(t)$

$$g_1(t) = e^{-Dqxt} \quad (3)$$

where D is the translational diffusion coefficient in m^2 s^{-1} and q is the length of the scattering vector in m^{-1} that is related to the scattering angle θ *via*:

$$q = \frac{4\pi n}{\lambda} sin\left(\frac{\theta}{2}\right) \quad (4)$$

with λ being the wavelength of the used light in the vacuum and n the refractive index of the sample. For polydisperse samples the exponential function in eqn (3) must be replaced by the weighted contribution of the individual populations. Then $g_1(t)$ becomes:

$$g_1(t) = \int_{\Gamma_{min}}^{\Gamma_{max}} e^{-\Gamma t} G(\Gamma) d\Gamma \quad (5)$$

where $\Gamma = Dq^2$ is the decay rate and $G(\Gamma)$ denotes the decay rate distribution function. Eqn (5) is the Laplace transform of $G(\Gamma)$ and it must be inversed in order to obtain the distribution function of the translational diffusion coefficients. For solving this equation for D, the software packages CONTIN was used.[13,14] According to Stokes–Einstein equation, the translational diffusion coefficient depends on the hydrodynamically effective sphere radius R_h

$$D_0 = \frac{k_B T}{6\pi\eta_0 R_h} \quad (6)$$

where k_B is the Boltzmann constant, T the absolute temperature and η_0 the solvent viscosity.

Cryo transmission electron microscopy cryo-TEM

The samples were prepared according to a conventional cryo-TEM protocol, using a controlled environment vitrification system (CEVS). Samples were prepared on hydrophilised (glow discharged) lacey carbón grids on which 5 µl of the sample solution was placed. The excess fluid was gently blotted away using filter paper and plunged into liquid ethane (freezing point −180 °C). All grids were stored in liquid nitrogen (−196 °C) until being transferred to the TEM. The vitrified sample was transferred to a liquid-nitrogen-cooled TEM cryo-holder (Oxford Instruments CT-3500) using a cryotransfer station designed for minimal air exposure and heat loss. Samples were imaged using a Philips CM120 BioTwin Cryo electron microscope operated at 120 kV. Images were recorded with a GIF 100 (Gatan Imaging Filter), using a CCD camera (MSC 791) in low-dose mode, giving a low electron beam intensity of around 10 e-/Å^2.[15]

3. Results and discussion

3.1 Density and sound velocity

From density measurements, apparent molar volumes can be calculated using the following equation

$$V_\phi = \frac{10^3(\rho_o - \rho)}{m\rho\rho_0} + \frac{M}{\rho} \quad (7)$$

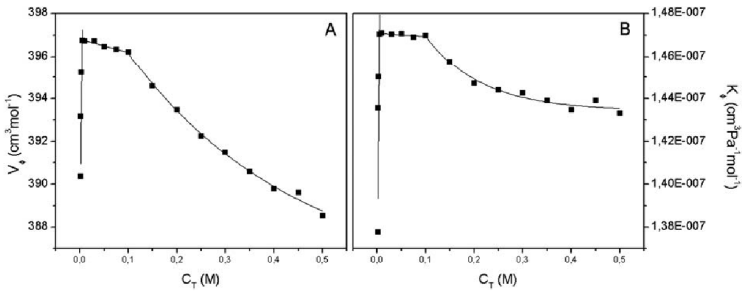

Fig. 1 Apparent molar volumes (graph A) and isentropic apparent molar compressibilities (graph B) as a function of total concentration.

where ρ is the density of the mixture at a given concentration, ρ_o is the density of pure water, M is the molecular weight of the surfactant, and m is the and molality of the solution. Fig. 1A shows plots of V_ϕ *versus* total concentration. Apparent molar isentropic adiabatic compressibilities, K_ϕ, can be calculated from ultrasound measurements

$$K_\phi = \frac{10^3(\beta - \beta_0)}{m\rho_0} + \beta_0 V_\phi \quad (8)$$

where β and β_0 are the isentropic compressibility coefficients of the solution and solvent, respectively. Fig. 1B shows plots of K_ϕ *vs.* total concentration for our system. Both plots provide a general overview of the system aggregation process. The two magnitudes increase linearly with increasing total concentration. A sharp break occurs at *ca.* 0.007 M. At higher concentrations apparent molar volumes decrease (also linearly) with concentration. However, compresibilities are almost invariant. After reaching a concentration value of 0.1 M., both quantities decrease exponentially. At very low concentrations the volumes are mainly characterized by the monomeric state, showing a rise of V_ϕ. Slope positive values imply that interactions between the charged species overcome the apolar–apolar and apolar–polar interactions. First break is related with the formation of aggregates due to the release of structured water in the hydration shell of the monomers upon aggregation. When the aggregate forms, the released water from the vicinity of the hydrophobic part of the molecule become bulk water. The water molecules around the hydrophobic part are highly structured, having a rather low compressibility compared to the bulk water.

If we continue increasing the concentration, we find that aggregates undergo a post-aggregation transition that takes place around 0.1 M. The solubilization behavior of the aggregates formed below and above the second transition is significantly different. Previous studies have reported positive values in changes of compressibility upon aggregation[16] which were attributed to the predominant role of the decrease in hydrophobic hydration in the association process.

3.2 Dynamic light scattering

In order to get additional information about the kind of self-assembled drug we prepared we performed DLS experiments with the same set of samples used in the density and sound velocity experiments. Fig. 2 shows the hydrodynamic radius

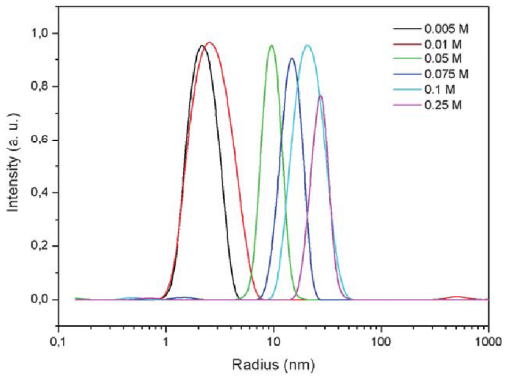

Fig. 2 Hydrodynamic radius distributions of the CTAB/DC system in water at different total concentrations.

distribution as obtained from dynamic light scattering of the CTAB/DC system at different concentrations. For all concentrations, the size distributions consist of only one narrow and symmetrical peak. As one can note, with increasing concentration, the peaks shift to higher radius without any broadening observed. Fig. 3 show the hydrodynamic radius values *versus* total concentration. For concentrations below 0.005 M no correlation function were found, which indicates the absence of

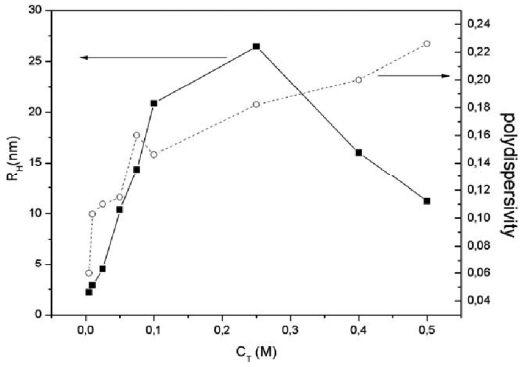

Fig. 3 Hydrodynamic radius (left hand axis) and polydispersivity (right hand axis) against total concentracion.

aggregates that can be observed with this technique. From this concentration and up to 0.1 M, hydrodynamic radius increase with concentration almost linearly. Micellar radius of CTAB micelles have been found to be (by means of SANS measurements) in the order of 2.2 nm.[17] Thus, it is reasonable to assume that mixed micelles are formed in the range from 0.005 to 0.025 M. Over this range the high value obtained for hydrodynamic radius suggest a micelle-to-vesicle transition. Such changes have been previously observed for the system CTAB-SOS.[18] Vesicle radius increase with concentration until reach a value of 22 nm for a concentration of 0.1 M (this value correlates well with the second break found for apparent molar volumes). From this point there are two remarkable effects. As the concentration increases the average radius decreases while the dispersion increases. These events are related with a new transition, probably vesicle-to-rodlike.[19] Finally, samples at highest concentration tend to show a very high polydispersivity which could be associated with longitudinal growth of the rodlike micelles towards wormlike ones. Samples at higher concentration were not available for light scattering techniques

3.3 Cryo-TEM

In order to gain insight in the structural nature of the self-assembled drug structures formed by combination of CTAB and DC we performed direct imaging experiments using cryo-TEM in the samples with moderate viscosity. The results show the presence of worm-like micelles as we can see in Fig. 4. No presence of spherical micelles was found in the samples under investigation.

In the Fig. 5 the arrows show the presence of Y-junctions characteristic of packing parameter P in between 1/2 and 1, also called threefold junctions. The black arrows show the junctions resulting for the interaction of two individual wormlike micelles. Here the end-cap of one fuse with the tubular region of the other. The white arrows show y-junctions resulting from the interaction of the end-cap of a wormlike micelle with his tubular part. Both phenomena are characteristic of the threefold junction.

Due to the interplay of the energy-entropy of the end-caps, elongated micelles and branch points, a transition between linear worm-like micelles and branched networks is possible.

In fact branched networks is an intermediate step between linear elongated and a lamellar phases.[20,21] The y-junctions are formed and disrupted constantly because is a dynamic process but this morphology is energetically stable, according to Porte *et al.*[21]

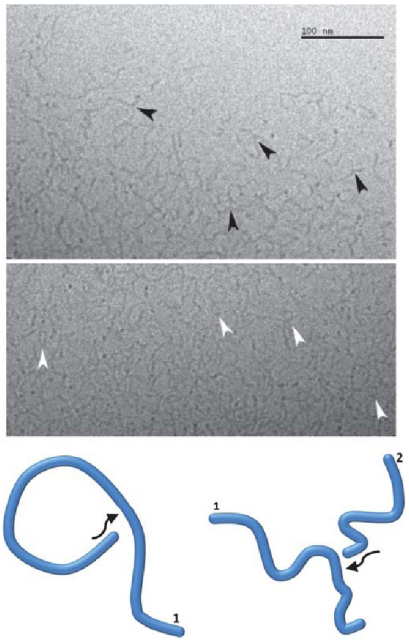

Fig. 5 (top) The cryo-TEM images show the presence of worm-like micelles. The black arrows show Y-junctions and the white ones the presence of different loops. The experiments have been carried out at room temperature. The scheme (bottom) shows two mechanism of worm-like micelle fusion resulting in a local Y-junction. On the left a micelle form a loop connecting the end-cap with their own body. On the right one micelle end-cap interact with the body of a second one, resulting in a Y-junction.

Additional TEM images are shown in the supporting information.

3.4 UV-vis spectra analysis

The data related to the UV-vis absorption spectra of dicloxacillin are shown in Fig. 6. In these plots, the time evolution of difference absorption spectra of pure DC (0.005 M) and DC/CTAB (0.01 M) can be observed (similar plots for the other concentrations have been obtained).

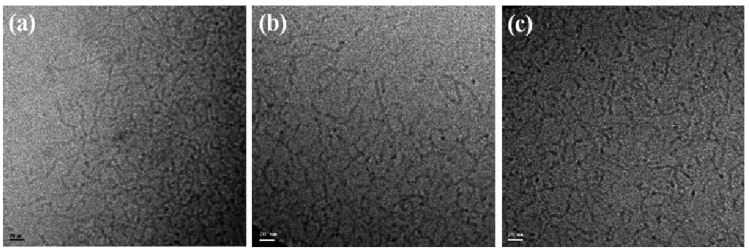

Fig. 4 (a–c) The cryo-TEM images show the presence of worm like micelles. The experiments have been carried out at room temperature.

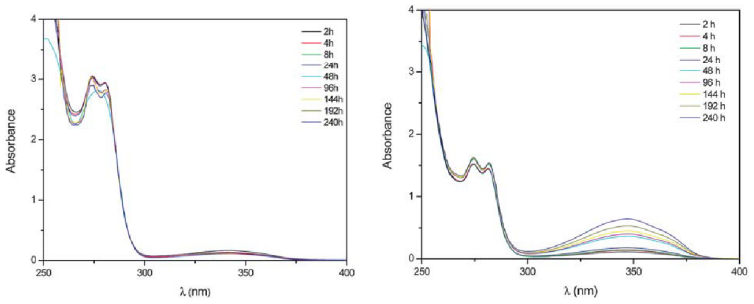

Fig. 6 Time evolution of difference absorption spectra of pure dicloxacillin 0.005 M (left hand gragh) and DC/CTAB 0.01 M (right hand graph).

Concerning penicillins the characteristic peak of these molecules were considered to be a shoulder around 270 nm. Some general trends can be inferred from the plots. First of all, no red or blue shifts have been observed for all systems under study. Consequently, we have not found isobestic points. This means that only one type of aggregate is present in the solution. On the other hand, absorbance peaks at 274 and 280 nm decrease with time for pure DC and DC/CTAB; meanwhile, for the DC/CTAB at 347 nm. a peak appears that grows up with time. Furthermore, the absorption curve is rather smooth at maximum absorbance. The detection wavelength is considered to be that at which maximum absorbance of a substance is observed. However, it is more interesting to check the variation with time of the peak placed at 347 nm. This peak does not exist for the pure DC, just in the presence of CTAB. Thus it is reasonable to assume that the origin of this peak is form the DC in the mixed aggregated. In Fig. 7 the absorbance of this peak as a function of time can be observed.

When mixed micelles are present in the solution (0.01 M) the absorbance does not present significant changes with time and it is quite similar to that of the pure DC. This can be explained on the basis of the dynamical equilibrium of the monomers and the aggregates. At concentrations of 0.05 M, vesicles are aggregates present. Now, the adsorption is clearly higher than those of the pure DC and increases with time until a maxima. So, most part of the DC molecules are in the vesicles. The maximum absorbances correspond to the rod- and worm-like structures (0.1 and 0.2 M). In these systems almost all DC molecules are incorporated into the structures, a large increase in adsorption can be seen to short times. This fact continues until 25 h, where the system precipitate and no further observation is possible.

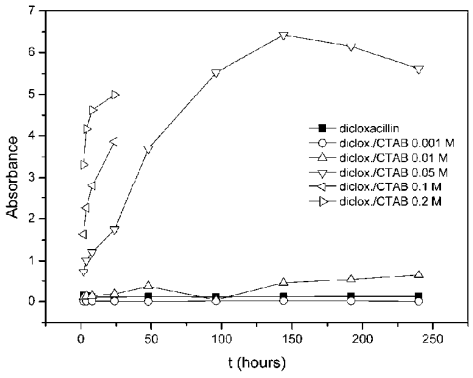

Fig. 7 Absorbance (at 347 nm) of the system DC/CTAB as a function of time.

4. Conclusions

In the current work we defined the concept of self-assembled drug and characterized an example of worm-like micelle drug by combination of two individual drugs with specific therapeutic effect. The combination of both compounds forming a self-assembled drug display the drug function as well as serve as a vector.

The complete characterization of this self-assembled drug was done using well established techniques like, density sound velocity, DLS, cryo electron microscopy. The investigation of the stability and time evolution was done using UV-visible experiments. This is a first step for further research about their therapeutic activity and the efficiency compared with other classical delivery methods using drugs embedded in vectors. Many other self-assembled drugs like vesicles and liquid crystals can be obtained by the appropriate combination of single therapeutic compounds. We expect our work to encourage the scientific community to investigate new self-assembled drugs and their advantages over more conventional strategies in drug delivery.

Acknowledgements

A. Gonzalez-Perez wants to acknowledge Prof. Thomas Heimburg for giving me the opportunity to work in his group at the Niels Bohr Institute. J. M. Ruso and N. Hassan thank the Xunta de Galicia for their financial support (Project No. 10PXIB206258PR).

References

1 T. K. Hodgdon and E. W. Kaler, Hydrotropic solutions, *Curr. Opin. Colloid Interface Sci.*, 2007, **12**(3), 121–128.
2 N. Dew, K. Edwards and K. Edsman, *Colloids Surf., B*, 2009, **70**, 187–197.
3 T. Bramer, N. Dew and K. Edsman, *J. Pharm. Sci.*, 2006, **95**, 769–780.
4 N. Dew, T. Bramer and K. Edsman, *J. Colloid Interface Sci.*, 2008, **323**, 386–394.
5 P. Martinez-Landeira, A. Gonzalez-Perez, J. M. Ruso, G. Prieto and F. Sarmiento, *Colloids Surf., A*, 2004, **236**, 121–131.

6 P. Taboada, D. Attwood, J. M. Ruso, M. García, F. Sarmiento and V. Mosquera, *J. Colloid Interface Sci.*, 1999, **220**, 288–292.
7 P. Taboada, V. Mosquera, J. M. Ruso, F. Sarmiento and M. N. Jones, *Langmuir*, 2000, **16**, 934–938.
8 P. Taboada, D. Attwood, M. García, M. N. Jones, J. M. Ruso, V. Mosquera and F. Sarmiento, *J. Colloid Interface Sci.*, 2000, **221**, 242–245.
9 P. Taboada, V. Mosquera, J. M. Ruso, F. Sarmiento and M. N. Jones, *Langmuir*, 2000, **16**, 6795–6800.
10 J. M. Ruso, D. Attwood, M. García, P. Taboada, L. M. Varela and V. Mosquera, *Langmuir*, 2001, **17**, 5189–5195.
11 D. P. Acharya and H. Kunieda, *Adv. Colloid Interface Sci.*, 2006, **123**, 401–413.
12 S. Liu, Y. I. Gonzalez, D. Danino and E. W. Kaler, *Macromolecules*, 2005, **38**, 2482.
13 S. W. Provencher, *Comput. Phys. Commun.*, 1982, **27**(3), 229–242.
14 S. W. Provencher, *Biophys. J.*, 1976, **16**, 27–41.
15 D. Danino, A. Bernheim-Groswasser and Y. Talmon, *Colloids Surf., A*, 2001, **183**, 113–122.
16 P. Taboada, D. Attwood, J. M. Ruso, M. García and V. Mosquera, *Langmuir*, 2001, **17**, 173–177.
17 V. K. Aswal, P. S. Goyal and P. Thiyagarajan, *J. Phys. Chem. B*, 1998, **102**, 2469–2473.
18 L. L. Brasher and E. W. Kaler, *Langmuir*, 1996, **12**, 6270–6276.
19 M. T. Yatcilla, K. L. Herrington, L. L. Brasher, E. W. Kaler, S. Chiruvolu and J. A. Zasadzinski, *J. Phys. Chem.*, 1996, **100**, 5874–5879.
20 A. Zilman, S. A. Safran, T. Sottmann and R. Stray, *Langmuir*, 2004, **20**, 2199–2204.
21 G. Porte, R. Gomati, O. El Haitamy, J. Appell and J. Marignan, *J. Phys. Chem.*, 1986, **90**, 5746–5751.

Langmuir ARTICLE
pubs.acs.org/Langmuir

Hydrogenated/Fluorinated Catanionic Surfactants as Potential Templates for Nanostructure Design

Natalia Hassan, Juan M. Ruso,* and Ángel Piñeiro*

Soft Matter and Molecular Biophysics Group, Department of Applied Physics, University of Santiago de Compostela, Campus Vida s/n, 15782, Santiago de Compostela, Spain

ABSTRACT: The structure and physicochemical properties of the nanoparticles spontaneously formed within aqueous mixtures of the hydrogenated/fluorinated catanionic surfactant cetyltrimetylammonium perfluorooctanoate in the absence of counterions as a function of its concentration are investigated by a combined experimental/computational study at room temperature. Apparent molar volumes, isentropic apparent molar compressibilities, and dynamic light scattering measurements together with transmission and cryo-scanning electron as well as confocal laser microscopy images, and computational molecular dynamics simulations indicate that a variety of structures of different sizes coexist in solution with vesicles of ~160 nm diameter. Interestingly, the obtained nanostructures were observed to self-assemble from a random distribution of monomers in a time scale easily accessible by atomistic classical molecular dynamics simulations, allowing to provide a comprehensive structural and dynamic characterization of the surfactant molecules at atomic level within the different aggregates. Overall, it is demonstrated that the use of mixed fluorinated hydrogenated surfactant systems represents an easy strategy for the design of specific nanoscale structures. The detailed structural analysis provided in the present work is expected to be useful as a reference to guide the design of new nanoparticles based on different hydrogenated/fluorinated catanionic surfactants.

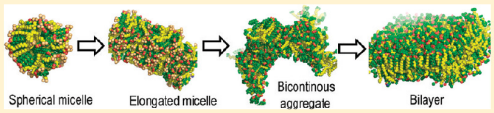

1. INTRODUCTION

Nowadays, there is a strong social and economical pressure that encourages the design of cheaper and more sustainable materials, products, and processes.[1] The self-assembly of relatively small molecules yielding new nano-objects opens unforeseen and unique opportunities for a variety of fields in science as well as for several industries. A number of commercial products based on nanostructures are already currently available for the public consumer.[2] For instance, architecturally complex assemblies and tailored functionalized polymers have been specifically employed in sensors, semiconductors and pharmaceuticals devices.[3,4] Mixtures of heterogeneous molecules which self-assemble in aqueous solution represent an interesting alternative for the design of nanoparticles due to its higher flexibility when compared to systems based on homogeneous molecules. Catanionic surfactants are chemical species consisting of an amphiphilic anionic and an amphiphilic cationic molecule. Their ability to self-assemble giving different arrangements both at the air/water interface and also in the bulk solution[5−8] is related to the strong synergism between the oppositely charged head groups,[8−10] with no chemical modifications or reactions. The effect that the combination of headgroups at fixed chain lengths, $(CH_2)_{16}$ vs $(CH_2)_8$, as well as the effect that the asymmetry in the chain lengths at fixed headgroups have on the self-assembly of catanionic surfactants has been recently studied in detail[11,12] revealing that both contributions are relevant. Catanionic surfactants resulting from the combination a fluorinated-chain and a hydrogenated-chain species are especially interesting due to the dual lipophobic/hydrophobic character of perfluorinated chains, allowing the formation of a variety of structures.[13−17] This has been revealed, for instance, from the phase separation of hydrocarbon/fluorocarbon chains in mixed monolayers observed by atomic force microscopy[18] and NMR measurements.[19] The competition between electrostatic interactions favoring the mixing and the lipophobicity of fluorinated chains, promoting segregation, may result in modulated phases or two-dimensional self-assembly. This has been suggested as a tactic for nanopatterning biologically relevant ligands on bilayers in vitro or in living cells.[20] Stable vesicles consisting of perfluorocarbon lipids have already been proved to be well suited as drug delivery vehicles of cytolytic peptides such as melittin upon their incorporation to the nanostructured bilayers.[21] We have recently reported a detailed characterization of the hydrogenated-cetyltrimethylammonium (CTA) perfluorooctanoate (PFO) catanionic surfactant system at the solution/air interface.[8] No segregation of the fluorinated molecules was observed in the obtained monolayers indicating that the electrostatic attraction between the cationic and the anionic head groups dominate on other less favorable contributions. Surface pressure vs molecular area isotherms show two transitions which were explained in terms of the molecular arrangement of both surfactants as well as of the internal ordering of CTA molecules from MD simulations. The structure of the nanoparticles resulting from the mixture of these two surfactants in the bulk solution is expected to depend also on the competition

Received: February 18, 2011
Revised: June 24, 2011
Published: July 05, 2011

dx.doi.org/10.1021/la2019346 | Langmuir 2011, 27, 9719–9728

between the electrostatic interactions of the head groups, on the dual lipophobic/hydrophobic character of the perfluorinated chain of perfluorooctanoate, and on the difference between the lengths of the two molecules (16 vs 8 C-atoms). The main objective of the present work is precisely to characterize in detail the nanoaggregates spontaneously formed in the bulk solution by the same molecules in the absence of counterions. A combined experimental/computational study involving density, sound velocity, and dynamic light scattering measurements, together with transmission and scanning electron, as well as confocal laser microscopy images, and molecular dynamics simulations of equimolar mixtures of these two surfactants at several concentrations and at room temperature was performed for this aim. Such study allows us to present a detailed characterization from the macroscopic to the atomistic resolution of the spontaneously formed structures. This level of detail was not achieved in previous studies based on hydrogenated/fluorinated catanionic systems.[13−17]

2. METHODOLOGY

2.1. Experimental Section. *Materials.* The studied catanionic system was synthetized by direct mixing of the anionic surfactant sodium perfluorooctanoate (S-PFO, 97% from Lancaster) and the cationic surfactant cetyltrimethylammonium bromide (CTA-B, 99% from Sigma) at equimolar concentrations (0.5×10^{-3} M) in water. Both chemicals were used as received, without further purification. The salt precipitate formed after mixing was removed by washing with Milli-Q water until the counterions Br^- and Na^+ could not be detected by elemental analysis.

Density and Ultrasound Velocities. Ultrasound velocities and densities were continuously, simultaneously, and automatically measured using a DSA 5000 Anton Paar density and sound velocity analyzer. This equipment possesses a new generation vibrating tube for density measurements and a stainless-steel cell connected to a sound velocity analyzer with resolution $\pm 10^{-6}$ g cm^{-3} and 10^{-2} m s^{-1}, respectively. Both speed of sounds and densities are extremely sensitive to temperature so this was controlled at 298 K within $\pm 10^{-3}$ K through a Peltier device incorporated in the equipment. Density and ultrasound measurements were reproducible within 10^{-6} g cm^{-3} and 10^{-2} m s^{-1}, respectively.

Transmission Electron Microscopy (TEM). The morphological examination of the self-assembled aggregates was performed by transmission electron microscopy (CM-12 Philips). The samples were prepared by the negative-staining technique with a 2% (w/v) phosphotungstic acid. A carbon Formvar-coated copper grid was put into the solution for 1 min and then into the sodium phosphotungstate for another minute. Then the grids were dried. In between and thereafter, excess liquid was sucked away with filter paper. For each system, at least three TEM samples were prepared and observed independently.

Confocal Laser Microscopy. Confocal microscopy was performed on a BIO-RAD MRC 1024 ES confocal system mounted on a Nikon Eclipse TE300 upright EPI-fluorescence microscope. The equipment is fitted with a line Ar laser, excitation line 514 nm, using a 20× objective.

Cryo-Scanning Electron Microscopy (Cryo-SEM). The scanning electron microscope used was a JSM- 6360 LV (Cryo-transfer Gatan Alto 2100). Samples were cryo-fixed by plunging it into subcooled liquid nitrogen where it remains frozen during imaging. The samples were examined at 5 KV at 143 K.

Dynamic Light Scattering. Dynamic light scattering measurements were made at 298.0 ± 0.1 K and at different scattering angles (30°, 50°, 60°, 70°, and 90°). Time correlation was analyzed by an ALV-5000 (ALV-GmbH) instrument with vertically polarized incident light of wavelength λ = 488 nm supplied by a CW diode-pumped Nd; YAG solid-state laser (Coherent. Inc.) operated at 400 mW. The analysis of the DLS measurements is based on the normalized time correlation function which is given by

$$g_2(t) = \frac{\langle i(0)i(t)\rangle}{\langle i(0)^2\rangle} \quad (1)$$

where $i(0)$ and $i(t)$ are the scattered-light intensity at certain starting time 0 and after a short time interval t. For theoretical evaluations mostly the electric field time correlation function is used $g_1(t)$, which is related to the intensity TCF $g_2(t)$ by the Siegert relationship

$$g_2(t) = 1 + |g_1(t)|^2 \quad (2)$$

Monodisperse spherical particles show a single-exponential decay in $g_1(t)$

$$g_1(t) = \exp(-Dqx^2t) \quad (3)$$

where D is the translational diffusion coefficient in m^2 s^{-1} and q is the length of the scattering vector in m^{-1} that is related to the scattering angle θ via

$$q = \frac{4\pi n}{\lambda}\sin\left(\frac{\theta}{2}\right) \quad (4)$$

with λ being the wavelength of the used light in the vacuum and n the refractive index of the sample. For polydisperse samples the exponential function in eq 3 must be replaced by the weighted contribution of the individual populations. Then $g_1(t)$ becomes

$$g_1(t) = \int_{\Gamma_{min}}^{\Gamma_{max}} \exp(-\Gamma t)G(\Gamma)d\Gamma \quad (5)$$

where $\Gamma = Dq^2$ is the decay rate and $G(\Gamma)$ denotes the decay rate distribution function. Equation 5 is the Laplace transform of $G(\Gamma)$ and it must be inversed in order to obtain the distribution function of the translational diffusion coefficients. For solving this equation for D, the software packages CONTIN was used. According to Stokes−Einstein equation, the translational diffusion coefficient depends on the hydrodynamically effective sphere radius R_h

$$D_0 = \frac{k_BT}{6\pi\eta_0R_h} \quad (6)$$

where k_B is the Boltzmann constant, T the absolute temperature, and η_0 the solvent viscosity.

2.2. Molecular Dynamics Simulations. *Setup of the Simulation Boxes.* MD simulation studies at eight different surfactant concentrations were performed to investigate the structure of the aggregates spontaneously formed along the trajectories. Each system was built by placing identical amounts of PFO and CTA molecules at random positions in a cubic box which is then filled with water molecules and energy-minimized using the steepest descent method. The local concentrations obtained in this way (see Table 1) are significantly larger than those of the solutions studied experimentally. However, it is expected to observe the formation of different self-assembled structures as a result of the limited number of surfactant molecules in each system.

MD Simulation Parameters. Thirty ns long trajectories at 298 K and 1 bar were performed for each of the eight systems using the GROMACS package[22−24] version 3.3.3. The two surfactant molecules were modeled as described in a previous paper[8] by using the GROMOS96 (53a6) force field[25] with the bonded parameters and partial charges that involve fluorine in PFO taken from Borodin et al.[26] The extended simple point charge (SPC/E) model[27] was utilized for water molecules. Three dimensional periodic boundary conditions with cubic boxes were used for all the trajectories. Water and surfactant molecules were separately coupled to a Berendsen thermostat with a common period of 0.1 ps.[28] The pressure was isotropically controlled by using a Berendsen barostat[28] with a

Table 1. Number of Water and PFO/CTA Catanionic Molecules Together with the Ratio between Both for the Systems Studied by MD Simulations

water molecules	catanionic molecules	ratio
16412	20	820.6
15664	40	391.6
14949	60	249.2
14243	80	178.0
13549	100	135.5
12000	100	120.0
12000	150	80.0
12000	200	60.0

coupling constant of 1.0 ps and considering an isothermal compressibility of 4.5×10^{-5} bar^{-1}. Long range electrostatic interactions were calculated using the Particle Mesh Ewald method[29,30] with a real-space cutoff of 0.9 nm, a 0.12 nm spaced grid, and fourth-order B-spline interpolation. Random initial velocities were assigned to the systems from a Maxwell−Boltzmann distribution at 298 K. The equations of motion were integrated using the leapfrog method[31] with a time step of 2 fs. Bond lengths and angles in water were constrained using the SETTLE algorithm,[32] while the LINCS algorithm[33] was used to constrain bond lengths within the surfactant molecules. During the MD simulations, coordinates, velocities, and energies were stored every 10 ps for further analysis.

Analysis of MD Trajectories. The viewers RASMOL 2.7,[34] VMD 1.8.2,[35] and PyMOL 0.99[36] were employed to roughly inspect the arrangement of surfactant molecules and to capture images throughout the trajectories. The density of each simulation box, the average volume per surfactant molecule, the area exposed to the solvent, the contact area between the PFO and the CTA molecules, the local order parameters and the diffusion coefficients were averaged over the last ns of the trajectory for both surfactant molecules. Densities, exposed areas and diffusion coefficients were calculated using tools from the GROMACS package. The surfactant volume for the different concentrations was determined by subtracting the volume corresponding to the number of water molecules contained in each system to the total box volume.[37] Local order parameters were defined by

$$S_i = (3 \cos \theta - 1)0.5 \tag{7}$$

where θ is the angle between the segments joining carbon atoms $(i - 1, i + 1)$ and $(i, i + 2)$ in a linear chain. This allows to quantify deviations from trans conformations of hydrocarbon and fluorocarbon chains regardless the orientation of the molecule (see below).

3. RESULTS AND DISCUSSION

Density and Ultrasound Velocities. Apparent molar volumes can be calculated from density measurements by using the following equation:

$$V_\phi = \frac{10^3(\rho_0 - \rho)}{m\rho\rho_0} + \frac{M}{\rho} \tag{8}$$

where ρ is the density of the mixture at a given concentration, ρ_0 is the density of pure water, M is the molecular weight of the surfactant, and m is the molality of the solution. Apparent molar isentropic adiabatic compressibilities are related to ultrasound measurements by

$$K_\phi = \frac{10^3(\beta - \beta_0)}{m\rho_0} + \beta_0 V_\phi \tag{9}$$

where β and β_0 are the isentropic compressibility coefficients of the solution and solvent, respectively. These two properties are highly sensitive to the intermolecular interactions having place into the solution[38] and so to the aggregation process (see Figure 1). Three different regions, separated by sharp slope changes, can be identified in the V_ϕ vs concentration profiles. Since these properties usually change smoothly when only monomers are present in the solution, each of these regions must correspond to a different aggregation state. The low concentration at which the first aggregates appear, on account of the well-known synergistic cmc reduction in catanionic mixtures,[39] do not allow a direct analysis of monomers. Initial increase in V_ϕ is typically related to the release of structured water molecules surrounding the monomers when the aggregates are formed. This has been connected to the formation of spherical aggregates.[40] At intermediate concentrations there is a short concentration region where V_ϕ remains constant. The third region observed at higher concentrations, presents a steady decrease of V_ϕ. These sharp breaks reflect postaggregation transitions of the surfactant molecules which should be due to relative rearrangements of the solute molecules like transitions to gauge conformations in addition to direct solute-water interactions.[41] The latter should also be affected by the structure of the aggregates since it is known that electrostriction of the water structure in contact with the surface of micelles formed by zwitterionic molecules is typically lower than for ionic surfactants.[42] The aggregates formed by PFO and CTA are expected to form ion pairs at their surface resembling zwitterionic surfactants and then forming relatively thin layers of structured water when compared to aggregates of ionic molecules.

Szleifer et al. calculated molecular properties for chains in aggregates of different shapes including cylinders, spheres, and planar bilayers.[43] Such studies indicated that geometric packing constraints lead to a gradient of conformational freedom along the chains. Those in spherical and rod-shaped micelles were reported to be more disordered than in bilayers due to the greater surface curvature of the former.[44] Those conclusions cannot be directly applied to our system, which is much more complex since it results from the combination of an anionic surfactant with a C8 long fluorocarbonated chain and a cationic surfactant with a C16 long hydrocarbonated chain. Nevertheless, the decrease in apparent molar volumes at higher concentrations could be related to the formation of vesicles involving conformational changes or/and redistributions of the surfactant molecules. Such rearrangements are expected to be more likely for CTA due to its longer and more flexible alkyl chain.[8]

Normally, negative volume differences between the two states of a given process lead to negative compressibility changes. Thus, the transitions between the different aggregates are reflected in the K_ϕ curve which also shows clear slope changes at surfactant concentrations similar to those observed in the V_ϕ curve. The negative slope may be explained in terms of the higher packing of the aggregates as the concentration increases. This suggests a strong transition at ~0.5 mM that could correspond to the formation of spherical micelles and another weaker transition at ~2.5 mM. The second transition is missing in the apparent molar volumes. The characterization of the behavior of this catanionic surfactant as a function of its concentration in aqueous solution obtained from the analysis of only these two properties is incomplete and so the same system was further studied by DLS, several microscopy techniques and computational methods.

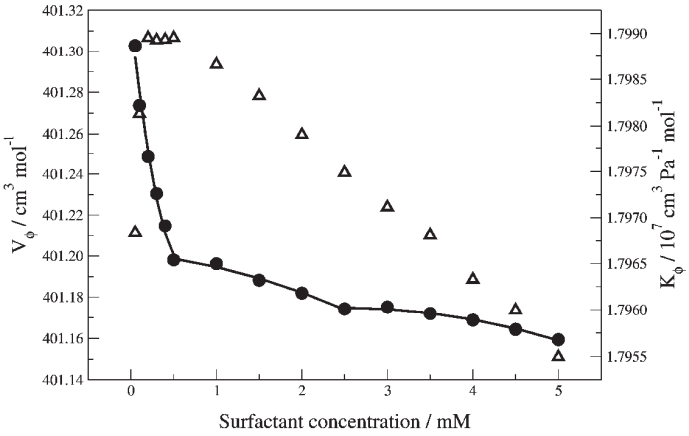

Figure 1. Apparent molar volumes (Δ) and isentropic apparent molar compressibilities (●) as a function of the PFO-CTA concentration.

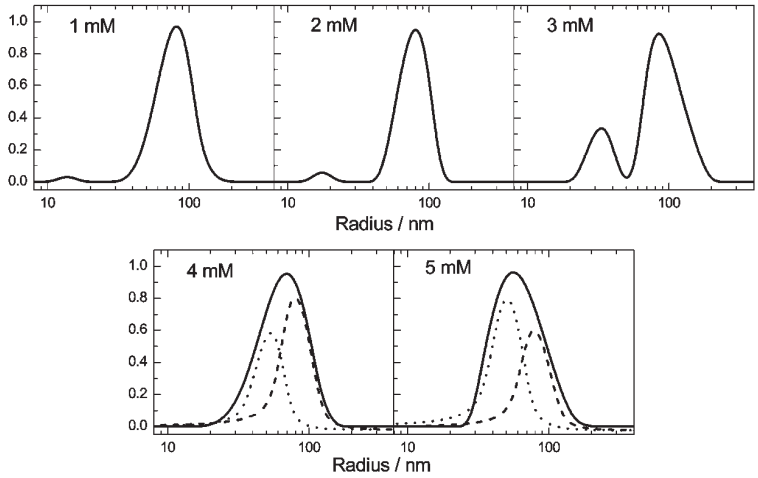

Figure 2. Size distributions obtained from DLS analysis for PFO-CTA solutions at the concentrations indicated in each panel.

Dynamic Light Scattering. In order to get further structural information about the aggregates spontaneously formed in aqueous PFO + CTA mixtures, DLS experiments at different concentrations were performed. The overall scattered light count rate show different linear trends which can be roughly associated to three concentration regions: from 1 to 2.5 mM, from 2.5 to 3.5 mM, and from 3.5 to 5 mM. This suggests again that the scattering arises primarily from the different aggregates present in the solution. Moreover, this also indicates that multiple scattering was not a significant issue and the sizes of the aggregates in the solution are approximately constant in each of these regions. No correlation function was observed for concentrations below 1 mM because the aggregates existing under those conditions are too small. The hydrodynamic radius distribution determined by using the ALV software, after fitting the dynamic light scattering of the PFO/CTA system at different concentrations, are shown in Figure 2. The size distributions are bimodal for all the studied concentrations. The weak angular dependence of the R_h values indicates that the suspended particles are in general isotropic in

Table 2. Mean Hydrodynamic Radius for the PFO/CTA Catanionic System As a Function of Total Concentration

total concentration (mM)	R_{DLS} (nm) 1st peak	R_{DLS} (nm) 2nd peak
1.00	13.7	82.4
2.00	17.5	80.9
3.00	33.6	87.6
4.00	52.8	79.8
5.00	50.6	78.7

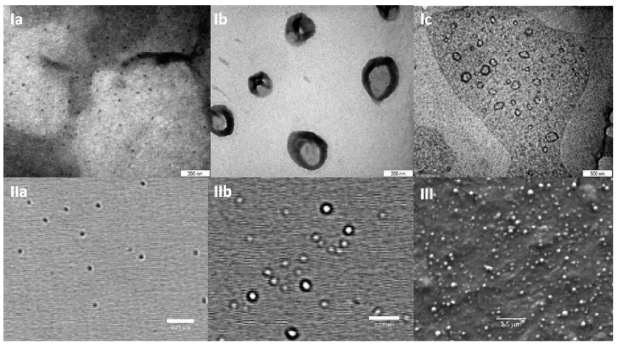

Figure 3. I. TEM micrographs of PFO-CTA solutions at 1 mM (Ia), 3 mM (Ib), and 5 mM (Ic). II. Confocal micrographs of PFO-CTA solutions at 2 mM (IIa), 4 mM (IIb) and III. Cryo-SEM micrograph of PFO-CTA at 4 mM. The scales are indicated within each panel: 200 nm for Ia and Ib, 500 nm for Ic, 250 nm for IIa and IIb, and 2.5 μm for III.

shape. The clear difference between the two peaks may be explained by the relative intensity of light scattered by structures of various sizes which in a Rayleigh approximation is proportional to r^6, with r being the radius of the corresponding structure. Numerical values of the mean radius for both peaks at five different concentrations are listed in Table 2. A deconvolution analysis was performed to get the mean radii at 4 and 5 mM. The patterns and implications of increasing total concentration in size distribution can be summarized as follows: (i) the surfactant concentration has not a significant effect on the second peak (see Table 2 and Figure 2) indicating that there is an almost constant amount of particles with a radius of approximately 80 nm; (ii) there is a population of smaller particles whose size increases as the surfactant concentration raises; (iii) the size of the observed particles in any of both populations is significantly larger than that of typical spherical micelles (the radius of CTA micelles has been estimated to be of about 2.2 nm by SANS measurements);[45] (iv) these observations, together with previous experiments for the system sodium octylsulfate-CTA,[46] allow to suggest that mixed PFO/CTA spherical micelles are formed below 1 mM and that the particle size increment with the surfactant concentration is due to a micelle-to-vesicle transition, although this will be further investigated by several microscopy techniques (see below). Typically, vesicle size distribution is kinetically determined by the size at which open fragments, growing as they fuse together, can rapidly make the transition to the vesicle state. Small vesicles, producing small DLS peaks, fuse themselves to form bigger ones, corresponding to the highest DLS peak observed in Figure 2. Our results suggest that the small vesicles grow with increasing surfactant concentration until the size of both vesicle populations is of the same order. The final size of vesicles is typically determined by the bilayer bending constant that restrains the radius of the resulting nanostructure avoiding energetically unfavorable curvatures.[47]

Microscopy Morphology Characterization. For further morphological insight into these self-assembled structures, transmission electron microscopic (TEM), cryo-scanning electron microscopy (Cryo-SEM), and confocal scanning laser microscopy studies were performed. Figure 3 sheds some light on the morphology of the resulting nanoparticles. Regular spherical vesicles are observed in TEM and confocal images of the solutions above 3 mM. The diameter of the spheres ranges from 180 to 280 nm which is in reasonable agreement with hydrodynamic radius obtained from DLS analysis. Increase in concentration results in the appearance of small defects on the surface of particles (Figure 3, panels Ib and Ic). On the other hand, although some vesicles fuse at the largest concentration studied, single vesicles can also be identified. Images taken at the same concentrations also revealed that these vesicles were separately dispersed. TEM and confocal images confirmed that these spherical structures were hollow in nature. Figure 3-Ib shows that as a result of sample treatment for the adquisition of the TEM images, the vesicles with flexible and deformable wall, seem to collapse getting a crumpled appearance. In contrast, in solution, all vesicles were found to be spherical as seen from confocal microscopy and DLS measurements at different angles. Similar structures were observed in the images obtained by cryo-SEM (Figure 3-III)

Catanionic systems typically form a number of phases and structures according to the packing parameter as well as to the concentration of each surfactant.[48] Generally, in catanionic mixtures of hydrogenated surfactants, precipitation of the catanionic salt equilibrated with the lamellar phase occurs close to the equimolar ratio.[49] On the dilute region, systems like hexadecylpyridinium octylsulfonate, hexadecyltrimethylammonium octylsulfate or alkyltrimethylammonium alkylsulfonates exhibit an interesting temperature-dependent phase behavior. Thus, at temperatures slightly higher than the solubilization temperature, polydisperse vesicles are found. However, at intermediate temperatures, vesicles undergo fusion into a planar lamellar phase. It was concluded that this phase behavior was mainly driven by combination of charge density of the headgroups, specific interactions between headgroups and the overall chain length of the catanionic compound.[11,12] In our system, the lamellar phase does not appear at 298 K in the studied concentration range, although it was observed in previously studied hydrogenated/fluorinated catanionic systems.[14] Spontaneous formation of unilamellar vesicles consisting of the same catanionic surfactant in the presence of NaBr salt has been observed by cryo-TEM and small angle neutron scattering experiments.[47]

Molecular Dynamics Simulations. The previous experimental results provide clear evidence on the existence of several aggregates, including vesicles with a radius of approximately 80 nm, which are spontaneously formed by mixing different equimolar concentrations of PFO and CTA in aqueous solution. Complementary structural and dynamical information at the atomic level

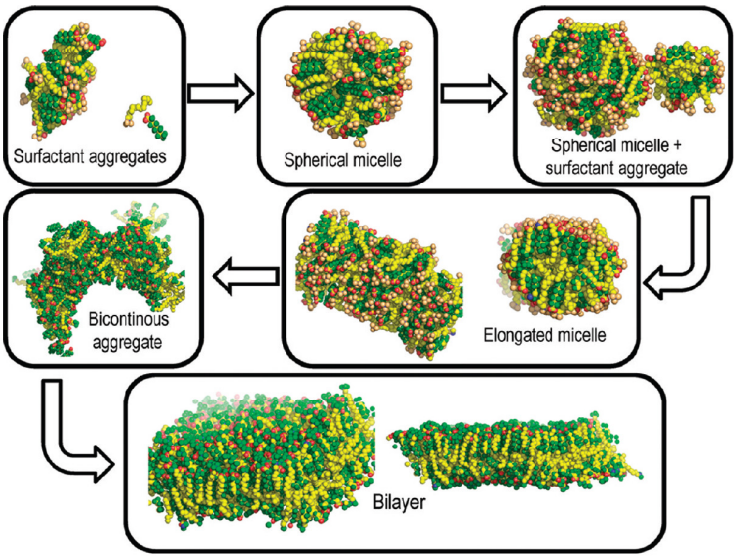

Figure 4. Snapshots of the different aggregate structures obtained for the PFO-CTA catanionic system at increasing surfactant concentration after 30 ns of MD simulation. The ratio water/catanionic molecules is 821, 392, 178, 136, 80, and 60 from the most diluted to the most concentrated system, following the sequence indicated by the arrows.

may be obtained by MD simulations of the same system if the experimental conditions: concentration, pressure and temperature; are reproduced. The pressure and temperature may be well controlled by standard algorithms (see the Methodology section). In contrast, the number of solvent molecules necessary to mimic the experimental concentrations is too large to be employed in the atomistic simulations: the largest surfactant concentration studied in this work is 5 mM which means about 11 thousand waters for each catanionic molecule, i.e., more than 10^6 waters to solvate 100 solute molecules. As an approach to model different surfactant concentrations, the method explained in the methodology section was followed. Briefly, different amounts of PFO-CTA catanionic molecules were solvated in about 12−17 thousand water molecules. Due to the solvent−solute and solute−solute interactions, the molecules aggregate quickly during the MD trajectories reaching different patterns which depend on the maximum amount or concentration of the catanionic molecules present in each system (Figure 4). The net effect is equivalent to reproducing different local concentrations of the catanionic system. Our results indicate that the spherical micelles consist of ∼50 catanionic molecules. The addition of more than ∼50 molecules results in a small aggregate in addition of one spherical micelle. More complex structures like bicontinuous aggregates or elongated micelles may be obtained by increasing the local concentration of the surfactant. The lowest water to surfactant ratio results in the spontaneous formation of bilayers. Unaffordable large systems would be needed to reproduce the spontaneous formation of an entire vesicle but the obtained bilayers may be taken as vesicle patches. Representative diameters for the spherical and elongated micelles are 4.5 and 3.7 nm, respectively. The cross-section diameter of the bicontinuous structures is equivalent to that of the elongated micelles while the thickness of the bilayers is approximately 2.6 nm. As expected, the total density of the simulated systems rises with the surfactant concentration increase (Figure 5). This is due to the larger amount of catanionic molecules, whose density is higher than that of the solvent, and also to their increased packing under those conditions. The diminution of volume when going from the aggregates shown in Figure 4 (top-left) to the bilayer is of ∼3−4% per catanionic molecule (Figure 5). As explained in the Methodology section, the molecular volume decrease determination is based on the difference between the volume of the entire simulation box and the volume of the solvent, assuming that its density corresponds to the density of pure water at 298 K. This approach is not strictly valid since the local water structure, and then its density, depends on its interactions with the solute molecules. Hence, it is convenient to further the analysis. It is well-known that molecular self-assembly in aqueous solution is typically accompanied by a significant loss of hydrophobic area exposed to the solvent. Both the PFO and CTA molecules reduce their exposed area to the solvent when the surfactant concentration increases (Figure 6). The average slope of the solvent-exposed area decrease for CTA is approximately twice that for PFO molecules. Thus, the contribution per carbon atom is practically identical for both molecules.

The above-mentioned packing change for the different structures should involve an increase of the contact area between the PFO and CTA molecules. This is also shown in Figure 6. However, since the PFO/CTA contact area increase cannot compensate for the solvent-exposed area decrease of the CTA molecules, the latter should be a consequence of the carbon-chain contraction involving an increase of gauche conformation. This can be observed in the cross-section views of the elongated micelle and of the bilayer (Figure 4). The central regions of those structures seem to be formed by a pure carbohydrated phase,

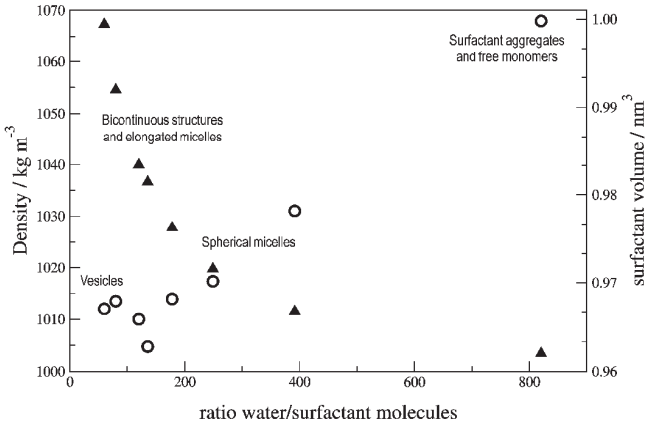

Figure 5. Density of the total simulated systems (▲) and volume per PFO-CTA catanionic molecule (○) as a function of the surfactant concentration. The structures obtained at the different concentration regions are indicated.

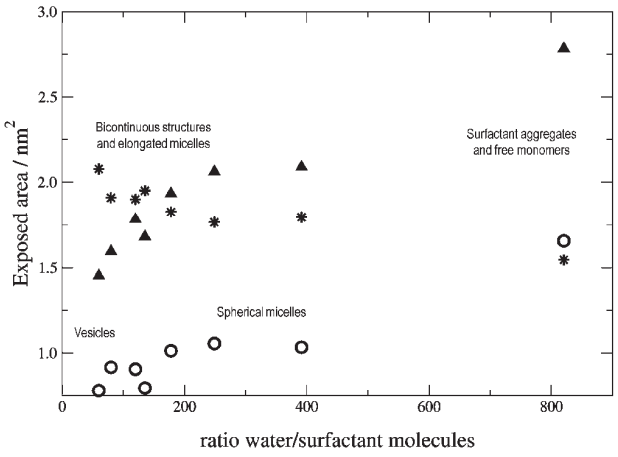

Figure 6. Average water-PFO (○), water-CTA (▲), and PFO-CTA (*) contact area per molecule as a function of the surfactant concentration. The structures obtained at the different concentration regions are indicated.

with no fluorine atoms. The differences between the PFO and the CTA molecules is also clear in the average local order parameters along the C-chains, calculated as indicated in the Methodology section. These parameters are defined in a way similar to the well-known deuterium order parameters typically reported in MD simulation studies of lipid membranes.[36] However, they allow to quantify C-chain bendings regardless molecular orientations since internal angles are used instead of angles formed with a reference external axis (Figure 7). This analysis shows that all the C-atoms in the PFO molecules are in the trans conformation except for the highest packed structures where the C-atoms closer to the anionic head of the surfactant clearly bend for some of the molecules (Figure 7). Such ionic head bending may be due to the electrostatic attraction of the CTA cationic head. The entire C-chain of the CTA molecule was observed to be significantly more disordered (note that the *y*-axis scales in both panels of Figure 7 are different). This disorder is even higher at the end of the chain. In contrast to the previous structural parameters analyzed for this molecule, the local order parameters obtained for CTA do not depend significantly on the surfactant concentration or aggregate structure. In order to achieve a more complete view on the molecular behavior in the different structures the diffusion coefficients for both PFO and CTA were determined by using the Einstein equation, from the linear fit of the root mean displacement corresponding to each of these molecules over the last 5 ns of the trajectories. Similar diffusion coefficient values were obtained for both molecules regardless the surfactant concentration. The dependence of this parameter

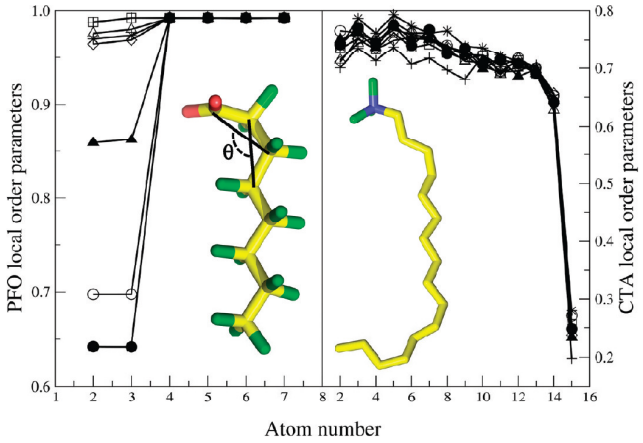

Figure 7. Average local order parameters for the PFO (left) and CTA (right) molecules as a function of the C atom number for different water to surfactant ratios: 821 (+), 392 (◇), 249 (□), 178 (Δ), 136 (·), 120 (▲), 80 (●), and 60 (○). Representative structures of each molecule are shown in the insets. The angles employed to define the order parameters (see the Methodology section) are illustrated in the PFO structure in the left panel.

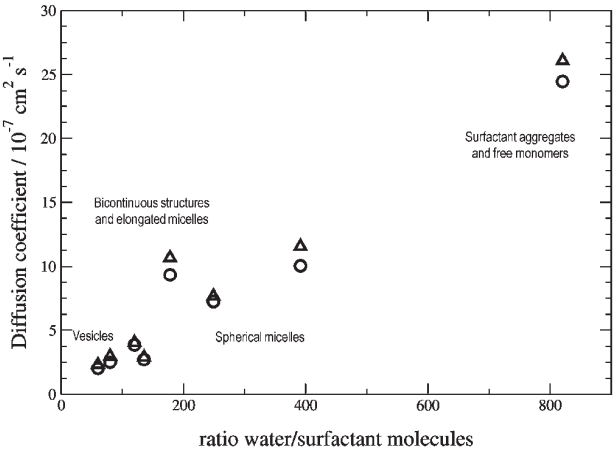

Figure 8. Average diffusion coefficients for PFO (○) and CTA (Δ) molecules as a function of the surfactant concentration. The structures obtained at the different concentration regions are indicated.

with the surfactant concentration is strong. As expected, the higher the molecular packing the lower the diffusion constant value (Figure 8).

4. CONCLUSIONS

Our results show that equimolar mixtures of the short anionic sodium perfluorooctanoate (PFO) molecule with the twice longer canionic cetyltrimethylammonium bromide (CTA) in the absence of counterions may form different structures at different concentrations in the bulk aqueous solution. The higher the catanionic surfactant concentration, the higher the density of the solution and the lower the compressibility, the available volume per solute molecule, the area exposed to the solvent, and the diffusion coefficient of both PFO and CTA molecules. Specifically, DLS experiments indicate that at least two populations of structures exist in the studied concentration range. While the structures present in the first population grow up with the surfactant concentration, the size of the structures in the second population, which were identified as vesicles, is practically constant with a radius of ~80 nm. At high surfactant concentration both populations tend to converge to these vesicles which were observed by TEM, cryo-SEM, and confocal microscopy in the same concentration range. The spontaneous formation of unilamellar homodispersed vesicles has already been observed in the literature for similar systems.[47] Lamellar phases, also common in

hydrogenated catanionic systems, were not found under the studied conditions. Molecular dynamics simulations allowed to observe how equimolar mixtures of PFO and CTA molecules initially located at random positions in water also form different structures, including vesicle patches, within time scales shorter than 20 ns. The variety of structures observed is ascribed to the balance between the different interactions occurring between PFO and CTA as well as with the solvent molecules. The well-known dual lipophobic/hydrophobic character of fluorocarbon molecules is expected to be an important contribution for the aggregation of this catanionic surfactant. Using a similar force field parametrization in nonionic fluorocarbon-hydrocarbon diblocks we recently observed the spontaneous formation of fluorine-rich and hydrogen-rich domains at the solution/air interface by MD simulations.[51] The lack of fluorinated/hydrogenated domains in the nanostructures obtained in the present work indicates that the electrostatic interactions are dominant in these systems. The increase in the PFO/CTA contact area when the surfactant concentration rises, supports this conclusion. Interestingly, since the length of the CTA molecule is twice that of the PFO molecule, the former does not fit well in the structures and the end of its chain forms a hydrocarbonated core in the aggregates. Unfortunately, our atomistic MD simulations did not allow observing the formation of entire vesicles. Coarse grain MD simulations of the same systems are expected to fill this gap in the future. Overall, this work shows the versatility of these molecules to form a variety of structures due to the balance between their different lengths, the electrostatic interactions between their heads with charge of different sign, and the particular interactions occurring between fluorinated and hydrogenated carbon chains. Our results are expected to be useful to guide the design of new nanostructures based on hydrogenated/fluorinated surfactants. In an upcoming work we pretend to study the stability of the obtained vesicles as well as their interaction with selected peptides in order to explore their potential biotechnological applications.

AUTHOR INFORMATION

Corresponding Author

*E-mail: JuanM.Ruso@usc.es; Angel.Pineiro@usc.es. Phone: +34 981 563 100. Fax: +34 881 814 112.

ACKNOWLEDGMENT

The authors thank the Xunta de Galicia for their financial support (Project No. 10PXIB206258PR). Á.P. is an Isidro Parga Pondal fellow (Xunta de Galicia). We are grateful to the to the "Centro de Supercomputación de Galicia" (CESGA) for computing time.

REFERENCES

(1) The President's Council of Advisors on Science and Technology. Report to the President and Congress on the third assessment of The National Nanotechnology Initiative. Executive Office of the President Washington, DC, 2010.
(2) Shapira, P.; Wang, J. *Nature* **2010**, *468*, 627.
(3) Cargnello, M.; Wieder, N. L.; Montini, T.; Gorte, R. J.; Fornasiero, P. *J. Am. Chem. Soc.* **2010**, *132*, 1402.
(4) Liu, Z.; Zhang, X.; Poyraz, S.; Surwade, S. P.; Manohar, S. K. *J. Am. Chem. Soc.* **2010**, *132*, 13158.
(5) Song, Y.; Dorin, R. M.; Garcia, R. M.; Jiang, Y.-B.; Wang, H.; Li, P.; Qiu, Y.; Swol, F. v.; Miller, J. E.; Shelnutt, J. A. *J. Am. Chem. Soc.* **2008**, *130*, 12602.
(6) Marques, E. F.; Regev, O.; Khan, A.; Lindman, B. *Adv. Colloid Interface Sci.* **2003**, *100−102*, 83.
(7) Joensson, B.; Jokela, P.; Khan, A.; Lindman, B.; Sadaghiani, A. *Langmuir* **1991**, *7*, 889.
(8) Blanco, E.; Piñeiro, Á.; Miller, R.; Ruso, J. M.; Prieto, G.; Sarmiento, F. *Langmuir* **2009**, *25*, 8075.
(9) Caillet, C.; Hebrant, M.; Tondre, C. *Langmuir* **2000**, *16*, 9099.
(10) Khan, A.; Marques, E. F. In *Specialist Surfactants*; Robb, I. D., Ed.; Blackie Academic and Professional: London, 1997; p 37.
(11) Silva, B. F. B.; Marques, E. F.; Olsson, U. *Soft Matter* **2011**, *7*, 225.
(12) Silva, B. F. B.; Marques, E. F.; Olsson, U.; Pons, R. *Langmuir* **2010**, *26*, 3058.
(13) Blanco, E.; Rodriguez-Abreu, C.; Schulz, P.; Ruso, J. M. *J. Colloid Interface Sci.* **2010**, *341*, 261.
(14) Hao, J.; Hoffmann, H.; Horbaschek, K. *Langmuir* **2001**, *17*, 4151.
(15) Iampietro, D. J.; Kaler, E. W. *Langmuir* **1999**, *15*, 8590.
(16) Jung, H.-T.; Lee, S. Y.; Kaler, E. W.; Coldren, B.; Zasadzinski, J. A. *Proc. Natl. Acad. Sci.* **2002**, *99*, 15318.
(17) Kang, S.-Y.; Seong, B.-S.; Han, Y. S.; Jung, H.-T. *Biomacromolecules* **2003**, *4*, 360.
(18) Oishi, Y.; Kato, T.; Narita, T.; Ariga, K.; Kunitake, T. *Langmuir* **2008**, *24*, 1682.
(19) Nordstierna, L.; Furó, I.; Stilbs, P. *J. Am. Chem. Soc.* **2006**, *128*, 6704.
(20) Yoder, N. C.; Kalsani, V.; Schuy, S.; Vogel, R.; Janshoff, A.; Kumar, K. *J. Am. Chem. Soc.* **2007**, *129*, 9037.
(21) Soman, N. R.; Lanza, G. M.; Heuser, J. M.; Schlesinger, P. H.; Wickline, S. A. *Nano Lett.* **2008**, *8*, 1131.
(22) Berendsen, H. J. C.; van der Spoel, D.; van Drunen, R. *Comput. Phys. Commun.* **1995**, *91*, 43.
(23) Lindahl, E.; Hess, B.; van der Spoel, D. *J. Mol. Model* **2001**, *7*, 306.
(24) Van der Spoel, D.; Lindahl, E.; Hess, B.; Groenhof, G.; Mark, A. E.; Berendsen, H. J. C. *J. Comput. Chem.* **2005**, *26*, 1701.
(25) Oostenbrink, C.; Villa, A.; Mark, A. E.; Van Gunsteren, W. F. *J. Comput. Chem.* **2004**, *25*, 1656.
(26) Borodin, O.; Smith, G. D.; Bedrov, D. *J. Phys. Chem. B* **2002**, *106*, 9912.
(27) Berendsen, H. J. C.; Grigera, J. R.; Straatsma, T. P. *J. Phys. Chem.* **1987**, *91*, 6269.
(28) Berendsen, H. J. C.; Postma, J. P. M.; Gunsteren, W. F. v.; DiNola, A.; Haak, J. R. *J. Chem. Phys.* **1984**, *81*, 3684.
(29) Darden, T.; York, D.; Pedersen, L. *J. Chem. Phys.* **1993**, *98*, 10089.
(30) Essmann, U.; Perera, L.; Berkowitz, M. L.; Darden, T.; Lee, H.; Pedersen, L. G. *J. Chem. Phys.* **1995**, *103*, 8577.
(31) Hockney, R. W.; Eastwood, J. W. *Computer Simulation Using Particles*; Adam Hilger: New York, 1988.
(32) Miyamoto, S.; Kollman, P. A. *J. Comput. Chem.* **1992**, *13*, 952.
(33) Hess, B.; Bekker, H.; Berendsen, H. J. C.; Fraaije, J. *J. Comput. Chem.* **1997**, *18*, 1463.
(34) Sayle, R. A.; Milner-White, E. J. *Trends Biochem. Sci.* **1995**, *20*, 374.
(35) Humphrey, W.; Dalke, A.; Schulten, K. *J. Mol. Graph.* **1996**, *14*, 33.
(36) The PyMOL Molecular Graphics System, Version 1.3, Schrödinger, LLC. www.pymol.org.
(37) Poger, D.; Van Gunsteren, W. F.; Mark, A. E. *J. Comput. Chem.* **2010**, *31*, 1117.
(38) De Lisi, R.; Milioto, S.; Muratore, N. *Langmuir* **2001**, *17*, 8078.
(39) Brito, R. O.; Marques, E. F.; Gomes, P.; Falcão, S.; Söderman, O. *J. Phys. Chem. B* **2006**, *110*, 18158.
(40) Perron, G.; De Lisi, R.; Davidson, I.; Genereux, S.; Desnoyers, J. E. *J. Colloid Interface Sci.* **1981**, *79*, 432.

(41) De Lisi, R.; Milioto, S.; De Giacomo, A.; Inglese, A. *Langmuir* **1999**, *15*, 5014.
(42) El Seoud, O. A. *J. Mol. Liq.* **1997**, *72*, 85.
(43) Szleifer, I.; Ben-Shaul, A.; Gelbart, W. M. *J. Chem. Phys.* **1985**, *83*, 3612.
(44) Holler, F.; Callis, J. B. *J. Phys. Chem.* **1989**, *93*, 2053.
(45) Aswal, V. K.; Goyal, P. S.; Thiyagarajan, P. *J. Phys. Chem. B* **1998**, *102*, 2469.
(46) Brasher, L. L.; Kaler, E. W. *Langmuir* **1996**, *12*, 6270.
(47) Jung, H. T.; Coldren, B.; Zasadzinski, J. A.; Iampietro, D. J.; Kaler, E. W. *Proc. Natl. Acad. Sci.* **2001**, *98*, 1353.
(48) Segota, S.; Tezak, D. *Adv. Colloid Interface Sci.* **2006**, *121*, 51.
(49) Marques, E. F.; Regev, O.; Khan, A.; Maria da Graça, M.; Lindman, B. *J. Phys. Chem. B* **1998**, *102*, 6746.
(50) Heller, H.; Schaefer, M.; Schulten, K. *J. Phys. Chem.* **1993**, *97*, 8343.
(51) Piñeiro, Á.; Prieto, G.; Ruso, J. M.; Verdes, P. V.; Sarmiento, F. *J. Colloid Interface Sci.* **2009**, *329*, 351.

J. Chem. Thermodynamics 43 (2011) 399–404

Contents lists available at ScienceDirect

J. Chem. Thermodynamics

journal homepage: www.elsevier.com/locate/jct

Assessment of interactions between four proteins and benzothiazole derivatives by DSC and CD

Natalia Hassan, Pedro V. Verdes *, Juan M. Ruso

Soft Matter and Molecular Biophysics Group, Department of Applied Physics, Faculty of Physics, Campus Vida, University of Santiago de Compostela, E-15782 Santiago de Compostela, Spain

ARTICLE INFO

Article history:
Received 16 July 2010
Received in revised form 15 September 2010
Accepted 16 October 2010
Available online 16 November 2010

Keywords:
3-(2-Benzothiazolylthio)-1-propanesulfonic acid (BTS)
Protein
Differential scanning calorimetry
Thermal denaturation
Circular dichroism

ABSTRACT

The thermal denaturation of ovalbumin, lysozyme, myoglobin and fibrinogen at different BTS concentrations have been investigated using differential scanning calorimetry (DSC) and circular dichroism (CD) spectroscopy. Thermodynamic parameters: melting temperatures (T_m), calorimetric enthalpy (ΔH), van't Hoff enthalpy (ΔH_v) were obtained for all the systems under study. Thermal denaturation of the four proteins was completely irreversible. Changes in the protein conformation due to the adsorption of BTS molecules have been monitored by using UV-CD spectra. Greater changes in α-helical contents correspond with the BTS higher concentrations. The lysozyme denaturation temperature increases at low concentrations BTS indicating that BTS acts as a structure stabilizer; meanwhile it acts as a destabilizer at higher concentrations in all the proteins studied. The major effect is observed in the case of myoglobin, the protein with the highest α-helical secondary structure (75%).

1. Introduction

Major examples of the biochemical functions of proteins include binding; catalysis; operating as molecular switches; and serving as structural components of cells and organisms. Proteins may bind to other macromolecules, such as DNA in the case of DNA polymerases or gene regulatory proteins, or to proteins in the case of a transporter or a receptor that binds a signalling molecule. This function exploits the ability of proteins to present structurally and chemically diverse surfaces that can interact with other molecules with high specificity. The extraordinary functional diversity and versatility of proteins derives from the chemical diversity of the side chains of their constituent amino acids, the flexibility of the polypeptide chain, and the very large number of ways in which polypeptide chains with different amino acid sequences can fold [1].

Biological function is generally possible only when a protein is folded into a specific three-dimensional conformation; unfolded proteins are impotent. Biological function also involves the interaction with other molecules: enzymes bind their substrates and products, and transport proteins bind their ligands. Folding involves the interaction of two initially flexible surfaces, whereas in binding, generally only the ligand is substantially flexible. The interaction of small molecules with macromolecules of biological systems and with specific receptor sites on surfaces of supramolecular organizations is one of the most extensively studied phenomena in biophysical research [2,3].

Among the anti-tumour drugs discovered recently, numerous papers have shown that the benzothiazole nucleus possesses a potent anticancer activity against human cancer [4–8]. It has been found that certain compounds containing the benzothiazol nucleus killed cells in a tumour-specific manner [9]. Benzothiazoles derivatives have been reported to possess potent anticancer properties due to their structural similarity with naturally occurring purines as they can easily interact with biomolecules of the living systems [10].

Alpha helices are the commonest secondary structural elements in a folded polypeptide chain, possibly because they are generated by local hydrogen bonding between C=O and N–H groups close together in the sequence. In an alpha helix, the carbonyl oxygen atom of each residue (n) accepts a hydrogen bond from the amide nitrogen four residues further along ($n + 4$) in the sequence, so that all of the polar amide groups in the helix are hydrogen bonded to one another except for the N–H group of the first residue in the helical segment (the amino-terminal end) and the C=O group of the last one (the carboxy-terminal end). The result is a cylindrical structure where the wall of the cylinder is formed by the hydrogen-bonded backbone, and the outside is studded with side chains. The protruding side chains determine the interactions of the alpha helix both with other parts of a folded protein chain and with other protein molecules.

* Corresponding author. Tel.: +34 881 814 042; fax: +34 981 520 676.
E-mail address: pedro.vazquez@usc.es (P.V. Verdes).

0021-9614/$ - see front matter © 2010 Elsevier Ltd. All rights reserved.
doi:10.1016/j.jct.2010.10.015

In contrast to the alpha helix, the beta pleated sheet involves hydrogen bonds between backbone groups from residues distant from each other in the linear sequence. In beta sheets, two or more strands that may be widely separated in the protein sequence are arranged side by side, with hydrogen bonds between the strands.

Nearly all polar amide groups are hydrogen bonded to one another in a beta-sheet structure, except for the N–H and C=O groups on the outer sides of the two edge strands. Edge strands may make hydrogen bonds in any of several ways. They may simply make hydrogen bonds to water, if they are exposed to solvent; or they may pack against polar side chains in, for example, a neighbouring alpha helix; or they may make hydrogen bonds to an edge strand in another protein chain, forming an extended beta structure that spans more than one subunit and thereby stabilizes quaternary structure. Or the sheet may curve round on itself to form a barrel structure, with the two edge strands hydrogen bonding to one another to complete the closed cylinder. Such beta barrels are a common feature of protein architecture [1].

Lysozyme is a small protein, molecular mass 14.3 kDa, of 129 amino acids, containing 18 cationic amino acid residues and 12 anionic residues. The α-helix content of its secondary structure is 30%. Its structure is stabilized by four disulfide bridges and the interior of the protein is almost hydrophobic while the surface is mostly polar. The isoelectric point is pI ~ 11.0, and the protein is therefore positively charged in an aqueous solution.

Myoglobin is a single-chain protein, molecular mass 16.7 kDa, of 153 amino acids, containing a heme group in the centre. Its secondary structure is unusual in that it contains a very high proportion (75%) of α-helical secondary structure. It is formed by eight α-helices named A–H [11]. Its isoelectric point is pI ~ 7.3. Myoglobin, like lysozyme, is positively charged in an aqueous solution.

Fibrinogen (also called factor I) is a 340 kDa glycoprotein and roughly (47 · 4.5 · 4.5) nm. It consists of two sets of three intertwined polypeptide chains designated as Aα, Bβ, and γ. which are held together by a network of disulfide bonds. Fibrinogen contains a total of 29 disulfide bonds and no free sulfhydryl groups. Its secondary structure contains a 35% of α-helical and a pI of 5.8 [12,13].

Ovalbumin has a molar mass of 45 kDa and consists of a single chain of 385 amino acid residues, with a total of 105 titratable residues [14] contains a single disulphide bond and a glycosylation site. Three different phosphate forms of ovalbumin occur in egg white, containing two, one or no phosphate groups per molecule. Typically, in egg white, the ratios of each are about 85:12:3 [15]. This protein has a globular shape with a radius of around 3 nm in an aqueous medium and an isoelectric point at pH 4.6 [14]. It contains a proportion of 33% of α-helical secondary structure. Ovalbumin is negatively charged in an aqueous solution.

The three-dimensional structure of proteins is maintained by various secondary forces such as hydrophobic interactions, hydrogen bonding, Van der Waals interactions, electrostatic forces and disulfide bonds. Physical and biological properties of a protein can be altered by conditions that affect its native conformation. The stability of a protein is generally estimated based on the analysis of its unfolding transitions induced by denaturants, such as urea, or by changes in the pH, ionic strength, or temperature, measured either spectroscopically or calorimetrically [16–19].

In order to understand the thermal stability of the four proteins and the effect of BTS on them we have carried out differential scanning calorimetric studies. Circular dichrosim (CD) spectroscopy has been also employed to determinate the effect of BTS concentration on the secondary structure of lysozyme, myoglobin, ovalbumin and fibrinogen. Measurements by DSC have yielded information regarding transition temperature (T_m), calorimetric enthalpy (ΔH), van't Hoff enthalpy (ΔH_v).

2. Materials and methods

2.1. Materials

The 3-(2-benzothiazolylthio)-1-propanesulfonic acid (BTS) were obtained from Aldrich Lancaster (see scheme 1). Lysozyme (from chicken egg white, product L-6876), myoglobin (from equine skeletal muscle, product M-0630), ovalbumin (from chicken egg, product A-5253) and bovine plasma fibrinogen (fraction I, type IV) obtained from Sigma and were used without further purification. Stock solutions of defined protein concentration were prepared by dissolving a certain amount of freeze-dried protein in an appropriate buffer volume. We used doubly distilled and degassed water for globular proteins pH of 5.5; and the buffer solution used for fibrinogen was 50 mN glycine plys sodium hydroxide to give a pH of 8.5 (fibrinogen will be negatively charged). Samples were prepared within two hours prior to usage. All chemical reagents were of analytical grade, and solutions were made using doubly distilled and degassed water.

2.2. Differential scanning calorimetry

Differential scanning calorimetry (DSC) measurements were performed using a VP-DSC (MicroCal Inc., Northampton, MA) calorimeter with 0.542 cm^3 twin cells for the reference and sample solutions. Prior to the DSC experiments, the samples and the references were degassed under vacuum while being stirred. Thermograms were recorded between the temperatures 293.15 K and 383.15 K at a scan rate of 60 K per hour. To check the reproducibility, each experiment was repeated three times. The baseline reference, obtained with both cells filled with buffer, was subtracted from the thermograms of the samples. The heat capacity curves were evaluated using the MicroCal Origin 7.0 software, provide with the equipment, to obtain ΔH and T_m values.

2.3. Circular dichroism (CD)

Far-UV circular dichroism spectra were obtained using a JASCO-715 automatic recording spectropolarimeter (Japan) with a JASCO PTC-343 Peltier-type thermostated cell holder. Quartz cuvettes with 0.2 cm pathlength were used. The CD spectra of pure proteins and proteins–BTS dilute solutions were recorded from 190 nm to 270 nm. The protein concentration was 0.5 mg · cm^{-3} and BTS concentrations varied from 0.1 mM to 0.5 mM. The following settings were used: resolution, 1 nm; bandwidth, 1 nm; sensitivity, 50 mdeg; response time, 8 s; accumulation, 3; and scan rate 50 nm · min^{-1}. Corresponding absorbance contributions of buffer solution and doubly distilled water were subtracted with the same instrumental parameters. Data are reported as molar ellipticity and determined as

$$[\theta]_\lambda = \theta_\lambda M_r / ncl, \quad (1)$$

where c is the protein concentration, l is the path length of the cell, θ_λ is the ellipticity given by the instrument at a wavelength λ, M_r is the molar mass of the protein, and n is the number of residues. The measured CD curves are a superposition of the individual spectra of α-helix, β-sheet, β-turn and randomly coiled conformations. The

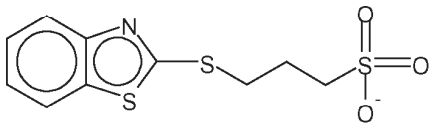

SCHEME 1.

secondary structure content was analyzed by Dichroweb program [20] using CONTIN algorithm.

3. Results and discussion

3.1. DSC measurements

A first set of DSC experiments at different proteins concentrations (0.5, 1, and 3) mg · cm^{-3} have been performed indicating that concentration does not influence the aspect of the thermograms. The DSC thermograms obtained for the four pure proteins are shown in figure 1. We have chosen a protein concentration of 0.5 mg · cm^{-3} for all the system under study.

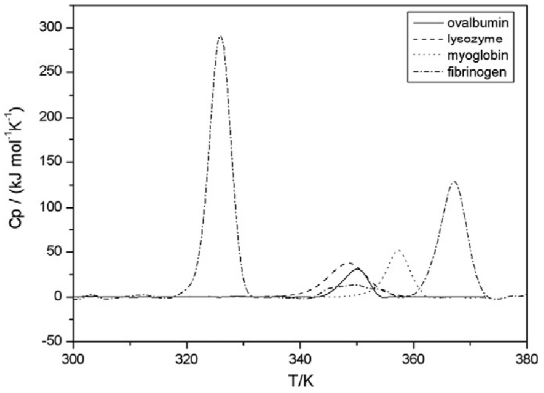

FIGURE 1. DSC thermograms of ovalbumin, lysozyme, myoglobin and fibrinogen, (0.5 g · dm^{-3}).

Thermograms for ovalbumin, lysozyme and myoglobin show a single endothermic and symmetrical peak: and the T_m at these peaks in absence of BTS were 349.3 K, 348.3 K, and 357.3 K, respectively. Three endothermic peaks can be observed in the thermal denaturation of pure fibrinogen. The narrow and symmetrical peaks located at the temperature 325.9 K and 367.1 K have been attributed to the denaturation of the end D and central E fragments of fibrinogen, respectively [21]. Meanwhile, the small and broad peak located at 347.7 K has been related with denaturation of the C-terminal of the Aα chains [22]. The entire T_m obtained agrees with the values available in the literature [22–25]. Thermal denaturation of the four proteins was completely irreversible, since no transition could be seen when the samples were subjected to a second heating scan after they were cooled from the first run.

Reversibility of protein unfolding decreases dramatically upon heating above T = 343.2 K for almost all mesophilic proteins because of some degradation of their chemical structure, particularly the oxidation of certain side chains by dissolved oxygen. Upon heating below T = 343.2 K, many small proteins show good reversibility in solutions preventing their aggregation, for example, at pHs away from the isoelectric point of the protein. However, even if protein unfolding does not show perfect reversibility, it might still be analyzed thermodynamically because its temperature-induced cooperative unfolding is a much faster process than the aggregation of unfolded protein and the degradation of its exposed groups [26].

The DSC thermograms for the four proteins, figure 2, were performed and analyzed for several BTS concentrations. In all these systems, no reversibility was found as in the case of pure proteins. Thus, only first scans are shown along this study.

It has been shown that the DSC thermograms for the thermal denaturation of several proteins can be interpreted in terms of the van't Hoff equation, in spite of the calorimetric irreversibility [27,28]. This can be explained if we assume that an irreversible alteration of the unfolded state takes place, with little heat effect, at temperatures higher than those at which the calorimetric transition occurs [29].

The thermodynamic characteristics of the thermal denaturation: melting temperatures (T_m, temperatures at which a maximum occurred in the endothermic peaks), calorimetric enthalpy (ΔH), van't Hoff enthalpy (ΔH_v) were obtained for all the systems under study and are listed in table 1. Taken together, these data provide information on the conformational stability of the protein. When estimated values of van't Hoff enthalpy for a particular reaction are compared to enthalpy values, obtained directly by calorimetric methods, there is often substantial disagreement between both values.

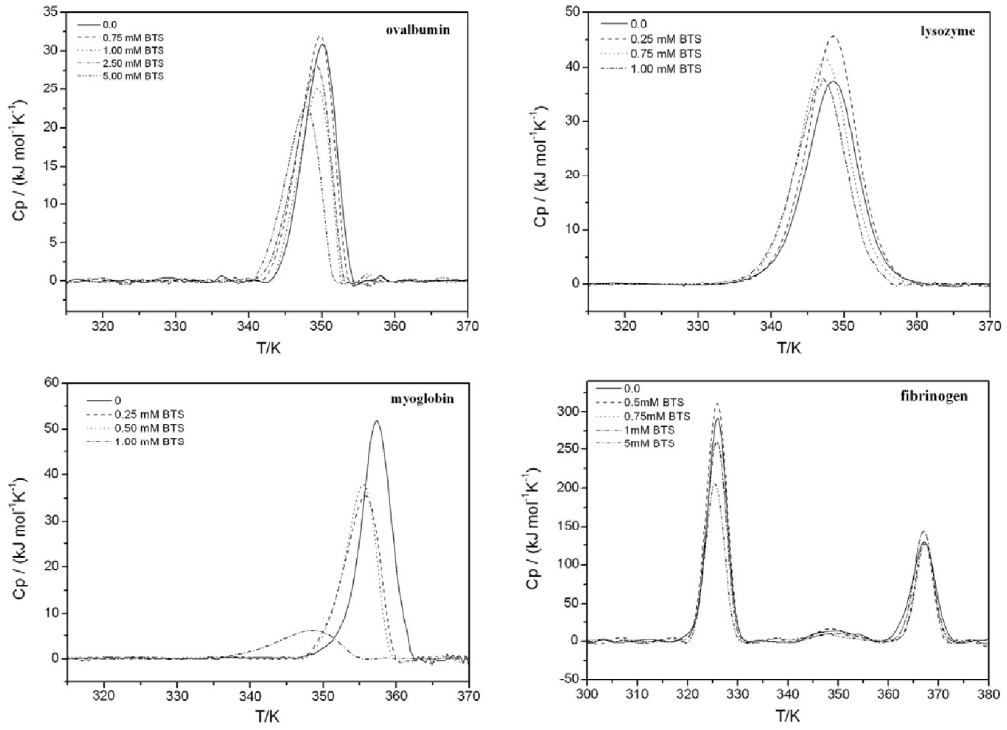

FIGURE 2. DSC thermograms of ovalbumin, lysozyme, myoglobin and fibrinogen, (0.5 g · dm^{-3}) in the presence of BTS.

TABLE 1
Thermodynamic parameters: transition temperature (T_m), calorimetric enthalpy (ΔH), and van't Hoff enthalpy (ΔH_v); obtained from DSC thermograms of ovalbumin, lysozyme, myoglobin, and fibrinogen in the presence of BTS.

[BTS]/mM	T_m/K	ΔH/(kJ · mol^{-1})	ΔH_v/(kJ · mol^{-1})
	Ovalbumin		
0.00	349.7 ± 1.2	171.5 ± 8.5	758.6 ± 8.4
0.25	349.5 ± 1.4	180.2 ± 9.0	720.5 ± 7.2
0.50	347.8 ± 1.3	139.0 ± 6.5	613.4 ± 7.7
0.75	349.2 ± 1.3	185.6 ± 7.4	714.6 ± 11.8
1.00	349.0 ± 1.4	132.6 ± 6.0	792.0 ± 11.4
2.50	348.7 ± 1.3	164.0 ± 8.2	707.5 ± 11.1
5.00	347.4 ± 1.3	131.8 ± 6.5	714.2 ± 11.8
	Lysozyme		
0.00	348.4 ± 1.1	336.0 ± 10.1	452.3 ± 13.6
0.25	348.4 ± 1.3	402.2 ± 14.1	460.7 ± 15.2
0.50	347.2 ± 1.4	381.0 ± 15.2	440.6 ± 15.4
0.75	347.2 ± 1.6	375.1 ± 11.3	446.9 ± 17.9
1.00	346.8 ± 1.8	331.9 ± 11.9	453.5 ± 18.1
	Myoglobin		
0.00	357.3 ± 1.1	272.3 ± 5.4	811.3 ± 16.2
0.10	355.7 ± 1.2	251.6 ± 7.5	770.3 ± 15.4
0.25	355.3 ± 1.8	214.4 ± 6.4	710.4 ± 14.2
0.50	355.1 ± 1.7	204.2 ± 7.1	791.6 ± 15.8
0.75	354.4 ± 2.0	163.3 ± 4.9	760.7 ± 22.8
1.00	347.7 ± 2.5	63.1 ± 3.2	401.8 ± 18.1

BTS/mM	T_m/K			ΔH/(kJ · mol^{-1})			ΔH_v/(kJ · mol^{-1})		
	T_{m1}	T_{m2}	T_{m3}	ΔH_1	ΔH_2	ΔH_3	ΔH_{v1}	ΔH_{v2}	ΔH_{v3}
				Fibrinogen					
0.0	325.9 ± 1.1	347.7 ± 2.0	367.1 ± 1.1	1205.8 ± 36.2	143.1 ± 7.2	653.1 ± 18.9	750.6 ± 23.3	512.1 ± 20.5	779.5 ± 24.4
0.50	326.1 ± 1.2	349.3 ± 2.1	367.4 ± 1.3	1561.1 ± 51.5	144.5 ± 7.9	579.5 ± 17.9	750.2 ± 30.3	462.3 ± 20.3	1080.7 ± 35.4
0.75	325.8 ± 1.2	349.2 ± 2.3	367.0 ± 1.4	1276.1 ± 44.7	103.8 ± 4.7	700.4 ± 22.9	767.3 ± 32.3	403.4 ± 20.2	974.5 ± 30.4
1.00	325.7 ± 1.4	348.5 ± 2.5	367.6 ± 1.6	964.8 ± 34.7	66.4 ± 3.3	587.4 ± 19.9	810.0 ± 30.8	559.0 ± 16.8	1050.2 ± 42.4
2.50	324.8 ± 1.7	349.4 ± 2.8	366.7 ± 1.7	1152.3 ± 42.6	246.0 ± 12.3	668.2 ± 28.9	713.0 ± 27.8	736.4 ± 24.3	977.0 ± 39.4
5.00	324.1 ± 1.6	348.5± 3.0	366.2 ± 2.1	1227.6 ± 49.1	178.4 ± 8.9	601.7 ± 24.1	608.8 ± 24.4	407.7 ± 13.3	955.6 ± 47.4

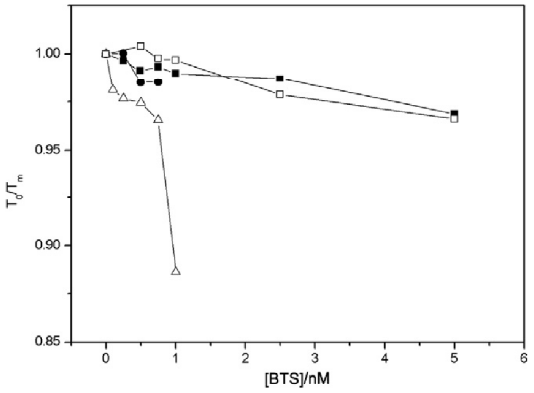

FIGURE 3. Protein unfolding temperature (normalized value T_0/T_m) as a function of BTS concentration. Transition temperatures, T_0, in the absence of BTS were as follows: ovalbumin 349.7 K, lysozyme 348.35 K, myoglobin 357.3 K °C, and fibrinogen (first peak) 325.9 K. ■ ovalbumen, ● lysozyme, Δ myoglobin, and □ fibrinogen.

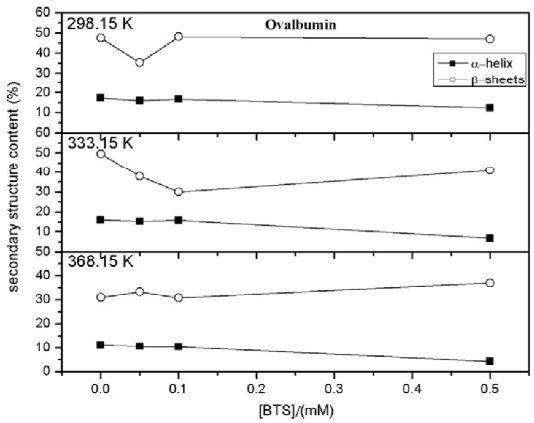

FIGURE 4. Contents (in %) of the α-helix (■) and β-sheets (○) elements in ovalbumin as a function of BTS concentration at different temperatures. Estimated uncertainties: ±10%.

Enthalpy of a reaction is most often determined through one of two means. It can be determined directly using calorimetry, or indirectly by measuring the temperature dependence of the equilibrium constant (van't Hoff method). Recently, discrepancies have been noted between the enthalpy measured by calorimetry and the enthalpy determined by the van't Hoff method. These have been suggested to indicate that binding reaction is more complex than the simple one-to-one binding model used to describe the data. It has been noted that binding reactions can include the displacement of solvent and counterions, as well as other linked equilibria such as protonation or conformational changes. It has been suggested that calorimetric enthalpy includes these contributions but that they are not observed in van't Hoff method. This suggests that the van't Hoff enthalpy is the "intrinsic" binding heat, whereas the calorimetric enthalpy includes other, concomitant reactions (*i.e.*, linked equilibria). All the proteins had different denaturation temperatures, indicating differences in thermal stability.

Application of Le Chatelier's principle, or simple equilibrium considerations, shows that if any ligand (small molecule or other protein or macromolecule) binds preferentially to the folded or native form of the protein, then this will stabilise the folded state, and unfolding of the protein will become progressively less favourable as ligand concentration increases. Conversely, ligands that bind preferentially to the unfolded protein will destabilise the fold and will encourage unfolding [30–33].

The effect of increasing BTS concentration in thermodynamic parameters, obtained from DSC thermograms (figures 1 and 2), can be seen in table 1 and figure 3.

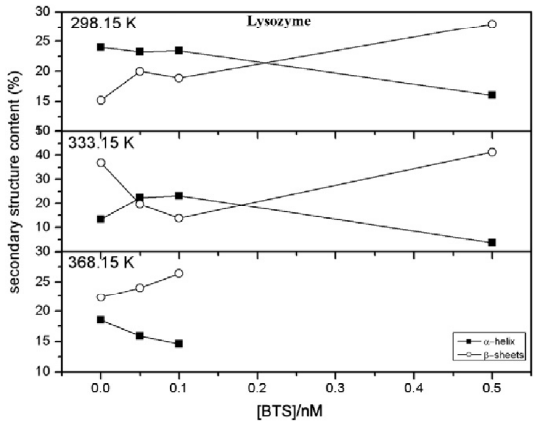

FIGURE 5. Contents (in %) of the α-helix (■) and β-sheets (○) elements in lysozyme as a function of BTS concentration at different temperatures. Estimated uncertainties: ±10%.

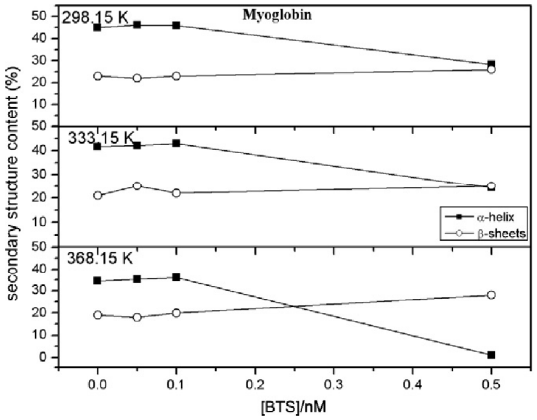

FIGURE 6. Contents (in %) of the α-helix (■) and β-sheets (○) elements in myoglobin as a function of BTS concentration at different temperatures. Estimated uncertainties: ±12%.

3.1.1. Ovalbumin

The T_m decreases from 349.7 K to 347.4 K as BTS concentration increases from 0 mM to 5 mM, so BTS binds to the unfolded protein. Not a clear trend is observed in ΔH values.

3.1.2. Lysozyme

Low BTS concentrations, [BTS] ⩽ 0.25 mM, cause a small increase in transition temperature and favour the stabilisation of the native state. Alongside this increment in T_m there is a consistent increase in the transition enthalpy, ΔH, changing from 335.5 kJ · mol $^{-1}$ to 402.2 kJ · mol $^{-1}$. The BTS acts as a denaturant at concentrations higher than 0.25 mM.

3.1.3. Myoglobin

This is a small and compact globular protein formed by eight α-helices. For all the proteins studied, it contains the highest proportion (75%) of α-helical secondary structure. The BTS destabilized myoglobin at all concentrations studied, according to the values obtained for T_m and ΔH, table 1. The decrease of those values indicates a concentration-dependent loss of folded stability induced by BTS.

Lysozyme and myoglobin aggregated and precipitated at BTS concentrations higher than 1 mM.

3.1.4. Fibrinogen

The T_{m1} decreases from 325.9 K to 324.1 K as BTS concentration increases up to 5 mM. The BTS binds to the unfolded state favouring the destabilisation of the native state and causing a reduction in transition temperature. Not a clear trend is observed in T_{m2} and T_{m3} values.

Figure 3 shows protein unfolding temperature (normalized value T_0/T_m) as a function of BTS concentration, for all the proteins studied. In all the cases, T_m decreases as BTS concentration increases. The major effect is observed in the case of myoglobin, which is protein with the highest α-helical secondary structure (75%).

The BTS acts like an ionic surfactant, so it can denature proteins by strong binding to charged and hydrophobic side chains at millimolar concentrations [34]. The consensus view [35–38] is that binding below the critical micelle concentration (cmc) proceeds through one to two different regions, starting in some but not all cases [39] with specific binding of surfactant to a few high-affinity sites on the protein surface (probably through both hydrophobic and electrostatic interactions). This causes some expansion in the protein structure to form a separate intermediate species [40] and is followed by unspecific and uncooperative binding before the protein binds a dramatically larger number of surfactant molecules and unfolds cooperatively. Based on the pH of the solution and the isoelectric point of the proteins, BTS binds mainly though electrostatic interactions to Arg and Lys residues, positively charged, placed on myoglobin and lysozyme surface, and through hydrophobic interactions to ovalbumin and fibrinogen. If we contrast calorimetric data with the type of interactions, it is possible to conclude that when electrostatic interactions are dominant the thermal stability of the proteins is considerably reduced with BTS concentration. However, when hydrophobic interactions are the dominant ones, thermal stability is slightly affected by BTS. Enthalpy results also support the idea that electrostatic interactions are the strongest (normalized to the protein weight). However, related to the effect of increasing BTS concentration, enthalpy data suggest that the type of interactions with the secondary structure exert the greatest influence. Thus, the unfolding enthalpy of myoglobin (75% of alpha helix) presents a decrease higher than 50 % with BTS concentration. Meanwhile, the other three proteins (30%, 33%, and 35% alpha helix) exhibit small changes with BTS concentration. The reason for these results arises from the fact that backbone hydrogen bonds of α-helix are generally slightly weaker than those found in β-sheets. This makes this structure more suitable to interact with BTS molecules.

3.2. CD Measurements

When BTS binds to some of the proteins under study, it acquires an induced CD (ICD) spectrum through chiral perturbation to its structure or electron rearrangements. The intensity of the ICD spectrum is determined by the strength of the interactions and both the geometry of the BTS molecule and the residue in protein backbone. Thus, ICD can be used to probe the binding of BTS molecules to the proteins under study [41].

Figures 4 to 7 show the secondary structure content, for the four proteins, at different temperatures as a function of BTS concentration. The secondary structure content was analyzed by the Dichroweb program [20] using CONTIN algorithm. Estimated uncertainties are between 10% and 15%.

The CD measurements provide information about the secondary structure on ovalbumin molecules. Figure 4 shows the changes of α-helices and β-sheet contents of ovalbumin at different temperatures and BTS concentrations. It can be seen that β-sheet content is always greater than α-helices content (around 50% and 15% at

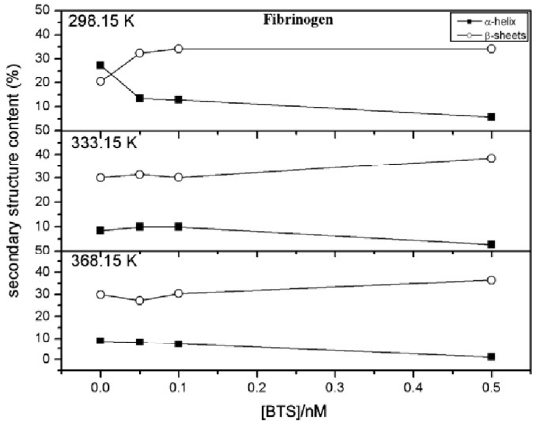

FIGURE 7. Contents (in %) of the α-helix (■) and β-sheets (○) elements in fibrinogen as a function of BTS concentration at different temperatures. Estimated uncertainties: ±15%.

T = 298.15 K respectively). As temperature increase, the α-helices and β-sheet contents decrease at all BTS concentrations. As can be observed from these results, ovalbumin exhibits the most resistant secondary structure against changes in temperature and BTS concentration.

Figure 5 shows lysozyme secondary structure content. Beyond T = 298.15 K, the helicity of the protein begins to decrease with rise of temperature and reaches 7% at T = 368.15 K. The helicity of 7% indicates that most of the helical structures are disrupted at T = 368.15 K.

At T = 298.15 K, the content of α-helices slowly decreases from 24% to 16% as BTS concentration increases until 0.5 mM. At T = 333.15 K, a small amount of BTS induces an increase of α-helices content, from 13.3% to 24%. On the other hand, the β-sheet decreases from 36% to 19%. These results agree with DSC results. Low BTS concentrations favour the stabilisation of the native state. These studies show that a higher BTS concentration, 0.5 mM, destabilizes lysozyme thereby increasing β-sheet content and decreasing the content of α-helices. On the whole, α-structures are dominant at lower temperature and BTS concentrations and β-structures are dominant at higher temperatures.

Myoglobin contains an abundant amount of helical structure. The helicity gradually decreases with rise of temperature (45% at 298.15 K, 34% at 368.15 K). A small among of BTS, between 0.05 mM and 0.1 mM, does not affect α-helix content. Higher BTS concentrations, >0.5 mM, destabilize myoglobin, figure 6. The β-sheet has a constant value, near 20%, at all temperatures and BTS concentrations. The results show that the α-helical content of myoglobin is more susceptible to temperature-induced unfolding with increasing concentrations of BTS, again indicating that BTS favours myoglobin unfolding.

Chen *et al.* [22] have estimated that the native fibrinogen molecule contains about 35% α-helix, 21% β-sheets, 13% β-turn and 31% random coil. Other authors have estimated 42% α-helix, 7% β-sheets, 20% β-turn and 30.8% random coil [42]. However, the trends are clear: with increasing temperature, the α-helix and β-sheets change little before the onset of the first peak but change dramatically (α-helix decreased and β-sheets increased) in the temperature range 328.15 K to 338.15 K. After this, the α-helix contents decrease moderately and finally an important decease is observed from 353.15 K to 373.15 K, figure 7.

At T = 298.15 K, BTS destabilizes fibrinogen and the α-helix content begins to decrease from 27% to 6%. It can be seen that the β-sheet content is always greater than the content of the α-helices, and its value is almost constant with temperature and BTS concentration, around 30%.

4. Conclusions

Benzothiazoles derivatives have been reported to possess potent anticancer properties due to their structural similarity with naturally occurring purines as they can easily interact with biomolecules of the living systems. We have studied the effect of BTS concentrations in thermal stability of lysozyme, myoglobin, ovalbumin and fibrinogen. All the proteins had different denaturation temperatures, indicating differences in thermal stability. The BTS binds though electrostatic interactions to myoglobin and lysozyme, and through hydrophobic interactions to ovalbumin and fibrinogen. From figure 3, it can be observed that higher concentrations of BTS decrease T_m and favour protein unfolding. A major effect is observed in the case of myoglobin, the protein with the highest α-helical secondary structure (75%). This could be related with the fact that backbone hydrogen bonds of α-helix are generally slightly weaker than those found in β-sheets. Thus, they are readily attacked by the surrounding BTS molecules.

Acknowledgements

The authors thank Dirección Xeral de Promoción Científica e Tecnológica do Sistema Universitario de Galicia for financial support. P.V. Verdes thanks "Xunta de Galicia" for his "Isidro Parga Pondal" research position.

References

[1] GregoryA. Petsko, D. Ringe, Protein Structure and Function, New Science Press Ltd., 2004.
[2] J.M. Ruso, P. Taboada, L.M. Varela, D. Attwood, V. Mosquera, Biophysical Chemistry 92 (2001) 141–153.
[3] J.M. Ruso, N. Deo, P. Somasundaran, Langmuir 20 (2004) 8988–8991.
[4] G. Wells, T.D. Bradshaw, P. Diana, A. Seaton, D.F. Shi, A.D. Westwell, M.F. Stevens, Bioorg. Med. Chem. Lett. 10 (2000) 513–515.
[5] I. Hutchinson, M.S. Chua, H.L. Browne, V. Trapani, T.D. Bradshaw, A.D. Westwell, M.F. Stevens, J. Med. Chem. 44 (2001) 1445–1446.
[6] I. Hutchinson, S.A. Jennings, B.R. Vishnuvajjala, A.D. Westwell, M.F. Stevens, J. Med. Chem. 45 (2002) 744–747.
[7] C.D. Hose, M. Hollingshead, E.A. Sausville, A. Monks, Mol. Cancer Ther. 2 (2003) 1265–1272.
[8] S. Saeed, N. Rashid, P.G. Jones, M. Ali, R. Hussain, Eur. J. Med. Chem. 45 (2010) 1323–1331.
[9] V.R. Solomon, C. Hu, H. Lee, Bioorg. Med. Chem. 17 (2009) 7585–7592.
[10] S.J. Tangeda, A. Garlapati, Eur. J. Med. Chem. 45 (2010) 1453–1458.
[11] T. Takano, J. Mol. Biol. 110 (1977) 537–568.
[12] P. Somam, Z. Rice, C.A. Siedlecki, Langmuir 24 (2008) 8801–8806.
[13] M. Wasilewska, Z. Adamczyk, B. Jachimsk, Langmuir 25 (2009) 3698–3704.
[14] E. Tatsumi, D. Yoshimatsu, M. Hirosi, Biochemistry 37 (1998) 12351–12359.
[15] R.A. Judge, M.R. Johns, E.T. White, J. Chem. Eng. Data 41 (1996) 422–424.
[16] M. Kavitha, Kishore Babu Bobbili, Musti J. Swamy, Biochimie 92 (2010) 58–64.
[17] E.M. Nicholson, J.M. Scholtz, Biochemistry 35 (1996) 11369–11378.
[18] V.R. Agashe, J.B. Udgaonkar, Biochemistry 34 (1995) 3286–3299.
[19] C.R. Johnson, P.E. Morin, C.H. Arrowsmith, E. Freire, Biochemistry 34 (1995) 5309–5316.
[20] L. Whitmore, B.A. Wallace, Nucl. Acids Res. 32 (2004) W668–W673.
[21] P.L. Privalov, L.V. Medev, J. Mol. Biol. 159 (1982) 665–683;
J.W. Donovan, E. Mihalyi, Proc. Natl. Acad. Sci. USA 71 (1974) 4125–4218.
[22] Y. Chen, H. Mao, X. Zhang, Y. Gong, N. Zhao, Inter. J. Biol. Macromol. 26 (1999) 129–134.
[23] Y.M. Efimova, S. Haemers, B. Wierczinski, Biopolymers 85 (2007) 264–273.
[24] V. Ya Grinberg, N.V. Grinberg, A.Y. Mashkevich, T.V. Burova, V.B. Tolstoguzov, Food Hydrocolloid 16 (2009) 333–343.
[25] E. Blanco, J.M. Ruso, J. Sabín, G. Prieto, F. Sarmiento, J. Therm. Anal. Cal. 87 (2007) 211–215.
[26] P.L. Privalov, in: John W. Shriver (Ed.), Protein Structure Stability and Interactions. Methods in Molecular Biology, Humana Press, Berlin, 2009, pp. 1–40.
[27] S.P. Manly, K.S. Matthews, J.M. Sturtevant, Biochemistry 24 (1985) 3842–3846.
[28] C.Q. Hu, J.M. Sturtevant, Biochemistry 26 (1987) 178–182.
[29] J.M. Sanchez-Ruiz, J.L. López-Lacomba, M. Cortijo, P.L. Mateo, Biochemistry 27 (1988) 1648–1652.
[30] J.M. Sturtevant, Ann. Rev. Phys. Chem. 38 (1987) 463–488.
[31] H. Fukada, J.M. Sturtevant, F.A. Quiocho, J. Biol. Chem. 258 (1983) 13193–13198.
[32] A. Cooper, J. Am. Chem. Soc. 114 (1992) 9208–9209.
[33] A. Cooper, K.E. McAuley-HechtPhil, Trans. R. Soc. Lond. A 345 (1993) 23–35.
[34] K.K. Andersen, P. Westh, D.E. Otzen, Langmuir 24 (2008) 399–407.
[35] C. LaMesa, J. Colloid Interface Sci. 286 (2005) 148–157.
[36] N.J. Turro, X-G. Lei, K.P. Ananthapadmanabhan, M. Aronson, Langmuir 11 (1995) 2525–2533.
[37] C. Tanford, The hydrophobic effect, second ed., Formation of Micelles and Biological Membranes, Wiley & Sons, New York, 1980.
[38] M.N. Jones, Biochem. J. 151 (1975) 109–114.
[39] E.D. Goddard, K.P. Ananthapadmanabhan (Protein–surfactant interactions), in: Interactions of Surfactants with Polymers and Proteins, CRC Press, Boca Raton, FL, 1993, pp. 319–365.
[40] M.M. Nielsen, K.K. Andersen, P. Westh, D.E. Otzen, Biophys. J. 92 (2007) 3674–3685.
[41] A. Rodger, R. Marrington, D. Roper, S. Windsor, G. Ulrich Nienhaus (Eds.), Protein–Ligand Interactions. Methods and Applications, Humana Press Inc., 2005, pp. 343–362.
[42] L. Razumovsky, S. Damodaran, Langmuir 15 (1999) 1392–1399.

Colloids and Surfaces B: Biointerfaces 82 (2011) 581–587

Contents lists available at ScienceDirect

Colloids and Surfaces B: Biointerfaces

journal homepage: www.elsevier.com/locate/colsurfb

Mechanisms of fibrinogen–acebutolol interactions: Insights from DSC, CD and LS

Natalia Hassan[a], Juan M. Ruso[a,*], P. Somasundaran[b]

[a] Soft Matter and Molecular Biophysics Group, Department of Applied Physics University of Santiago de Compostela, Campus Vida s/n, 15782, Santiago de Compostela, Spain
[b] Langmuir Center for Colloids & Interfaces, Columbia University, New York, NY 10027, USA

ARTICLE INFO

Article history:
Received 20 July 2010
Received in revised form 6 September 2010
Accepted 11 October 2010
Available online 15 October 2010

Keywords:
Fibrinogen
Drug
Betablockers
Interaction
DSC
CD
Light scattering

ABSTRACT

The complex formed due to the interaction of the amphiphilic betablocker acebutolol with fibrinogen in a buffer solution (50 mN glycine, pH of 8.5) has been investigated using a multipronged physicochemical approach. Differential scanning calorimetry measurements of the complexes have shown no reversibility of thermal denaturation as indicated by the three observed peaks and the opposite role that acebutolol plays in the folding different domains of the fibrinogen molecule and the stability of such domains. While circular dichroism measurements have revealed that interaction of acebutolol with fibrinogen affects the protein secondary structure to a different extent depending on the temperature and drug concentration, dynamic light scattering analysis showed evidence for protein aggregation mainly to tetramers and dimers.

1. Introduction

The interaction of small molecules with macromolecules with specific receptor sites on surfaces of supramolecular organizations of biological systems is one of the extensively studied phenomena in recent biochemical research as it plays a role in a vast range of vital biochemical phenomena. Regardless of whether the interactions are specific or not, they constitute an important part of the protein function and a full description of such interactions is of great value in the understanding the behavior of proteins [1–4].

Many pharmacologically active compounds are amphiphilic molecules: analgesics, peptide and non-peptide, antibiotics, tricyclic antidepressants, antihistamines, anticholinergics, L-blockers, local anesthetics, non-steroidal antiinflammatory drugs, anticancer drugs. Many of these drugs contain one or more aromatic nuclei. These structures are interesting for their resonance properties and for the cyclic delocalization of the charge [5]. Some drugs exhibit the same behavior as traditional surfactants, i.e., they tend to self-associate to form micelles when dispersed in aqueous solutions, usually with a small aggregation number, and this phenomenon is very important for their pharmacological applications, particularly for their effects upon membranes or pharmaceutical formulations [6]. When the drugs are delivered through proteins or micelle drug carriers, the diffusion and release rates of the drug molecules may be affected. Also, the free energies for the micellization of the surface-active drug molecules in solutions are of the same magnitude as the free energy for absorption of drug molecules to the carrier vector. Consequently, the hydrophobic moieties of the drug can interact and tend to stabilize a cluster-like structure with the carriers. Identification of these structure properties will be leading to the molecular assembly and the transport kinetics of the drug components [7]. Previously, we have studied the complexation of different proteins with amphiphilic ligands (surfactants, lipids and drugs) using as physicochemical methods such as equilibrium dialysis, difference spectroscopy, microcalorimetry, zeta potential, static and dynamic light scattering and circular dichroism [8–13]. Results from these studies have permitted us to obtain a thermodynamic picture of the nature of the protein–amphiphilic interactions.

Acebutolol, a beta-selective betablocker, is one of most prescribed drugs for treating hypertension. It has an aryloxipropranolamine chain as non-selective blocker, but linked to an aromatic ring containing a polar-4 substituent (see Scheme 1). The rigidity and planarity of the aromatic ring is not the only feature influenc ing the mode of association, the hydrocarbon chain attached to it also plays a relevant role. The study of this compound is interesting because many of the β-adrenoceptor blocking agents exhibit a range of pharmacological effects that are independent of their β-blocking activity and which arise as a result of modification of the cell membrane. These effects, collectively referred to as the membrane stabilizing activity, include nonspecific cardiac depression as well as depression of myocardial conduction velocity and

* Corresponding author. Tel.: +34 981 563 100; fax: +34 981 520 676.
E-mail address: juanm.ruso@usc.es (J.M. Ruso).

0927-7765/$ – see front matter © 2010 Elsevier B.V. All rights reserved.
doi:10.1016/j.colsurfb.2010.10.020

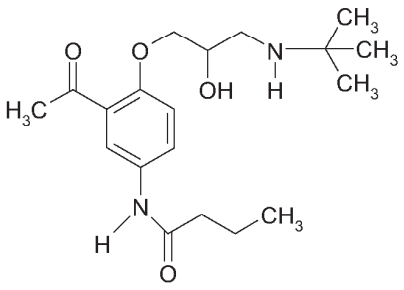

Scheme 1.

local anaesthetic activity. One of the routes of administration of acebutolol is intravenous, where it is immediately delivered to the bloodstream to interact with plasma proteins as fibrinogen.

Fibrinogen is a complex multidomain protein whose major function is to form fibrin clots that prevent the loss of blood upon vascular injury. Bovine fibrinogen (340 kDa) is a 45 nm long and 5 nm round disulfide-linked dimer of three nonidentical polypeptide chains, Aα, Bβ, and γ (see Scheme 2). The NH_2 terminal portions of the six chains are linked together to the central region of the molecule by 11 disulfide bonds forming a small globular domain, the so-called disulfide knot, in the center [14,15]. The C termini of each of the three chains end in globular domains, those of the Bβ and γ chains are located at the ends of the molecule. The COOH-terminal portion of each fibrinogen Aα chain forms a compact αC-domain attached to the bulk of the molecule with a flexible αC-connector. In addition, fibrinogen shows a unique characteristic in its folding. According to the current view, in fibrinogen, two αC-domains interact intramolecularly with each other and with the central region of the molecule, while in fibrin, they switch to an intermolecular interaction to form αC-polymers. This structural organization involves fibrinogen in fibrin assembly process and promotes cell adhesion and migration through their RGD sequences [16]. Contemporary studies have centered on the use of fibrinogen for non viral vector delivery [17], scaffolds [18] and biocompatibility applications [19,20]. Despite the many interesting applications of this protein, there are very few studies focusing on their interactions on with surfactants even though encounter surfactants that are present in many natural and industrial systems at concentrations lower than those required by weakly binding chemicals denaturants such as guanidinium chloride or urea for denaturing proteins. Even the individual binding of a small number of surfactant molecules can induce substantial conformational changes, since the surfactant molecules can wedge themselves into the interior of the protein. Structural studies of proteins complexed with individual surfactant molecules at sub-denaturation concentrations reveal that their high affinity is achieved by a combination of electrostatic and hydrophobic interactions, in which the sulfate head and alkyl chain contact charged and hydrophobic residues of the protein respectively. As a rule, most proteins follow the same sequence of binding events: initial interaction between ionic surfactants and proteins, partial unzipping, exposing of more binding sites and subsequent expansion of the polypeptide chain. However,

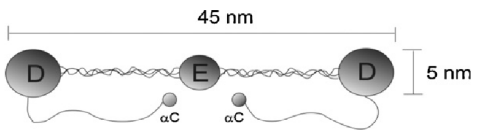

Scheme 2.

the exact number of binding events and associated conformational changes will depend on the structure and amino acid composition of the protein in question [21].

Hence, in this paper we investigated the nature of the interactions of acebutolol with fibrinogen using different techniques, differential scanning calorimetry, dynamic light scattering and circular dichroism.

2. Materials and methods

2.1. Materials

Bovine plasma fibrinogen, fraction I, type IV, was purchased from Sigma and used as received. Acebutolol (*N*-[3-acetyl-4-(2-hydroxy-3-[isopropylamino] propoxy) phenyl] butanamide) hydrochloride (No. A-3669) were purchased from Sigma Chemical Co. and sufficiently well characterized as pure to be used as received. The buffer solution used was 50 mN glycine plus sodium hydroxide to give a pH of 8.5. Samples were prepared within 2 h prior to using. All chemical reagents were of analytical grade and solutions were made using doubly distilled and degassed water.

2.2. Differential scanning calorimetry

Differential scanning calorimetry (DSC) measurements were performed using a VP-DSC (MicroCal Inc., Northampton, MA) calorimeter with 0.542 ml twin cells for the reference and sample solutions. Prior to the DSC experiments, the samples and the references were degassed under vacuum while being stirred. Thermograms were recorded between 20 and 110 °C at a scan rate of 60 °C per hour. To check the reproducibility, each experiment was repeated three times. The baseline reference, obtained with both cells filled with buffer, was subtracted from the thermograms of the samples. The heat capacity curves were evaluated using the MicroCal Origin 7.0 software to obtain ΔH and T_m values

2.3. Circular dichroism

Far-UV circular dichroism (CD) spectra were obtained using a JASCO-715 automatic recording spectropolarimeter (Japan) with a JASCO PTC-343 Peltier-type thermostated cell holder. Quartz cuvettes with 0.2 cm pathlength was used. CD spectra of pure fibrinogen and fibrinogen–acebutolol dilute solutions were recorded from 190 to 270 nm. Protein concentration used was 0.5 mg/ml and surfactant concentrations used ranged from 1 to 10 mM. The following settings were used: resolution, 1 nm; bandwidth, 1 nm; sensitivity, 50 mdeg; response time, 8 s; accumulation, 3; and scan rate 50 nm/min. Corresponding absorbance contributions of buffer solution and water were subtracted with the same instrumental parameters. Data are reported as molar ellipticity and determined as

$$[\theta]_\lambda = \frac{\theta_\lambda M_r}{ncl}$$

where c is the protein concentration, l is the path length of the cell, $[\theta]_\lambda$ is the measured ellipticity at a wavelength λ, M_r is the molecular mass of the protein, and n is the number of residues. The secondary structure content was analysed with the Dichroweb program [22] using CONTIN algorithm. Estimated uncertainties in α-helix and β-sheets content was ±3%

2.4. Dynamic light scattering

Dynamic light scattering measurements were made at 298 ± 0.1 K and at a scattering angle of 90°. Time correlation was

analysed using an ALV-5000 (ALV-GmbH) instrument with vertically polarized incident light of wavelength $\lambda = 488$ nm supplied by a CW diode-pumped Nd; YAG solid-state laser operated at 400 mW. Solutions were clarified as described above. In dynamic light scattering, a time correlation function (TCF) of the scattering intensity is obtained by with autocorrelator from the scattering intensities measured at a certain starting time $i(0)$ and at a very short time interval t later. In normalized form the TCF is given by

$$g_2(t) = \frac{\langle i(0)i(t)\rangle}{\langle i(\infty)\rangle} \quad (1)$$

where $i(\infty)$ is the scattering intensity at very low delay times. For theoretical evaluations, mostly the electric field time correlation function is used $g_1(t)$, which is related to the intensity TCF $g_2(t)$ by the Siegert relationship

$$g_2(\iota) = 1 + \left|g_1(\iota)\right|^2 \quad (2)$$

Monodisperse spherical particles show a single-exponential decay in $g_1(t)$

$$g_1(t) = e^{-Dqx^2t} \quad (3)$$

where D is the translational diffusion coefficient in $m^2\ s^{-1}$ and q is the length of the scattering vector in m^{-1} that is related to the scattering angle θ via:

$$q = \frac{4\pi n}{\lambda}\sin\left(\frac{\theta}{2}\right) \quad (4)$$

with λ being the wavelength of the light used in the vacuum and n the refractive index of the sample. For polydispersed samples the exponential function in Eq. (3) is replaced by the weighted contribution of the individual populations. Then $g_1(t)$ becomes:

$$g_1(t) = \int_{\Gamma_{\min}}^{\Gamma_{\max}} e^{-\Gamma t} G(\Gamma) d\Gamma \quad (5)$$

where $\Gamma = Dq^2$ is the decay rate and $G(\Gamma)$ denotes the decay rate distribution function. Eq. (5) is the Laplace transform of $G(\Gamma)$ and it must be inversed in order to obtain the distribution function of the translational diffusion coefficients. For solving this equation for D, the software packages CONTIN was used. According to Stokes–Einstein equation, the translational diffusion coefficient depends on the hydrodynamically effective sphere radius R_h

$$D_0 = \frac{k_B T}{6\pi\eta_0 R_h} \quad (6)$$

where k_B is the Boltzmann constant, T the absolute temperature and η_0 the solvent viscosity.

3. Results and discussion

First the thermal stability of the protein is characterized and the overall energetics of the transitions of the fibrinogen in the presence of different concentrations of acebutolol is obtained from the DSC data.

Results from the DSC experiments performed at different protein concentrations showed that the concentrations used here do not influence the nature of the thermograms. On the other hand, for some samples thermograms obtained at three different scan-rates (see inset in Fig. 1) revealed that the temperature corresponding to the maximum heat capacity is dependent on the scan rate (from 52.58 to 53.32 °C for the lowest and highest scan-rate, respectively), suggesting that the denaturation process of fibrinogen is kinetically controlled [23]. All subsequent scans were performed at 60 °C per hour.

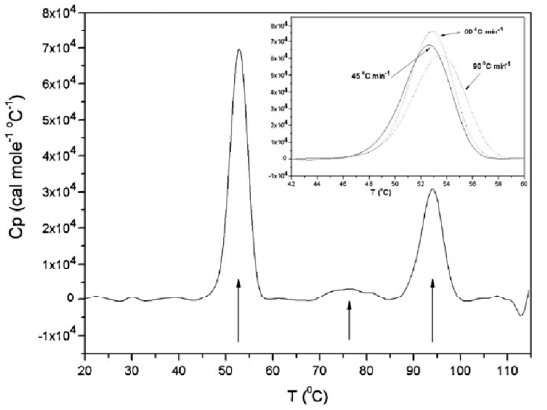

Fig. 1. Thermogram of fibrinogen (0.5 g dm^{-3}, glycine buffer, pH 8.5) at scan-rate 60 °C per hour. Inset shows thermograms of fibrinogen at different scan-rates.

A DSC scan of fibrinogen (0.5 g dm^{-3}) in buffer solution (glycine, pH 8.5) is shown in Fig. 1. Three endothermic peaks can be observed. The narrow and symmetrical peaks located at 52.85 and 93.97 °C have been attributed to the denaturation of the end D and central E fragments of fibrinogen respectively [24] while, the small and broad peak located at 76.62 °C has been related to the denaturation of the C-terminal of the Aα chains. The reversibility of the transitions was checked by reheating the samples in the calorimetric cell after cooling from the first run. Absence of peaks in the consecutive scans suggests total denaturation of the fibrinogen upon heating. However, with the aim of knowing whether each endothermic peak is reversible, we first scanned a sample until a peak was completed, cooled it, and then scanned it again. When the sample was heated until the first peak at 60 °C was completed, subsequent scan had the spectrum with the peaks except the first peak. The disappearance of the first step is thus irreversible. The same procedure was repeated for the other two peaks, with the results suggesting that all the denaturation steps are irreversible. Hence, only the first scans are shown in this paper.

DSC thermograms obtained for fibrinogen in the presence of acebutolol were next analysed for several drug concentrations (Fig. 2). As in the case of pure fibrinogen no reversibility was found for all these systems. The thermodynamic characteristics of the thermal denaturation, melting temperatures (T_m, temperatures at

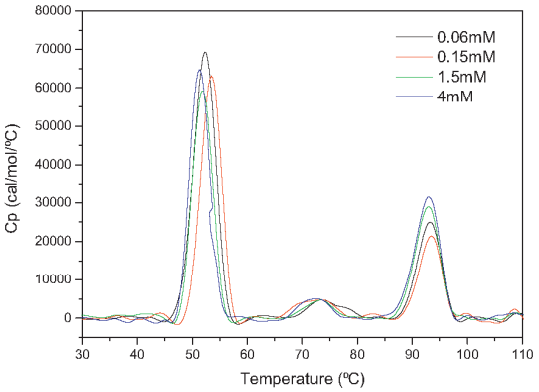

Fig. 2. DSC thermograms of fibrinogen (0.5 g dm^{-3}) in the presence of acebutolol.

Table 1
Thermodynamic parameters obtained from DSC thermograms of fibrinogen in the presence of acebutolol (uncertainties in T_m, ΔH and ΔH_v values for the first and third peak are ±1%. Uncertainties for the second peak are ±5).

Aceb. (mM)	T_m (°C)			ΔH (kcal/mol)			ΔH_v (kcal/mol)			Cooperativity		
	T_{m1}	T_{m2}	T_{m3}	ΔH_1	ΔH_2	ΔH_3	ΔH_{v1}	ΔH_{v2}	ΔH_{v3}	n_1	n_2	n_3
0.00	52.70	74.51	93.94	288.2	34.2	156.1	179.4	122.4	186.3	1.61	0.28	0.84
0.04	52.24	73.36	92.81	298.7	33.88	136.7	196.1	153.2	201.8	1.52	0.22	0.67
0.06	52.25	74.21	93.13	349.0	37.05	134.9	178.4	123.2	210.2	1.96	0.30	0.64
0.15	53.44	72.37	93.34	293.0	42.58	109.9	197.6	115.2	221.1	1.48	0.36	0.49
0.30	52.26	72.85	92.87	324.3	33.24	123.9	182.5	147.7	216.4	1.77	0.22	0.57
0.40	53.31	72.27	93.48	307.7	38.44	118.2	193.7	104.2	218.7	1.58	0.65	0.54
0.50	53.11	73.15	93.17	344.4	47.11	106.5	182.4	108.9	237.3	1.88	0.43	0.44
0.80	52.06	72.41	93.01	292.9	37.38	172.8	195.9	146.9	189.3	1.49	0.25	0.91
1.00	51.99	71.67	92.86	308.5	36.44	132.6	184.3	101.5	206.5	1.67	0.75	0.64
1.50	51.86	73.03	92.76	271.6	29.45	162.4	199.6	156.4	199.6	1.36	0.18	0.81
2.00	51.76	72.69	92.89	339.8	30.97	158.0	186.0	141.9	210.1	1.82	0.21	0.75
4.00	51.35	72.24	92.78	294.5	33.71	180.8	200.2	156.2	194.1	1.47	0.21	0.93

which a maximum occurred in the endothermic peaks), calorimetric enthalpy (ΔH), van't Hoff enthalpy (ΔH_v) and cooperativity (n, the ratio of calorimetric enthalpy to van't Hoff enthalpy), were obtained for all the systems studied and listed in Table 1

It can be seen from the peaks, that temperatures of unfolding show different patterns depending on the peak. The first peak exhibits an initial increase (at low drug concentration) followed by a decrease at higher concentrations (see Fig. 3). The second peak shows a steady decrease with drug concentration. In the case of the third peak, the changes are minor at low concentrations, while at high concentrations a gradual decrease can be observed. On the whole, changes in T_m are of the order of 2%, 5.7% and 1% for the 1, 2, and 3 peak, respectively. On the basis of these observations, it is proposed that acebutolol plays two opposite roles in the folding and stability of the end D fragments of fibrinogen with it acting as a structure stabilizer at low molar concentrations (enhancing T_m) and as a destabilizer at higher concentrations (diminishing T_m). A similar behavior has been observed for BSA and catalase in the presence of SDS and CTAB, respectively [25,26]. The role of acebutolol in the case of the other domains along the protein structure is that of a denaturant for the C-terminal of the Aα chains and denaturant at higher concentrations for the central E domain.

In general, cationic amphiphiles bind cooperatively to most proteins to form complexes similar to those formed by SDS, but with diminished affinity for complexation. The reason for this difference has been suggested to be the side chains involved. Favorable electrostatic interactions for cationic amphiphiles are Glu and Asp, which have only two and one methylene side chain groups, whereas

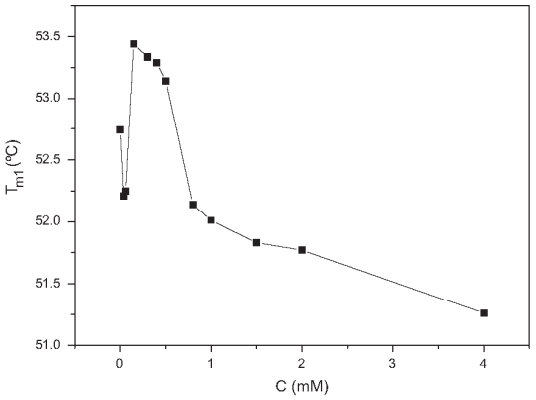

Fig. 3. Fibrinogen unfolding temperature (T_{m1}) as a function of acebutolol concentration.

the corresponding side chains for anionic amphiphiles are Lys and Arg, amino acids with four and three methylene groups. This makes a significant hydrophobic contribution to binding as well as a favorable electrostatic interaction in the case of anionic amphiphiles. Thus, changes in the unfolding temperature have been interpreted to be due to the fact that small amounts of amphiphiles induces a protective effect due to some cross-linking function of the ionic groups. In other words, the native conformation is stabilized by a cross-linking function of the aromatic chain between a group of nonpolar residues and a negatively charged residue located on different loops of the protein [27]. In region corresponding to the lowest drug concentrations, the interaction is due to the electrostatic binding of the drug to specific high-energy sites on the protein. Binding in the next region is attributed to noncooperative interactions where hydrophobic interaction is the driving force. However, Liu et al. [28] has previously studied the interactions between nucleic acids with cationic surfactants and anionic surfactants by resonance light scattering spectroscopy to show that hydrophobic attractive force exists even at low concentrations. Thus, due to the higher hydrophobicity of the aromatic rings in acebutolol structure this will be the most probable event in the system discussed here.

With increasing drug concentration, endothermic peaks tend to shift. However, no further significant T change i.e. no widening or dissymmetry can be observed, in all the studied thermograms. These set of measurements points out a decrease in stability of the fibrinogen with increase in acebutolol concentration. Such observations have been made previously in other systems. When amphiphile concentration is increased hydrophobic interactions become increasingly more dominant with the result that hydrophobic moieties will penetrate into the hydrophobic domains of the protein in order to reduce their contacts with water. Due to such penetration the protein may deform somewhat, resulting in lower thermal stability [29].

Enthalpies of thermal denaturation calculated for the three observed peaks can be seen in Table 1. Highest test values were obtained for the first peak, whereas for the second peak the values are the lowest. In the presence of acebutolol, enthalpies calculated for the first and second peak tend to decrease with the drug concentration. However, the third peak shows the opposite behavior. Cooperativity, n, depends on a number of factors such as the validity of the two state approximations, reversibility of the transition. When $n > 1$, the unfolding is not a two state process, but it involves unfolding of intermediates or independent domains. In the case of $n < 1$, this implies that not all the protein is correctly folded (probably due to irreversible or aggregation effects) [30]. For all the systems under study it can be concluded that $n > 1$ for the first peak and $n < 1$ for the second and third. This implies that one or more intermediate states are populated in the lowest temperature

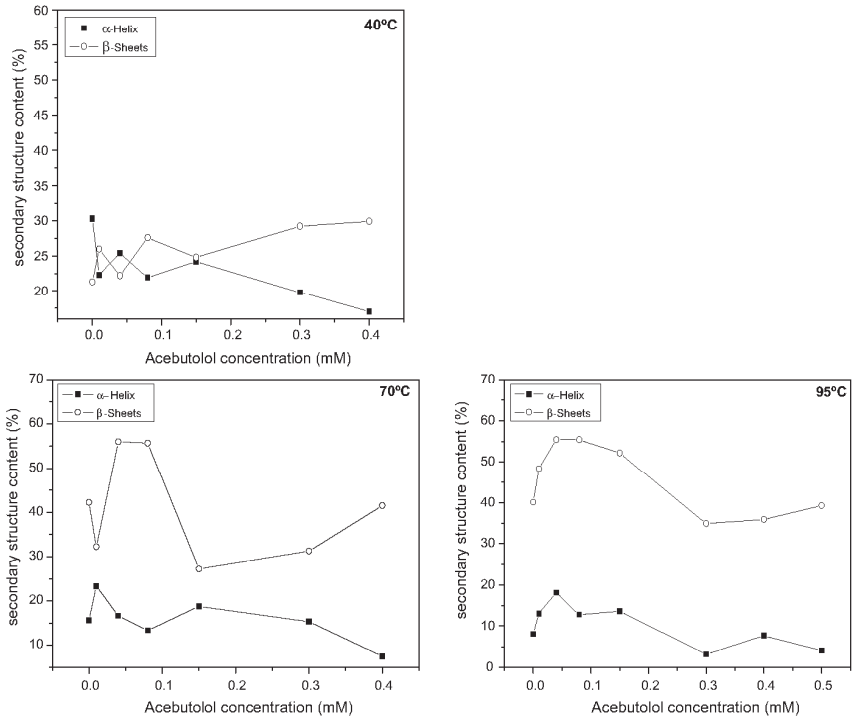

Fig. 4. Contents (in %) of the α-helix (■) and β-sheets (○) elements in fibrinogen as a function of acebutolol concentration at different temperatures.

change involving intramolecular cooperation, while denaturation at higher temperatures involves intermolecular cooperation [25].

For a better understanding of these processes, a study of conformational changes in the protein structure is required. A protein molecule is a macroscopic system; the disruption of this structure should be regarded as a change of the macroscopic state of the system. Circular dichroism spectroscopy measurements provide information about secondary structure of proteins molecules and of how a polypeptide chain folds into different arrangements due to the binding of different ligands to these types of macromolecules [31]. Chen et al. [23] have estimated that the native fibrinogen molecule contains about 35% α-helix, 21% β-sheets, 13% β-turn and 31% random coil. Other authors have estimated 42% α-helix, 7% β-sheets, 20% β-turn and 30.8% random coil [32]. However, the trends are clear: with increasing temperature α-helix and β-sheets change little before the onset of the first peak but change dramatically (α-helix decreased and β-sheets increased) in the range 55–65 °C. After this, α-helix contents decrease moderately and finally an important decease is observed from 80 to 100 °C. This behavior indicates that the decreases of α-helix occur only in the denaturated domain in this temperature range (see Fig. 2) the coiled-coil portion of fragment D [33]. Some authors have reported that the decrease in α-helix content is due to a conformational change of the β-structure, on the basis that the ellipticity of the negative peaks in the CD spectrum for fibrinogen changed from slightly negative values and the fact that the fluorescence intensity decreased.

Further studies were performed to determine the effects of acebutolol concentrations at different temperatures (25, 40, 70 and 95 °C). The first two temperatures correspond to the area below the first peak (native fibrinogen structure), the second between the second and third peaks (just the D domain is unfolded) and the final one beyond the third peak. Fragment D contains a distribution of secondary structure values of 35% α-helix, 29% β-sheet segments and 17% turn structures. Fragment D has two domains: a portion of the original coil and also a thermally labile globular domain. The coiled-coil portion showed an α-helical content of around 70% and the globular domain is estimated to be rich in β-sheet structures. Fragment E is shown to contain 50% α-helical values, attributed to its coiled-coil portions, and minor β-strands and turn structures [34]. Fig. 4 shows plots of the contents of α-helix and β-sheets in the fibrinogen structure at different temperatures and drug concentrations. As expected, acebutolol was found to interact with fibrinogen and to affect the protein secondary structure. At 25 °C changes in secondary structure are insignificant for drug concentrations below 0.1 mM: However, for the other temperatures changes can be observed even at lower concentrations. The backbone hydrogen bonds of α-helix are generally slightly weaker than those in β-sheets. Thus, they are readily attacked by the surrounding molecules. In this study both α-helix and β-sheets exhibit changes with added surfactant molecules. The interaction with acebutolol leads to greatest protein conformational changes particularly at 70 and 95 °C. These findings suggest the strength of the interactions between fibrinogen and acebutolol. Previous studies have explained the different interactions between fibrinogen and ligands in terms of ligand molecular structure [35,36]. In the present case, the potent hydrophobic moiety of acebutolol was found to interact strongly with fibrinogen, and such interactions can be powerful enough to cause unfolding of the protein. Similar conclusion has been arrived at by comparing the adsorption of β-endorphin and epinephrine to different domains of the fibrinogen through electrostatic, polar, and hydrophobic

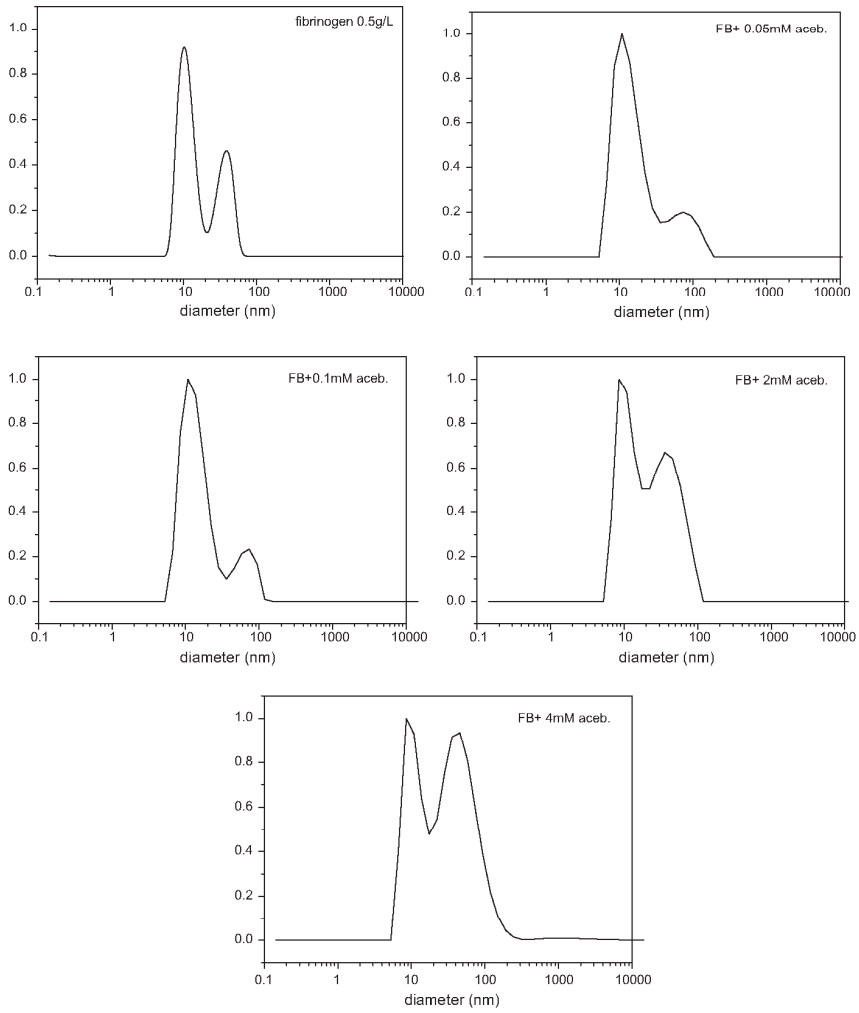

Fig. 5. Size distribution for fibrinogen 0.5 g/L and at different acebutolol concentration.

interactions, resulting in protein unfolding, which may in turn expose the receptor induced binding sites [37].

To evaluate the size of the fibrinogen altered by acebutolol, as well as the size of the complex formed, the hydrodynamic size of fibrinogen plus acebutolol was monitored at different drug concentration by dynamic light scattering. The dimensions of an individual molecule of fibrinogen are 5×45 nm [38]. DLS profile of fibrinogen at 25 °C shows two peaks with hydrodynamic diameters of 10 and 42 nm (Fig. 5). Thus, based on these results, fibrinogen molecules are proposed to form dimers. Upon the addition of acebutolol to fibrinogen solution, the higher hydrodynamic diameter of the complexes increased from 42 nm to 73 nm. This is a clear evidence for fibrinogen undergoing partial unfolding or loosening of the structure on binding with acebutolol which in turn results in the aggregation of dimers (probably to tetramers). At higher acebutolol concentrations, hydrodynamic diameters revert to the initial values of 10 and 42 nm respectively. This is because tetramers dissociate to dimers, which suggests that the formation of the tetramers from dimers is a reversible process. On the other hand, the sequence of plots shows an increase of the relative height of the second peak as the drug concentration is increased being most pronounced at high drug concentrations. The protein is behaving in a manner similar to an adsorbent interface, adsorption onto which is energetically more favorable for dimers than for tetramers (see Scheme 3).

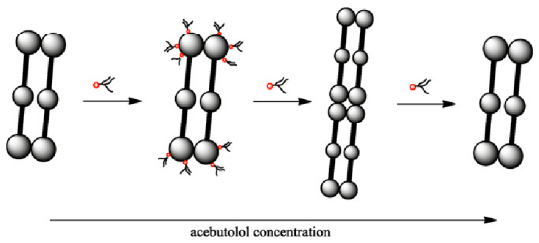

Scheme 3.

On the whole, we have observed from DLS measurements how the addition of acebutolol molecules modifies the cluster formation of fibrinogen molecules.

4. Summary

The interactions and complex formation between the amphiphile betablocker acebutolol and bovine fibrinogen have been studied in aqueous buffered solution by several techniques. It was found that acebutolol plays two opposite roles in the folding and stabilizing the end D fragments of fibrinogen: promotes stability at low concentrations and unfolding at the higher ones. With the other domains along the protein structure, acebutolol acts as a potent denaturant for C-terminal of the Aα chains and denaturant at higher concentrations for the central E domain. Transitions from the native to the unfolded state of fibrinogen induced by acebutolol have been found to be a multiple step process with intermediate molten globule states. It was also observed that the presence of acebutolol causes an increase in the content of β-sheets at the expense of α-helix structures at lower temperatures. Meanwhile, this effect is attenuated when the temperature is raised. It is postulated that fibrinogen form dimers in the absence of additives due to electrostatic interactions between the negative domains (D and E) of one molecule and the positive domains (C) of the another The addition of small amounts of acebutolol results in the aggregation of the dimers to tetramers. However, when the concentration of acebutolol is high, tetramers dissociate to dimers. These findings could be useful for applicatons in biomaterial science where devices should be created with improved hemmocompatibility.

Acknowledgements

The authors acknowledge financial support from Dirección Xeral de Promoción Científica e Tecnológica do Sistema Universitario de Galicia. Authors also thank Prof. J.L. Mascareñas (Department of Organic Chemistry, University of Santiago de Compostela) for the use of CD spectrometer equipment.

References

[1] E. Dickinson, Colloid Surf. B 15 (1999) 161–176.
[2] L.A. MacManus-Spencer, M.L. Tse, P.C. Hebert, H.N. Bischel, R.G. Luthy, Anal. Chem. 82 (2010) 974–981.
[3] R.A.R. Bowen, G.L. Hortin, G. Csako, O.H. Otanez, A.T. Remaley, Clin. Biochem. 43 (2010) 4–25.
[4] K. Hu, Y. Gao, W. Zhou, J. Lian, F. Li, Z. Chen, Langmuir 25 (2009) 12404–12407.
[5] S. Schreier, S.V.P. Malheiros, E. Paula, Biochim. Biophys. Acta 1508 (2000) 210–234.
[6] D.M. Shackleford, R.J. Prankerd, M.J. Scanlon, W.N. Charman, Pharm. Res. 20 (2003) 465–472.
[7] R.S.G. Krishnan, S. Thennarasu, A.B. Mandal, Chem. Phys. 291 (2003) 195–205.
[8] E. Blanco, P. Messina, J.M. Ruso, G. Pieto, F. Sarmiento, J. Phys. Chem. B 110 (2006) 11369–11376.
[9] P. Messina, G. Pieto, V. Dodero, J.M. Ruso, P. Schulz, F. Sarmiento, Biopolymers 79 (2005) 300–309.
[10] J.M. Ruso, N. Deo, P. Somasundaran, Langmuir 20 (2004) 8988–8991.
[11] P. Martínez-Landeira, J.M. Ruso, G. Pieto, F. Sarmiento, M.N. Jones, Langmuir 18 (2002) 3300–3305.
[12] J.M. Ruso, P. Taboada, P. Martinez-Landeira, G. Pieto, F. Sarmiento, J. Phys. Chem. B 105 (13) (2001) 2644–2648.
[13] J.M. Ruso, D. Attwood, M. García, P. Taboada, L.M. Varela, V. Mosquera, Langmuir 17 (2001) 5189–5195.
[14] J.H. Brown, N. Volkmann, G. Jun, A.H. Henschen-Edman, C. Cohen, Proc. Natl. Acad. Sci. 97 (2000) 85–90.
[15] S. Yakovlev, L. Medved, Biochemistry 48 (2009) 5171–5179.
[16] G. Tsurupa, R.R. Hantgan, R.A. Burton, I. Pechik, N. Tjandra, L. Medved, Biochemistry 48 (2009) 12191–12201.
[17] A. Rieux, A. Shikanov, L.D. Shea, J. Controlled Release 136 (2009) 148–154.
[18] R. Uibo, I. Laidmäe, E.S. Sawyer, L.A. Flanagan, P.C. Georges, J.P. Winer, P.A. Janmey, Biochim. Biophys. Acta 1793 (2009) 924–930.
[19] I. Keere, R. Willaert, A. Hubin, J. Vereecken, Langmuir 24 (2008) 1844–1852.
[20] L.C. Xu, C.A. Siedlecki, Langmuir 25 (2009) 3675–3681.
[21] J. H. Hansen, S. V. Petersen, K. K. Andersen, J. J. E., T. Damhus, D. Otzen Biopolymers 91 (2008) 221-231.
[22] DICHROWEB. Nucleic Acids Research, 2004, Vol. 32, Web Server issue.
[23] Y. Chen, H. Mao, X. Zhang, Y. Gong, N. Zhao, Int. J. Biol. Macromol. 26 (1999) 129–134.
[24] (a) P.L. Privalov, L.V. Medev, J. Mol. Biol. 159 (1982) 665–683;
(b) J.W. Donovan, E. Mihalyi, Proc. Natl. Acad. Sci. U.S.A. 71 (1974) 4125–4218.
[25] S. Deep, J.C. Ahluwalia, Phys. Chem. Chem. Phys. 3 (2001) 4583–4591.
[26] E. Blanco, J.M. Ruso, G. Prieto, F. Sarmiento, J. Phys. Chem. B 111 (2007) 2113–2118.
[27] E.P. Vieira, H. Hermes, H. Möhwald, Biochim. Biophys. Acta 1645 (2003) 6–14.
[28] R. Liu, J. Yang, C. Sun, X. Wu, L. Li, B. Su, Colloid Surf. B 34 (2004) 59.
[29] A.W.P. Vermeer, W. Norde, Colloid Surf. A 161 (2000) 139–150.
[30] A. Cooper, M.A. Nutley, A. Wadood, in: S.E. Harding, B.Z. Chowdhry (Eds.), Differential Scanning Microcalorimetry In Protein–Ligand Interactions: Hydrodynamics And Calorimetry, Oxford University Press, Oxford, 2001.
[31] R.W. Woody, Methods Enzymol. 246 (1995) 34–71.
[32] L. Razumovsky, S. Damodaran, Langmuir 15 (1999) 1392–1399.
[33] P.L. Privalov, L.V. Medved, J. Mol. Biol. 159 (1982) 665–683.
[34] I. Azpiazu, D. Chapman, Biochim. Biophys. Acta 1119 (3) (1992) 268–274.
[35] S. Martini, M. Consumi, C. Bonechi, C. Rossi, A. Magnani, Biomacromolecules 8 (2007) 2689–2696.
[36] C. Bonechi, S. Martini, C. Rossi, Bioorg. Med. Chem. 17 (2009) 1630–1635.
[37] R. Barbucci, S. Lamponi, A. Magnani, Biomacromolecules 4 (2003) 1506–1513.
[38] J.W. Weisel, C.V. Stauffacher, E. Bullitt, C. Cohen, Science (1985) 1388–1391.

THE JOURNAL OF PHYSICAL CHEMISTRY B

ARTICLE

pubs.acs.org/JPCB

Surface Characterization and AFM Imaging of Mixed Fibrinogen–Surfactant Films

Natalia Hassan,[†] Julia Maldonado-Valderrama,[‡,§] A. Patrick Gunning,[‡] Victor J. Morris,[‡] and Juan M. Ruso*[,†]

[†]Soft Matter and Molecular Biophysics Group, Department of Applied Physics University of Santiago de Compostela, Campus Sur s/n, 15782, Santiago de Compostela, Spain

[‡]Institute of Food Research, Norwich Research Park, Colney, Norwich NR4 7UA, U.K.

ABSTRACT: This study describes the adsorption behavior of mixed protein/surfactant systems at the air–water interface: specifically fibrinogen and the fluorinated and hydrogenated surfactants (C_8FONa, C_8HONa, and C_{12}HONa). Surface tension techniques and atomic force microscopy (AFM) have been combined to investigate the adsorption behavior of these mixed systems. Interfacial rheology showed that fibrinogen has a low dilatational modulus at the air–water interface when compared to other proteins, suggesting the formation of a weak surface network. Fluorinated and hydrogenated surfactants severely decreased the dilatational modulus of the adsorbed fibrinogen film at the air–water interface. These measurements suggest the progressive displacement of fibrinogen from the air–water interface by both types of surfactants. However, in the case of fibrinogen/fluorinated surfactant systems, surface tension and dilatational rheology measurements suggest the formation of complexes with improved surface activity. AFM imaging of fibrinogen in the presence and absence of surfactants provided new information on the structure of mixed surface films, and revealed new features of the interaction of fibrinogen with hydrogenated and fluorinated surfactants. These studies suggest complexes formed between fibrinogen and fluorinated surfactants which are more surface active than fibrinogen, while the absence of interaction between fibrinogen and hydrogenated surfactants (C_8HONa and C_{12}HONa) results in compaction of the surface layer.

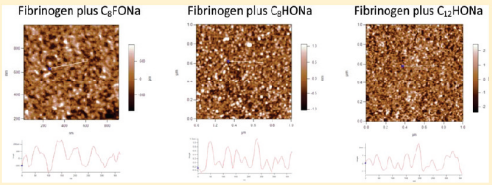

1. INTRODUCTION

The behavior of proteins at interfaces is important to numerous phenomena in biology and biochemistry where adsorption occurs onto biomaterial surfaces. Due to the strong amphipatic nature of proteins, they tend to adsorb at fluid interfaces, lowering the interfacial tension. Proteins and low molecular weight surfactants can interact in the bulk and at the surface in different ways, resulting in complexes with different surface activity.[1−4] Proteins and surfactants stabilize interfaces through different mechanisms. Surfactants form mobile surface layers which are stabilized by the Gibbs–Marangoni mechanism. In contrast, proteins stabilize interfaces by forming a strong viscoelastic network through electrostatic, hydrophobic, and covalent interactions with neighboring proteins. These two mechanisms can be incompatible, and thus, the study of the specific interactions occurring between proteins and surfactants and the characterization of the interfacial structures is essential for rational manipulation of interfacial structures for future technological applications.

The use of anionic surfactants like sodium alkyl carboxylates in mixed systems with proteins has been shown to result in complex behavior. At low concentrations of surfactant, the effect is usually to induce compaction of protein (folding), whereas, at moderate concentrations just below the critical micellar concentration (cmc), the surfactant can act as a potent denaturant of proteins in solution.[5,6] Previous studies have demonstrated that both hydrogenated and fluorinated surfactants can act either as a stabilizer (at low surfactant concentration) or as a denaturant (at high surfactant concentration) of proteins.[7−9] Several studies of the interactions of proteins with hydrogenated surfactants have been reported in the literature.[10,11] However, details of the specific interactions occurring between proteins and fluorinated surfactants are still unknown. In fluorinated surfactants, the hydrogen in the hydrophobic tail is replaced by fluorine atoms; the substitution of the larger and highly electronegative fluorine atom for the smaller hydrogen increases the amphiphilic nature of surfactants and lowers both the surface tension and the critical micelle concentration (cmc); the rigidity of the C–F bond causes stiffening of the perfluoroalkanoate chain, affecting interchain interactions. The increased use of fluorinated surfactants in pharmaceutical and medical systems requires an improved knowledge of their interactions with proteins.[12,13]

Fibrinogen is a plasma protein that has received much attention due to its important biological role in the regulation of both thrombosis and hemostasis.[14,15] The conversion of fibrinogen to fibrin and the subsequent polymerization of fibrin is a key step in blood clot formation: the main biological function of fibrinogen is to facilitate the formation of a three-dimensional network of fibrin fibers which constitutes the structural basis of the blood

Received: January 26, 2011
Revised: March 21, 2011
Published: April 14, 2011

dx.doi.org/10.1021/jp200835j | J. Phys. Chem. B 2011, 115, 6304–6311

The Journal of Physical Chemistry B ARTICLE

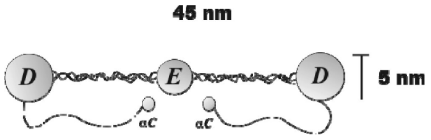

Figure 1. Schematic diagram of the fibrinogen molecule.

clot. Fibrinogen is considered to be a major inhibitor of lung surfactants' function at the lining layer of alveoli.[16,17] It is also one of the most relevant proteins that adsorb onto biomaterial surfaces because it affects many biological processes, for example, the adhesion and activation of platelets and thrombus formation and the triggering of acute inflammatory reactions in experimental animals. Fibrinogen adsorbs rapidly onto a thrombogenic surface, and it is often the major protein found on the surface.[18−20] It is a very large protein (~340 kDa), and its native structure has been described as triglobular with two terminal globular regions (D domains) being connected to a smaller central domain (E domain) by α-helical coiled coil domains. The COOH-terminal portion of each fibrinogen Aα chain forms a compact αC-domain attached to the bulk of the molecule with a flexible αC-connector (Figure 1). The length of an individual fibrinogen molecule is 45−50 nm.[21,22]

This article reports studies on the adsorption behavior of fibrinogen in the presence of hydrogenated and fluorinated surfactants at the air−water interface. Sodium perfluorooctanoate (C_8FONa), sodium octanoate (C_8HONa), and sodium dodecanoate ($C_{12}HONa$) have been chosen because their solution properties have been widely characterized in previous studies. In addition, these surfactants allow a comparison of the differences between hydrocarbon/fluorocarbon mixtures with the same alkyl chain and with mixtures where the hydrocarbon chain is 1.5 times longer than the fluorocarbon chain (it is well-known that in this case both surfactants have the same critical micellar concentration[23]).

The adsorption of fibrinogen was investigated using a number of surface techniques including surface tension, surface dilatational rheology, and atomic force microscopy (AFM). Interfacial rheological measurements are especially appropriate for characterizing the adsorption layers formed by surfactants, proteins, and their complexes and can provide new insights into the physical nature of the adsorbed layers at the air−water interface. AFM complements rheological data by sampling the surface layers through the use of the Langmuir−Blodgett technique and then visualizing the structures formed at the air−water interface.

2. EXPERIMENTAL SECTION

2.1. Materials. Bovine plasma fibrinogen, fraction I, type IV, was purchased from Sigma and used without further purification. Sodium octanoate (C_8HONa) and sodium perfluorooctanoate (C_8FONa) were obtained from Lancaster Synthesis Ltd. Sodium dodecanoate ($C_{12}HONa$) with purity over 99% was obtained from Sigma Chemical Co. The protein was dissolved in 50 mM glycine−NaOH buffer (pH 8.5), the only applicable buffer for bovine fibrinogen.[24] The protein solution was not dialyzed, and the samples were prepared within 12 h prior to use. All chemical reagents were of analytical grade and solutions were made using ultrapure water, cleaned using a Barnstead-Nanopore water purification system. All glassware was cleaned with 10% Micro-90 cleaning solution and isopropanol and then repeatedly rinsed with distilled and ultrapure water. The surface tension of the clean air−water surface was measured before every experiment at 20 °C, in order to confirm the absence of surface contaminants, yielding values of 72.6 ± 0.2 mN/m.

2.2. Methods. *Pendant Drop Technique.* The interfacial tension and dilatational rheology of the adsorbed layers at the air−water interface were measured by the pendant drop technique using a FTA200 pulsating drop tensiometer (First Ten Angstroms, Portsmouth, VA). The apparatus is computer-controlled; the analysis software fits the experimental drop profile to the Young−Laplace capillarity equation and provides, as output, the drop volume V, the interfacial tension γ, and the interfacial area A. A protein drop was formed at the tip of a Teflon coated needle (0.94 mm inside diameter) fitted to a 100 μL syringe. The adsorption process was monitored by observing the change in interfacial pressure $\pi = \gamma_0 - \gamma$, where γ_0 is the interfacial tension of the clean surface. Measurements of the dilatational rheology were made by inducing a triangular shaped time-dependent perturbation to the interfacial area by injecting and extracting solution into and from the drop. The system records the response of the interfacial tension to the deformation in surface area, and a fast Fourier transformation is applied to the data to determine the dilatational response of the interfacial layer. The dilatational modulus is a complex quantity given by the equation

$$E = |E(i\nu)| = \sqrt{\varepsilon^2 + \eta^2\nu^2} \quad (1)$$

where ε is the interfacial elasticity, η is the interfacial viscosity, and ν is the angular frequency of the applied oscillation. The applied oscillations in interfacial area were maintained at amplitude values <5% in order to avoid excessive perturbation of the interfacial layer, and the measurement frequency (ν) was 0.1 Hz. At this relatively high frequency (compared to typical relaxation processes in protein films), the viscous component of the dilatational modulus will be very small and the adsorbed layer will be predominantly elastic.

AFM Imaging of Interfacial Films. A glass Petri dish of total volume 500 mL was used for the preparation of the interfacial films to be imaged with the AFM. First, the absence of surface-active contaminants in the water was verified by surface tension measurements. The protein was applied to the surface by spreading from a stock solution (1 g/L) and a mixture of fibrinogen/surfactant (1 mM). A volume of 100 μL was very carefully spread onto the air−water interface. The mounted piece of mica was driven at a constant rate of 8.4 mm min^{-1}. The surface layer was left to equilibrate for 1 h. The interfacial film was sampled by transferring material onto freshly cleaved mica using the Langmuir−Blodgett (LB) technique. The images were obtained by tapping mode in air on an Asylum Research MFP-3D atomic force microscope using Olympus AC 160 cantilevers with a spring constant quoted at 42 N m^{-1} at a drive frequency of 351.4 kHz (10% below resonance) and a scan rate of 2 Hz. The damping was kept to <10% in order to minimize the tracking force. Structures that present lesser diameters than the tip diameter can be overestimated, so it cannot be sure of the real diameter of the structure. Z-scale accuracy was checked once a day by means of a silicon grating (TGZ silicon grating, from Mikromasch), ensuring a nominal height deviation lower than 2% at the highest scan size. To eliminate imaging artifacts, the scan direction was varied to ensure a true image.

RESULTS AND DISCUSSION

3.1. Surface Tension Measurements. The effect of the bulk concentration of fibrinogen in 50 mM glycine−NaOH buffer on

dx.doi.org/10.1021/jp200835j |J. Phys. Chem. B 2011, 115, 6304–6311

The Journal of Physical Chemistry B ARTICLE

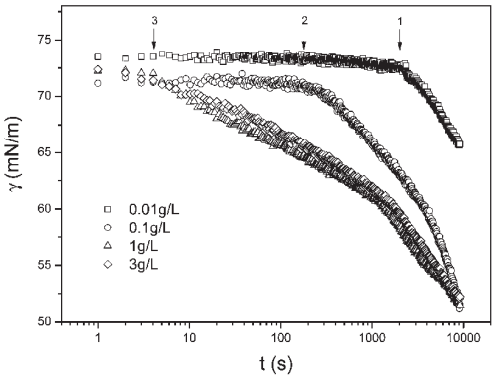

Figure 2. Dynamic surface tension of fibrinogen in 50 mM glycine–NaOH buffer (pH 8.5) adsorbed at the air–solution interface from different bulk concentrations. The arrows indicate the change in the slope at (1) 0.01 g/L, (2) 0.1 g/L, (3) 1 g/L, and 3 g/L.

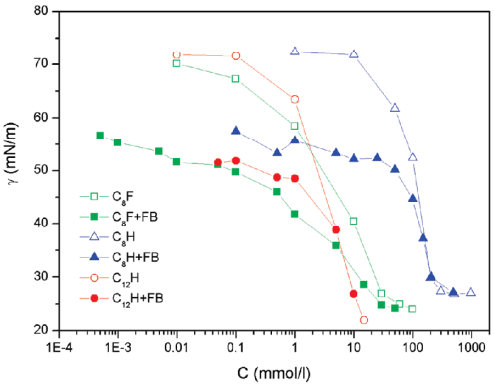

Figure 3. Surface tension versus concentration of fibrinogen and fibrinogen–surfactant mixtures at the air–water interface.

the dynamic surface tension is shown in Figure 2. All concentrations exhibit an apparent lag time (first change in slope indicated by an arrow in Figure 2 for the lowest bulk concentration). This phenomenon is called an induction time, and it is attributed to noninteracting adsorbed molecules that have little effect on the surface tension, or to molecules adsorbed at the interface which do not appreciably reduce the interfacial tension. The induction period was found to decrease as the concentration of fibrinogen increased. Thus, for fibrinogen concentrations of 1×10^{-2}, 0.1, 1, and 3 g/L, the surface tension remained constant for 5760, 600, 12, and 10 s., respectively (Figure 2, arrows 1, 2, and 3, respectively). It is reported in the literature that for low protein concentration the initial stage of the adsorption process is diffusion limited, and this is true for all of the adsorption processes at lower protein concentrations.[25] Interestingly, after this period, the surface tension dropped continuously and then exhibited another change in rate (arrowed in Figure 2) which is particularly marked for the three highest fibrinogen concentrations (Figure 2).

Franses and co-workers have reported studies on the adsorption of fibrinogen at the air–pure water and air–phosphate buffered saline (PBS - pH 7.2) interfaces.[26] The authors reported similar behavior at both interfaces: the layer thickness increased as the fibrinogen concentration in the bulk phase was raised, reaching a final value of 46 nm. This increase is attributed to the fact that, as the fibrinogen concentration at the interface increases with increasing bulk concentration, the protein molecules no longer lie flat on the surface but become more oriented, with their molecular axis on average at an angle to the surface. The αC domains, which are rich in Arg and Lys residues, are actually positively charged. The hydropathic index for human plasma fibrinogen (HPF) indicates that the E and D domains are substantially more hydrophobic than the αC domains.[27] Thus, at first, the fibrinogen molecules could be adsorbed parallel to the interface with the αC domains oriented into the aqueous solution. When the interfacial concentration is increased, the adsorption process may involve dynamic conformational reorientation of the fibrinogen molecules at the surface.

According to this hypothesis, the αC domains in fibrinogen interact intramolecularly with each other, and with the central region of the molecule (the E domains).[28] Experimental studies of the conformational changes in fibrinogen at the air–water interface suggest an increase in β-sheet and a loss of α-helix and aperiodic structure.[29] However, when the number of adsorbed molecules at the interface is high, the known flexibility of the C-terminal segments of the γ chains[30] exists in different configurations within dimeric cross-linked molecules. This may be related to the observed final zone in the surface tension time plots (Figure 2) for the highest protein concentrations.

The behavior of protein/surfactant mixtures was investigated at a constant concentration of protein (1 g/L) while varying the surfactant concentration. Figure 3 shows the surface tension isotherms of the pure surfactants and those corresponding to their mixture with fibrinogen (1 g/L) at the air–water interface. Surface tension has been demonstrated to be a very powerful technique for determining the critical micellar concentration of surfactants (the concentration that provides a saturated interface, i.e., constant interfacial tension).[31] Perfluorinated and hydrogenated amphiphiles present similar thermodynamic behavior; perfluorinated amphiphiles with an alkyl chain two-thirds the length of a corresponding hydrogenated amphiphile have been shown to have the same cmc.[32] In the present studies, the cmc values are 30, 400, and 20 mM for C_8FONa, C_8HONa, and $C_{12}HONa$, respectively. These values are in perfect agreement with those reported previously by other researchers.[33,34]

For the mixed systems, it can be seen that a rather similar pattern appears for the three surfactants. At low surfactant concentrations, the surface tension of the mixtures is lower than that of the pure systems. At very high surfactant concentrations, the plots for the pure surfactants and the mixtures converge. This supports the hypothesis that the surfactant displaces the protein from the interface. However, around the cmc of the surfactants, the shapes of the curves differ when hydrogenated or perfluorinated surfactants are contained in the mixture. In the case of hydrogenated surfactants, the saturation of the surface layer of the mixed systems (critical aggregation concentration, cac) coincides with the cmc of the pure surfactant (Figure 3), whereas the saturation of the surface of mixtures of fibrinogen and fluorinated surfactants is slightly displaced to lower concentrations (Figure 3). This suggests an interaction between fibrinogen and fluorinated surfactants that might result in the formation of complexes with improved surface properties. This interaction

dx.doi.org/10.1021/jp200835j | J. Phys. Chem. B 2011, 115, 6304–6311

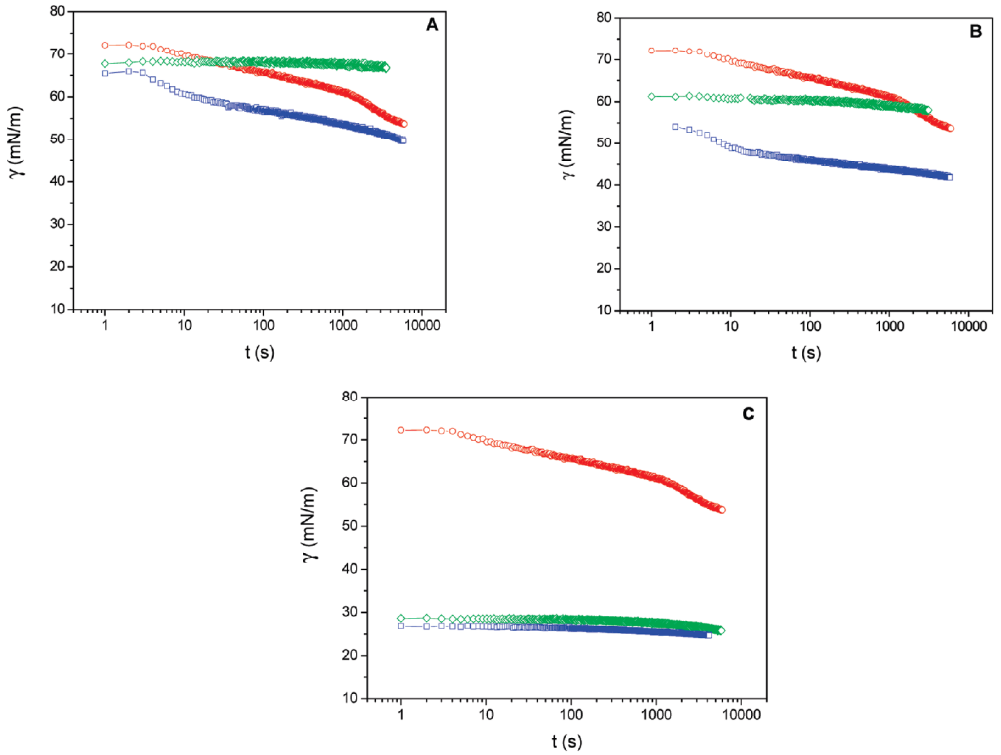

Figure 4. Dynamic surface tension of (○) fibrinogen 1 g/L; (◊) pure C_8FONa (A, 0.1 mM C_8FONa; B, 1 mM C_8FONa; C, 30 mM C_8FONa), and (□) fibrinogen/C_8F mixtures at the following surfactant concentrations (A, 0.1 mM C_8FONa; B, 1 mM C_8FONa; C, 30 mM C_8FONa).

can be studied in more detail by looking into the dynamic behavior of the system.

Figure 4 shows the dynamic surface tension of fibrinogen (1 g/L) and fibrinogen/C_8FONa mixtures (fibrinogen/fluorinated surfactant). The induction period does not change in the presence of the surfactant (a similar behavior to that seen for C_8HONa was observed for $C_{12}HONa$, not shown). However the surface tension of the mixtures changed considerably at higher surfactant concentrations. At low surfactant concentrations (Figure 4A and B), the surface tension values for the mixtures are very different when compared with those of pure fibrinogen and pure surfactant. Similar patterns have been found for the other surfactants. The presence of surfactant results in a strong cooperative or synergistic effect leading to increased surface activity of the mixed system. This agrees with the findings in Figure 3, and supports the proposal that there is an interaction between fibrinogen and fluorinated surfactants which results in the formation of complexes of enhanced surface activity. As the surfactant concentration is increased, the surface tension of the mixture gradually approaches the value for the surfactant alone (Figure 4C). This finding strongly supports the idea that the surfactant finally displaces the protein from the surface. Several studies have reported partial or full displacement of proteins from the air—water interface by surfactants.[35] Proteins can be displaced by surfactants when the surface energy decreases upon adsorption of the surfactants.[36] On the basis of the results obtained in Figure 4A and B, we can infer that, at low surfactant concentrations, the surfactants not only reach the air—water interface, but they might also bind to fibrinogen, forming complexes which appear to be more surface active than the pure protein or pure surfactant alone. Thus, adsorption from the mixtures results in an initial enhancement in the total fibrinogen adsorption. As the concentration of surfactant increases, more surfactants are adsorbed to the interface and the surface tension decreases, giving rise to a thermodynamic driving force which expels fibrinogen from the surface.

Reported studies have revealed that certain proteins can act as a sink for surfactant adsorption which is energetically more favorable than the formation of surfactant micelles.[37,38] This would tend to support the idea that surfactants adsorb to and form complexes with fibrinogen but only in very low numbers.

3.2. Dilational Rheology Measurements. The dilatational modulus has been measured for pure fibrinogen and also for the mixed fibrinogen/surfactant systems (Figure 5). The experimental studies were made at an oscillation frequency (0.1 Hz) which was chosen such that it was too fast to allow any protein exchange with the bulk phase. Hence, at this relatively high frequency, the viscous component of the dilatational modulus will be very small,

The Journal of Physical Chemistry B ARTICLE

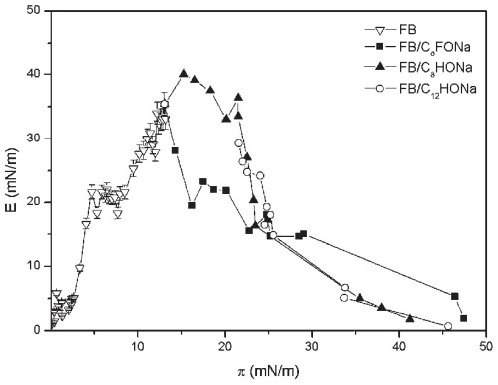

Figure 5. Dilatational elastic modulus of fibrinogen and fibrinogen/surfactant mixtures at the air—water interface. Surfactant concentrations range from 0.05 mM (lower surface pressure) to 10 mM (higher surface pressure).

and the adsorbed layer will be predominantly elastic.[39] Figure 5 shows the dilatational elastic modulus of pure fibrinogen (1 g/L) as a function of surface pressure. The elasticity of the surface layer increases as the protein saturates the interface, reaching a final value of ≈35 mN/m for a surface tension value of 15 mN/m. This value is lower than that reported for other globular proteins such as β-lactoglobulin.[40] Fibrinogen is a trinodular protein and this structure seems to prevent the formation of a cohesive structure upon adsorption, yielding a low surface dilatational modulus. The dilatational elastic modulus of fibrinogen has not been studied previously and thus data is not available for comparison with the present results, but the data presented here provide the first demonstration to our knowledge that fibrinogen does not form a cohesive network at air—water interfaces.

Figure 5 shows the evolution of the dilatational elastic modulus as the concentration of surfactant increases in the system. In all cases, addition of surfactant results in a reduction of the elasticity of the surface layer, accompanied by an increase in the surface pressure. Pure surfactant solutions display a negligible surface elasticity at this frequency of oscillation (results not shown). Accordingly, the null value reached by the surface elasticity at sufficiently high surfactant concentrations (Figure 5) suggests that the surface would be covered by surfactants, indicating that the protein is displaced by the surfactant. At low concentration of surfactant in the mixtures, the dependence of the dilatational modulus on surface pressure is different for different surfactants. Clearly, the rate of reduction in the value of the elasticity with surface pressure appears to be steeper in the case of the fluorinated surfactant than for the hydrogenated surfactants (Figure 5). Moreover, fibrinogen/hydrogenated surfactant mixtures show a slight increase in the elasticity of the surface layer prior to the drop in elasticity with increasing surface pressure. The elasticity of the surface layers only diminishes above a certain surface pressure, which appears to be the dominant factor, rather than the concentration of surfactant in the mixture. This nonmonotonous transition between a protein-dominated interface and a surfactant-dominated interface has been reported previously for other protein/nonionic surfactant systems.[41] This is due to the presence of adsorbed surfactant compressing and compacting the protein surface layer prior to displacement. Importantly, Figure 5

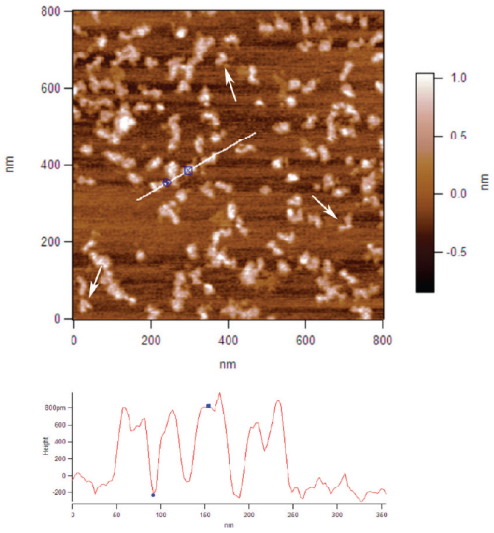

Figure 6. AFM topographic image of fibrinogen on mica. The interfacial structure has been sampled by LB methods and deposited onto mica. The white line indicates the region over which the height profile has been measured. The arrows indicate examples of V-shaped molecules.

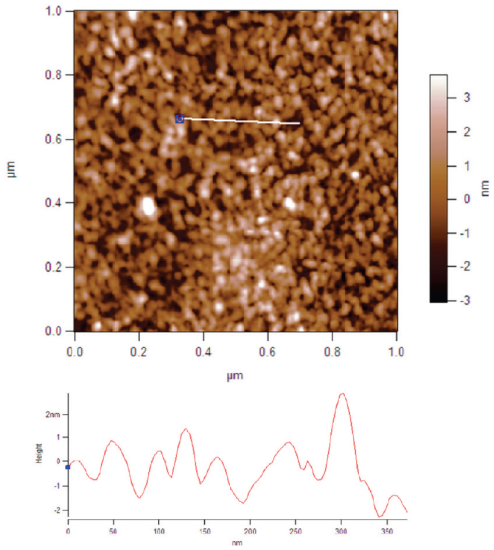

Figure 7. AFM topography image of a spread native fibrinogen LB film at the air—water interface. The interfacial structure has been sampled by LB methods and deposited onto mica. The white line indicates the region over which the height profile has been measured.

shows how, in the case of fibrinogen/fluorinated surfactant, the dilatational modulus decreases monotonously. This feature indicates a

dx.doi.org/10.1021/jp200835j | J. Phys. Chem. B 2011, 115, 6304–6311

The Journal of Physical Chemistry B ARTICLE

progressive weakening of the surface network. Possibly the formation of protein/surfactant complexes prevents the formation of the cohesive network seen in the hydrogenated mixtures.

3.3. AFM Imaging. In order to evaluate the influence of various substrate surface characteristics on fibrinogen−surfactant adsorption processes, we have investigated the adsorption of fibrinogen onto model surfaces in order to select the best substrate for studying fibrinogen and fibrinogen/surfactant mixtures. The surfaces chosen were mica (hydrophilic) and graphite (hydrophobic). Good images of the molecules were obtained on mica (Figure 6), showing a mixture of elongated and V-shaped molecules (arrowed in Figure 6). The topology of adsorbed individual fibrinogen molecules was found to resemble the native structure with the effective lengths of ~45 nm and heights of ~1 nm in all cases. The images obtained on both surfaces showed individual molecules and a few small aggregates. However, the distribution is more uniform on mica. Consequently, the mica surface has been chosen due to its better capacity to immobilize individual fibrinogen molecules and because the mica surface has been widely used to sample interfacial protein structures.

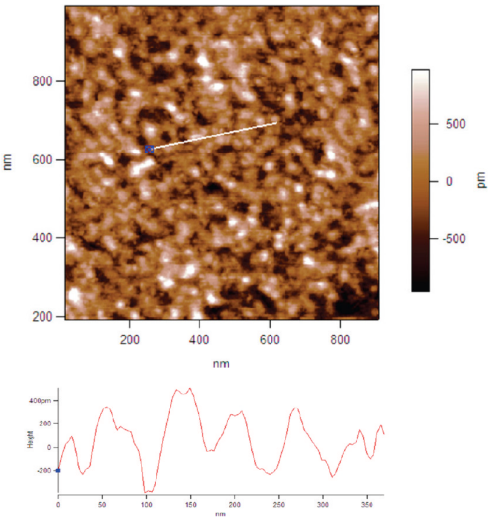

Figure 8. AFM topography image of spread native fibrinogen plus C_8FONa (1 mM) LB film at an air−water interface. The interfacial structure has been sampled by LB methods and deposited onto mica. The white line indicates the region over which the line profile has been measured.

Figures 7, 8, and 9 show AFM images of fibrinogen and mixtures with C_8HONa, C_8FONa, and $C_{12}HONa$, respectively. Images were taken following transfer of spread layers at the air−water interface onto freshly cleaved mica using the Langmuir−Blodgett technique. In the case of native fibrinogen, the images (Figure 7) show closely packed structures containing individual molecules and small clusters of molecules probably formed by a few (two or three) molecules. The adsorption of proteins is the net result of various types of interactions which depend on the nature of the protein, the surface, and the aqueous solution. Several driving forces determine the overall protein adsorption process, including redistribution of charged groups in the interfacial film, dehydration of the protein and substratum surface, and structural rearrangements in the protein molecule. Mica is a hydrophilic surface, and it was proposed that fibrinogen interacts with hydrophilic surfaces through the carboxyl terminus of the α-chains.[42,43] For this reason, the internal structure of fibrinogen cannot be clearly observed. From the height profiles, it is difficult to distinguish individual molecules or domains. Overall, the maximum height fluctuations across the layer vary between 2 and 3 nm. These findings are quite consistent with those obtained in previous studies for fibrinogen in phosphate buffer pH 7.0.[44,45]

Figure 8A shows AFM images of the mixed system formed by FB/fluorinated surfactant (C_8FONa). The image shows clear differences with respect to that of pure FB. The system appears composed of larger (in the *x* and *y* dimension) units which could be due to the formation of clusters. Again, it is difficult to distinguish individual molecules. However, the most pronounced change in the image is the smaller variation in height across the

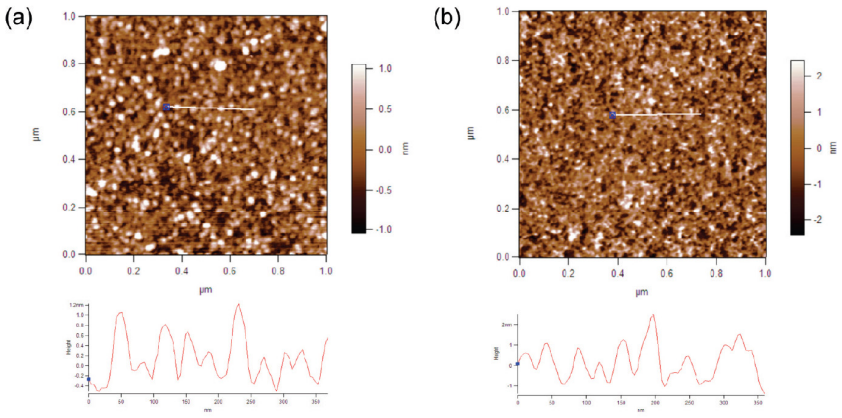

Figure 9. AFM topography image of spread native fibrinogen film at the air−water interface plus (a) C_8HONa (1 mM) and (b) $C_{12}HONa$ (1 mM). The interfacial structure has been sampled by LB methods and deposited onto mica. The white lines on the images indicate the regions over which the height profiles have been measured.

dx.doi.org/10.1021/jp200835j |J. Phys. Chem. B 2011, 115, 6304–6311

The Journal of Physical Chemistry B ARTICLE

images, suggesting an interaction between the surfactant and the protein. These results are consistent with the formation of complexes inferred from the previous surface characterization studies (Figures 3−5) and are more consistent with expected behavior for the adsorption of fibrinogen on hydrophobic surfaces like graphite, where the interaction is likely to occur through the hydrophobic regions of fibrinogen, leaving the Aα chains unanchored from the E domain. A possible explanation is that the Aα chains are free because the hydrophobic moiety of C_8FONa interacts with the hydrophobic pocket of fibrinogen.

Finally, Figure 9 shows the mixtures of FB/hydrogenated surfactants. It is difficult to measure the size of individual molecules. The average maximum height fluctuations across the layers are similar to those observed for fibrinogen alone (Figure 7) and larger than those seen for the fibrinogen/fluorinated surfactant mixtures (Figure 8). Indeed, the mesh appears more compact than that seen for the pure FB system. The images show largely single molecules with little evidence for larger units or cluster formation, as seen in Figure 8A. This denser structure is consistent with the compaction of the surface layer, induced by the hydrogenated surfactants, and reported from the dilatational moduli shown in Figure 4. This compaction is more noticeable in the case of C_{12}HONa (Figure 9B), possibly due to the increase of the alkyl chain length.

4. CONCLUSIONS

The present surface tension measurements suggest complex formation of fibrinogen with the fluorinated surfactant, as indicated by the slight displacement to lower concentration of the cac with respect to the value for the pure surfactant. For fibrinogen/hydrogenated surfactant mixtures, the cac coincides with the cmc of the pure surfactant. The interaction between fibrinogen and fluorinated surfactant causes a strong cooperative or synergistic effect resulting in an increased surface activity of the mixed system relative to fibrinogen. Fibrinogen seems to prevent the formation of a cohesive structure upon adsorption with a low surface dilatational modulus, and in all cases, addition of surfactant results in a reduction of the elasticity of the surface layer accompanied by an increase of the surface pressure. However, in the case of fibrinogen/hydrogenated surfactant mixtures, the elasticity of the surface layers only diminishes over a certain concentration of surfactant. Thus, based on this fact, and on the absence of interaction of fibrinogen/hydrogenated mixtures, compaction on the surface layer could be expected. AFM images are consistent with the surface characterization studies. Formation of clusters in the case of fibrinogen/fluorinated mixtures is consistent with results inferred from surface characterization. In the case of fibrinogen/hydrogenated surfactant mixtures, no cluster formation is seen; indeed, the size of the individual molecules is similar to that of the pure FB system. These observations are consistent with the results reported from the dilatational moduli data.

AUTHOR INFORMATION

Corresponding Author

*E-mail: juanm.ruso@usc.es. Phone: +34 981 563 100. Fax: +34 981 520 676.

Present Addresses

§Biocolloids and Fluid Physics Group, University of Granada, Campus de Fuentenueva, sn. 18071, Granada, Spain.

ACKNOWLEDGMENT

The authors thank the Xunta de Galicia for their financial support (Project No. 10PXIB206258PR). N.H. thanks E. U. for the LLP/Erasmus grant. The experimental studies at IFR were supported by the BBSRC through the core research grant to the Institute.

REFERENCES

(1) Li-Chong, X.; Siedlecki, C. A. *Langmuir* **2009**, *25*, 3675–3681.
(2) Zhdanor, V. P.; Kasemo, B. *Biophys. Chem.* **2010**, *146*, 60–64.
(3) Miller, R.; Fainerman, V. B.; Makievski, A. V.; Krägel, J.; Grigoriev, D. O.; Kazakov, V. N.; Sinyachenko, O. V. *Adv. Colloid Interface Sci.* **2000**, *86*, 39–82.
(4) Joshi, O.; Lee, H. J.; McGuire, J.; Finneran, P.; Bird, K. E. *Colloids Surf., B* **2006**, *50*, 26–35.
(5) Moriyama, Y.; Kawasaka, Y.; Takeda, K. *J. Colloid Interface Sci.* **2003**, *257*, 41–46.
(6) Cooper, A.; Nutley, M. A.; Wadood, A. *Differential scanning microcalorimetry in Protein-Ligand Interactions: hydrodynamics and calorimetry*; Harding, S. E., Chowdhry, B. Z., Eds.; Oxford University Press: Oxford, U.K., 2001.
(7) Blanco, E.; Ruso, J. M.; Sabín, J.; Prieto, G.; Sarmiento, F. *J. Therm. Anal. Calorim.* **2007**, *87*, 211–215.
(8) Ruso, J. M.; Deo, N.; Somasundaran, P. *Langmuir* **2004**, *20*, 8988–8991.
(9) Blanco, E.; Ruso, J. M.; Prieto, G.; Sarmiento, F. *Int. J. Biol. Macromol.* **2008**, *42*, 22–26.
(10) Ling, L.; Yingxi, W.; Gongwu, S.; Shuilin, W.; Paul, C. K.; Zushun, X. *J. Fluorine Chem.* **2009**, *130*, 870–877.
(11) Yoshiko, M.; Kunio, T. *J. Phys. Chem. B* **2010**, *114*, 2430–2434.
(12) Kissa, E. *Fluorinated surfactants, Synthesis, Properties, Applications*; Marcel Dekker Inc.: New York, 1994.
(13) Ananathapadmanabhan, K. P. *Interactions of Surfactants with Polymers and Proteins*; CRC Press: Boca Raton, FL, 1993; Chapter 8.
(14) Cacciafesta, P.; Humphris, A. D. L.; Jandt, K. D.; Miles, M. J. *Langmuir* **2000**, *16*, 8167–8175.
(15) Tsapikouni, T. S.; Missirlis, Y. F. *Colloids Surf., B* **2007**, *57*, 89–96.
(16) Holm, B. A.; Enhorning, G.; Notter, R. H. *Chem. Phys. Lipids* **1988**, *49*, 49–55.
(17) Yin, C.; Chang, C. *Langmuir* **2006**, *22*, 6629–6634.
(18) Van De Keere, I.; Willaert, R.; Hubin, A.; Vereecken, J. *Langmuir* **2008**, *24*, 1844–1852.
(19) Marchin, K. L.; Berrie, C. L. *Langmuir* **2003**, *19*, 9883–9888.
(20) Yongli, C.; Xiufang, Z.; Yandao, G.; Nanming, Z.; Tingying, Z.; Xinqi, S. *J. Colloid Interface Sci.* **1999**, *214*, 38–45.
(21) Ta, T. C.; Sykes, M. T.; McDermott, M. T. *Langmuir* **1998**, *14*, 2435–2443.
(22) Katherine, L.; Marchin, L.; Berrie, C. L. *Langmuir* **2003**, *19*, 9883–9888.
(23) Blanco, E.; González-Pérez, A.; Ruso, J. M.; Pedrido, R.; Prieto, G.; Sarmiento, F. *J. Colloid Interface Sci.* **2005**, *288*, 247–260.
(24) Feng, L.; Andrade, J. D. *J. Biomed. Mater. Res.* **1994**, *28*, 735–743.
(25) Miller, R.; Fainerman, V. B.; Aksenenko, E. V.; Leser, M. E.; Michel, M. *Langmuir* **2004**, *20*, 771–777.
(26) Hernández, E. M.; Franses, E. I. *Colloids Surf., A* **2003**, *214*, 249–262.
(27) Jung, S. Y.; Lim, S. M.; Albertorio, F.; Kim, G.; Gurau, M. C.; Yang, R. D.; Holden, M. A.; Cremer, P. S. *J. Am. Chem. Soc.* **2003**, *125*, 12782–12786.
(28) Burton, R. A.; Tsurupa, G.; Hantgan, R. R.; Tjandra, N.; Medved, L. *Biochemistry* **2007**, *46*, 8550–8560.
(29) Damodaran, S. *Anal. Bioanal. Chem.* **2003**, *376*, 182–188.
(30) Murthy, S. N. P.; Wilson, J. H.; Lukas, T. J.; Veklich, Y.; Weisel, J. W.; Lorand, L. *Proc. Natl. Acad. Sci. U.S.A.* **2000**, *97*, 44–48.

(31) Funasaki, N.; Hada, S. *J. Phys. Chem.* **1979**, *83*, 2471–2475.
(32) Blanco, E.; González-Pérez, A.; Ruso, J. M.; Pedrido, R.; Prieto, G.; Sarmiento, F. *J. Colloid Interface Sci.* **2005**, *288*, 247–260.
(33) López-Fontán, J. L.; Sarmiento, F.; Schulz, P. C. *Colloid Polym. Sci.* **2005**, *283*, 862–871.
(34) González-Pérez, A.; Ruso, J. M.; Prieto, G.; Sarmiento, F. *Colloid Polym. Sci.* **2004**, *282*, 1133–1139.
(35) Phang, T. L.; McClellan, S. J.; Franses, E. I. *Langmuir* **2005**, *21*, 10140–10147.
(36) Kim, S. H.; Franses, E. I. *J. Colloid Interface Sci.* **2006**, *295*, 84–92.
(37) Ruso, J. M.; Taboada, P.; Varela, L. M.; Attwood, D.; Mosquera, V. *Biophys. Chem.* **2001**, *92*, 141–153.
(38) Ruso, J. M.; Attwood, D.; García, M.; Taboada, P.; Varela, L. M.; Mosquera, V. *Langmuir* **2001**, *17*, 5189–5195.
(39) Benjamins, J.; Lyklema, J.; Luccasen-Reynders, E. H. *Langmuir* **2006**, *22*, 6181–6188.
(40) Maldonado-Valderrama, J.; Woodward, N. C.; Gunning, A. P.; Ridout, M. J.; Husband, F. A.; Mackie, A. R.; Morris, V. J. *Langmuir* **2008**, *24*, 6759–6767.
(41) Kotsmar, C; Pradines, V; Alahverdjieva, V. S.; Aksenenko, E. V.; Fainerman, V. B.; Kovalchuk, V. I.; *Adv. Colloid Interface Sci.* **2009**, *150*, 41–54.
(42) Denis, F. A.; Hanarp, P.; Sutherland, D. S.; Gold, J.; Mustin, C.; Rouxhet, P. G.; Dufrene, Y. F. *Langmuir* **2002**, *18*, 819–828.
(43) Agnihotri, A.; Siedlecki, C. A. *Langmuir* **2004**, *20*, 8846–8852.
(44) Marchin, K. L.; Berrie, C. L. *Langmuir* **2003**, *19*, 9883–9888.
(45) Keere, V.; Willaert, R.; Hubing, A.; Vereecken, J. *Langmuir* **2008**, *24*, 1844–1852.

Colloids and Surfaces B: Biointerfaces 87 (2011) 489–497

Contents lists available at ScienceDirect

Colloids and Surfaces B: Biointerfaces

journal homepage: www.elsevier.com/locate/colsurfb

Investigating the effect of an arterial hypertension drug on the structural properties of plasma protein

Natalia Hassan [a], Julia Maldonado-Valderrama [b,1], A. Patrick Gunning [b], V.J. Morris [b], Juan M. Ruso [a,*]

[a] Soft Matter and Molecular Biophysics Group, Department of Applied Physics University of Santiago de Compostela, Campus Sur s/n, 15782, Santiago de Compostela, Spain
[b] Institute of Food Research, Norwich Research Park, NR47UA Norwich UK

ARTICLE INFO

Article history:
Received 16 March 2011
Received in revised form 2 May 2011
Accepted 9 June 2011
Available online 16 June 2011

Keywords:
Fibrinogen
Propranolol
DSC
Surface tension
AFM

ABSTRACT

Propanolol is a betablocker drug used in the treatment of arterial hypertension related diseases. In order to achieve an optimal performance of this drug it is important to consider the possible interactions of propanolol with plasma proteins. In this work, we have used several experimental techniques to characterise the effect of addition of the betablocker propanolol on the properties of bovine plasma fibrinogen (FB). Differential scanning calorimeter (DSC), circular dichroism (CD), dynamic light scattering (DLS), surface tension techniques and atomic force microscopy (AFM) measurements have been combined to carry out a detailed physicochemical and surface characterization of the mixed system. As a result, DSC measurements show that propranolol can play two opposite roles, either acting as a structure stabilizer at low molar concentrations or as a structure destabilizer at higher concentrations, in different domains of fibrinogen. CD measurements have revealed that the effect of propanolol on the secondary structure of fibrinogen depends on the temperature and the drug concentration and the DLS analysis showed evidence for protein aggregation. Interestingly, surface tension measurements provided further evidence of the conformational change induced by propanolol on the secondary structure of FB by importantly increasing the surface tension of the system. Finally, AFM imaging of the fibrinogen system provided direct visualization of the protein structure in the presence of propanolol. Combination of these techniques has produced complementary information on the behavior of the mixed system, providing new insights into the structural properties of proteins with potential medical interest.

1. Introduction

Amphiphilic molecules are used widely in both consumer and industrial applications such as food processing, medicines and pharmaceuticals. Because of their peculiar self-assembly behavior, their properties have evolved from being of a purely scientific interest to become a key concept in nano and biotechnology applications, such as drug delivery, sensors, and catalysts. The design of drugs must take into account several attributes, such as the size of the encapsulation system and stability. For applications in drug delivery, previous reports emphasized that the distribution of nanoparticles in tissues and organs is a function of size. In addition, nanoparticles must be sufficiently stable (able to withstand mechanical stress) to increase circulation time in blood and with adequate thermal stability to reduce side effects [1]. Thus, molecular architecture should be involved in the design of self-assembling systems for preparation of nanoparticles [2,3].

Many pharmacological active compounds are amphiphilic molecules, containing one or more aromatic nuclei. These structures are interesting for their resonance properties and for the cyclic delocalization of the charge [4]. Many of these drugs tend to self-assemble like surfactants; associating to form aggregates, usually with a small aggregation number. Proteins and amphiphilic molecules can interact in different ways in the bulk and at the interfaces, due to the strong amphipatic nature of proteins, resulting in complexes with different surface activity [5–8]. Protein–amphiphilic molecule interactions have been extensively studied by a variety of experimental methods [9,10]. In general ionic surfactants are chosen for these studies due to the fact that these kinds of amphiphilic molecules and the proteins have both charged groups and hydrophobic residues. This implies that the properties of the complexes in solution could be very different to those observed for solutions of the individual components. The understanding of molecular recognition in protein–ligand complexes is crucial so as to better comprehend the associated biological function. Non-covalent interactions such as a hydropho-

* Corresponding author. Tel.: +34 981 563 100, fax: +34 981 520 676.
E-mail address: juanm.ruso@usc.es (J.M. Ruso).
[1] Present address: Biocolloids and Fluid Physics Group, University of Granada, Campus de Fuentenueva, sn. 18071, Granada, Spain.

0927-7765/$ – see front matter © 2011 Elsevier B.V. All rights reserved.
doi:10.1016/j.colsurfb.2011.06.015

bic, electrostatic, van der Waals, and hydrogen bonding govern this ligand-binding process. Elucidating the role of these interactions and the time scales involved provides insights into the mechanism of molecular recognition and the role of binding cooperatively in protein dynamics [11]. It has also a practical importance in the discovery, for instance, of new drugs, and in the understanding of diseases like respiratory distress syndrome (dysfunction attributed to a competition for the air–lung interface between plasma proteins and surfactants).

Recently, we have studied the complexation of different proteins with amphiphilic ligands, including surfactants, lipids and drugs [12–15]. These experiments have used a combination of different experimental methods (equilibrium dialysis, difference spectroscopy, microcalorimetry, zeta potential, static and dynamic light scattering, circular dichroism) which allowed us to obtain a very complete characterization and deep understanding of the physicochemical phenomena involved in these interactions [12,16].

Propranolol is a β-adrenergic blocking agent (Scheme 1). It is a racemic compound, with only the 1-isomer having adrenergic blocking activity. It is the most prescribed drug in treating hypertension; it is also applied to manage chronic stable angina. Previous studies on β-adrenoceptor blocking agents have shown that their pharmacological effects arise as a result of modification of the cell membrane [17].

Fibrinogen (FB) is a plasma protein whose major function is related to blood coagulation and this prevents the loss of blood upon vascular injury [18,19]. This protein is also considered as a major inhibitor of lung surfactants function at the layer lining the alveoli [20,21]. FB adsorbs rapidly onto a thrombogenic surface and it is often the major protein found on the surface [22–24]. It is a very large protein (~340 kDa) and the length of an individual fibrinogen molecule is 45–50 nm [25,23]. Its native structure has been described as trinodular protein with three hydrophobic domains connected by α-helical coiled-coil domains. FB is composed of two identical subunits, each containing three dissimilar polypeptide chains Aα, Bβ, and γ, which are linked by disulfide bonds. The NH_2 terminal portions of the six chains are linked together in the central region of the molecule by 11 disulfide bonds forming a small globular domain, the so-called disulfide knot, in the center [26,27].

In this study we have investigated the nature of the interactions of propranolol with fibrinogen by using different experimental techniques; differential scanning calorimetry (DSC), dynamic light scattering, circular dichroism (CD), surface tension and atomic force microscopy (AFM). This combination of techniques has offered new insights into the nature of the interaction between propanolol and fibrinogen. Such characterization may provide crucial information towards the design of drugs with optimal performance.

2. Experimental

2.1. Materials

Bovine plasma fibrinogen, fraction I, type IV, was purchased from Sigma (9001-32-5) and used without purification. Propranolol (1-[Isopropylamino]-3-[1-naphthyloxy]-2-propranol) hydrochloride was obtained from Sigma Chemical Co. (no. P-0884). The buffer solution used was 50 mM glycine plus sodium hydroxide to give a pH of 8.5. Samples were prepared two hours prior to use. All chemical reagents were of analytical grade, and solutions were made using doubly distilled and degassed water.

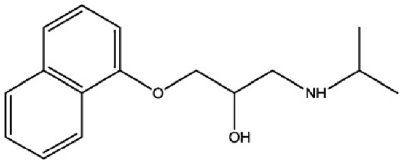

Scheme 1. Propranolol structure.

2.2. Methods

2.2.1. Differential scanning calorimetry (DSC)

DSC measurements were performed using a VP-DSC (MicroCal Inc., Northampton, MA) calorimeter with 0.542 ml twin cells for the reference and sample solutions. Prior to the DSC experiments, the samples and the references were degassed under vacuum while being stirred. Thermograms were recorded between 20 and 110 °C at a scan rate of 60 °C h^{-1}. To check the reproducibility each experiment was repeated three times. The baseline reference, obtained with both cells filled with buffer, was subtracted from the thermograms of the samples. The heat capacity curves were evaluated using MicroCal Origin 7.0 software provided with the equipment to obtain ΔH and T_m values

2.2.2. Circular dichroism

Far-UV circular dichroism spectra were obtained using a JASCO-715 automatic recording spectropolarimeter (Japan) with a JASCO PTC-343 Peltier-type thermostated cell holder using Quartz cuvettes with 0.2 cm pathlength. CD spectra of pure fibrinogen and fibrinogen-surfactants dilute solutions were recorded from 190 to 270 nm. The Protein concentration was fixed at 0.5 mg ml^{-1} and the propanolol concentrations varied from 1 to 10 mM. The following settings were used: resolution, 1 nm; bandwidth, 1 nm; sensitivity, 50 mdeg; response time, 8 s; accumulation, 3; and scan rate 50 nm min^{-1}. The corresponding absorbance contributions of buffer solution and water were subtracted with the same instrumental parameters. Data are reported here as molar ellipticity and determined as

$$[\theta]_\lambda = \frac{\theta_\lambda M_r}{rcl}$$

where c is the protein concentration, l is the path length of the cell, $[\theta]_\lambda$ is the measured ellipticity at a wavelength λ, M_r is the molecular mass of the protein, and r is the number of residues. The secondary structure content was analysed by Dichroweb program [28] using CONTIN algorithm.

2.2.3. Dynamic light scattering (DLS)

DLS measurements were made at (298.0 ± 0.1) K and at a scattering angle of 90°. The time correlation function was using an ALV-5000 (ALV-GmbH) instrument equipped with a vertically polarized incident light beam of wavelength λ = 488 nm supplied by a CW diode-pumped Nd; YAG solid-state laser supplied by Coherent. Inc. and operated at 400 mW. Solutions were clarified as described above. In DLS a time correlation function (TCF) of the scattering intensity is measured. This is formed by an autocorrelator from the scattering intensities measured at a certain starting time $i(0)$ and at a very short time interval t later. In normalized form the TCF is given by

$$g_2(t) = \frac{\langle i(0)i(t)\rangle}{\langle i(\infty)\rangle^2} \quad (1)$$

where $i(\infty)$ is the scattering intensity at very long delay times. For theoretical evaluations mostly the electric field time correlation function is used $g_1(t)$, which is related to the intensity TCF $g_2(t)$ by the Siegert relationship

$$g_2(t) = 1 + |g_1(t)|^2 \quad (2)$$

Monodisperse spherical particles show a single-exponential decay in $g_1(t)$

$$g_1(t) = e^{-Dq^2t} \quad (3)$$

where D is the translational diffusion coefficient in $m^2\ s^{-1}$ and q is the length of the scattering vector in m^{-1} that is related to the scattering angle θ via:

$$q = \frac{4\pi n}{\lambda}\ \sin\left(\frac{\theta}{2}\right) \quad (4)$$

with λ being the wavelength of the light in the vacuum and n the refractive index of the sample solution. For polydisperse samples the exponential function in Eq. (3) must be replaced by the weighted contribution of the individual scatters within the population. Then $g_1(t)$ becomes:

$$g_1(t) = \int_{\Gamma_{\min}}^{\Gamma_{\max}} e^{-\Gamma t} G(\Gamma) d\Gamma \quad (5)$$

where $\Gamma = Dq^2$ is the decay rate and $G(\Gamma)$ denotes the decay rate distribution function. The inverse of Eq. (5), which is the Laplace transform of $G(\Gamma)$ can be used to obtain the distribution function of the translational diffusion coefficients. The software package CONTIN was used to determine the average diffusion coefficient D. An effective hydrodynamic sphere radius R_h from the measured diffusion coefficient:

$$D_0 = \frac{k_B T}{6\pi\eta_0 R_h} \quad (6)$$

where k_B is the Boltzmann constant, T the absolute temperature and η_0 the solvent viscosity.

2.2.4. Pendant drop technique

The surface tension of the adsorbed protein and the protein/propanolol mixed layers at the air–water interface was measured by the pendant drop technique using a FTA200 pulsating drop tensiometer (First Ten Angstroms, Portsmouth, VA). The whole apparatus is computer-controlled; the analysis software fits the experimental drop profile to the Young–Laplace capillarity equation and provides, as output, the drop volume V, the surface tension γ, and the surface area A. A solution droplet was formed at the tip of a Teflon coated needle (0.94 mm inside diameter) fitted to a 100 μl syringe. The absence of surface impurities was tested before each experiment by measuring the surface tension of the clean air–water interface obtaining values of $(72.6 \pm 0.2)\ mN\ m^{-1}$ at 20 °C). The adsorption process of the protein or that of the mixed system was monitored by observing the change in surface tension

2.2.5. AFM imaging of interfacial films

A glass Petri dish of total volume 500 mL was used for the preparation of the interfacial films to be imaged with the AFM. First, the absence of surface active contaminants in the water was verified by surface tension measurement. The protein was applied to the surface by spreading from a stock solution of $1\ g\ l^{-1}$, or a mixture with 1.10^{-3} mM of propranolol. A volume of 100 μl was very carefully spread onto the air/water interface. The mounted piece of mica was driven at a constant rate of $8.4\ mm\ min^{-1}$. The surface layer was left to equilibrate for 1 h. The surface film was sampled by transferring the material onto freshly cleaved mica using the Langmuir Blodgett (LB) technique. The images were obtained in Tapping mode in air, using an Asylum Research Olympus AC 160 cantilever ($42\ Nm^{-1}$) in an MFP-3D BIO (Asylum instrument, Santa Barbara CA). The grain analysis was carried out using Image Pro 5 (Media Cybernetics). A watershed filter (set at 35% of feature height) was applied to the images in order to separate the globular features into discrete units in order that the area of each could be quantified by segmentation analysis.

3. Results and discussion

3.1. Differential scanning calorimetry

Fig. 1 shows the DSC thermogram for FB ($0.5\ g\ dm^{-3}$) in buffer solution (pH 8.5) in the presence of propranolol at different concentrations. Table 1 shows the thermodynamic characteristics of the thermal denaturation obtained for all the systems studied: namely, the melting temperatures (T_m, temperatures at which a maximum occurred in the endothermic peaks), the calorimetric enthalpy (ΔH), and the van't Hoff enthalpy (ΔH_v).

As in the case of pure fibrinogen, we identified no reversible transitions in any of the systems. In contrast, we observed three endothermic peaks (Fig. 1). The narrow and symmetrical peaks located at 52.85 and 93.97 °C can be attributed to the denaturation of the D end and central E fragments of fibrinogen, respectively. Meanwhile, the small and broad peak located at 76.62 °C is attributed to the denaturation of the C-terminal of the Aα chains [29]. We observed that the endothermic peaks shifted to lower temperatures with increasing drug concentration. However, the effect of increasing drug concentration on the location and height of each individual peak (i.e. heat capacity) was different. The height of the first peak at 52.85 °C exhibited an initial increase at low drug concentrations. However, the height of the peak then decreased as the concentration of propanolol increased in the mixture (see Fig. 2). By contrast, the second peak located around 76 °C shows random changes both in form and height that do not allow us to obtain clear conclusions about this process. The effect on the third peak at 93.97 °C only became noticeable at the highest propanolol concentrations where the height of the peak decreased substantially and the peak became asymmetric in shape. In summary, the maximum changes in melting temperatures (T_m) of fibrinogen due to the presence of the drug are of the order of 2.5%, 2.7% and 0.2% for the 1st, 2nd, and 3rd peaks respectively.

This first set of measurements suggests that the structural stability of the fibrinogen decreases with increasing concentration of propanolol in the mixture. This instability is most marked for the largest surfactant concentration, possibly indicating a structural modification of the protein. These results might imply that propranolol can play two opposite roles in the folding and stability of the D end fragments of fibrinogen depending on the concentration. At low molar concentrations, propanolol acts as a structure stabilizer, as seen by the increase of T_m for the 1st peak (Fig. 1).

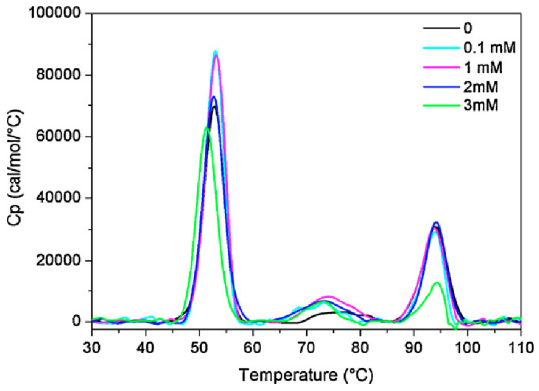

Fig. 1. DSC thermograms of fibrinogen ($0.5\ g\ dm^{-3}$) in the presence of propranolol.

Table 1
Thermodynamic parameters obtained from DSC thermograms of fibrinogen in the presence of propranolol. Uncertainties in T_m, ΔH and ΔH_v values for the first and third peak are ±1%. Uncertainties for the second peak are ±5%.

Propranolol (mM)	T_m (°C)			ΔH (kcal mol^{-1})			ΔH_v (kcal mol^{-1})		
	T_{m1}	T_{m2}	T_{m3}	ΔH_1	ΔH_2	ΔH_3	ΔH_{v1}	ΔH_{v2}	ΔH_{v3}
0.0	52.7	74.5	93.9	288.2	34.2	156.1	179.4	122.4	186.3
0.1	52.8	72.4	93.6	388.2	51.9	137.5	196.2	105.3	235.1
0.5	53.5	76.7	92.9	400.0	95.3	145.4	178.8	81.92	297.5
1.0	53.0	74.3	93.6	401.7	79.8	166.5	187.1	99.90	200.7
1.5	52.1	73.2	93.8	325.1	58.0	178.1	184.0	109.8	181.1
2.0	52.6	73.0	94.0	353.9	67.5	161.9	176.5	67.5	219.1
2.5	51.0	73.5	94.0	267.6	80.0	158.9	181.9	100.4	190.2
3.0	51.4	72.5	93.7	302.4	43.0	54.2	178.4	146.2	241.5

At high drug concentrations it acts as a destabilizer, as seen by the decrease of T_m (Fig. 1). This dual nature of the interaction has been previously observed in other systems; lysozyme and myoglobin in presence of hydrogenated and fluorinated surfactants [30], and BSA and catalase in the presence of SDS and CTAB, respectively [31,32]. Published studies state that when the concentration of surfactant increases in the mixture, the hydrophobic interactions become more dominant. In such a case, the surfactant hydrophobic moieties tend to penetrate into the hydrophobic domains of the protein in order to reduce their contact with water. As a result of this penetration, the protein may then change its conformation resulting in a lower thermal stability [33].

Vieria and coworkers have reported that small amounts of amphiphiles can induce a protective effect on protein structure due to some cross-linking function of the ionic groups [34]. According to these authors, the native conformation is stabilized by a cross-linking function of the aromatic chain between a group of nonpolar residues and a negatively charged residue located on different loops of the protein. Thus it is proposed that, in the region corresponding to the lowest drug concentrations, the interaction is due to the electrostatic binding of the drug to specific high-energy sites on the protein. Binding in the next higher concentration region is attributed to non-cooperative interactions, where the hydrophobic interaction is the driving force.

Other thermodynamics characteristics of the thermal denaturation were obtained from the DSC experiments and they are listed in Table 1. The enthalpies of thermal denaturation (ΔH) exhibited similar tendencies to the heat capacity, being highest for the first peak and lowest for the second peak. The dependence on the concentration of propanolol was irregular and appeared to be different for each peak. For the 1st peak, ΔH increased up to a drug concentration of 1 mM and then decreases afterwards. The 2nd peak did not show a clear systematic dependence on the concentration of surfactant. The ΔH values for the 3rd peak became smaller at higher propranolol concentrations and the values of the enthalpy of thermal denaturation decreased.When the calculated values of the van't Hoff enthalpy for a particular reaction are compared to the enthalpy estimates for the same reaction obtained directly by calorimetric methods, there is often substantial disagreement between the two estimates. The enthalpy of a reaction is most often determined through either one of the two methods. It can be determined directly using calorimetry or indirectly by measuring the temperature dependence of the equilibrium constant (van't Hoff method). The discrepancies between the enthalpy measured by calorimetry, and the enthalpy determined by the van't Hoff method might indicate that the binding reaction is more complex than the simple one-to-one binding model used to describe the data. Binding reactions can include the displacement of solvent and counterions, as well as other linked equilibria, such as protonation or conformational changes. Actually, calorimetric enthalpy includes these contributions but that they are not observed in the van't Hoff method. Accordingly, the van't Hoff enthalpy is considered as the "intrinsic" heat of binding, whereas the calorimetric enthalpy includes other, concomitant reactions (i.e. linked equilibria).

3.2. Circular dichroism

Further understanding of the structural changes undergone by fibrinogen in the presence of propanolol requires information on conformational changes in the protein structure. The secondary structure of proteins molecules can be determined by circular

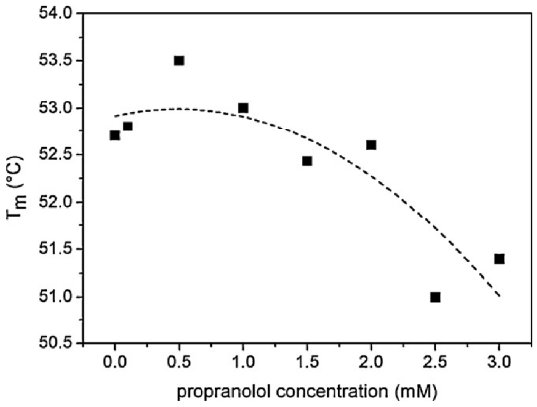

Fig. 2. Fibrinogen first unfolding temperature (T_m) as a function of propranolol concentration.

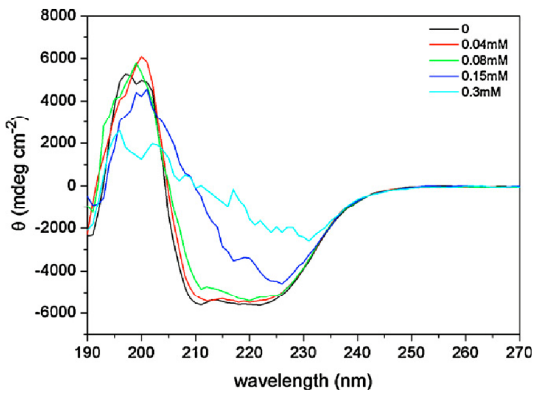

Fig. 3. Concentration dependence of the far-ultraviolet CD spectra of fibrinogen at 25 °C.

dichroism spectroscopy. This technique allows one to obtain information on the effect of the binding of different ligands [35,36] on the conformation of the protein structure. Fig. 3 shows typical UV–CD spectra of pure fibrinogen and fibrinogen in the presence of increasing concentrations of propranolol. In agreement with the reported results of Razumovsky and coworkers [37] native fibrinogen shows a range of secondary structures (Fig. 3) interpreted as 42% α-helix, 7% β-sheets, 20% β-turn and 30.8% random coil. The effect of propanolol on the secondary structure is very clear: importantly increasing propanolol decreased the height of the peak at ~200 nm and decreased the depth of the trough at ~220 nm (Figure 3). Accordingly, the drug diminished the α-helix and β-sheet content with the effect becoming more pronounced as the concentration of propanolol increased in the mixture. Based on the CD spectra we have determined how the α-helix and β-sheet content of FB and FB/propranolol mixtures (Fig. 4) varied at different temperatures (25, 40, 60 and 95 °C). All the measurements were made at low concentrations of propanolol below the cmc (Fig. 1). At 25 and 40 °C, when fibrinogen is the native state (completely folded), the changes induced by propanolol in the secondary structure are only noticeable for drug concentrations above 0.05 mM. However, at both 70 and 95 °C, the percentage of secondary structure clearly decreases at very low concentrations of drug. The backbone hydrogen bonds of the α-helix are generally slightly weaker than those found in β-sheets regions. Thus, they are more easily affected by the surrounding molecules. However, in the case of fibrinogen, both α-helix and β-sheet regions exhibit changes with added drug molecules. Similar conclusions have been obtained by comparing the adsorption of β-endorphin and epinephrine to the different domains of the fibrinogen through electrostatic, polar, and hydrophobic interactions, resulting in protein unfolding which may in turn expose the receptor induced binding sites [38].

3.3. Dynamic light scattering

The effect of propanolol on the size of fibrinogen was monitored at different drug concentration by dynamic light scattering (Fig. 5). The size of one molecule of fibrinogen is 45 nm × 5 nm as reported by Weisel and coworkers [39].

For the typical light scattering setup with $\lambda = 488$ nm (or greater), 90°, in water ($n = 1.33$) one needs 125 nm to observe the

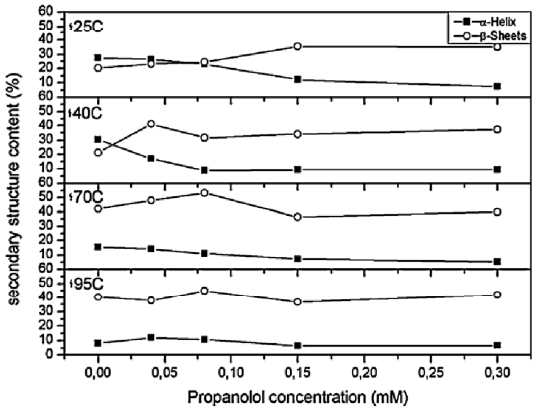

Fig. 4. Contents (in %) of the α-helix (■) and β-sheets (○) elements in fibrinogen as a function of Propranolol concentration at different temperatures. Estimated uncertainties in α helix and β sheets content were ⊥3%.

terms dependent on the rotational diffusion coefficient. There must be a significant separation in the decay rates. A difference of a factor of 2 in diffusion coefficient (or radius) is probably close to the limit of resolution of the technique. If the particle is nonspherical, then Rh is often referred to as the apparent hydrodynamic radius. Our results for pure fibrinogen (Fig. 5) show two peaks with hydrodynamic diameters of 10 and 42 nm at 25 °C. Thus, on the basis or our equipment setup and protein size, the terms dependent on the rotational diffusion coefficient is neglected. Also due to the significant separation between the two modes, an apparent hydrodynamic radius can be associated with each peak [40].

Configurations of the FB structures can be inferring, from the hydrodrodynamic radii measurements, following the analysis performed by Wasilewska et al. [41] using the Brenner theory. These authors have obtained a single R_h of 12 nm at pH 9.5, based on the above theory the most probable configuration is an individual FB protein that can be approximated by a cylinder of the 80 nm length bent to the form resembling roughly a semicircle. Consequently, the 10 nm peak could represent individual fibrinogen molecules of the

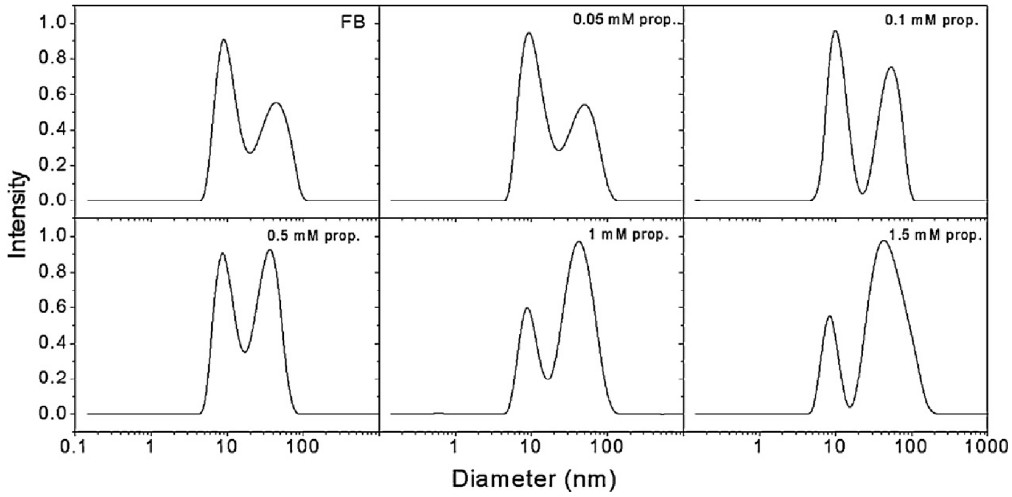

Fig. 5. Size distribution for fibrinogen 0.5 g l^{-1} and at different propranolol concentration.

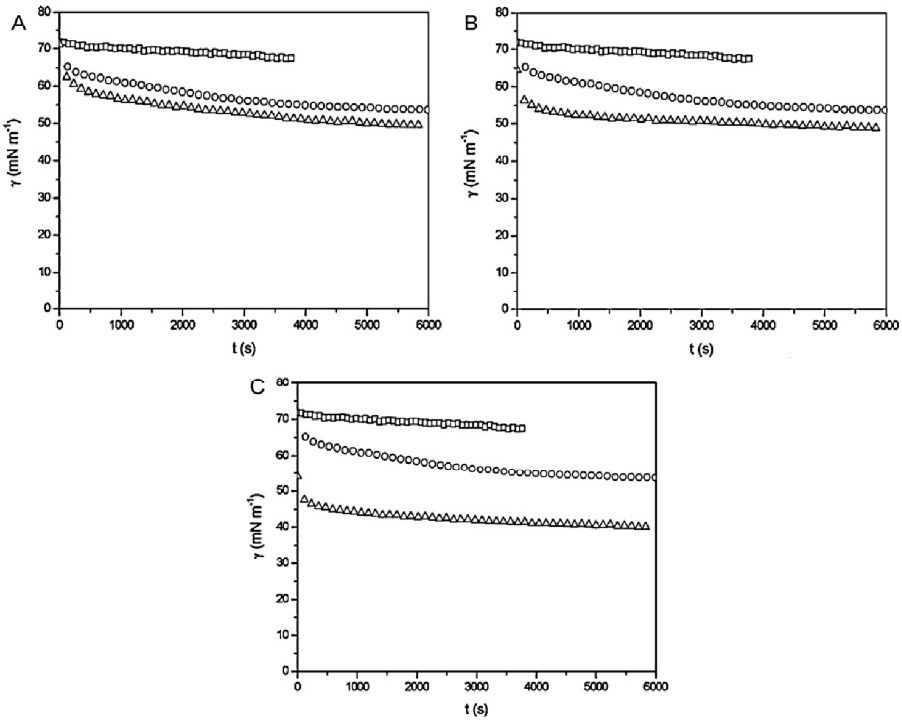

Fig. 6. Surface Tension at the air/water interface of: (A) FB 1 g l^{-1} (○), propranolol 0.05 mM (□), FB/propranolol 0.05 mM (△), (B) FB 1 g l^{-1} (○), propranolol 1 mM (□), FB/propranolol 1 mM (□), (C) FB 1 g^{-1} l (○), propranolol 5 mM (□), FB/propranolol 5 mM ().

64 nm length bent to the form resembling a semicircle. The value of the length bent observed is related, somehow, with the rupture of the electrostatic bridge between αC arms and the E domain. It has been found in previous studies that these domains are easily trimmed away [42]. Meanwhile, for the peak placed at 42 nm the structure is approximated by the same structure but with 228 nm length. This larger diffusive mode likely represents a significantly larger aggregation state involving several FB molecules. Based on the fibrinogen structure and net charge distribution, it could be reasonable to assume that such structure arises from electrostatic interaction between the positive αC domains of one molecule and the negative D and E domains of the other.

The presence of propanolol affects differently both populations. The second peak (centered at 42 nm) is displaced slightly to higher diameters up to a maximum of 54 nm (293 nm length bent) at a concentration of propranolol of 1 mM. For higher concentrations of propranolol this peak decreases to the initial values. Differently, the position of the first peak (centered at 10 nm) remains practically invariant throughout the range of concentration studied. Nevertheless, the weight of the first peak decreases importantly as the concentration of propanolol increases. Simultaneously, the weight of the second peak increases with the amount of drug. This increase is related to both the increase in the number of aggregates and the rise in the length of the same. In this sense, also electrostatic interaction could be responsible for the initial interaction between negative areas of the proteins and the positive charge of propranolol, very probably with the movable flap of two negatively charged amino acids (Gluβ397 and Aspβ398) with side chains pinned back to the coiled coil [43].

3.4. Surface tension measurements

In order to gain more insight into the effect on propanolol on the properties of FB, we have investigated the surface tension of the mixed systems compared to that of pure FB. In particular, we have investigated the effect of an increasing concentration of propanolol on the surface tension of a solution of fibrinogen (1 g l^{-1}). Fig. 6

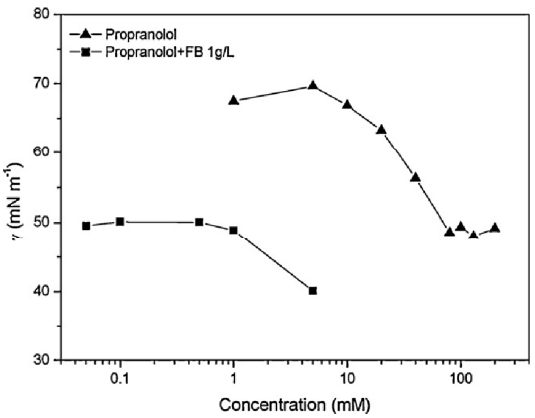

Fig. 7. Surface Tension of fibrinogen and FB/propranolol mixtures at different concentrations.

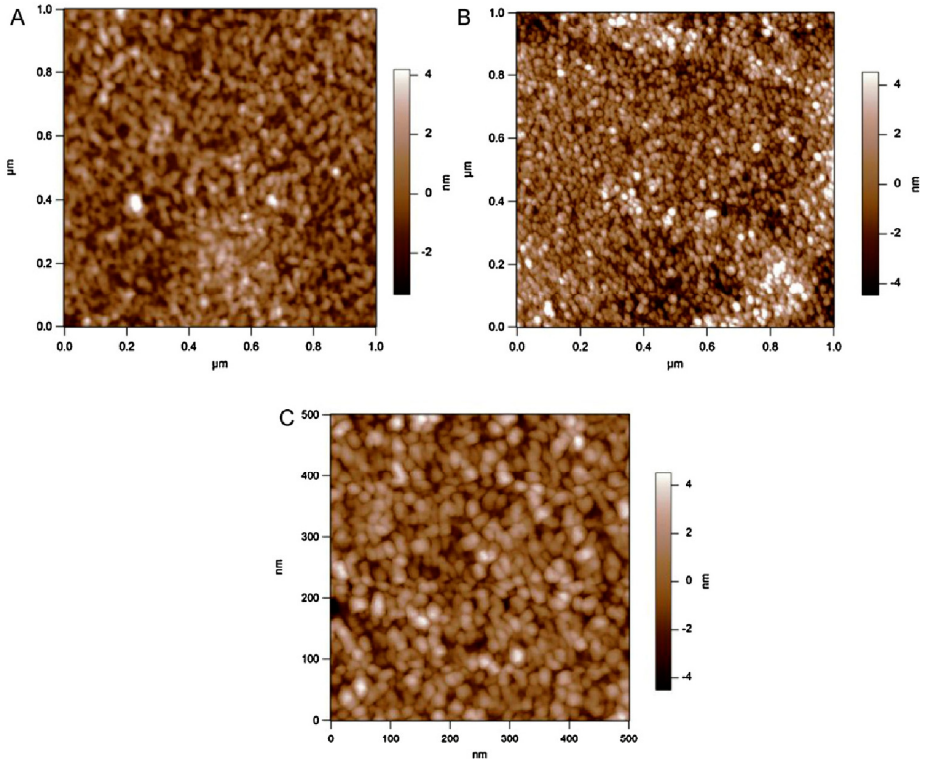

Fig. 8. Topography AFM image of: (A) spread native fibrinogen LB film at the air–water interface: scan size 1 μm × 1 μm, (B) spread FB/propranolol 1 mM LB film at the air–water interface: scan size 1 μm × 1 μm, (C) spread FB/propranolol 1 mM LB film at the air–water interface: scan size 500 μm × 500 μm.

shows the dynamic surface tension curves of fibrinogen (1 g l^{-1}), pure propanolol and fibrinogen/propranolol mixtures. It can be seen that the presence of propanolol causes a remarkable change in the surface tension of the pure protein, even if the concentration of propanolol used in the mixture does not affect the surface tension on its own (Fig. 6). In fact, we could not use higher concentrations of propanolol since the system precipitated above 10 mM of propranolol. Still, the presence of propanolol has strong synergistic effect on the surface tension of the protein resulting in an increased surface activity of the mixed system. This could be due to the formation of complexes of enhanced surface activity, to an overall enhancement of the adsorbed amount or to a further contribution of the FB to the surface tension due to propanolol-induced surface denaturation [44,45]. Literature studies support the idea that surfactants can displace protein from the surface at sufficiently high concentrations of surfactant in the system. Once the surface tension of the mixed systems overcomes that of the pure surfactant, the surfactant dominates and the surface tension of the system tends to that of the pure surfactant [46–48]. However, this is not the same as the situation seen in Fig. 6. In the case of propanolol, the surface tension of the mixed system differs significantly from that of the pure surfactant (Fig. 6). Moreover, there was no surface activity of the propanolol at the concentrations used (Fig. 6). Accordingly, the origin of the substantial enhancement of the surface activity of FB is most probably due to a conformational change of the protein induced by the drug. This is consistent with the CD results in which the percentage secondary structure of FB decreases in the presence of similar concentrations of propanolol. Increased unfolding of the protein molecule can result in a lower surface tension.

Consider now the final surface tension attained by the pure propanolol and that of the mixtures with FB. Fig. 7 shows the surface tension isotherms of the pure propranolol as compared to the mixture with fibrinogen (1 g l^{-1}). From the pure surfactant curve we can estimate the cmc of propranolol at a value of 128 ± 1 mmol l^{-1} in agreement with literature results [49]. The surface tension isotherm of the mixed FB/propanolol systems clearly reflects the extreme synergistic effect discussed above in terms of the dynamic curves. The surface tension of the mixture decreases steeply even with very low concentrations of propanolol in the mixture. The surface tension of the mixture overcomes the minimum surface tension attained by pure propanolol at drug concentrations in the mixture well before its cmc. This behavior again points towards a conformational change undergone by the protein induced by propanolol, which results in a lower surface tension attained by the mixed solution.

3.5. AFM imaging

Fig. 8 shows AFM images of FB and FB/propranolol mixture. Images were taken following transfer of spread layers at the air–water interface onto freshly cleaved mica using the Langmuir Blodgett technique. In the case of native fibrinogen (Fig. 8A) individual molecules and small clusters can be observed. In view of the size, these are probably formed by two or three molecules mainly (each molecule of fibrinogen has a size of 45 nm × 5 nm). The adsorption of proteins is the net result of various types of interactions which depend on the nature of the protein, the surface and the aqueous solution. Fig. 8B and C shows the mixed FB/propranolol system.

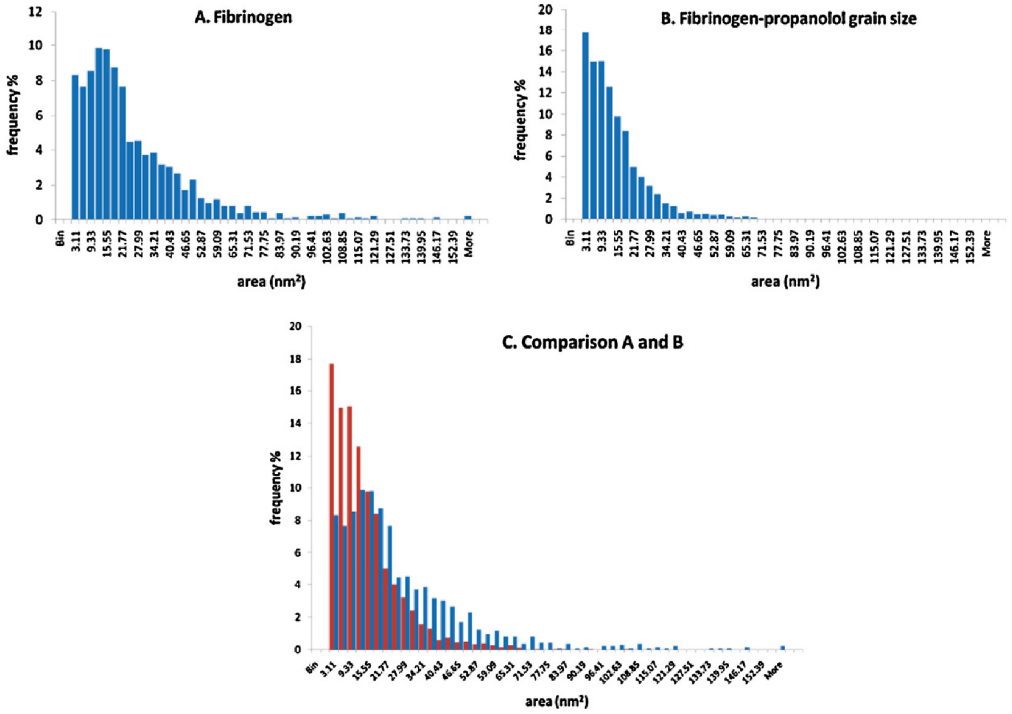

Fig. 9. Grain size analysis of AFM images for: (A) Fibrinogen, (B) fibrinogen–propranolol and (C) A and B together.

The image shows clear differences with respect to that of pure FB. The structures appear to be more associated into larger aggregate structures on the surface in the case of the FB–propanolol mixed system and the surface layer appears to be much more compact. The appearance of the surface layer for the mixed system (Fig. 8B and C) suggests an enhancement of the adsorption process with a greater coverage of the interface. A grain size analysis was performed on the AFM images to quantify the differences in the images obtained for the FB and FB–propranolol images. The data obtained is shown in Fig. 9. The effect of the addition of the propranolol is seen to reduce the mean grain size and to narrow the distribution of grain sizes. Measurement of rms roughness data yield average values of 1.05 nm and 1.66 nm for the FB and FB–propranolol samples suggesting that the FB–propranolol structures are taller than the FB structures. Together these data suggest that the propranolol makes the FB structures more compact allowing the molecules to pack more densely on the surface. The AFM images thus complement the surface tension data shown above. An increase in the number of molecules adsorbed per unit area would result in a lower surface tension for the mixed system. Accordingly, the positive synergism seen in Figs. 6 and 7 is due to a higher surface concentration of FB molecules in the presence of propranolol. Possibly, the origin of this effect is found in a conformational change induced in the FB by propranolol which increases the hydrophobicity of the protein. As a result, the surface activity of the protein improves, and the surface concentration of proteins increases, thus decreasing the surface tension.

4. Conclusions

In this study, we have characterized the interactions and complexation between fibrinogen and propranolol. The results obtained are summarized as follow. First of all, propranolol plays two opposite roles on thermal structural stability of fibrinogen, acting as structure stabilizer and destabilizer, at low and higher molar concentrations respectively. Complexation between fibrinogen and propranolol results in changes in the secondary structure of the protein. This event increase the surface activity of the complex as surface tension measurements have demonstrated. Based on DLS measurements two size distribution have been found: the ~10 nm distribution represent individual fibrinogen proteins and the larger diffusive mode ~45 nm likely represents a significantly larger aggregation state involving several proteins. The addition of propranolol just affects the larger one, which increases in size. AFM images have corroborated that the fibrinogen–propranolol structures are taller than the fibrinogen structures. This enlargement has been attributed to the rupture of the electrostatic bridge between αC arms and the central E domain. Also, the AFM images of fibrinogen and fibrinogen–propranolol films suggest that the effect of the propranolol is to change the conformation of the protein leading to a more compact structure which packs more efficiently onto the interface lowering the surface tension more than the fibrinogen alone. Considering the obtained information, this kind of research on plasma proteins and drug complexation has a promising future developing in better drug delivery systems.

Acknowledgements

The authors thank the Xunta de Galicia for their financial support (project no. 10PXIB206258PR). J. M. V. thanks MICINN (JCI-2009-03823) and EU (FP7-PEOPLE-PERG07-GA-2010-268315). Research at IFR was supported by the BBSRC core strategic grant. N. H. thanks E.U. for LLP/Erasmus Programme Grant.

References

[1] L. Cheng, D. Cao, Langmuir 25 (2009) 2749.
[2] K. Ariga, J.P. Hill, M.V. Lee, A. Vinu, R. Charvet, S. Acharya, Sci.Technol. Adv. Mater. 9 (2008) 14109.
[3] J.T. Davis, G.P. Spada, Chem. Soc. Rev. 36 (2007) 296.
[4] S. Schreier, S.V.P. Malheiros, E. Paula, Biochim. Biophys. Acta 1508 (2000) 210.
[5] X. Li-Chong, C.A. Siedlecki, Langmuir 25 (2009) 3675.
[6] V.P. Zhdanor, B. Kasemo, Biophys. Chem. 146 (2010) 60.
[7] R. Miller, V.B. Fainerman, A.V. Makievski, J. Krägel, D.O. Grigoriev, V.N. Kazakov, O.V. Sinyachenko, Adv. Colloid Interface Sci. 86 (2000) 39.
[8] O. Joshi, H.J. Lee, J. McGuire, P. Finneran, K.E. Bird, Colloids Surf. B 50 (2006) 26.
[9] J. Maldonado-Valderrama, J.M. Rodríguez Patino, Curr. Opin. Colloid Interface Sci. 15 (2010) 271.
[10] R. Lua, A. Caoa, L. Lai, J. Xiao, Colloids Surf. B: Biointerface 64 (2008) 98.
[11] D. Zhong, A. Douhal, A.H. Zewail, Proc. Natl. Acad. Sci. U.S.A. 19 (2000) 14056.
[12] P. Messina, G. Pieto, V. Dodero, J.M. Ruso, P. Schulz, F. Sarmiento, Biopolymers 79 (2005) 300.
[13] J.M. Ruso, N. Deo, P. Somasundaran, Langmuir 20 (2004) 8988.
[14] J.M. Ruso, P. Taboada, P. Martinez-Landeira, G. Pieto, F. Sarmiento, J. Phys. Chem. B 105 (2001) 2644.
[15] J.M. Ruso, D. Attwood, M. García, P. Taboada, L.M. Varela, V. Mosquera, Langmuir 17 (2001) 5189.
[16] P. Martínez-Landeira, J.M. Ruso, G. Pieto, F. Sarmiento, M.N. Jones, Langmuir 18 (2002) 3300.
[17] D. Hellenbrecht, B. Lemmer, G. Wiethold, H. Grobecker, Naunyn-Schmiedeberg's Arch. Pharmacol. 277 (1973) 211.
[18] P. Cacciafesta, A.D.L. Humphris, K.D. Jandt, M.J. Miles, Langmuir 16 (2000) 8167.
[19] T.S. Tsapikouni, Y.F. Missirlis, Colloid Surf. B 57 (2007) 89.
[20] B.A. Holm, G. Enhorning, R.H. Notter, Chem. Phys. Lipid 49 (1988) 49.
[21] C. Yin, C. Chang, Langmuir 22 (2006) 6629.
[22] I. Van De Keere, R. Willaert, A. Hubin, J. Vereecken, Langmuir 24 (2008) 1844.
[23] K.L. Marchin, C.L. Berrie, Langmuir 19 (2003) 9883.
[24] C. Yongli, Z. Xiufang, G. Yandao, Z. Nanming, Z. Tingying, S. Xinqi, J. Colloid Interface Sci. 214 (1999) 38.
[25] T.C. Ta, M.T. Sykes, M.T. McDermott, Langmuir 14 (1998) 2435.
[26] J.H. Brown, N. Volkmann, G. Jun, A.H. Henschen-Edman, C. Cohen, Proc. Natl. Acad. Sci. U.S.A. 97 (2000) 85.
[27] S. Yakovlev, L. Medved, Biochemistry 48 (2009) 5171.
[28] (a) A. Lobley, L. Whitmore, B.A. Wallace, DICHROWEB: an interactive website for the analysis of protein secondary structure from circular dichroism spectra, Bioinformatics 18 (2002) 211;
(b) L. Whitmore, B.A. Wallace, DICHROWEB, an online server for protein secondary structure analyses from circular dichroism spectroscopic data, Nucleic Acids Res. 32 (2004) W668.
[29] (a) P.L. Privalov, L.V. Medev, J. Mol. Biol. 159 (1982) 665;
(b) J.W. Donovan, E. Mihalyi, Proc. Natl. Acad. Sci. U.S.A. 71 (1974) 4125.
[30] E. Blanco, J.M. Ruso, J. Sabín, G. Prieto, F. Sarmiento, J. Therm. Anal. Calorim. 87 (2007) 211.
[31] S. Deep, J.C. Ahluwalia, Phys. Chem. Chem. Phys. 3 (2001) 4583.
[32] E. Blanco, J.M. Ruso, G. Prieto, F. Sarmiento, J. Phys. Chem. B 111 (2007) 2113.
[33] A.W.P. Vermeer, W. Norde, Colloid Surf. A 161 (2000) 139.
[34] E.P. Vieira, H. Hermes, H. Möhwald, Biochim. Biophys. Acta 1645 (2003) 6.
[35] R.W. Woody, Methods Enzymol. 246 (1995) 34.
[36] F.X. Schmid, in: T.E. Creighton (Ed.), Protein Structure: A Practical Approach, IRL Press, Oxford, 1989.
[37] L. Razumovsky, S. Damodaran, Langmuir 15 (1999) 1392.
[38] R. Barbucci, S. Lamponi, A. Magnani, Biomacromolecules 4 (2003) 1506.
[39] J.W. Weisel, C.V. Stauffacher, E. Bullitt, C. Cohen, Science (1985) 1388.
[40] R. Flambergt, Pecora, J. Phys. Chem. 88 (1984) 3026.
[41] M. Wasilewska, Z. Adamczyk, B. Jachimska, Langmuir 25 (2009) 3698.
[42] Z. Yang, I. Mochalkin, L. Veerapandian, M. Riley, R.F. Doolittle, Proc. Natl. Acad. Sci. U.S.A. 97 (2000) 3907.
[43] M.S. Kostelansky, L. Betts, O.V. Gorkun, S.T. Lord, Biochemistry 41 (2002) 12124.
[44] T. Croguennec, A. Renault, S. Bouhallab, S. Pezennec, J. Colloid Interface Sci. 302 (2006) 32.
[45] T. Croguennec, A. Renault, S. Beaufils, J.J. Dubois, S. Pezennec, J. Colloid Interface Sci. 315 (2007) 627.
[46] J. Maldonado-Valderrama, A. Martin-Molina, A. Martin-Rodriguez, M.A. Cabrerizo-Vílchez, M.J. Gálvez-Ruiz, D. Langevin, J. Phys. Chem. C 111 (2007) 2715.
[47] T.L. Phang, S.J. McClellan, E.I. Franses, Langmuir 21 (2005) 10140.
[48] S.H. Kim, E.I. Franses, J. Colloid Interface Sci. 295 (2006) 84.
[49] V. Mosquera, J.M. Ruso, D. Attwood, M.J. Malcolm, G. Prieto, F. Sarmiento, J. Colloid Interface. Sci. 210 (1999) 97.

Journal of Colloid and Interface Science 362 (2011) 118–126

Contents lists available at ScienceDirect

Journal of Colloid and Interface Science

www.elsevier.com/locate/jcis

Fibrinogen stability under surfactant interaction

Natalia Hassan [a], Leandro R.S. Barbosa [b], Rosangela Itri [b,*], Juan M. Ruso [a,*]

[a] Soft Matter and Molecular Biophysics Group, Department of Applied Physics, University of Santiago de Compostela, Campus Vida s/n, 15782 Santiago de Compostela, Spain
[b] Instituto de Física, Universidade de Sao Paulo, Cx. Postal 66318, CEP 05315-970, Sao Paulo, SP, Brazil

ARTICLE INFO

Article history:
Received 9 March 2011
Accepted 2 June 2011
Available online 15 June 2011

Keywords:
Fibrinogen
Fluorinated
Hydrogenated
DSC
SAXS

ABSTRACT

Differential scanning calorimetry (DSC), circular dichroism (CD), difference spectroscopy (UV–vis), Raman spectroscopy, and small-angle X-ray scattering (SAXS) measurements have been performed in the present work to provide a quantitatively comprehensive physicochemical description of the complexation between bovine fibrinogen and the sodium perfluorooctanoate, sodium octanoate, and sodium dodecanoate in glycine buffer (pH 8.5). It has been found that sodium octanoate and dodecanoate act as fibrinogen destabilizer. Meanwhile, sodium perfluorooctanoate acts as a structure stabilizer at low molar concentration and as a destabilizer at high molar concentration. Fibrinogen's secondary structure is affected by all three studied surfactants (decrease in α-helix and an increase in β-sheet content) to a different extent. DSC and UV–vis revealed the existence of intermediate states in the thermal unfolding process of fibrinogen. In addition, SAXS data analysis showed that pure fibrinogen adopts a paired-dimer structure in solution. Such a structure is unaltered by sodium octanoate and perfluorooctanoate. However, interaction of sodium dodecanoate with the fibrinogen affects the protein conformation leading to a complex formation. Taken together, all results evidence that both surfactant hydrophobicity and tail length mediate the fibrinogen stability upon interaction.

1. Introduction

In the last decade, a significant amount of different proteins have been applied to several nanotechnology applications as biomimetic materials, tissue engineering, printing of proteins, drug delivery, bioelectronics and nanoparticle patterning [1–3]. Certainly, the interactions between small molecules with proteins affect their respective biological functions and determine their stability in solution with respect to aggregation, liquefaction, and other phase transformations. Furthermore, the pathways of protein aggregation, crystal formation, folding, or unfolding are largely defined by the forces acting between the molecules [4]. The understanding of molecular recognition in protein–ligand complexes is crucial to better comprehend the associated biological function and of practical importance in the discovery, for instance, of new drugs. The weak, noncovalent interactions (hydrophobic, electrostatic, van der Waals, and hydrogen bonding) govern the ligand-binding process. Elucidating the role of these interactions concomitantly with the involved time scales must provide insights into the mechanism of molecular recognition and the role of binding cooperativity in the protein dynamics [5].

Fibrinogen is a complex multidomain protein whose major function is to form fibrin clots that prevent the loss of blood upon vascular injury. Bovine fibrinogen (340 kDa) is a 45-nm-long (with an approximate diameter of 5 nm) disulfide-linked dimer of three nonidentical polypeptide chains, Aα, Bβ, and γ. The NH_2 terminal portions of the six chains are linked together in the central region of the molecule by 11 disulfide bonds forming a small globular domain, the so-called disulfide knot, in the center [6,7]. The C-termini of each of the three chains end in globular domains, and those of the Bβ and γ chains are located at the ends of the molecule. Cleavages in all three chains then yield two D domains and one E domain. The E domain consists of the NH_2 terminal regions of α-, β-, and γ-chains chains held together by disulfide bonds. The majority of the D region is formed by the C-terminal portions of the β- and γ-chains folded into similar structures. The COOH-terminal portion of each fibrinogen Aα chain forms a compact αC domain attached to the bulk of the molecule with a flexible αC-connector (see Fibrinogen Scheme 1).

In addition, fibrinogen shows a unique characteristic in its folding. According to the current view, in fibrinogen, two αC-domains interact intramolecularly with each other and with the central region of the molecule, while in fibrin, they switch to an intermolecular interaction to form αC-polymers. This structural organization involves fibrinogen in fibrin assembly process and promotes cell adhesion and migration through their RGD sequences [8].

Contemporary studies have been centered on the use of fibrinogen for nonviral vector delivery [9], scaffolds [10], and

* Corresponding authors.
E-mail addresses: itri@if.usp.br (R. Itri), juanm.ruso@usc.es (J.M. Ruso).

0021-9797/$ - see front matter © 2011 Elsevier Inc. All rights reserved.
doi:10.1016/j.jcis.2011.06.010

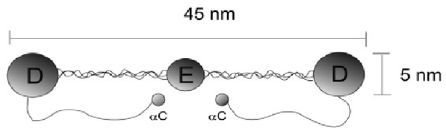

Scheme 1. Fibrinogen scheme.

biocompatibility studies [11,12]. Despite the very interesting applications of this protein, its interaction with small molecules as surfactants has not been exploited yet. It is well known that surfactants can denature proteins at smaller molar ratio than that required by weakly binding chemical denaturants such as guanidinium chloride or urea. Even the binding of a restrict number of surfactant molecules can induce substantial conformational changes, since the surfactants can wedge themselves into the interior of the protein. Structural studies of proteins interacting with surfactants at sub-denaturation concentrations reveal that the high affinity is achieved by a combination of electrostatic and hydrophobic interactions. As a rule, most proteins follow the same sequence of binding events: initial interaction between surfactants [13] and proteins, partial unfold, exposing of more binding sites, and subsequent expansion of the polypeptide chain. However, the exact number of binding events and associated conformational changes will depend on the structure and amino acid composition of the protein in question [14–16].

We have focused our research on the interactions between proteins and surfactants with a view of better understanding the mechanisms that are responsible for the adsorption of amphiphile molecules to biopolymers [15,17]. In particular, fluorinated surfactants are considered less denaturing for proteins than their hydrocarbon-base counterparts [18]. Understanding the possible interactions that occur between fluorinated surfactants and proteins can be helpful to guide the design of new systems for gel electrophoresis applications [16]. Recently, the interaction between such surfactants and proteins has also received great attention because it has been shown that fluorinated surfactants can control the insertion of pore-forming proteins in lipid membranes [19]. In this way, it is very important to explore and to understand the physicochemical properties of hydrocarbon/fluorocarbon surfactant in the presence of proteins.

In this sense, the current work is undertaken to investigate the stability, interactions, and possible conformational changes in bovine fibrinogen in the presence of different surfactants. Sodium perfluorooctanoate, sodium octanoate, and sodium dodecanoate have been chosen because their solution properties have been widely characterized in previous works. Furthermore, these surfactants allow us to compare the differences between hydrocarbon and fluorocarbon surfactants with the same alkyl chain with those where the hydrocarbon chain is 1.5 times longer than the fluorocarbon chain. (It is well known that in this relation both surfactants have similar critical micellar concentration, 27 mM and 30 mM for sodium dodecanoate and sodium perfluorooctanoate, respectively, whereas cmc = 380 mM for sodium octanoate [20]). To this end, we made use of differential scanning calorimetry to get insight into thermodynamic parameters, absorbance spectroscopy, and circular dichroism to infer about changes in the protein secondary structure as well as small-angle X-ray scattering to have information on protein conformational changes. Interestingly, we observed that sodium octanoate and perfluorooctanoate do not affect the fibrinogen conformation. Such findings could be of interest for applications in biomaterial science where devices should be created with improved hemocompatibility.

2. Materials and methods

2.1. Materials

Bovine plasma fibrinogen, fraction I, type IV, was purchased from Sigma and used without purification. Sodium octanoate (C_8HONa) and sodium perfluorooctanoate (C_8FONa) were obtained from Lancaster Synthesis Ltd. Sodium dodecanoate ($C_{12}HONa$) with purity over 99% was obtained from Sigma Chemical Co. The buffer solution consisted of 50 mN glycine and adjusted sodium hydroxide to give a pH value of 8.5. Samples were prepared within 2 h prior to usage. All chemical reagents were of analytical grade, and solutions were made using doubly distilled and degassed water.

2.2. Differential scanning calorimetry

Differential scanning calorimetry (DSC) measurements were taken using a VP-DSC (MicroCal Inc., Northampton, MA) calorimeter with 0.542 ml twin cells for the reference and sample solutions. Prior to the DSC experiments, the samples and the references were degassed under vacuum while being stirred. Thermograms were recorded between 20 and 110 °C at a scan rate of 60 °C per hour. Each experiment was conducted in triplicate to check the reproducibility. The baseline reference, obtained with both cells filled with buffer, was subtracted from the thermograms of the samples. The heat capacity curves were evaluated using the MicroCal Origin 7.0 software provided with the equipment to obtain ΔH and T_m values.

2.3. Difference spectroscopy

Difference spectra were measured using a Beckman spectrophotometer (model DU 640), with six microcuvettes, which operates in the UV–vis region. All measurements were taken using fibrinogen solutions with a fixed concentration of 0.5 g dm^{-3} in carefully matched quartz cuvettes (50 μl capacity). For absorbance difference spectra, just two cells were used. The first microcuvette containing just protein in the buffer solution was used as a blank reference; meanwhile, the other one was filled with fibrinogen in the presence of surfactant solution. The microcuvettes were then placed in the same orientation for all the tests. Measurements were taken under the condition that protein and surfactant had been incubated for over 2 h, after which the difference spectra did not change. For absorbance measurements with varying temperature, a Beckman (DU Series) temperature controller was used, following the Peltier methods of controlling temperature, in the range of 25–80 °C.

2.4. Circular dichroism

Far UV circular dichroism (CD) spectra were obtained using a JASCO-715 automatic recording spectropolarimeter (Japan) with a JASCO PTC-343 Peltier-type thermostated cell holder. Quartz cuvettes with 0.2-cm pathlength were used. CD spectra of pure fibrinogen and fibrinogen-surfactants dilute solutions were recorded from 190 to 270 nm. Protein concentration was 0.5 g dm^{-3}, and surfactant concentrations varied from 1 to 10 mM. The following setting was used: resolution, 1 nm; bandwidth, 1 nm; sensitivity, 50 mdeg; response time, 8 s; accumulation, 3; and scan rate 50 nm/min. Corresponding absorbance contributions from buffer solution was subtracted with the same instrumental parameters. Data are reported as molar ellipticity and determined as

$$[\theta]_\lambda = \frac{\theta_\lambda M_r}{NcI} \quad (1)$$

where c is the protein concentration, l is the pathlength of the cell, $[\theta]_\lambda$ is the measured ellipticity at a wavelength λ, M_r is the molecular mass of the protein, and N is the number of residues. The secondary structure content was analyzed by Dichroweb program [21] using CONTIN algorithm.

2.5. Raman spectroscopy

The Raman scattering measurements were taken using a Raman microprobe instrument consisting of a Jobin–Yvon T64000 spectrometer equipped with a microscope, which allows a spatial resolution on the sample of about 1 μm. The Raman signal was detected by a multichannel CCD detector cooled with liquid nitrogen. Raman spectra over the whole optical frequency range were recorded using the subtractive configuration of the spectrometer, with a spectral resolution of about 2 cm^{-1}. To improve the resolution of closely spaced peaks, high-resolution scans of some frequency regions were recorded using the triple additive configuration, with a spectral resolution better than 1 cm^{-1}. The light was collected in backscattering geometry through an objective of numerical aperture 0.95. The 785 nm line of an Ar^+ laser was used as excitation, focused on a spot of ≈1 μm in diameter, with an incident power on the sample of ≈2 mW.

2.6. Small-angle X-ray scattering (SAXS)

The experiments were performed in a commercially available NanoStar small-angle X-ray instrument (Bruker AXS) with Cu $K\alpha_1$ radiation ($\lambda = 1.54$ Å), sample-to-detector distance of ~650 mm. The scattering data were collected by a two-dimensional position sensitive gas detector (HiSTAR) over a scattering vector of q ($=(4\pi\sin\theta)/\lambda$, being 2θ the scattering angle) ranging from $q_{min} = 0.013$ Å $^{-1}$ to $q_{max} = 0.33$ Å $^{-1}$. The q_{min} value allowed us to determine the macromolecules' maximum dimension, D_{max}, of ca. 480 Å ($D_{max} = 2\pi/q_{min}$) that is compatible to FB longest axis, and q_{max} allowed us to monitor the micelles' formation concomitantly. Samples were conditioned in glass capillaries with 2.0 mm inner-diameter, perpendicular to the incident X-ray beam. Data collection took from 2 to 4 h, according to protein concentration. No radiation damage was observed. The obtained scattering curves were corrected for buffer scattering and sample attenuation.

It is well known that the scattering intensity from a set of monodisperse particles randomly distributed is given by [22]

$$I(q) = \gamma n_p P(q) S_M(q) \quad (2)$$

where γ is a calibration factor related to the experimental setup and n_p corresponds to the particle number density. $P(q)$ is the scattering particle form factor that depends on the electron density contrast between the particle and the surrounding medium, and $S_M(q)$ is the so-called 'measured' structure factor, which is equal to 1 for noninteracting particles. In the current work, we made use of the human fibrinogen crystallographic structure (code: 3GHG from PDB website) to calculate the protein form factor $P(q)$ by Monte Carlo simulations (MCS), as previously described [22].

Concerning micellar aggregates in solution, $P(q)$ was calculated supposing that the micelle resembles small prolate ellipsoids [23]. In this way, the ellipsoid shortest semi-axis is on the order of paraffinic chain length, R_{par}, whereas the largest semi-axis is νR_{par}, with ν equal to the micellar axial ratio. The model assumes that the micelle is constituted by two shells of different electron densities: an inner core of paraffinic moiety, with electron density ρ_{par}, and an external shell, surrounding the core, with a respective polar headgroup thickness σ that includes the hydration water and with electron density ρ_{pol}, relative to the continuous medium (buffer solution with electron density similar to that of water $\rho_w = 0.334$ e/Å^3). $S_M(q)$ function was modeled according to the well-known *Mean Spherical Approximation* (MSA) [24]. In this methodology, the micelles are treated as charged spheres interacting through a screened-Coulomb potential (the repulsive contribution of the DLVO potential). The fitting parameters of such procedure are: the amount of charges on the micelle surface (ionization coefficient, α) and the effective diameter of the sphere. Details of this methodology can be found elsewhere [23].

For micelles interacting with fibrinogen, we analyzed the SAXS curve through the pair distribution function, $p(r)$, according to the procedure recently reported for protein complexes with sodium alkyl sulfates [16]. Such a function is a Fourier transform of the scattering intensity $I(q)$, which gives information about the scattering particle shape and maximum dimension [25]. In the case of micelles associated with polypeptide chains, it has been shown that three structural parameters can be retrieved directly from $p(r)$. These are the average length of the complex, the micelle radius, and the distance between neighboring micelles [16]. In this work, the $p(r)$ function was calculated by means of a generalized indirect Fourier transform (GIFT software) developed by Glatter et al. [26].

3. Results and discussion

3.1. DSC, CD, absorbance difference, and Raman spectroscopy: samples containing 0.5 g dm^{-3} of fibrinogen in the absence and presence of surfactant concentration below cmc

A first set of DSC experiments at different protein concentrations (from 0.1 to 4 g dm^{-3}) have been performed and revealed that the concentration does not influence on the main features of the thermograms. On the other hand, three thermograms were obtained from some samples at different scan-rates (45, 60 and 90 °C per hour) and showed that the temperature corresponding to the maximum heat capacity is scan-rate-dependent (from 52.58 to 53.32 °C for the lowest to the highest scan rate, respectively). This fact indicates that the fibrinogen denaturation process is kinetically controlled [27]. Therefore, we decided to perform the scans at 60 °C per hour.

A DSC scan of fibrinogen (0.5 g dm^{-3}) in buffer solution (glycine, pH 8.5) is shown in Fig. 1A. Three endothermic peaks can be observed. The narrow and symmetrical peaks located at 52.85 and 93.97 °C have been attributed to the denaturation of the end D and central E fragments of fibrinogen, respectively [28,29]. On the other hand, the small and broad peak at 76.62 °C has been related to the denaturation of the C-terminal of the Aα chains [27].

The reversibility of the transitions was checked by heating the samples in the calorimetric cell after cooling them down from the first run. Consecutive scans show no peaks because of total fibrinogen denaturation after heating. However, with the aim of investigating the reversibility of each endothermic peak, we performed distinct heating and cooling cycles as follows. Firstly, the sample was heated up to 60 °C, cooled down to room temperature, and reheated up to 110 °C (Fig. 1B-II). As one can see, the first peak disappeared showing the irreversibility of such a transition. Similarly, the other two calorimetric peaks also disappeared after heating and cooling processes as displayed in the Fig. 1B-III and IV. Consequently, all calorimetric peaks were found to be irreversible under temperature. Thus, only the first scan is shown for each studied sample.

The DSC thermograms from fibrinogen in the surfactant-containing solutions are shown in Fig. 2. In all studied systems, no reversibility was found as in the case of pure fibrinogen. The thermodynamic characteristics of the thermal denaturation, namely, melting temperatures (T_m, temperatures at which a maximum occurred in the endothermic peaks), calorimetric enthalpy

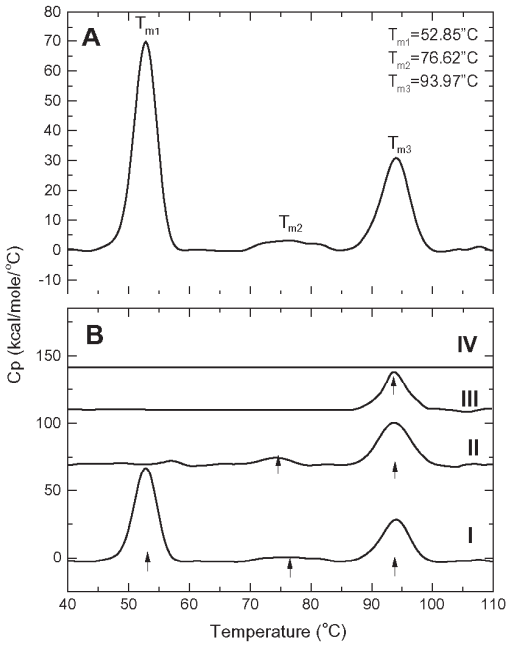

Fig. 1. (A) Heat capacity curve of fibrinogen (0.5 g dm $^{-3}$) in buffer solution, pH 8.5; (B) heat capacity curves of fibrinogen: (I) first scan; (II) heating up to 60 °C, cooled down, and heated up again; (III) heating up to 85 °C, cooled, and heated again; (IV) heating up to 98 °C, cooled, and heated again. The thermograms were vertically displaced for clarity.

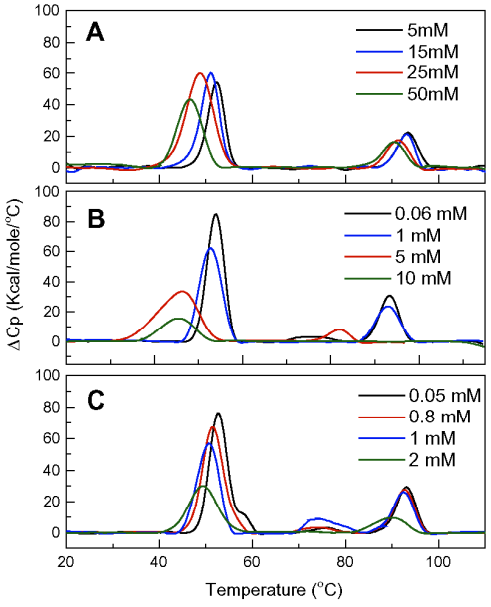

Fig. 2. DSC thermograms of fibrinogen (0.5 g dm $^{-3}$) in the presence of (A) C_8HONa, (B) C_8FONa, and (C) C_{12}HONa.

(ΔH), van't Hoff enthalpy (ΔH_v), and cooperativity (n, the ratio of calorimetric enthalpy to van't Hoff enthalpy) were obtained and listed in Table 1.

As one can note, with increasing hydrogenated surfactant concentration, endothermic peaks shift to lower temperatures or disappear as in the case of the second peak in respect to pure fibrinogen. Significant changes in the peaks features are induced by the highest surfactant concentrations. Regarding the effect of the fluorinated surfactant, the first endothermic peak shifts to higher temperatures up to 1 mM C_8FONa concentration (acting as a stabilizer), followed by a decrease in T_m afterwards. This behavior may be attributed to the effect of the CF_3 group on the hydration shell of the peptides. This fact has been interpreted on the basis that small amount of surfactants must induce a protective effect due to some binding function of the surfactant ions. In other words, the native conformation is stabilized by a cross-linking function of the surfactant between a group of nonpolar residues and a positively charged residue located on different loops of the protein [30]. The first peak thus becomes broader, and the second and third ones disappear when C_8FONa is present at high concentrations. Concomitantly, the heat capacity varies with surfactant concentration.

This first set of measurements points out a decrease in stability of fibrinogen with increase in the surfactant concentration. Such a fact has been previously observed in other systems; when surfactant concentration is increased, hydrophobic interactions become more dominant, and surfactant hydrophobic moieties will tend to penetrate into the hydrophobic domains of the protein in order to reduce their contacts with water. Thus, due to such a penetration, the protein may change its conformation somewhat, which results in a lower thermal stability [31].

Enthalpies of the protein thermal denaturation exhibit the highest values for the first peak, whereas values for the second are the lowest (Table 1). In the presence of C_8FONa and C_{12}HONa, these values tend to decrease with the surfactant concentration. However, with C_8HONa, such a behavior is only corroborated for the third peak. Comparing the values among the different systems, one can notice that the enthalpies increase in the order of C_8HONa < C_{12}HONa < C_8FONa.

Concerning cooperativity, n, it depends on a number of factors. When estimated values of van't Hoff enthalpy for a particular reaction are compared with enthalpy values obtained directly by calorimetric methods, substantial disagreement between both values often takes place. Such discrepancies have been suggested to indicate that unfolding is more complex than the simple one-to-one model used to describe the data. It has been noted that binding reactions can include the displacement of solvent and counterions, as well as other linked equilibria such as protonation or conformational changes. It has been suggested that calorimetric enthalpy includes these contributions, which are not observed in the van't Hoff method. This suggests that the van't Hoff enthalpy is the "intrinsic" binding heat, whereas the calorimetric enthalpy includes other concomitant reactions (i.e., linked equilibria). Thus, when $n > 1$, the unfolding is not a two-state process but involves unfolded intermediates or independent domains significantly populated. In the case of $n < 1$, this implies that the overall protein is not correctly folded (probably due to irreversible or aggregation effects). For all studied systems, one can conclude that $n > 1$ for the first peak and $n < 1$ for the second and third ones. This implies that one or more intermediate states are populated in the lowest temperature change, while denaturation at higher temperatures involves intermolecular cooperation [32].

In order to get more information about changes in the fibrinogen secondary structure, we have also performed measurements of circular dichroism and absorbance difference as described below.

Table 1
Thermodynamic parameters obtained from DSC thermograms of fibrinogen in the presence of C_8FONa, C_8HONa, and C_{12}HONa.

	T_m (°C)			ΔH (kcal/mol)			ΔH_v (kcal/mol)			Cooperativity		
	T_{m1}	T_{m2}	T_{m3}	ΔH_1	ΔH_2	ΔH_3	ΔH_{v1}	ΔH_{v2}	ΔH_{v3}	n_1	n_2	n_3
Surfactant-free	52.7	74.5	93.9	288.2	34.2	156.1	179.4	122.4	186.3	1.61	0.28	0.84
C_8FONa (mM)												
0.06	53.8	75.7	93.2	416.3	24.5	167.5	182.9	126.8	202.6	2.27	0.19	0.82
0.08	54.2	76.8	93.2	475.0	76.5	195.8	167.0	47.0	182.7	2.84	1.62	1.07
0.2	54.1	74.7	93.2	429.5	35.9	181.0	178.0	103.7	190.0	2.41	0.34	0.95
0.5	53.4		93.2	391.3		184.6	180.6		183.2	2.11		1.00
0.8	53.6		93.2	364.3		148.1	182.1		199.5	2.00		0.74
1	53.0		93.2	372.8		153.0	176.8		194.9	2.10		0.78
1.5	52.8		93.1	306.7		142.4	182.3		196.4	1.68		0.72
3	51.9		88.0	278.9		42.4	138.6		186.7	2.01		0.22
5	45.3		81.7	185.8		43.3	113.6		183.4	1.63		0.22
10	45.2			143.3			89.6			1.59		
C_8HONa (mM)												
1	52.2		93.4	190.3		137.5	191.8		170.0	0.99		0.80
5	52.1		93.2	250.8		123.7	185.8		195.8	1.34		0.63
15	50.8		92.8	309.6		99.4	163.4		235.0	1.89		0.42
25	49.6		92.2	444.9		99.7	118.4		209.0	3.75		0.47
50	47.5		91.3	289.9		100.7	132.9		186.7	2.18		0.53
C_{12}HONa (mM)												
0.05	53.0	75.8	93.2	390.1	17.9	152.1	166.0	166.5	209.1	2.35	0.10	0.72
0.2	51.7	74.3	93.7	298.6	44.1	157.1	154.4	93.5	201.5	1.93	0.47	0.77
0.8	51.7	74.2	92.8	392.2	24.9	151.1	151.6	136.7	209.3	2.58	0.18	0.72
1	50.5	74.9	92.3	336.2	75.6	145.6	144.0	118.6	196.0	2.33	0.63	0.75
2	49.4		89.5	234.6		78.1	108.7		136.7	2.15		0.57

Chen et al. [27] have estimated that the native fibrinogen molecule contains about 35% α-helix, 21% β-sheets, 13% β-turn, and 31% random coil. Other authors have estimated 42% α-helix, 7% β-sheets, 20% β-turn, and 30.8% random coil [33]. However, the trends are clear: with increasing temperature, α-helix and β-sheets change little before the onset of the first peak but change dramatically (α-helix decreased and β-sheets increased) in the range of 55–65 °C. After this, α-helix contents decrease moderately and finally an important decrease is observed from 80 to 100 °C. This behavior indicates that the decrease in α-helix occurs in domain E and in the coiled-coil portion of fragment D [28]. Some authors have found that the decrease in α-helix content is due to a conformational change to a β-structure, on the basis that the ellipticity of the negative peaks in the CD spectrum for fibrinogen changed from more to less negative values and their observation that the fluorescence intensity decreased [34].

Here, we make use of CD measurements on fibrinogen solutions containing surfactants at different temperatures (40, 70, and 90 °C) (see Fig. 3). The first temperature corresponds to the area below the first calorimetric peak (native fibrinogen structure), the second is placed between the second and third peaks (just D domain is unfolded), and the final one is located over the third peak. Fragment D contains a distribution of secondary structure values of 35% α-helix, 29% β-sheet segments, and 17% turn structures. Fragment D has two domains: a portion of the original coiled-coil and also a thermally labile globular domain. The coiled-coil portion showed an α-helical content around 70%, and the globular domain is estimated to be rich in β-sheet structures. Fragment E is shown to contain 50% α-helical values, attributed to its coiled-coil portions, and minor β-strands, and turn structures [35].

From our results, we can estimate that the native fibrinogen molecule at 40 °C contains about 30% α-helix and 18% β-sheets. Furthermore, all three surfactants interact with fibrinogen and affect the protein secondary structure to a different extent. At 40 °C, changes in secondary structure are insignificant for surfactant concentrations below 3 mM. However, by heating up the samples (70 and 90 °C), greater changes take place at lower surfactant concentrations. The backbone hydrogen bonds of α-helix are generally slightly weaker than those found in β-sheets. Thus, they are readily attacked by the surrounding molecules. In this study, both α-helix and β-sheets exhibit changes with added surfactant molecules. The interaction with C_8FONa leads to the greatest protein conformational changes (particularly at 70 and 90 °C), whereas C_8HONa leads to smallest changes. These findings suggest that the strength of the interactions between fibrinogen and the three surfactants followed the order C_8FONa > C_{12}HONa > C_8HONa. Previous studies have explained the different interactions between fibrinogen and ligands in terms of ligand molecular structure [36,37]. In this case, the most hydrophobic surfactants (C_8FONa, C_{12}HONa) were found to interact stronger with fibrinogen. On the other hand, because of the small size of C_8FONa, a greater number of molecules can interact with fibrinogen, and such interactions can be strong enough to cause the protein unfolding. Similar conclusion has been obtained by comparing the adsorption of β-endorphin and epinephrine to the different domains of the fibrinogen through electrostatic, polar, and hydrophobic interactions, resulting in protein unfolding, which may in turn expose the receptor-induced binding sites [38].

Difference absorption spectra of fibrinogen in the presence of different C_8HONa concentrations are presented in Fig. 4 (spectra corresponding to the other surfactants follow the same pattern). It is assumed that in the near-UV, the major factors responsible for the absorbance are tryptophan and tyrosine with a maximum at 280 nm [39]. Although fibrinogen contains appreciable amounts of phenylalanine, the perturbation spectrum of these residues is situated at a much shorter wavelength and has a much lower intensity than those of tyrosine and tryptophan and do not need to be considered here. The primary structure of fibrinogen contains a total of 72 tryptophan [40] and 88 tyrosine residues distributed along the molecule, with each Aα, Bβ, and γ chains having 21, 27, and 32 of these residues, respectively (NCBI Protein Database). Two isodichroic points, when the concentration of surfactant is varied, can be observed at 280 nm and 292 nm approximately. This fact reveals that two species are present in the solution [41]. Assuming that the surfactants do not contribute to the absorption spectrum, the two species should, indeed, correspond to different

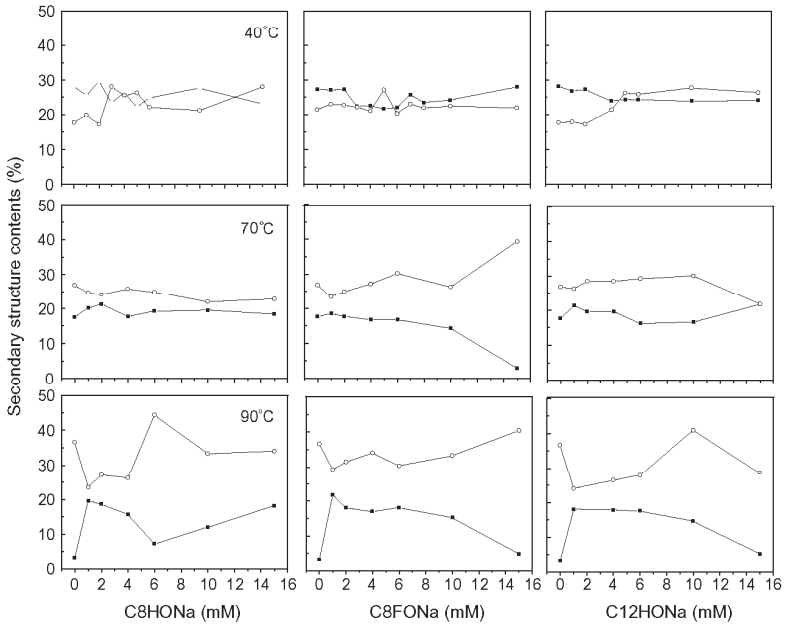

Fig. 3. Contents (in%) of the α-helix (■) and β-sheet (○) elements in fibrinogen as a function of surfactant concentration at different temperatures.

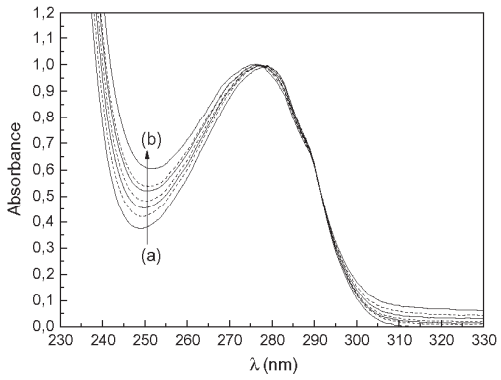

Fig. 4. Difference absorption spectra of fibrinogen (0.5 g dm ^{3}) in the presence of different C_8HONa concentrations from: 2 (a) to 16 mM (b).

unfolded states of the fibrinogen molecule, which is in good agreement with the cooperativity obtained from DSC measurements. There were no great changes in the overall shape of the adsorption spectra. Very slight decrease in the maximum region was noticed, but there was distinct increase in the minimum region. Shifts of 2–3 nm towards blue have been observed for C_8HONa and $C_{12}HONa$. Meanwhile, blue shift is only of 1 nm for C_8FONa. In a previous study, Guo et al. [42] have found a blue shift for different fibrinogen concentrations (without added surfactants), which has been attributed to concentration-dependent self-association where amino acid residues are exposed to an apolar environment. In our study, the protein concentration remains constant, so blue shift arises from the hydrophobic interactions of tryptophan with the hydrophobic moiety of the surfactants. Transition midpoints (T_m) were also checked by UV–vis showing a good agreement with those obtained from DSC.

In order to discuss how the surfactants affect the secondary structure of the protein, we have analyzed Raman spectra for fibrinogen in the presence of hydrogenated and fluorinated surfactants (Fig. 5). The band at 1641 cm^{-1} corresponds to the amide I band, which is sensitive to the secondary structure in fibrinogen. In the presence of surfactants, this band shifts slightly from 1641 cm^{-1} to 1648 cm^{-1}, 1651 cm^{-1}, and 1649 cm^{-1} for C_8FONa, C_8HONa, and $C_{12}HONa$ respectively. These slight changes in the position (and intensity) of the amide I band indicate that the surfactant adsorption on protein is accompanied by changes in the secondary structure of the protein: from a high α-helix content to the β-sheet structure [43] (Fig. 5). These results correlated well with CD analysis.

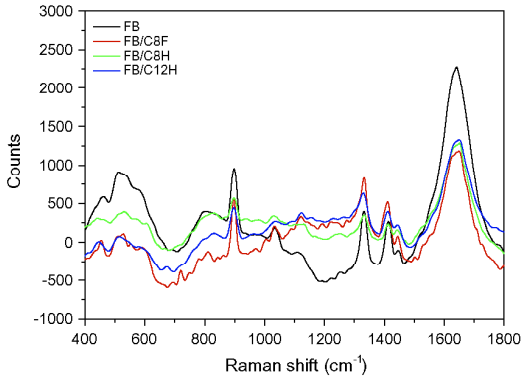

Fig. 5. Raman spectra of fibrinogen in presence of C_8FONa, C_8HONa, and $C_{12}HONa$.

At 1448 cm^{-1}, this band is assigned to the deformation modes of both CH_3 and CH_2 vibrations. The ratio of the Raman peak area of CH_3 and CH_2 deformation mode related to the Raman peak area of the amide I band (1641 cm^{-1}) is increasing from 0.0056 to 0.0170, 0.0115, and 0.0171 for C_8FONa, C_8HONa, and C_{12}HONa respectively. The decreasing Raman peak area of the amide I band is clearly observed in the presence of three surfactants. With these results, one can assume that the adsorption takes place via the amino acid side-chains, accompanied by changes in the secondary structure content but not in the overall structure of the protein.

3.2. SAXS analysis of fibrinogen in the absence and presence of surfactants

In the following, we describe the SAXS results with the aim of better understanding how the surfactant interaction impacts on the fibrinogen quaternary conformation at room temperature ($T = 22$ °C), *i.e.*, on the native fibrinogen structure. First of all, in the absence of surfactants, Fig. 6 shows the scattering intensity, normalized by the protein concentration, of fibrinogen at 1, 3, and 6.6 g dm^{-3} in the presence of 50 mM glycine–NaOH buffer, pH 8.5. SAXS measurements from samples composed of 0.5 g dm^{-3} did not result in any detectable SAXS signal (data not shown). However, the normalized scattering curves are practically the same for the three studied concentrations. Such a fact evidences that the protein conformational state is concentration-independent from 1 to 6.6 g dm^{-3}. Moreover, effects of interaction between proteins do not take place over the SAXS curves ($S_M(q) = 1$ in the Eq. (2)) once they do not present any interference peak [22]. Therefore, we calculate $P(q)$ through the fibrinogen crystallographic structure as a disulfide-linked dimer of three nonidentical polypeptide chains (Fibrinogen Scheme 1), but the corresponding scattering curve fails to fit the experimental data at low q values (dashed line in the inset on Fig. 6). On the other hand, the scattering of a paired-dimer configuration as found in the crystallographic native structure (pdb code: 3GHG, depicted in the inset on Fig. 6) reproduces quite well the data (solid line in the inset on Fig. 6). So, the SAXS curves are compatible to the scattering of paired-dimers (arrangement of two FB dimers) in this studied concentration range.

Therefore, we decide to proceed with the investigation by using a protein concentration of 3 g dm^{-3}. In terms of surfactant concentration, we studied the influence of 60 mM of each surfactant on the fibrinogen structure. Note that such a concentration keeps the same molar ratio used in the DSC and spectroscopic measurements as 0.5 g dm^{-3} and 10 mM of surfactant.

Interestingly, the samples composed of hydrogenated surfactants C_8HONa and C_{12}HONa, in the absence of protein, did not produce any detectable scattering signal at 60 mM. Such a fact is easily understood because C_8HONa micelle-like aggregates are not expected to be formed at this concentration (CMC of 380 mM). In respect to C_{12}HONa (CMC of 27 mM), a quite small number of micelles must be self-assembling in solution but they are not detectable by our experimental setup. On the other hand, the fluorinated surfactant, C_8FONa, shows clearly a typical scattering curve from surface charged micelle-like aggregates [23] (Fig. 7), although it has a CMC value similar to that of C_{12}HONa. The presence of CF_2 group in the hydrophobic medium contributes to a larger extent to the electron density contrast in $P(q)$ form factor (Eq. (2)) than does the CH_2 group, even though the number of scattering particles n_p is small.

The analysis of the scattering curve from C_8FONa micelles, by assuming that the micelle shape can be described as a prolate ellipsoid-like aggregate (solid line in Fig. 6), resulted in a value of $R_{par} = 11.5$ Å that is compatible to the CH_3–$(CH_2)_7$ extended-chain length. Moreover, the anisometry ν (ratio between the longest and the smallest axes), the polar shell thickness, σ, and its electron density ρ_{pol} were equal to 2, 3.5 Å, and 0.40 e/Å^3, respectively. The hydrophobic volume of the surfactant was determined as 340 Å^3, in accordance with the value reported in the literature [44] of 343 Å^3. An aggregation number of 35 was then calculated in good agreement with the value found in the literature of 50 ± 21 [45]. From $S_M(q)$ modeling, 14e charges were found in the micellar surface, indicating that ca. 40% of the surfactants in the aggregate are ionized, in very good agreement with 39% determined for cesium perfluorooctanoate [42].

Concerning the influence of the surfactants on the fibrinogen structure, Fig. 8 shows the SAXS curves of 3 g dm^{-3} of protein in the absence and presence of 60 mM of C_8HONa, C_8FONa, and C_{12}HONa. The scattering curves are displayed in log scale in the inset on Fig. 8 to emphasize the differences. As one can observe, the presence of C_8HONa did not promote any significant change in fibrinogen scattering curve. Therefore, our results give support to conclude that the presence of C_8HONa molecules below CMC do not affect significantly the protein conformation that remains in its paired-dimer state, although small (or even subtle) local changes in the domains may be occurring according to DSC and spectroscopic measurements.

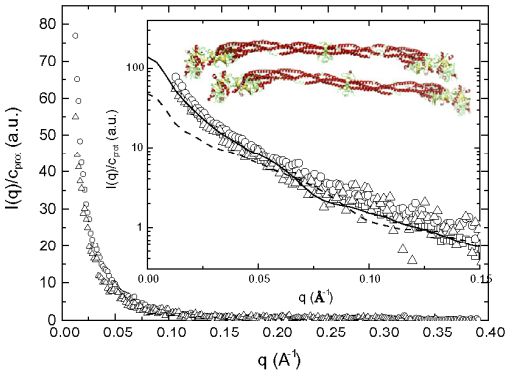

Fig. 6. SAXS curves normalized by the protein concentration, c, at three different values: 1 (open triangle), 3 (open circle), and 6.6 (open square) g dm^{-3}. Inset: theoretical scattering curves corresponding to the protein crystallographic structure (code 3GHG from PDB website) from the paired-dimer (solid line) and the dimer (dashed line) configuration. See text for details.

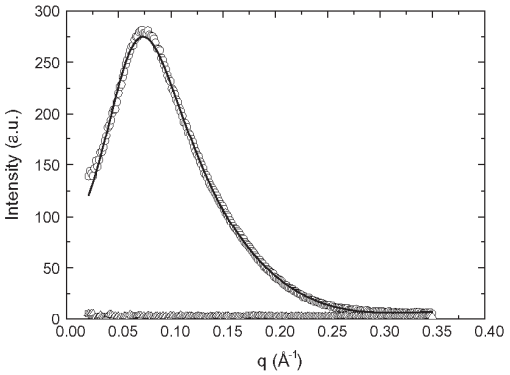

Fig. 7. SAXS curves of 60 mM of C_8FONa (open circles) and C_{12}HONa (open triangles) for comparison, at 50 mM glycine-NaOH buffer solution, pH 8.5. The solid line represents the best fit obtained with the prolate ellipsoidal model to C_8FONa SAXS data. The fitting parameters are described in the text.

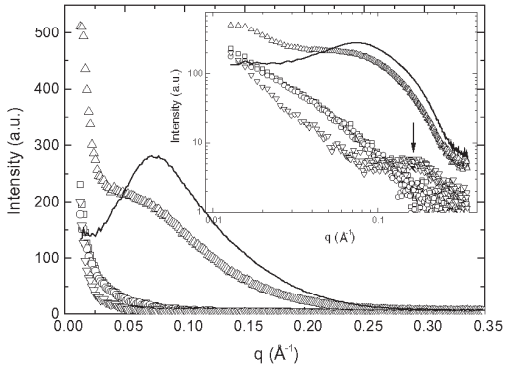

Fig. 8. SAXS curves of bovine fibrinogen (3 g dm $^{-3}$) in the absence (open squares) and presence of 60 mM of C_8HONa (open circles), C_8FONa (open triangles), and C_{12}HONa (open inverted triangle). Inset: the scattering curves are shown in log scale to remark the differences. The solid line represents the scattering curve of 60 mM C_8FONa in protein-free solution (Fig. 7) for comparison purpose.

On the other hand, the presence of fluorinated surfactants (C_8FONa) alters the scattering profile. There is an increase in the intensity in the small q region concomitantly with the appearance of a shoulder around 0.08 Å^{-1} (Fig. 8) related to the fluorinated surfactant micelle formation. The scattering profile is indeed due to a sum (solid line on Fig. 9) of two independent scatterings: one is due to the FB in the paired-dimer configuration and the other one to the fluorinated surfactant micelles coexisting in solution. The structural parameters from the FB and the micelles previously analyzed, Figs. 6 and 7, remain practically the same. Just the micelle ionization coefficient is reduced from 40% to 30%. Knowing that the fibrinogen pI (isoelectric point) is 5.5, at pH 8.5, the protein has a negative net charge in such a way that there are a large number of cationic counterions in the bulk in order to keep the electro-neutrality. As a consequence, some positive counterions must be screening the micelle surface charge. Therefore, our SAXS results indicate that at 60 mM, C_8FONa monomers may interact with fibrinogen paired-dimer without promoting dissociation or significant conformational changes, whereas micelle-like aggregates coexist in solution. Small local changes in the secondary structure of the fibrinogen as evidenced by DSC and spectroscopic measurements are not reflected in the overall protein conformation as seen by SAXS at room temperature.

Finally, the presence of sodium dodecanoate changes the scattering profile of the protein and induces the appearance of a broad peak around $q \approx 0.17$–0.18 Å^{-1} (black arrow in the inset on Fig. 8), which is related to the formation of micelle-like aggregates in solution similar to those formed by sodium dodecyl sulfate [15]. Therefore, our results evidence that the presence of fibrinogen favors the formation of C_{12}HONa micelle-like aggregates at concentrations lower than CMC of the surfactant in protein-free solution, as previously reported for other proteins and sodium alkyl sulfates [15,16]. Further, the fibrinogen scattering is also modified. Nevertheless, in this case, the SAXS curve is not well represented by the sum of the two independent scatterings related to the protein and the micelles. In fact, the micelles probably grow around specific hydrophobic regions of fibrinogen, inducing changes in the protein conformation as we explore below.

Different models have been described with the aim of monitoring the complexation between proteins and surfactants as "*pearl necklace model*" [15,16,46,47] and "*polypeptide unfolded chain wrapping around micelles*" [48]. However, the three polypeptide chains of fibrinogen are held together by 29 disulfide bonds [49]. These chains conserve secondary structure in the presence of the three surfactants as it has been demonstrated by CD measurements. Thus, fibrinogen complexes cannot behave as flexibly as a random coil. For this reason, we analyzed the SAXS curve of bovine fibrinogen (3 g dm^{-3}) in the presence of C_{12}HONa through the $p(r)$ function [16]. Fig. 10 shows the SAXS data along with the best fit obtained with the GIFT software [26] corresponding to the $p(r)$ function shown in the inset on Fig. 10. The first oscillation in the $p(r)$ function for $r < 50$ Å is a fingerprint of micelle formation [16], while the following maxima are associated with micelle dimension and the mean distance between two adjacent micelles. Accordingly, these values are equal to 57 Å and 138 Å, respectively. The micelle dimension is compatible to the values reported for sodium alkyl sulfate micelles [15,16]. Furthermore, the extension of the protein–surfactant complex can be inferred from the position where $p(r)$ goes to zero and amounts to ca. 400 Å. Such a value is near the FB longest dimension (see Fibrinogen Scheme 1). Based on this model, we may infer that C_{12}HONa interacts with the protein, forming a complex, where probably micelle-like aggregates are locally assembled at some hydrophobic moieties of the polypeptide chains.

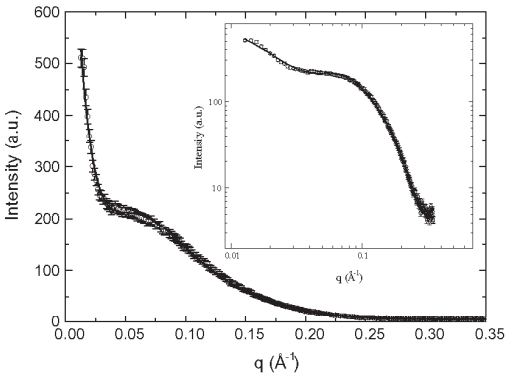

Fig. 9. SAXS data of fibrinogen 3 g dm $^{-3}$ in the presence of 60 mM of C_8FONa (open circles): the data are well fitted as a sum of independent scatterings due to paired-dimers FB and fluorinated surfactant micelles. The same scattering data can be appreciated in the log scale in the inset.

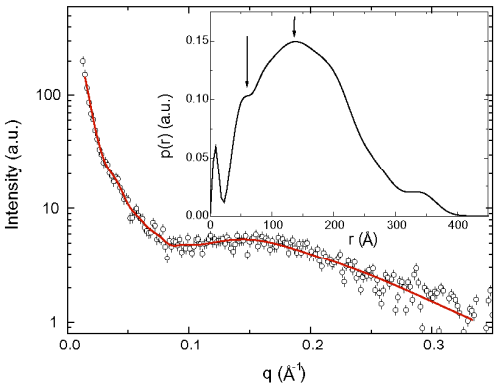

Fig. 10. SAXS curve of fibrinogen 3 g dm $^{-3}$ in the presence of 60 mM of C_{12}HONa in the glycine buffer. The solid line represents the best fit obtained with the GIFT software [26], and the correspondent $p(r)$ function can be appreciated in the inset. The arrows indicate the micelle diameter (equal to 57 Å) and the micelle–micelle mean distance (equal to 138 Å). See text for details.

4. Conclusions

The supramolecular assembly between bovine fibrinogen and sodium perfluorooctanoate, octanoate, and dodecanoate in buffer solution has been studied using different experimental techniques and theoretical models. The results obtained are summarized as follows. As a first step, we have studied the thermal stability of fibrinogen in the presence of the surfactants. Addition of hydrogenated surfactants results in decrease in melting temperatures. However, the fluorinated plays two opposite roles in the folding and stability of fibrinogen: acting as a structure stabilizer at low molar concentrations (enhancing T_m) and as a destabilizer at higher concentrations (diminishing T_m). Unfolding process of fibrinogen does not follow a two-state process but involves intermediate states for all studied systems. Increasing temperature and/or surfactant concentration results in a decrease in α-helix (and β-sheet increase) content. However, both the quaternary and tertiary structure does not undergo large variations as can be inferred from UV–vis and Raman spectra. SAXS measurements have shown that pure fibrinogen exists as a paired-dimer in this medium. In the presence of surfactant, the map of the configurations of the protein changes, depending on the hydrophobicity of surfactant. The presence of C_8HONa (lowest hydrophobicity) did not promote any significant change in fibrinogen. C_8FONa monomers interact with fibrinogen paired-dimer without promoting dissociation or significant conformational changes. On the other hand, the interaction between C_{12}HONa (highest hydrophobicity) and the protein promotes the surfactant self-assembling at hydrophobic moieties. Finally, we would like to point out that the picture of the fluorocarbon/hydrocarbon plus fibrinogen system reported here could provide a key that paves the way for future biochemical and biomedical applications, for example, in the recovery of proteins and protein conformation on support materials for regenerative therapies.

Acknowledgments

The authors thank the Xunta de Galicia for financial support (Project No. PXI20615PN). Authors also thank Prof. J.L. Mascareñas (Department of Organic Chemistry, University of Santiago de Compostela) for the use of CD spectrometer equipment. RI and LRSB thank Fundação de Amparo à Pesquisa do Estado de São Paulo (FAPESP) for financial support. RI also acknowledges Conselho Nacional de Pesquisa (CNPq) for research fellowship.

References

[1] O. Svensson, K. Thuresson, T. Arnebrant, Langmuir 24 (2008) 2573.
[2] J.J. Feng, P. Hildebrandt, D.H. Murgida, Langmuir 24 (2008) 1583.
[3] M.J. Meziani, Y.P. Sun, J. Am. Chem. Soc. 125 (2003) 8015.
[4] D.N. Petsev, P.G. Vekilov, Phys. Rev. Lett. 84 (2000) 1339.
[5] D. Zhong, A. Douhal, A.H. Zewail, Proc. Natl. Acad. Sci. 97 (2000) 14056.
[6] J.H. Brown, N. Volkmann, G. Jun, A.H. Henschen-Edman, C. Cohen, Proc. Natl. Acad. Sci. 97 (2000) 85.
[7] S. Yakovlev, L. Medved, Biochemistry 48 (2009) 5171.
[8] G. Tsurupa, R.R. Hantgan, R.A. Burton, I. Pechik, N. Tjandra, L. Medved, Biochemistry 48 (2009) 12191.
[9] A. Rieux, A. Shea, L.D. Shea, J. Controlled Release 136 (2009) 148.
[10] R. Uibo, I. Laidmäe, E.S. Sawyer, L.A. Flanagan, P.C. Georges, J.P. Winer, P.A. Janmey, Biochim. Biophys. Acta 1793 (2009) 924.
[11] I. Keere, R. Willaert, A. Hubin, J. Vereecken, Langmuir 24 (2008) 1844.
[12] L.C. Xu, C.A. Siedlecki, Langmuir 25 (2009) 3675.
[13] (a) E.L. Gelamo, M. Tabak, Spectrochim. Acta Part A 56 (2000) 2255;
(b) W. Cong, Q. Liu, Q. Liang, Y. Wang, G. Luo, Biophys. Chem. 143 (2009) 154.
[14] J.H. Hansen, S.V. Petersen, K.K. Andersen, J.J.E.T. Damhus, D. Otzen, Biopolymers 91 (2008) 221.
[15] (a) S.F. Santos, D. Zanette, H. Fischer, R. Itri, J. Colloid Interface Sci. 261 (2003) 400;
(b) B. Shweitzer, D. Zanette, R. Itri, J. Colloid Interface Sci. 277 (2004) 285.
[16] M. Ospinal-Jiménez, D.C. Pozzo, Langmuir 27 (2011) 928.
[17] (a) J.M. Ruso, P. Taboada, P. Martinez-Landeira, G. Pieto, F. Sarmiento, J. Phys. Chem. B 105 (2001) 2644;
(b) J.M. Ruso, N. Deo, P. Somasundaran, Langmuir 20 (2004) 8988.
[18] E. Chabaud, P. Barthelemy, N. Mora, J.L. Popot, B. Pucci, Biochimie 80 (1998) 515.
[19] P. Raychaudhuri, Q. Li, A. Mason, E. Mikhailova, A.J. Heron, H. Bayley, Biochemistry 50 (2011) 1599.
[20] E. Blanco, A. González-Pérez, J.M. Ruso, R. Pedrido, G. Prieto, F. Sarmiento, J. Colloid Interface Sci. 288 (2005) 247.
[21] (a) A. Lobley, L. Whitmore, B.A. Wallace, Bioinformatics 18 (2002) 211;
(b) L. Whitmore, B.A. Wallace, Nucleic Acids Res. 32 (2004) W668.
[22] L.R.S. Barbosa, M.G. Ortore, F. Spinozzi, P. Mariani, S. Bernstorff, R. Itri, Biophys. J. 98 (2010) 147.
[23] (a) L.R.S. Barbosa, W. Caetano, R. Itri, P. Homem-de-Mello, P.S. Santiago, M. Tabak, J. Phys. Chem B 110 (2006) 13086;
(b) W. Caetano, L.R. S Barbosa, R. Itri, M. Tabak, J. Colloid Interface Sci. 260 (2003) 414.
[24] (a) J.B. Hayter, J.B. Penfold, Mol. Phys. 42 (1981) 109;
(b) J. Hayter, J. Penfold, J. Chem. Soc. Faraday Trans. 1 77 (1981) 1851;
(c) J.P. Hansen, J.B. Hayter, Mol. Phys. 46 (1982) 651.
[25] P.T. Campana, L.R.S. Barbosa, R. Itri, Int. J. Biol. Macromol. 48 (2011) 398.
[26] A. Bergmann, G. Fritz, O. Glatter, J. Appl. Crystallogr. 33 (2000) 1212.
[27] Y. Chen, H. Mao, X. Zhang, Y. Gong, N. Zhao, Int. J. Biol. Macromol. 26 (1999) 129.
[28] P.L. Privalov, L.V. Medev, J. Mol. Biol. 159 (1982) 665.
[29] J.W. Donovan, E. Mihalyi, Proc. Natl. Acad. Sci. USA 71 (1974) 4125.
[30] Y. Moriyama, K. Takeda, Langmuir 15 (1999) 2003.
[31] A.W.P. Vermeer, W. Norde, Colloid Surf., A 161 (2000) 139.
[32] (a) A. Cooper, M.A. Nutley, A. Wadood, Differential Scanning Microcalorimetry in Protein–Ligand Interactions: Hydrodynamics and Calorimetry, in: S.E. Harding, B.Z. Chowdhry (Eds.), Oxford University Press, Oxford, 2001;
(b) S. Deep, J.C. Ahluwalia, Phys. Chem. Chem. Phys. 3 (2001) 4583.
[33] L. Razumovsky, S. Damodaran, Langmuir 15 (1999) 1392.
[34] N. Ohta, T. Totsuyanagi, Biol. Pharm. Bull. 16 (1993) 631.
[35] I. Azpiazu, D. Chapman, Biochim. Biophys. Acta 1119 (1992) 268.
[36] S. Martini, M. Consumi, C. Bonechi, C. Rossi, A. Magnani, Biomacromolecules 8 (2007) 2689.
[37] C. Bonechi, S. Martini, C. Rossi, Bioorg. Med. Chem. 17 (2009) 1630.
[38] R. Barbucci, S. Lamponi, A. Magnani, Biomacromolecules 4 (2003) 1506.
[39] J.R. Lakowicz, Principles of Fluorescence Spectroscopy, Kluwer Academic/Plenum Publishers, New York, 1999.
[40] S. Goncalves, N.C. Santos, J. Martins-Silva, C.J. Saldanha, Photochem. Photobiol. B: Biol. 86 (2007) 170.
[41] K.A. Connors, Binding Constants: The Measurements of Molecular Complex Stability, Wiley, New York, 1987.
[42] J. Guo, N. Harn, A. Robbins, R. Dougherty, C.R. Middaugh, Biochemistry 45 (2006) 86.
[43] G.J. Thomas, Biophys. J. 46 (1984) 763.
[44] S.S. Berr, R.R.M. Jones, J. Phys Chem. 93 (1986) 2555.
[45] H. Iijima, T. Kato, H. Yoshida, M. Imai, J. Phys. Chem. B 102 (1998) 990.
[46] K. Shirahama, K. Tsujii, T. Takagi, J. Biochem. 75 (1974) 309.
[47] S.H. Chen, J. Teixeira, Phys. Rev. Letter 57 (1986) 2583.
[48] A. Chakraborty, D. Seth, P. Setua, N. Sarkar, J. Phys. Chem. B 110 (2006) 16607.
[49] A. Henschen, J. McDonagh, Fibrinogen, fibrin and factor XIII, in: R.F.A. Zwaal, H.C. Hemker (Eds.), Blood Coagulation, Elsevier Science, Amsterdam, 1986.

International Journal of Biological Macromolecules 48 (2011) 495–500

Contents lists available at ScienceDirect

International Journal of Biological Macromolecules

journal homepage: www.elsevier.com/locate/ijbiomac

Rheological properties of ovalbumin hydrogels as affected by surfactants addition

Natalia Hassan [a], Paula V. Messina [b], Veronica I. Dodero [b], Juan M. Ruso [a,*]

[a] Soft Matter and Molecular Biophysics Group, Department of Applied Physics, University of Santiago de Compostela, E-15782, Spain
[b] Department of Chemistry, Universidad Nacional del Sur, INQUISUR-CONICET, 8000 Bahía Blanca, Argentina

ARTICLE INFO

Article history:
Received 22 November 2010
Received in revised form 4 January 2011
Accepted 13 January 2011
Available online 22 January 2011

Keywords:
Gels
Complexation
Ovalbumin
Hydrogenated surfactants
Perfluorinated surfactants

ABSTRACT

The gel properties of ovalbumin mixtures with three different surfactants (sodium perfluorooctanoate, sodium octanoate and sodium dodecanoate) have been studied by rheological techniques. The gel elasticities were determined as a function of surfactant concentration and surfactant type. The fractal dimension of the formed structures was evaluated from plots of storage modulus against surfactant concentration. The role of electrostatic, hydrophobic and disulfide SS interactions in these systems has been demonstrated to be the predominant. The viscosity of these structures tends to increase with surfactant concentration, except for the fluorinated one. Unfolded ovalbumin molecules tend to form fibrillar structures that tend to increase with surfactant concentration, except for the fluorinated one. This fact has been related to the particular nature of this molecule.

1. Introduction

Ovalbumin (OVA), a major component of egg white proteins, has important implications in food systems improving sensory perception [1,2]. This protein is grouped into the serine proteinase family inhibitors, which controls serine proteinases involved in diverse physiological reactions, because of the close similarity in the primary and tertiary structures. It has a molecular weight of 45,000 Da and consists of a single chain of 385 amino acids with 105 titrable residues [3], containing a single disulfide bond (interconnecting two parts of the chain) and a glycosylation (mainly mannose) site. Three different ovalbumin phosphate forms containing two, one or zero phosphate groups per molecule (85:12:3 ratio respectively) occur in egg white. This protein presents a globular shape with a radius of ≈3 nm in an aqueous medium and an isoelectric point at pH 4.6 [4]. When stored for extended periods of time, or by heat processing, the native R-ovalbumin converts to S-form that is more resistant to denaturation by heat, urea, or guanidine [5]. The ovalbumin globules are also known to make a self-organized mesoscopic structure, which is governed by several factors: temperature, concentration or electrolyte [6]. As a result, solutes are often added to regulate these transformations during the processing of proteins or proteins-containing food materials. To effectively control and optimise this food processing, a deep understanding of how added solutes influence protein morphology is essential.

Studying the interactions of OVA with surfactants has been a hotspot these days [7,8]. Interaction of proteins with surfactants is of great importance in the fields of industrial (cosmetic, paints, food), biological and pharmaceutical sciences. Due to the existence of nonpolar and ionic amino acid side chains in protein molecules, the formations of these complexes is driven by electrostatic interactions between the charged headgroups of the surfactants and the oppositely charged units of the proteins, as well as by hydrophobic interactions between the alkyl chains and different parts of the proteins [9–11]. Concerning the interest of the industry in ovalbumin hydrogels range from emulsifying activity (it is higher at acidic pH) or drug delivery systems. Also, acid-sensitive microgels for the development of protein-based vaccines under acidic conditions, like those found in the phagosomes of antigen-presenting cells, are highly demanded [12].

In the present study, we have investigated the effect of sodium perfluorooctanoate, sodium octanoate, and sodium dodecanoate, on the properties and structure of the ovalbumin gels. The ability to form a gel is an important function of proteins in food systems. Most food protein gels are formed by denaturation, aggregation, and gelation during heating process. In flurry of studies, researches have focused on gel formation upon protein heating. However, few studies have dealt with protein gel formation without heating or have analyzed the effect of surfactants on protein gel properties. The studied surfactants allow us to analyze how the presence of fluorine atoms in the alkyl chain affects the gel structure. For this purpose several samples, covering a range of concentrations of surfactant from 1 mM to 10 mM, were prepared. These concentrations guarantee the non existence of micelles [13]. The physicochemical properties of these samples were evaluated by using rheological

* Corresponding author. Tel.: +34 981 563 100; fax: +34 981 520 676.
E-mail address: juanm.ruso@usc.es (J.M. Ruso).

0141-8130/$ – see front matter © 2011 Elsevier B.V. All rights reserved.
doi:10.1016/j.ijbiomac.2011.01.015

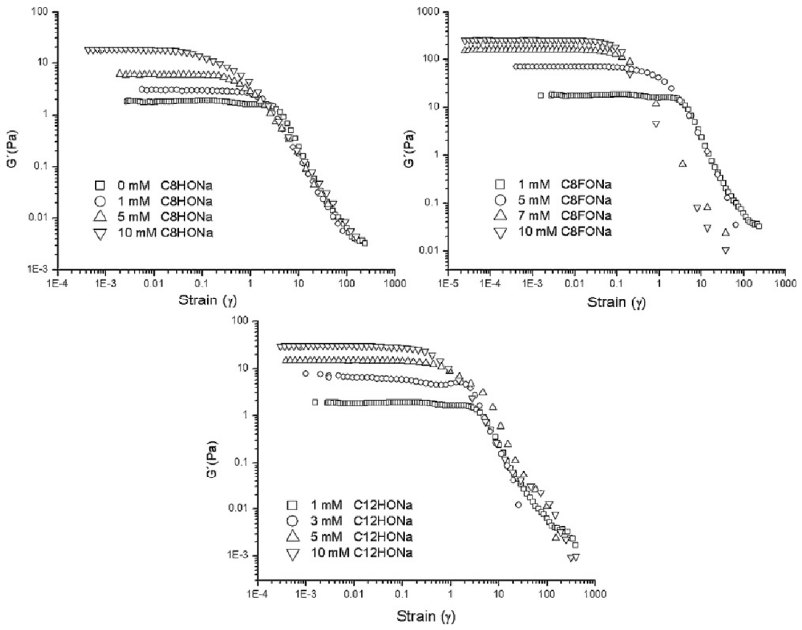

Fig. 1. The dependence of storage modulus (G') of ovalbumin surfactant mixtures on strain (γ) for different concentrations of the three surfactants under study. Ovalbumin concentration, 40 g/l.

measurements that are easy to conduct, especially in the high concentration range of proteins [14].

2. Experimental

2.1. Materials

Ovalbumin (Albumin, Chicken Egg, product A-5253, Sigma Chemical Company) was used without further purification. Sodium octanoate (C8HONa) and sodium perfluorooctanoate (C8FONa) were obtained from Lancaster Synthesis Ltd. Sodium dodecanoate (C12HONa) with purity over 99%, were obtained from Sigma Chemical Co. The protein was dissolved in water, the pH was adjusted to pH 3.0 with HCl 0.1 M. All materials were of analytical grade and solutions were made in double distilled water.

2.2. Rheology

Rheological experiments were performed on a Bohlin CS-10 stress-controlled rheometer. A Couette geometry with a cup of 27.5 mm diameter and a bob type Mooney cell was used. The cell was heated by a reservoir of fluid circulating from a Julabo thermostated bath. The sample was equilibrated for at least 20 min prior to each experiment. Both steady and dynamic rheological experiments were performed at each temperature. Dynamic frequency sweep measurements were performed in the linear viscoelastic regime of the samples, as determined previously by dynamic stress sweep measurements. For the steady-shear experiments, an equilibration time of 90 s was given at each shear stress. All experiments were performed at 25 °C.

3. Results and discussion

In order to understand the effect of surfactant type and concentration on structural properties of ovalbumin gels, the storage modulus (G'), loss modulus (G''), and phase angle were recorded. However, both G' and G'' developed similarly and the G' values were considerably greater in magnitude than the G'' values for all gels, suggesting predominantly elastic behavior. Therefore, at this point, only G' values are discussed. Fig. 1 shows the effect of surfactant type and concentration on the strain dependent elastic modulus, G'. A first general point to note is the wide variation in large deformation rheological behavior exhibited by the different systems. A second more specific point is that, irrespective of whether the gelation is triggered by surfactant type, the extent of the linear viscoelastic region, the range of constant G', is much shorter for the surfactant–ovalbumin gels that for the pure ovalbumin gels.

As can be observed, gel strength is dependent on both parameters tested: surfactant type and surfactant concentration. At lower surfactant concentrations, rigidity values were much lower than at the higher values and variations in rigidity values with different surfactants are significant. At this pH, the protein is not close to its isoelectric point of 4.9, and as a result protein has a positive net charge. Increased interactions due to the presence of surfactants result in increased rigidity presumably because the interactions involved contribute to structure development. It would appear that the ability to promote aggregation was higher for the surfactants under study despite the fact that probably the three surfactants did not bind to the same extent. The highest rigidity values were observed for the fluorinated surfactant, followed by sodium dodecanote and sodium octanoate. The fact that for both sodium perfluorooctanoate, and sodium dodecanoate, higher gel rigidity were obtained demonstrates that the type of atoms and the alkyl chain length present can affect this relationship. The lowest G' values obtained with sodium octanoate reveals that electrostatic interactions resulting from surfactant binding at this pH were not sufficient to overcome the net repulsive force associated with the protein. Consequently, this dramatic difference can be seen in gel rigidity values for this system.

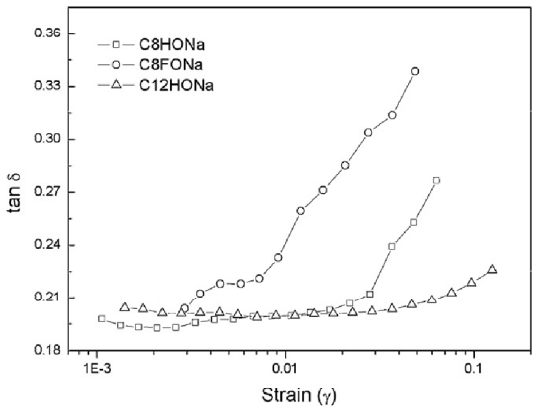

Fig. 2. Loss tangent ($\tan\delta$) versus strain (γ) for the different surfactant under study. Surfactant concentration 10 mM. Ovalbumin concentration, 40 g/l.

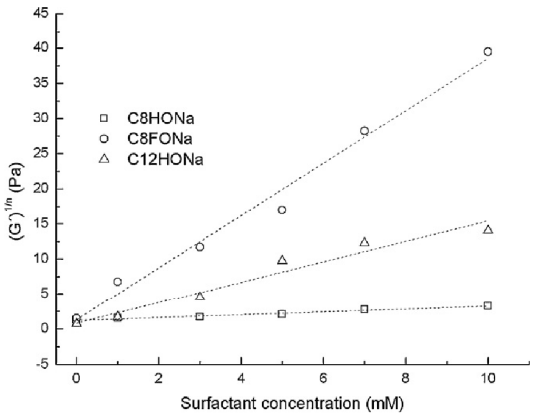

Fig. 3. Surfactant concentration dependence of G' values of ovalbumin gels.

Another parameter that provides some information on network structure is the loss tangent value, $\tan\delta$, the ratio of the loss modulus or viscous component to the storage modulus or elastic component. The $\tan\delta$ value can give indication of the type of structure formed [15]. Low $\tan\delta$ values are normally associated with a well crosslinked network where the elastic component is high compared to the viscous component. Meanwhile, high $\tan\delta$ values are associated with a lack of crosslinking due to either excessive aggregation or excessive solubilization of the protein. For all our systems, variations in $\tan\delta$ values show decrease with increasing surfactant concentration. This supported the G' data suggesting that the inclusion of surfactant served to counteract the electrostatic repulsion by providing a bridge between protein molecules. The increased protein gel network should theoretically arise from physical cross-links instead of chemical cross-links. For a fixed surfactant concentration $\tan\delta$ values are markedly higher for C8FONa than for the hydrogenated surfactants, Fig. 2. Interestingly, this dramatic difference was not seen in gel rigidity values. The influence of hydrogenated surfactants on network formation appeared to give a more elastic product, but this did not translate into increased gel rigidity.

Various experimental techniques in rheology have been applied to elucidate fractal structures in aggregates or proteins gels [16–19]. In the framework of fractal theories, the network structure of protein gels is considered as closely packed fractal flocs with the fractal dimension of n [14]. The elastic properties of a floc are dominated by its effective backbone, which can be approximated as a linear chain of springs. The elastic constant (K) of the individual flocs is inversely related to their size (ξ), by means of $K \sim K_0/\xi^{2+x}$ where K_0 is the local bending constant between two adjacent springs that belong to the effective backbone of a floc and x is the fractal dimension of the elastic backbone. Since fractal flocs are considered scale invariant, the size of the flocs is related to the volume fraction (ϕ) as $\xi \sim \phi^{1/(n-3)}$. When the links between the neighboring flocs have a higher elasticity than those in the flocs, which is the so-called strong-link regime, the macroscopic elastic constant of the gel (G') is dominated by K. Since G' of a system of size L can be related to K as $G' \sim (L/\xi)K$, the dependence of G' on ϕ is derived as $G' \sim \phi^{(3+x)/(3-n)}$.

Later, several works based on percolation and fractal theories found a generic description of gel elasticity [20,21]. In this case, G', can be written as a power law according to $G' \sim (c - c_p)^n$, where c is the concentration of monomers in the system, c_p is the critical percolation threshold concentration, and n is a scaling exponent, which depends on the type of Hamiltonian that describes the network elasticity. In contrast, the fractal models assume $c_p = 0$ and predict a power law behavior written as $G' \sim c^w$, where the exponent w is related to the fractal dimension of so-called flocs that form the network. The fractal dimension depends on the interaction between the monomers. Finally, van der Linden et al. [22] found that most data can be described by one percolation model and the scaling exponent (n) can be determined by their graphical method. This method uses plots of $(G')^{1/n}$ versus concentration, c, and extrapolates these plots to 0. This procedure makes use of the fact that independent of the value of n, the curves must all intersect the concentration axis at the same value. When the assumed value for n is close to the actual value, the plot will be linear. If n is too small or too large the lines are curved. From the plots of $(G')^{1/n}$ versus c for various n, those n values that give an approximately straight line were selected.

Returning to our systems, we analyzed the surfactant concentration dependence of storage modulus of the ovalbumin plus surfactant gels. The value for G' was obtained in the linear regime, where it is independent of the applied strain. The experimental points and the corresponding selected fits are plotted in Fig. 3. Values of n obtained for our systems were 1.3, 1.5 and 2.5 for dodecanoate, perfluorooctanoate and octanoate, respectively. As we have previously pointed out, the exponent n is a function of the gel structure. High values, $n > 3$, suggest that network is composed by branched linear particles or large cluster with a low density. Meanwhile, low values indicate that structures are larger, compact and homogeneous [23]. These results correlate well with those found by Veerman et al. for ovalbumin [24], β-lactoglobulin [25] and bovine serum albumin [26] at low pH.

Viscosity curves are reported in Fig. 4 and show the trend of viscosity as a function of the shear rate for all investigated samples. All measurements were performed controlling the shear stress, so that the shear rate range depends on the sample viscosity. Initial experimental values are $1\ s^{-1}$ in all cases.

In general, one common data pattern can be concluded: under steady shear flows, no Newtonian regions were observed either at the high or low limiting shear rates (the low shear Newtonian region can lie outside the shear rate range accessible to the instrument). Meanwhile, a strong shear thinning in the intermediate shear rate region was found. Generally, solutions of interacting colloidal particles at high concentrations tend to order into crystalline lattices at rest. When shear is applied, the flow concentrates stress above all at lattice dislocations where particles are loosely trapped [27]. Under flow, the microstructure of the solution can be mod-

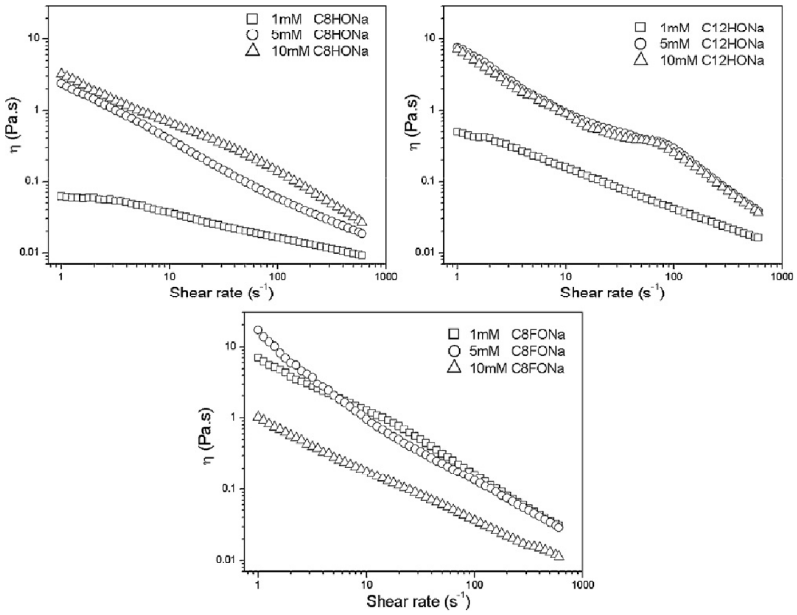

Fig. 4. Experimental viscosity as a function of shear rate for samples of ovalbumin gels in the presence of different concentration of surfactants. Ovalbumin concentration, 40 *g*/l.

eled as a solid ordered phase coexisting with a fluid disordered phase and when shear rate increases the fluid disordered phase rises above the solid ordered one. This is, the shear destroys part of the ordered structure (disruption of entanglements and other intermolecular interactions) and the so-called shear-thinning behavior is observed. Finally, the non existence of a Newtonian region at high shear rates suggests that these systems are not capable of maintaining part of its initial overall structure. It can be seen that the amplitude of the shear-thickening is not strongly dependent on the surfactant concentration.

A more detailed description of the plots allows us to discover some divergences among the systems. At this level, significant differences arise from the varied nature of the surfactant and their interactions with the protein network. For both hydrogenated surfactants at the lowest concentration, the shear stress was less dependent on the shear rate on decreasing the rate to 3 s^{-1}, indicating that an apparent yield stress might exist, as has been observed in some colloidal systems [28]. On the other hand, for C8HONa and C12HONa viscosity increased with surfactant concentration, whereas for C8FONa the lowest viscosity was found for the highest concentration, for all shear rate range. The differences in these flow behaviors among the surfactants may reflect the differences in nature of the formed aggregates, for example, the extent in flexibility of fibrillar aggregates. Former studies have demonstrated that upon heating, ovalbumin molecules denature and aggregate into thin strands (linear aggregates) or more dense particles (random aggregates) depending on the conditions used for the heat treatment: pH, ionic strength or protein concentration. Under conditions of high electrostatic repulsions, far from p*I*, denatured ovalbumin mainly formed linear semi-flexible aggregates of approximately 5–12 nm while their level of branching considerably increased when the electrostatic repulsions are screened [29]. The nonlinear dependence of the viscosity with surfactant concentration reflects that linear structures are not perfect, probably upon addition of surfactants protein is unfolded and different interactions between complexes of polypeptide–surfactant arise [30]. It is well known that the formation of protein surfactant complexes is driven by electrostatic interactions between the charged headgroup of the surfactants and the oppositely charged units of the protein, as well as by hydrophobic interactions between the alkyl chain of the surfactants and the nonpolar protein residues. In aqueous media surfactants ions compete with water molecules for binding sites on the protein, for which in the case of ovalbumin it was found an average number of 33 mol water bound per mole of ovalbumin [31]. On the other hand, the overall gelation process requires that the proteins unfold or undergo some conformational changes initially and that the second aggregation step proceeds relatively more slowly than the first to allow the denatured protein molecules to orient themselves and interact at specific points, thus forming a three dimensional network [32]. Arntfield et al. [33] investigated the role of disulfide (SS) bonds in heat-induced networks from ovalbumin, and found that SS bonds may contribute to the elasticity and strength of protein networks. The nature of crosslinks in protein gels has been discussed by several authors [34]. The consensus view is that with the exception of SS bonds in some protein gels, the molecules are held together by a combination of weak intermolecular forces, i.e., hydrogen bonds, electrostatic forces, van der Waals forces. and hydrophobic interactions. These results implicate essentially all of the potential interaction sites or functional groups of the molecules in the gelation process, including –SH groups. Also, it was suggested that critical number of sulfhydryl groups can be introduced beyond which the microstructure of the aggregates transforms from fibrillar into amorphous. Rheological studies further suggested that covalent networks, once formed, do not have the possibility to rearrange, reducing the possibility to attain a stronger network. These results show that, even though aggregation of ovalbumin may be primarily driven by physical interactions, formed disulfide bonds are important to determine the resulting aggregate morphology and rheological properties [35]. From our results it can be inferred that there is an initial electrostatic interaction between surfactant and protein. This interaction unfolds partially protein structure, enhancing SS interactions

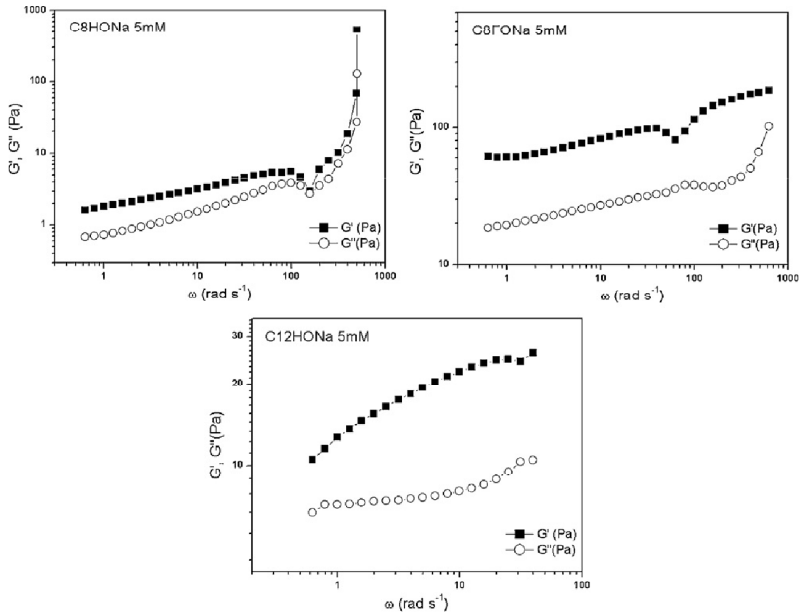

Fig. 5. Storage (G') and loss (G'') moduli as a function of frequency for ovalbumin surfactant mixture. Ovalbumin concentration, 40 g/l. Surfactant concentration 5 mM.

and gel strength. However, in the case of the fluorinated surfactant, at high concentrations there is a disruption of the network and a decrease in viscosity. This result could be simultaneously related with the high hydrophobicity of this surfactant, similar to those of the C12HONa, and the stiffer fluorinated alkyl chain, which results in lower gauche conformations that become more important when viscosity of samples is increased.

Fig. 5 shows the surfactant type dependence of the dynamic viscoelastic behavior of the gels (similar patterns were found for the other surfactant concentrations). Both the storage and the loss moduli increased with frequency. We note that, for the three surfactants, the storage modulus was always larger than the loss modulus throughout the frequency domain studied at all concentrations, which is a characteristic feature of systems exhibiting elastic behavior. This fact also suggests that frequency did not significantly change the network structures of the ovalbumin–surfactant gels, and that such network behavior was not due to the limited frequency range available.

4. Conclusions

In this work, we have provided some novel insight about the gelation of ovalbumin–surfactant mixtures. The main features from this study can be summarized as follows. Firstly, gelation of ovalbumin–surfactant systems for three different surfactants (C8HONa, C8FONa and C12HONa) at different surfactant concentration mixture ratios in the range 0–10 mM was studied, and the strength of the gel was observed to increase with increasing surfactant concentration. For the three surfactant under study gel strength follows the order C8FONa > C12HONa > C8HONa. Secondly, the surfactant concentration dependence of the storage modulus can be described by power laws. The results suggest a fibrillar structure of the gels and a fractal dimension dependent of the surfactant nature. Finally, based on viscosity measurements, the different nature of the fluorinated surfactant provokes a disruption of the gel network at high concentrations.

Acknowledgements

The authors thank the Xunta de Galicia for their financial support (Project No. 10PXIB206258PR). P.V.M. acknowledges the financial support from the Universidad Nacional del Sur, Agencia Nacional de Promoción Científica y Tecnológica (ANPCyT), Concejo Nacional de Investigaciones Científicas y Técnicas de la República Argentina (CONICET) and Education, Audiovisual Culture, Executive Agency, European Commission. EMUNDUS18. V.I.D. thanks CONICET (PIP 114-200801-00090), ANPCyT (PICT-2008-00083) and PGI-UNS (PGI 24/ZQ07).

References

[1] K. Broersen, A.M.M. van Teefelen, A. Vries, A.G.J. Voragen, R.J. Hamer, H.H.J. de Jongh, J. Agric. Food Chem. 54 (2006) 5166–5174.
[2] Y. Sun, S. Hayakawa, J. Agric. Food Chem. 50 (2002), 1636-1624.
[3] E. Tatsumi, D. Yoshimatsu, M. Hirosi, Biochemistry 37 (1988) 12351–12354.
[4] R.A. Judge, M.R. Johns, E.T. White, J. Chem. Eng. Data 41 (1996) 422–424.
[5] B. Egelandsdal, J. Food Sci. 44 (1980) 1651–1654.
[6] M. Sugiyama, A. Nakamura, N. Hiramatsu, M. Annaka, S. Kuwajima, K. Hara, Biomacromolecules 2 (2001) 1071–1073.
[7] G. Martos, P. Contreras, E. Molina, R. Lopez-Fandi, J. Agric. Food Chem. 58 (2010) 5640–5648.
[8] A.C. Miller, A. Bershteyn, W. Tan, P.T. Hammond, R.E. Cohen, D.J. Irvine, Biomacromolecules 10 (2009) 732–741, and references therein.
[9] J.M. Ruso, N. Deo, P. Somasundaran, Langmuir 20 (2004) 8988–8991.
[10] J.M. Ruso, P. Taboada, P. Martinez-Landeira, G. Prieto, Felix Sarmiento, J. Phys. Chem. B 105 (2001) 2644–2648.
[11] J.M. Ruso, P. Taboada, L.M. Varela, D. Attwood, V. Mosquera, Biophys. Chem. 92 (2001) 141–153.
[12] N. Murthy, M. Xu, S. Schuck, J. Kunisawa, N. Shastri, J.M.J. Fréchet, Proc. Natl. Acad. Sci. U. S. A. 100 (2003) 4995–5000.
[13] E. Blanco, A. González-Pérez, J.M. Ruso, R. Pedrido, G. Prieto, F. Sarmiento, J. Colloid Interface Sci. 288 (2005) 247–260.
[14] S. Ikeda, E.A. Foegeding, T. Hagiwara, Langmuir 15 (1999) 8584–8589.
[15] S.D. Arntfield, E.D. Murray, M.A.H. Ismond, A.M. Bernatsky, J. Food Sci. 54 (1989) 1624–1631.
[16] L.G.B. Bremer, B.H. Bijsterbosch, P. Walstra, T. van Vliet, Adv. Colloid Interface Sci. 46 (1993) 117–128.
[17] R. Vreeker, L.L. Hoekstra, D.C. den Boer, W.G.M. Agterof, Food Hydrocolloid. 6 (1992) 423–435.
[18] J.C. Gimel, D. Durand, T. Nicolai, Macromolecules 27 (1994) 583–589.

[19] T. Hagiwara, H. Kumagai, T. Matsunaga, J. Agric. Food Chem. 45 (1997) 3807–3812.
[20] D. Stauffer, A. Coniglio, M. Adam, Adv. Polym. Sci. 44 (1982) 103–158.
[21] W.H. Shih, W.Y. Shih, S. Kim, J. Liu, I.A. Aksay, Phys. Rev. A 42 (1990) 4772–4779.
[22] E. van der Linden, L.M.C. Sagis, Langmuir 17 (2001) 5821–5824.
[23] M. Weijers, L.M.C. Sagis, C. Veerman, B. Sperber, E. van der Linden, Food Hydrocolloid. 16 (2002) 269–276.
[24] C. Veerman, G. Schiffart, L.M.C. Sagis, E. van der Linden, Int. J. Biol. Macromol. 33 (2003) 121–127.
[25] C. Veerman, H. Ruis, L.M.C. Sagis, E. van der Linden, Biomacromolecules 3 (2002) 869–873.
[26] C. Veerman, L.M.C. Sagis, J. Heck, E. van der Linden, Int. J. Biol. Macromol. 31 (2003) 139–146.
[27] B. van der Vorst, D. van den Ende, N.J.J. Aelmans, J. Mellema, Phys. Rev. E 56 (1997) 3119–3125.
[28] S. Ikeda, K. Nishinari, Biomacromolecules 1 (2000) 757–763.
[29] T. Croguennec, A. Renault, S. Beaufils, J.J. Dubois, S. Pezennec, J. Colloid Interface Sci. 315 (2007) 627–636.
[30] M.G. McKee, G.L. Wilkes, R.H. Colby, T.E. Long, Macromolecules 37 (2004) 1760–1767.
[31] A. Gonzalez-Perez, J.M. Ruso, G. Prieto, F. Sarmiento, Colloid Polym. Sci. 282 (2004) 351–356.
[32] Y. Sun, S. Hayakawa, J. Agric. Food Chem. 50 (2002) 1636–1642.
[33] S. Arntfield, D. Murray, M.A.H. Isomond, J. Agric. Food Chem. 39 (1991) 1378–1385.
[34] G.R. Ziegler, E.A. Foegeding, in: J.E. Kinsella (Ed.), Advances in Food and Nutrition Research, vol. 34, Academic Press, New York, 1990.
[35] K. Broersen, A.M.M. van Teeffelen, A. Vries, A.G.J. Voragen, R.J. Hamer, H.H.J. de Jongh, J. Agric. Food Chem. 54 (2006) 5166–5174.

Langmuir ARTICLE
pubs.acs.org/Langmuir

Mimicking Natural Fibrous Structures of Opals by Means of a Microemulsion-Mediated Hydrothermal Method

Natalia Hassan,[‡] Valeria Verdinelli,[†] Juan M. Ruso,[‡] and Paula V. Messina*[,†]

[†]INQUISUR-CONICET, Department of Chemistry, Universidad Nacional del Sur, (8000) Bahía Blanca, Argentina

[‡]Soft Matter and Molecular Biophysics Group, Department of Applied Physics, University of Santiago de Compostela, Santiago de Compostela, 15782, Spain

Supporting Information

ABSTRACT: Silica-based nanomaterials are of great interest because of their potential applications in constructing electronic and optoelectronic nanodevices. Especially significant are those that combine the properties of photonic crystal with a fibrous semiconductor structure. Here we report the use of microemulsion droplet systems as a simple and controllable route for the synthesis of 3D opals materials with an unusual fibrous microstructure similar to those that exist in nature. By this method, we demonstrate the creation of very long fibrils of 30−50 nm diameter and more than 20 μm length showing simultaneous short and long wavelength light emissions and band gap values (5.50 and 4.41 eV) comparable to those obtained for silicon-based metal oxide semiconductors.

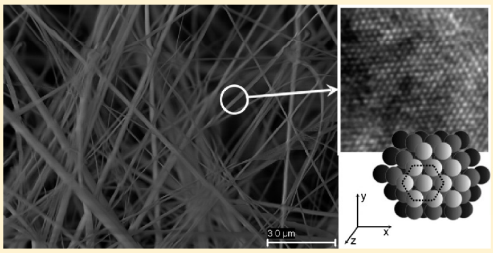

INTRODUCTION

Silicon-based fiber devices are the backbone of modern optoelectronic[1−8] and telecommunication[9,10] systems and are widely used for guiding and distributing light in optical arrangements.[11] A novel type of optical fiber developed mainly during the past decade and pioneered by Russell[12] and coworkers is the microstructured fiber, frequently called the photonic crystal fiber (PCF). PCFs are fibers with an internal periodic structure made of capillaries, filled with air, laid to form a hexagonal lattice. The capillary stack-and-draw procedure proved to be highly versatile, allowing the construction of complex lattices to be assembled from individual stackable units of the correct size and shape. Functional defects can be precisely introduced during the stacking process, allowing fabrication of a wide range of different PCFs.[12]

Opals were identified as natural photonic crystals (PCs) in 1995,[13] and thereafter there have been numerous reports on their structural and optical properties because of their ability to manipulate the flow of light. Most reference describes them as a perfect stacking of amorphous, hydrous silica spheres of identical diameter ranging from 150 to 300 nm.[6,7,14] Nevertheless, in extreme and specific geological conditions they crystallize in the unusual form of nanometer-scale fibrils.[15] Accordingly, one might think of these types of natural opals as photonic crystal nanofibers.

In this paper, we take a significant step toward generating PCFs in a nanometric scale similar to those that exist in nature. For this purpose, we show a bottom-up reverse microemulsion-based method[16] to control the stacking morphology and growth of the opal crystals. The formation and the morphological control of colloidal assemblies during a microemulsion-mediated hydrothermal synthesis is a complex process which depends on the particular combination of all the relevant microemulsion parameters. The effect of various factors on the final particle size is actually system specific, including the rate and the order of reactants addition.[16] Crystalline oxide nanorods can be prepared directly by alkoxide hydrolysis in microemulsions at room temperature. To illustrate, γ-V_2O_5 nanorods of the orthorhombic structure were obtained by direct hydrolysis of a vanadium alkoxide in sodium bis-(2-ethylhexyl) sulfosuccinate (so-called "Aerosol-OT", abbreviated as AOT) reverse micelles,[17] while rodlike ZnO nanoparticles of the hexagonal wurtzite structure were produced by the ammonia-catalyzed hydrolysis of zinc dibutoxide in nonionic reversed micelles.[18] Particularly, the microemulsion-mediated hydrothermal method has been shown to be useful in the synthesis of a variety of 1-D nanostructures. Single-crystalline nanowires/nanorods of CdS,[19] BaF_2,[20] SnO_2,[21] $AlPO_4$-5,[22,23] and $Ca_{10}(PO_4)_6(OH)_2$[24] have been successfully obtained by reverse micelles under hydrothermal conditions.

Here, the microemulsion was treated as a pseudoternary system with oil, water, and surfactant components. The effects of microemulsion oil phase, the hydrothermal treatment time,

Received: February 8, 2011
Revised: May 26, 2011
Published: June 14, 2011

and the calcination temperature on the final material structure were investigated. Thus, two different materials constituted by opal microstructured fibrils were created by sodium tetraethyl orthosilicate hydrolysis inside water/AOT/*n*-hexane and water/AOT/cyclohexane nanodroplets after 24 h of hydrothermal treatment at 100 °C and 7 h of calcination at 650 °C in an air flux. Depending of the microemulsion template system, they showed simultaneous short and long wavelength light emissions and band gap values comparable to those obtained for silicon-based metal oxide semiconductors (MOS). In general, the combination of a fibrous structure and photonic crystal proterties just with a semiconductor structure provides to the PCFs a series of unique properties impossible to achieve in classical silicon fibers. For example: PCFs maximize nonlinear interactions between laser light and low-density media such as gases; in PCFs small dielectric particles can be trapped, levitated, or propelled in a laser beam using the dipole forces exerted by light; and PCFs with extremely small solid glass cores and very high air-filling fractions not only display unusual chromatic dispersion but also yield very high optical intensities per unit power.[1,9,12]

The reduction of such materials at the nanometer scale offers a number of outstanding optical and mechanical properties, including (1) large evanescent fields, (2) high nonlinearity, (3) strong confinement, and (4) low-loss interconnection to other optical fibers and fiberized components.[25] These facts open an even greater range of possibilities for the PCFs future applications.

MATERIALS AND METHODS

Materials. Sodium bis(2-ethylhexyl) sulfosuccinate (AOT, 99% Sigma), isooctane (Merck, MW = 114.23 g mol $^{-1}$, δ = 0.688 g cm $^{-3}$), *n*-heptane (Merck, MW = 100.21 g mol $^{-1}$, δ = 0.684 g cm $^{-3}$), *n*-hexane (Merck, MW = 86.18 g mol $^{-1}$, δ = 0.6548 g cm $^{-3}$), cyclohexane (Merck, MW = 84.16 g mol $^{-1}$, δ = 0.776 g cm $^{-3}$), and sodium tetraethyl orthosilicate (TEOS, Aldrich, 98%) were used without further purification. For microemulsion preparation, only triple-distilled water was used.

Materials Synthesis. Experiments were performed on water/AOT/alkane microemulsion systems. The composition of the microemulsion is given in terms of W_0, the ratio of water to surfactant molar concentrations, and S_0, the ratio of oil to surfactant molar concentration. Microemulsion systems of S_0 = 30 and W_0 = 60 were prepared using the injection method[26] by mixing an appropriate quantity of water with an AOT solution in oil. The resulting microemulsions were placed in Teflon-stoppered test tubes and aged for 24 h at 40 °C before used. Four microemulsion template systems were tested using isooctane, *n*-heptane, *n*-hexane, and cyclohexane as the oil phase. As the critical micellization concentration (CMC) of AOT[27] in both oil and water is low compared with the concentration used here, it can be presumed that all the surfactant molecules are localized at the interface between water and oil.

To obtain the SiO_2 materials, 11.6 mL of TEOS was dissolved in 2 mL of water and stirred for 10 min at 500 rpm. Then, a solution of 1.1 g of NaOH in 20 mL of water was added drop-by-drop to the TEOS solution while stirring. A minute later, the above-described microemulsion systems were poured into the mixture and stirred for 5 min. The resulting gels were left for 8, 15, and 24 h in an autoclave at 100 °C. The obtained materials were filtered, washed with triple-distilled water, and left to dry at room temperature. Finally, they were calcined for 7 h at various temperatures from 500 to 800 °C in an air flux.

Field Emission Scanning Electron Microscopy (FE-SEM). Field emission scanning electron microscopy (FE-SEM) was performed using a FESEM ULTRA PLUS. Resolution: 0.8 nm at 30 kV; accelerating voltage: 0.02 V−30 kV (continuously adjusted in steps of 10 V); magnification range 12−1000000×; sizes of openings: 7.5, 10, 20, 30, 60, and 120 μm. Local compensation of charge, by injecting nitrogen gas.

Transmission Electron Microscopy (TEM). Transmission electron microscopy was performed using a Philips CM-12 transmission electron microscope equipped with a digital camera MEGA VIEW-II DOCU and operated at 120 kV with magnification of 730000×. High-resolution transmission microphotographs were taken using a Libra 200 FE OMEGA transmission electron microscope operated at 200 kV with magnification of 1000000×. Observations were made in a bright field. Powdered samples were placed on cooper supports of 2000 mesh.

X-ray Powder Diffraction. Powder X-ray diffraction (XRD) data were collected with a Philips PW 1710 diffractometer with Cu Kα radiation (λ = 1.5418 nm) and graphite monochromator operated at 45 kV, 30 mA, and 25 °C.

FT-IR Spectroscopy. Infrared spectra were collected using a Varian 670 Fourier transform infrared spectrometer (FT-IR) equipped with a pneumatic motion interferometer. The spectra is a result of 100 accumulating scans measured peak to peak with a spectral resolution of 4 cm $^{-1}$. To avoid coadsorbed water, the samples were dried under vacuum until constant weight was achieved and diluted with KBr powder before the FT-IR spectra were recorded.

UV−vis and Fluorescence Spectroscopy. The UV−vis and fluorescence absorption spectrum was recorded at 298 K by a UV−vis−NIR scanning spectrophotometer (Beckman, model DU 640) and a Varian Cary Eclipse spectrofluorometer (under excitation by UV light at 220 nm), respectively, using a 1 cm path length quartz cell. The spectrum was obtained for the M1 and M2 materials that had been sonicated in ethanol to yield homogeneous dispersions. Pure ethanol solution was used as blank.

RESULTS AND DISCUSSION

Synthesis Conditions. In general, several factors should be considered carefully when selecting a suitable surfactant for a specific synthesis reaction in reverse micelles. Among the various surfactants exploited in formulating microemulsions for nanoparticle synthesis, we choose the anionic double-chained surfactant AOT because it can form reverse micelles without the need of cosurfactants.[16] Furthermore, irrespective of the nature of the apolar solvent, AOT molecules form nearly spherical and monodisperse water-containing reverse micelles, the size of which is quite dependent on the surfactant concentration and regulated mainly by W_0. For the nanoparticle synthesis we worked inside the AOT isotropic fluid phase L_2 where the structures of aggregates are only spheres.[28]

The dynamic nature of the reverse micelles plays a key role in the formation of the final nanoparticle morphology. This, in turn, is closely related to the rigidity of the nanodroplet oil−water interface.[16] Figure 1 shows the SEM microphotographs of the four different materials obtained by TEOS hydrolysis inside microemulsion droplets of different film rigidity (obtained by changing the oil template microemulsion phase), after hydrothermal treatment (100 °C, 24 h) and calcination (650 °C, 7 h) in air flux. Fibrils were obtained only when the oil phases used in the template microemulsion are *n*-hexane and cyclohexane. When isooctane or *n*-heptane was used as oil phase, a bicontinuous material was obtained. The film flexibility is increased by augmenting oil molecular weight (from cyclohexane to isooctane); contrary to what might be expected, the fiber structures are formed in those emulsions whose droplets have a more rigid film. That is, fibrils formation requires a certain stiffness in the oil−water interface.

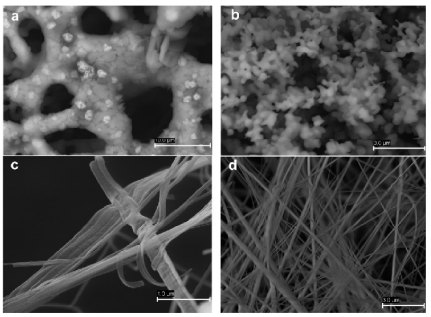

Figure 1. SEM microphotographs of SiO_2 materials templated with (a) water/AOT/isooctane, (b) water/AOT/*n*-heptane, (c) water/AOT/*n*-hexane, and (d) water/AOT/cyclohexane microemulsions.

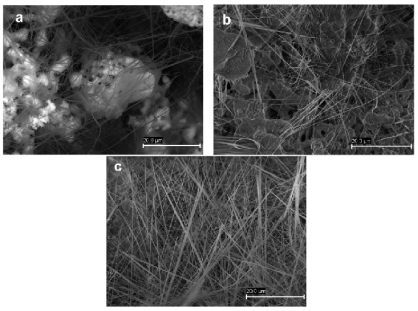

Figure 2. SEM microphotographs of SiO_2 materials obtained from water/AOT/cyclohexane template microemulsion after (a) 8 h, (b) 15 h, and (c) 24 h of hydrothermal treatment.

To explain this we must remember that in our case the syntesis is performed through a hydrothermal treatment. Essentially, there are two mechanisms proposed for the microemulsion-mediated synthesis of inorganic nanowires/nanorods: the template-directed growth and the oriented aggregations.[16,29] In the template-directed growth mechanism, elongated water droplets or interconnected water channels play the role of template to induce the formation of elongated nuclei, which finally grow into nanorods with dimensions considerably larger than the templates. In the oriented aggregation mechanism, precipitation within spherical water droplets initially results in the formation of surfactant-encapsulated primary nanoparticles which subsequently undergo oriented aggregation involving linear attachment and coalescence owing to specific interactions of inorganic crystals with surfactants leading to the growth of single-crystalline nanowires. Under hydrothermal conditions, an oriented aggregation mechanism is usually adopted because reverse micelles may be destroyed under synthesis conditions.[16] When the film is flexible (oil phase: isooctane, *n*-heptane), the resulting material presents a spongy structure denoting the formation of an interconnected water channels in the template microemulsion. By

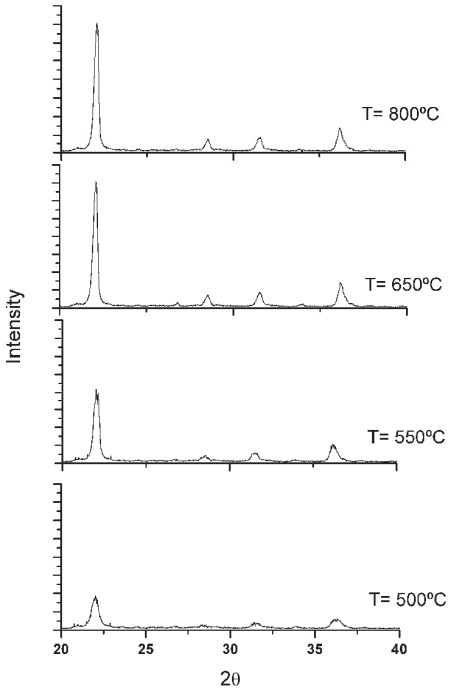

Figure 3. X-ray diffraction patterns of SiO_2 materials templated with water/AOT/hexane microemulsion calcined at 500, 550, 650, and 800 °C.

subjecting the microemulsion to the effects of hydrothermal treatment, reverse micelles are broken as shown in the oriented aggregation mechanism, and due to their flexible interface, the nanodroplets merge adopting a bicontinuous structure. When *n*-hexane and cyclohexane are used instead of isooctane or *n*-heptane, the nanodroplet films seems to be rigid enough to prevent the formation of interconnected channels.

At light of the obtained results, it was found that hydrothermal treatment is a crucial point in the synthesis of materials. Therefore, for those microemulsion systems giving rise to fibrils (water/AOT/*n*-hexane and water/AOT/cyclohexane), different times of treatment were tested. Figure 2 shows the SEM microphotographs of materials obtained from water/AOT/cyclohexane template microemulsion after 8, 15, and 24 h of hydrothermal treatment. It can be seen that the number of fibrils increases with the time of hydrothermal treatment, no differences in the material structure were seen after 24 h. Similar results were seen for the material templated with water/AOT/*n*-hexane (see Supporting Information).

Usually, the products obtained by alkoxide hydrolysis reverse micelles are amorphous or poorly crystallized, and subsequent calcinations are necessary for obtained the desired crystalline nanophase.[16,30,31] Figure 3 shows X-ray diffraction patterns (XRD) of M1 calcinated at 500, 550, 650, and 800 °C. The decrease in the full width at half-maximum (FWHM) of peaks

Table 1. Final Synthesis Conditions of Fibrous Materials

material	microemulsion system	hydrothermal treatment	calcination conditions
M1	water/AOT/*n*-hexane	24 h, 100 °C	7 h, 650 °C
M2	water/AOT/cyclohexane	24 h, 100 °C	7 h, 650 °C

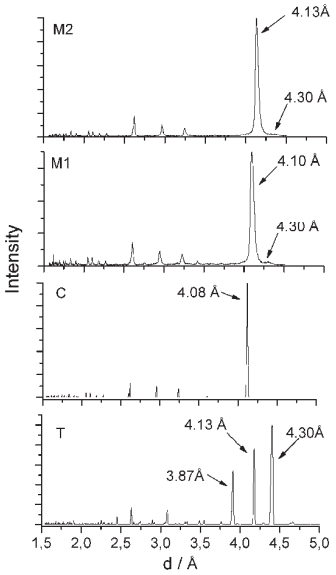

Figure 4. X-ray diffraction patterns of SiO_2 materials templated with water/AOT/hexane (M1) and water/AOT/cyclohexane (M2) microemulsions. C: α- cristobalite; T: α-tridymite.

with increasing temperature indicates an increase in the material crystallinity. No considerably differences were seen between the material calcined at 650 and 800 °C.

The synthetic conditions that resulted in unusual fibrous structure materials are summarized in Table 1. Their characterization is discussed below.

Material Characterization. Sample diffractograms were compared to the RRUFF database:[32] R061107.9 for α-cristobalite and R090042.9 for orthorhombic α-tridymite. Hydrous SiO_2 phases are widespread in volcanic sedimentary rocks associated with postvolcanic hydrothermal activity, devitrification, and diagenetic alteration. Opals are micro- and noncrystalline forms of hydrated silica with high degree of structural disorder.[33] On the basis of powder X-ray diffraction (XRD) data, Jones and Segnit[34] distinguished three hydrous silica phases at low temperatures: amorphous opal (opal-A), disordered cristobalite with significant tridymite stacking (opal-CT), and more ordered cristobalite with minor tridymite stacking (opal-C). Opal-CT and opal-C are considered as microcrystalline varieties of hydrous silica.

The two fibrous synthesized materials, M1 and M2, present the structure of opal-CT (Figure 4). They exhibit XRD patterns strongly resembling that of α-cristoballite with slight broadening

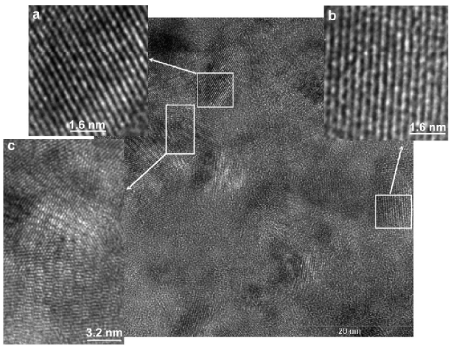

Figure 5. High-resolution TEM microphotograph of a single fiber section, showing the lattice planes. Cristobalite stacking (a, b) interrupted by several planar trydimite boundaries (c).

of the Bragg reflections, slight shift to larger *d*-spacings, and a weak extra peak near 4.30 Å—all which are characteristics of opal-CT and due to the presence of trydimite-type layers within the cristobalite structure. M2 exhibits a slight shift to larger *d*-spacing with respect to M1, which corresponds to a major abundance of tridymite-type stacking faults in the [111] direction of the cristobalite three-layered structure.[33] No peaks related to quartz ($2\theta = 26°$) or phyllosilicates ($2\theta = 6°$)[35] are identified (see Supporting Information).

Using transmission electron microscopy (TEM) and XRD, Elsea and Rice[36] concluded that the dominant phase in opal-CT samples was essentially α-cristobalite with a high degree of stacking disorder. Figure 5 shows the cristobalite stacking (a, b) interrupted by several planar tridymite boundaries (c) in M1 material; similar results were obtained for M2. The results are consistent with X-ray diffractions.

The FT-IR spectroscopic study performed on both samples show the characteristic peaks of α-cristobalite (1200 and 622 cm^{-1}) just with weak additional absorption bands at the 3700−3200 cm^{-1} range belonging with tridymite (see Supporting Information).

Opal-CT Microstructure. FE-SEM (Figure 1c,d) and TEM (Figure 6) microphotographs revealed an unusual fibrous arrangement. Both samples present a very similar microstructure; they are long fibrils of 30−50 nm diameter and greater than 20 μm length. These form bundles of 100−200 nm distributed in different orientations. Opals fibrils are made up of α-SiO_2 polyhedral spheres that are monodisperse in size ($d \approx 2$ Å) (Figure 7). They form, as usual, (111) hexagonal layers superimposed on one another along the [111] axis to form an fcc (face-centered-cubic) lattice.[37] Each layer perpendicular to the [111] direction is a triangular lattice with periodicity equal to sphere diameter, $d = a/\sqrt{2}$, where a is the fcc lattice constant, and it is shifted with respect to the previous one by a quantity equal to $d/\sqrt{3}$ as shown in Figure 7c; this is the so-called graphite layer arrangement.[38] A vertical cross section of the opal structure in the *yz* plane is shown Figure 7d. The distance between two planes of spheres d_{111} along the [111] direction is given by[38]

$$d_{111} = \sqrt{\frac{2}{3}}d = \frac{a}{\sqrt{3}} \quad (1)$$

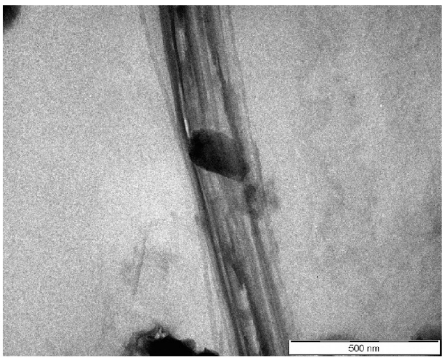

Figure 6. TEM microphotograph of M1 opal-CT fibrils.

The height H_{cap} of the sphere caps and their radius R_{cap}, also shown in Figure 7d, at the contact point between sphere caps are the following:[38]

$$H_{cap} = \left(1 - \sqrt{\frac{2}{3}}\right) d, \quad R_{cap} = \frac{d}{2\sqrt{3}} \qquad (2)$$

The lattice constant (a = 2.83 Å) is on the order of angstroms as for ordinary crystals as well as the computed values of d_{111} = 1.63 Å, H_{cap} = 0.37 Å, and R_{cap} = 0.58 Å. The fibrous microstructure of opals is remarkable and unusual; to our knowledge only some natural pink opals have this structure.[15] Natural fibrous opals may occur only in a very specific geological environment, and its fibrous microstructure is due to the presence of a phyllosilicate.[15] As we have confirmed the absence of phyllosilicates in the materials, it can be said that fibril microstructure is a consequence of the specific conditions of the microemulsion-hydrothermal mediated synthetic route. We believe that an oriented aggregation mechanism may be operative in our molecular sieve synthesis influenced by the film rigidity and that the final opal-CT microcrystalline structure was achieved after calcination.

It cannot be appreciate any significant effect on particle size by changing the oil phase in microemulsion template system; however, the changes of the oil phase from *n*-hexane to cyclohexane and the consequent increment of the film rigidity cause a change in the opals-CT microstructure. M1 fibrils appear to be somewhat more flexible than those of M2 in accordance with an increase in the film stiffness going from hexane to cyclohexane. Furthermore, the material synthesized by water/AOT/cyclohexane microemulsion (M2) presents a small increase of stacking disorder in the cristobalite layers. It is assumed that an increase of film stiffness hinders the TEOS hydrolysis and leads to a less tidy end product. This apparently minimum effect has a great influence in the material optical properties as shown below.

Optoelectronic Studies of Synthetic Opals. There are mainly two types of photoluminescence (PL) emission in Si nanostructures at room temperature. The yellow−orange−red PL bands with a slow decay of the order of μs to ms (the so-called "slow bands", abbreviated as the S-band) is usually dominant and receives the most attention, while the fast blue−green PL bands (the so-called F-band with a characteristic decay time on the order of ns) is observed and reported infrequently. The last ones are predominantly in rapidly oxidized porous silicon structures.[39]

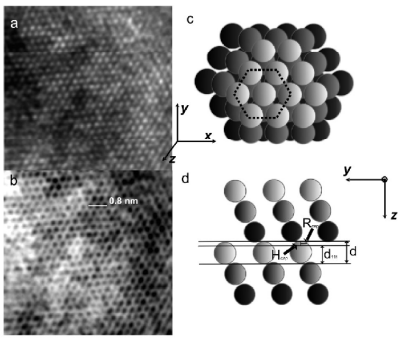

Figure 7. (a) High-resolution TEM microphotograph of a single fiber section, showing the close-packed fcc lattice. (b) For better viewing of the (a), the image colors were reversed. (c) Scheme of the close-packed fcc lattice seen from [111] direction; hexagonal face in dashed black line. (d) Cross-sectional view of an fcc lattice oriented along [111] direction; the region between two consecutive planes is defined by two straight lines.

Figures 8 and 9 show the photoluminescence (PL) emission spectra of M1 and M2 materials excited at 220 nm. Both samples exhibited largely Stokes-shifted (short wavelength) and band-edge (long wavelength) emissions that depend largely from their microestructure. M1 presents a high intensity ultraviolet A (UVA) PL while M2 emits ultraviolet A and B radiations. Also, both materials PL spectra show two peaks of much less intensity that correspond to visible radiation: orange and green PL for M1 and bright red and yellow PL for M2. The dissimilarities between emission spectra of the two samples confirm the fact that they have different morphological properties.

Besides the differences in PL decay time, the F- and S-bands have different spectral behavior. While the S-band has an almost stable position under different excitation wavelengths, the F-band peak is shifted with the excitation wavelength.[39] From the analysis of Figure 10, it can be seen that bands around 550−700 nm present an almost stable spectra location with the increment of excitation wavelength, while there is an increment of intensity. Nevertheless, those bands at 270−350 nm shifts toward fewer wavelengths with the augment of excitation energy. The intensity and form of spectral bands are also very different. So, we identify the first as S-bands and the seconds as F-bands. We think that different types of luminescence centers in the Si oxide layers with energy around 3.6−3.8 and 1.9−2.1 eV are responsible for the ultraviolet (F-bands) and visible light emissions (S-bands). The luminescence mechanism of siliceous materials is persistently a focus of research, and many models have been proposed;[40] but so far it is still not entirely understood. Some authors proposed that more than one type of mechanism were needed for interpret the PL from nanoscale Si/Si oxide systems. It was suggested that for the S (slow)-band luminescence the quantum confinement (QC) model[41] works. The F (fast)-band luminescence has been interpreted as a part of two districts mechanisms: (i) intrinsic optical recombination in ultrasmall Si nanoparticles, with strong quantum-confinement effect and a large bandgap opening,[42] or (ii) recombination in defective silicon oxide particles.[43] It is difficult to distinguish the correct model of the F-bands in a given Si nanostructure.[39]

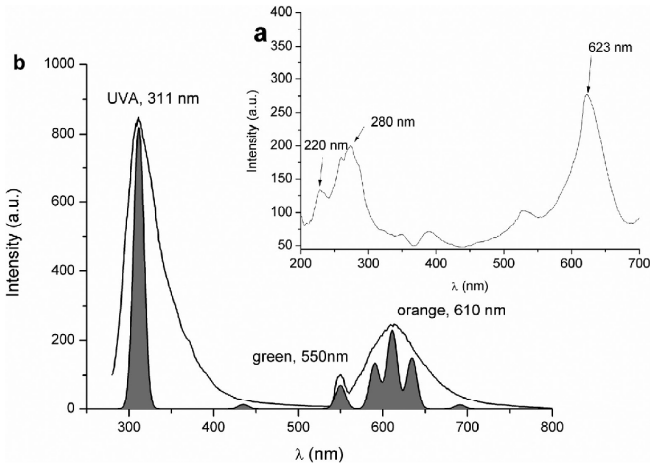

Figure 8. (a) Excitation and (b) PL spectra (λ = 220 nm) of M1. Relevant deconvolute peaks (shown in dark gray).

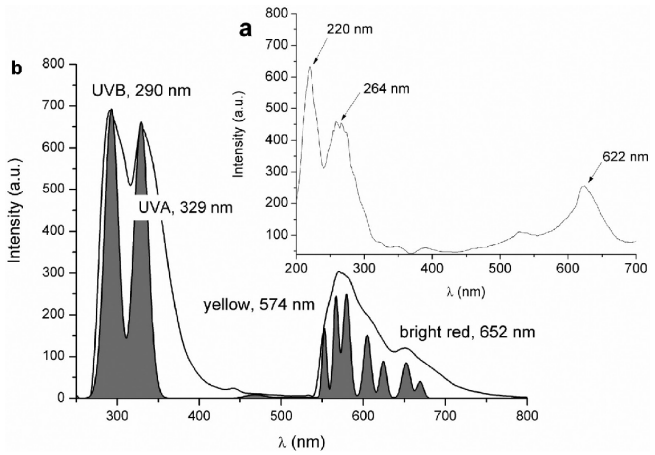

Figure 9. (a) Excitation and (b) PL spectra (λ = 220 nm) of M2. Relevant deconvolute peaks (shown in dark gray).

It was known that crystalline Si (c-Si) nanoparticles of sizes comparables to or smaller than the Si exciton Bohr radius in bulk (4.3 nm) show a quantum confinement effect resulting in an enhanced recombination of excitons. Therefore, the optical properties of c-Si nanoparticles and nanostructures are also sensitive to the surface geometry and chemistry.[44] On basis of these assumptions, we think that a combination of both mechanisms operate simultaneously in our materials and leads to orange−red luminescence (S-band luminescence) and blue−green and ultraviolet (F-band luminescence) components. In our materials, the F-bands (UV bands) are of greater intensity and different according to the material oxide layers distribution in the materials; consequently, we can assume that the predominant effect seems to be the distortion of the oxide layers on the quantum confinement. M2 with a high proportion of defective layer oxide surfaces shows two F-band emissions. In general, photoexited charge carriers (electron and hole) recombine with each other through several recombination processes such as direct band-to-band coupling and/or shallow/deeply trapped potential states.[45] Defect sites existing on the surface oxide layers provide deeply trapped potential states which induce such largely Stokes-shifted emissions.[45] The intensity change of the largely Stokes-shifted emission is believed to be due to the surface density change of defective emission states,[46] and in our materials this density change of surface defect states come from the different array of oxide layers in the material microcrystalline structures.

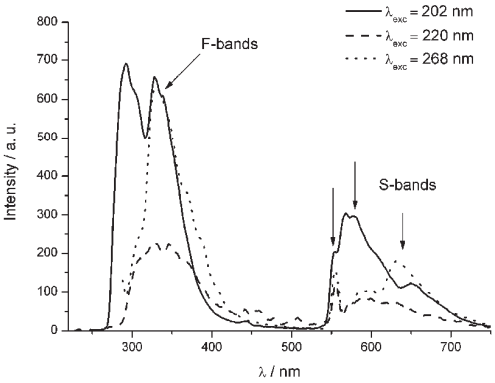

Figure 10. Photoluminescence spectra of M2 excited at different wavelengths.

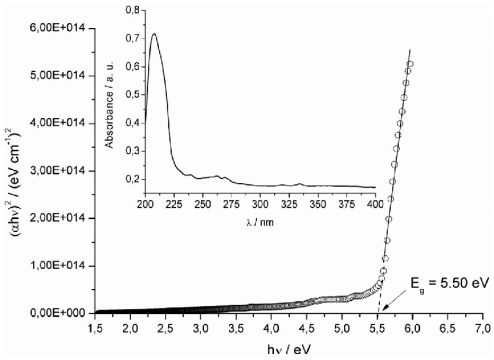

Figure 11. Estimation of band gap energy by plotting $(\alpha h\nu)^2$ vs $h\nu$. Inset: M1 absorption spectrum.

The band gap energy was estimated by plotting $(\alpha h\nu)^m$ of the microcrystalline opals against the photon energy ($h\nu$), as shown in Figure 11 where α is the absorption coefficient, $h\nu$ is the photon energy, and E_g is the band gap energy. We assume that the transition of electrons through the forbidden zone occurs between states corresponding to the maximum of the gap and the valence band minimum conductance, taking into account only direct transitions $m = 2$. The adsorption (A) is converted to the absorption coefficient using the following relationship:[47] $\alpha = (2.303 \times 10^3/lc)A\rho$, where A is the adsorption of the sample, ρ is the density of crystobalite (2.33 g cm^{-3}), l is the cuvette length (1 cm), and c is the concentration of the sample (c_{M1} = 0.001 g cm^{-3} and $c_{M2} = 2.1 \times 10^{-4}$ g cm^{-3}). The band gap energy was determined by extrapolating the adsorption coefficient (α) to zero. The computed band gap values ($E_{g,M1}$ = 5.50 eV and $E_{g,M2}$ = 4.41 eV) are highly inferior to the experimental band gap values obtained for SiO_2 polymorphs (8.9 eV for α-quartz and superior values for β-quartz, α-cristobalite, β-cristobalite, and tridymite[48]) and similar to those obtained for silicon-based metal oxide semiconductors (MOS).[49,50]

CONCLUSIONS

In the above study, we have designed a simple and controllable route for the synthesis of opals-CT materials with unusual fibrous microstructure similar to those existed in the nature using a bottom-up microemulsion droplet system as chemical microreactor. The microcrystalline structure of opals and consequently their optoelectronic properties are a result of a particular combination of all the relevant microemulsion parameter, hydrothermal treatment time, and calcination temperature.

The obtained fibrils are longer than 20 μm with a diameter of 30−50 nm and are clustered forming bundles of 100−200 nm distributed in different orientations. Fibrils are composed by α-SiO_2 polyhedral spheres that are monodisperse in size ($d \approx 2$ Å) packed, as usual in photonic crystals, in (111) hexagonal layers superimposed on one another along the [111] axis to form a 3D fcc lattice. The lattice constant (a = 2.83 Å) is on the order of angstroms as for ordinary crystals and very inferior to those obtained until now for synthetic opals. Because of their unusual microstructure, they exhibited short and long wavelengh photolumiscence emissions which differ according to the crystobalite−trydimite stacking. The material with high content of trydimite-type stacking faults shows high intensity ultraviolet A and B just with minor intensity bright-red and yellow emission, while the material that presents a high ordered script of cristobalite emits ultraviolet A, orange, and green light radiations. It is believed that a combination of a quantum mechanism and the presence of defective Si oxide layers are the responsible for the simultaneous emissions of S- and F-bands.

Additionally, the computed band gap values (5.50 and 4.41 eV) for both synthesized materials are similar to those obtained for silicon-based metal oxide semiconductors and highly inferior to the experimental band gap values obtained for pure crystalline SiO_2 polymorphs (8.9 eV).

ASSOCIATED CONTENT

Supporting Information. Characterization of M1 and M2 materials by DRX patterns, d-spacing, FT-IR spectra, and SEM microphotographs. This material is available free of charge via the Internet at http://pubs.acs.org.

AUTHOR INFORMATION

Corresponding Author

*Tel: +54 291 4595159. Fax: +54 291 4595160. E-mail: pmessina@uns.edu.ar.

ACKNOWLEDGMENT

The authors acknowledge Universidad Nacional del Sur (PGI 24/ZQ07), Concejo Nacional de Investigaciones Científicas y Técnicas de la República Argentina (CONICET, PIP-11220100100072.), Xunta de Galicia (Project No. PXI20615PN), and Education Audiovisual Culture, Executive Agency European Commission (EMUNDUS18) for their financial support. V.V. has a postdoctoral fellowship of CONICET. P.M. is an adjunct researcher of CONICET.

REFERENCES

(1) Hansen, K. P.; Iman, H. *Optik Photonik.* **2010**, *2*, 37–41.
(2) Alivisatos, P. *Nature Biotechnol.* **2004**, *22* (1), 47–52.
(3) Zhu, J.; Peng, H.; Connor, S. T.; Cui, Y. *Small* **2009**, *5* (4), 437–439.

(4) Gordon, R.; Sinton, D.; Kavanagh, K. L.; Brolo, A. G. *Acc. Chem. Res.* **2008**, *4* (8), 1049–1057.
(5) Blanco, A.; Chomski, E.; Grabtchak, S.; Ibisate, M.; John, S.; Leonard, S. W.; Lopez, C.; Meseguer, F.; Miguez, H.; Mondia, J. P.; Ozin, G. A.; Toader, O.; van Driel, H. M. *Nature* **2000**, *405*, 437–440.
(6) Vlasov, Y. A.; Bo, X.-Z.; Sturm, J. C.; Norris, D. J. *Nature* **2001**, *414*, 289–293.
(7) Rogach, A. L.; Kotov, N. A.; Koktysh, D. S.; Ostrander, J. W.; Ragoisha, G. A. *Chem. Mater.* **2000**, *12*, 2721–2726.
(8) Nebel, C. E. *Nature Photonics* **2009**, *3*, 564–566.
(9) Badding, J. V.; Copalan, V.; Sazia, P. *Photonic Spectra* **2006**, 1–6.
(10) Gorelik, V. S.; Zlobina, L. I.; Troitskii, O. A.; Chanieva, R. I. *Inorg. Mater.* **2009**, *45* (7), 785–790 and references therein.
(11) Kirchhof, J.; Kobelke, F.; Schuster, K.; Barteli, H.; Iliew, R.; Etrich, C.; Ledere, F. Photonic crystal fibers. In *Photonic Crystals: Advances in Design, Fabrication and Characterization*; Busch, K., Lölkes, S., Wehrspohn, R. B., Föll, H., Eds.; Wiley-VCH Verlag GmbH & Co.: Weinheim, 2004; pp 266−286.
(12) Russell, P. *Science* **2003**, *299*, 358–362 and references therein.
(13) Astratov, V. N.; Bogomolov, V. N.; Kaplyanskii, A. A.; Prokofiev, A. V.; Samoilovich, L. A.; Samoilovich, S. M.; Vlasov, Y. A. *Nuovo Cimento Soc. Ital. Fis., D* **1995**, *17*, 1349–1354.
(14) Sakoda, K. In *Optical Properties of Photonic Crystals*; Springer-Verlag: Berlin, 2005.
(15) Fritsch, E.; Gaillou, E.; Ostroumov, M.; Rondeau, B.; Devouard, B.; Barreau, A. *Eur. J. Mineral.* **2004**, *16*, 743–752.
(16) Qi, L. *Encycl. Surf. Colloidal Sci.* **2006**, 6183–6207 and references therein.
(17) Pinna, N.; Wild, U.; Urban, J.; Schlögl, R. *Adv. Mater.* **2003**, *15*, 329–331.
(18) Kaneko, D.; Shouji, H.; Kawai, T.; Kon-No, K. *Langmuir* **2000**, *16*, 4086–4089.
(19) Zhang, P.; Gao, L. *Langmuir* **2003**, *125*, 208–210.
(20) Cao, M. H.; Hu, C. W.; Wang, E. B. *J. Am. Chem. Soc.* **2003**, *125* (11), 196–197.
(21) Zhang, D. F.; Sun, L. D.; Yin, J. L.; Yan, C. H. *Adv. Mater.* **2003**, *15*, 1022–1025.
(22) Yates, M. Z.; Ott, K. C.; Birnbaum, E. R.; McCleskey, T. M. *Angew. Chem., Int. Ed.* **2002**, *41*, 476–478.
(23) Lin, J. C.; Diere, J. T.; Yates, M. Z. *Chem. Mater.* **2003**, *15*, 2764–2773.
(24) Cao, M. H.; Wang, Y. H.; Guo, C. X.; Qi, Y. J.; Hu, C. W. *Langmuir* **2004**, *20*, 4784–4786.
(25) Brambilla, G.; Xu, F.; Horak, P.; Jung, Y.; Koizumi, F.; Sessions, N. P.; Koukharenko, E.; Feng, X.; Murugan, G. S.; Willkinson, J. S.; Richardson, D. J. *Adv. Inf. Opt. Photonics* **2009**, *1*, 107–161.
(26) Alexandridis, P.; Holzwarth, J. F.; Hatton, T. A. *Langmuir* **1993**, *9*, 2045–2052.
(27) Moha-Ouchane, M.; Peyrelasse, J.; Boned, C. *Phys. Rev. A* **1987**, *35*, 3027–3032.
(28) Alexandridis, P.; Holzwarth, J. F.; Hatton, T. A. *J. Phys. Chem.* **1995**, *99*, 8222–8232 and references therein.
(29) Qi, L. *Coord. Chem. Rev.* **2010**, *254*, 1054–1071.
(30) Hung, I.-M.; Hung, D.-T.; Fung, K.-Z.; Hon, M.-H. *J. Eur. Ceramic Soc.* **2006**, *26*, 2627–2632.
(31) Chen, S.-Y.; Tang, C.-Y.; Lee, J.-F.; Jang, L.-Y.; Tatsumi, T.; Cheng, S. *J. Mater. Chem.* **2011**, *21*, 2255–2265.
(32) http://rruff.info/.
(33) Ilieva, A.; Mihailova, B.; Tsintsov, Z.; Petrov, O. *Am. Mineral.* **2007**, *92*, 1325–1333.
(34) Jones, J. B.; Segnit, I. R. *J. Geol. Soc. Aust.* **1971**, *18*, 57–68.
(35) Ghisoli, C. *Sci. Acta* **2008**, *2*, 27–34.
(36) Elzea, J. M.; Rice, S. B. *Clays Clay Miner.* **1996**, *44*, 492–500.
(37) Baryshev, A. V.; Kaplyanskii, A. A.; Kosobukin, V. A.; Samusev, K. B.; Usvyat, D. E.; Limonov, M. F. *Phys. Rev. B* **2004**, *70*, 1131041.
(38) Grosso, G.; Pastori Parravicini, G. *Solid State Physics*; Academic Press: New York, 2000.
(39) Valenta, J.; Fucikova, A.; Pelant, I.; Kůsová, K.; Dohnalová, K.; Aleknavičius, A.; Cibulka, O.; Fojtík, K. G. *New J. Phys.* **2008**, *10*, 073022 and references therein.
(40) Qin, G. G.; Li, Y. J. *Phys. Rev. B* **2003**, *68*, 085309 and references therein.
(41) Qin, G. G.; Jia, Y. Q. *Solid State Commun.* **1993**, *86*, 559–563.
(42) Kanemitsu, Y. *J. Lumin.* **2002**, *100*, 209–214.
(43) Švrček, V.; Sasaki, T.; Shimizu, Y.; Koshizaki, N. *Appl. Phys. Lett.* **2006**, *89*, 213113.
(44) Komuro, S.; Kato, T.; Morikawa, T.; ÓKeeffe, P.; Aoyagi, Y. *J. Appl. Phys.* **1996**, *80*, 1749.
(45) Gaponenko, S. V. *Optical Properties of Semiconductor Nanocrystals*; Cambridge University Press: New York, 1998.
(46) Chang, C. L.; Fogler, H. S. *Langmuir* **1997**, *13*, 3295–3307.
(47) Serpone, N.; Lawless, D.; Khairutdinov, R. *J. Phys. Chem.* **1995**, *99*, 16646–16654.
(48) Gnani, E.; Reggiani, S.; Colle, R.; Rudan, M. *VLSI Design* **2001**, *13* (1−4), 311–315.
(49) Yamasaki, T.; Kaneta, C.; Uchiyama, T.; Uda, T.; Terakura, K. *Phys. Rev. B* **2001**, *63*, 1153141–1153145.
(50) Städale, M.; Tuttle, B.; Fischer, B.; Hess, K. *J. Comput. Electron.* **2002**, *1*, 153–159.

4.2 Articles preparing for publication.

Fibrinogen Hydrogels for the directed synthesis of Stishovite nanostructures

Fibrinogen Hydrogels

Self-assembly of biomolecules is now emerging as a new route to produce novel materials and to complement other materials (e.i. ceramics, metals, alloys, synthetic polymers and other composite materials). Rapid developments in biotechnology have rekindled the field of materials science. Considerable advances have been made in the use of peptides and proteins as building blocks to produce a wide range of biological materials for diverse applications[85-88].

Understanding the mechanical properties of protein gels is of great importance to deciphering basic biological functions and to developing new health care and food technologies. In the simplest definition, a gel is a material that is composed primarily of liquid, typically water, but exhibits solid-like mechanical properties. Important proteins that can form biological gels include fibrin, collagen, actin, vimentin, neurofilaments, microtubules and casein[89-93].

The study of gelation dynamics and gel network structure of fibrinogen is of significance not only for the characterization and understandings of physicochemical properties of gels, but also physicochemically, such as hemostasis and thrombosis. Blood coagulation mechanism is constituted of a complex cascade accompanied by various factors, and this cascade amplifies and enhances an efficiency of the coagulation like an avalanche. The final stage of the cascade is the fibrin network formation induced by serine protease, thrombin. The effect of additives to the coagulation mechanism is quite important for the medical fields, and the action of heparin in antithrombosis is representative.

Blood clots are highly extensible supramolecular protein polymers formed from well-separated, relatively straight and stiff fibers ∼200 nm in diameter. When stretched, the fiber network aligns in the direction of the applied strain and the individual fibers stretch, forcing the fibrin monomers that make up the fibers to extend. Ultimately, it is this molecular unfolding that allows clots to stretch so far. Thus, understanding fibrin clot mechanics requires knowledge of the mechanical response and the corresponding structural changes spanning from the centimeter scale to the nanometer scale[94].

Fibrinogen (FB) is one of the most abundant plasma proteins in the human body that has received much attention because of its role in mediating clot formation, cellular and matrix interactions, fibrinolysis, and wound healing. The conformation of surface-bound FB has been shown to play an important role in platelet adhesion and thrombus formation. In addition, human plasma FB has some intrinsic characteristics such as self-assembly[95-96] promotion of cell adhesion, and dual roles in calcium phosphate formation[97], that make the FB molecule a potential building block for the preparation of advanced biomaterials. Recent light scattering investigation ascertained clearly that the formation of fibrin gel proceed in a stepwise manner: activation of fibrinogen to originate the fibrin monomers and half-staggered polymerization of fibrin monomers (protofibril formation) in the first step, and a side-by-side association of protofibril (fiber growth) resulting the gel formation in the succeeding step[98-99].

The interaction between αC domain is the critical step in the fibrin gel formation. In fact, it has been reported that the fragment of the αC domain functions to inhibit (delay) the lateral aggregation by interfering the αC domains dissociated from the E domain. Furthermore, the NMR study on bovine fibrinogen showed that there is a structured region restricted by S-S bond in the αC fragment and αC domain is intrinsically unstable. Although it has been expected that the αC domain participates essentially in the process of lateral aggregation, the detailed interacting mechanism has not been clarified yet.

Several experimental parameters, such as concentration, pH value, and ionic strength, strongly affected the formation of FB fibrils as fibril networks, specifically under low pH conditions[100-101]. Mališauskas et al. reported that the charge state of the protein affects its self assembly into filamentous structures[104], and Arnaudov et al. suggested that the protein fibrils will form when the protein solution exists in an acidic environment with a pH that is far from the protein isoelectric point (IP)[105]. Results have lead to understanding of possible mechanisms for the pH-mediated self-assembly of FB molecules and the formation of FB fibrils and fibril networks in the absence of thrombin and has been provide feasible strategy that mat enable the design and fabrication of new functional biomaterials based on self-assembled protein fibrils and the formation of fibrinogen gels[102]. The change in the pH value induced the self-assembly of FB molecules and the subsequence formation of FB fibrils to form a three dimensional network (Fig. 4.1).

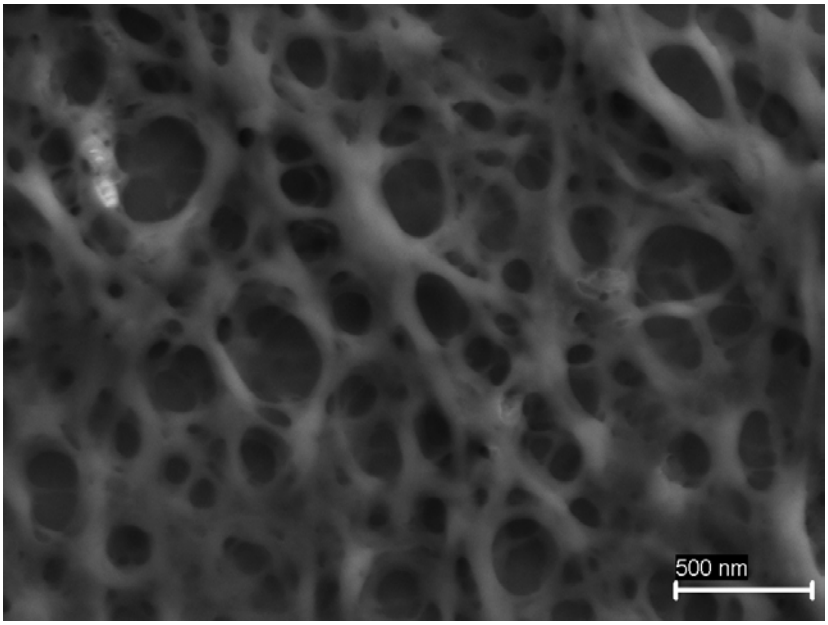

Figure 4.1: SEM images of fibrinogen gel formed at pH 3.

Fibrinogen has been shown to have three dependent thermal transitions when analyzed by differential scanning calorimeter[103-104]. The initial melting peak is located at 52.85 ^{o}C and 93.97 ^{o}C have been attributed to the denaturation of the end D and central E fragments of fibrinogen, respectively[105-106]. On the other hand, the peak at 76.62 ^{o}C has been related to the denaturation of the C-terminal of the Aα chains.[103] Thus, loss of solubility and turbidity increase observed in a study appeared to correlate well with the first thermal transition seen in calorimetry studies that is related to the formation of fibrinogen gels[107].

Ferry[107] proposed a two-step mechanism for gelation of denatured proteins. The initial phase being the conversion of native protein to the denatured state, and the second phase being the orientation of denatured protein into a gel network. Hermansson[108] further defined denatured

protein aggregation as “coagulation” when the interaction is random, and “gel forming” when there is order in the aggregation. The main factor driving the denatured protein to coagulation or gel formation is the rate of association, with slower rates favoring gel formation.

Materials and Methods

Materials. Bovine plasma fibrinogen, fraction I, type IV, was purchased from Sigma and used without purification. For the preparation of fibrinogen hydrogels protein solutions of different

concentrations, ranging from 10×10^{-3} to 40×10^{-3} g l^{-1}, were incubated in a water bath at 37 ^{o}C for 30 min. After that, the fibrinogen solutions were adjusted to pH 3 by addition of HCl 0.1 M. The solutions were incubated in a water bath at 37 ^{o}C or 70 ^{o}C for 2 hours. All chemical reagents were of analytical grade, and solutions were made using doubly distilled and degassed water.

Synthesis mesoporous silica materials. 0.2 g of fibrinogen was dissolved in 20 g of destilled water and then 3.067 g of sodium silicate was added at room temperature with magnetic stirring, giving a clear solution. To this reaction mixture, 6.1349 g of c-HCl was quickly added with vigorous magnetic stirring. The resulting gel mixture was stirred for 1 day at room temperature and subsequently heated for 1 day at 373 K in qan oven to increase the degree of silanol group condensation. The solid product was filtered off and dried at 373 K. The product was calcined in air under static conditions at 823 K.

*Conductivity***.** Conductivities were measured using a Kyoto Electronics conductometer model CM-117 with a K-121 cell type. The cell constant was determined using KCl solutions following the procedure suggested by Monk. All measurements were performed in a Polyscience model PS9105 thermostatted water bath. The protein was dissolved in water, the pH was adjusted to pH 3.0 with HCl 0.1 M, and the protein for pH 8.0 was dissolved in buffer Glycine-NaOH 50mM. The proteins solutions were heated at a linear rate of 24 ^{o}C/h.

Rheology. Rheological experiments were performed on a Bohlin CS-10 stress-controlled rheometer. A Couette geometry with a cup of 27.5 mm diameter and a bob type Mooney cell was used. The cell was heated by a reservoir of fluid circulating from a Julabo thermostated bath. The sample was equilibrated for at least 20 min prior to each experiment. Both steady and dynamic rheological experiments were performed at each temperature. Dynamic frequency sweep measurements were performed in the linear viscoelastic regime of the samples, as determined previously by dynamic stress sweep measurements. For the steady-shear experiments, an equilibration time of 90 s was given at each shear stress.

Field emission scanning electron microscopy (FE-SEM). Field emission scanning electron microscopy (FE-SEM) was performed using a FESEM UTLTA PLUS. This instrument operates in high vacuum, which added to its field lighting system, its detectors and its unique system of load balancing, enabling work to levels high resolution and low voltage in samples without shading. Resolution: 0.8 nm at 30 kV; accelerating voltage: 0.02V-30kV, continuously adjusted in steps of 10 volts; magnification range 12-1000000x; sizes of openings: 7.5 μm,10μm, 20μm, 30μm, 60μm and 120μm. Local compensation of charge, by injecting nitrogen gas.

X-ray powder diffraction. Powder X-ray diffraction (XRD) data were collected with a Philips PW 1710 diffractometer with Cu K_{α} radiation (λ = 1.5418Å) and Graphite monochromator operated at 45 kV; 30 mA and 25^{o}C.

Results and Discussion

It was previously reported that temperature, denaturants, ionic strength, concentration and pH are important for the aggregation and self assembly of proteins. Consequently, we have considered the effect of some of these factors on the conformation change of fibrinogen molecules and their self assembly. Fig. 4.2 shows the influence of temperature, pH and fibrinogen concentration on the ionic conductivity of the hydrogels. The fibrinogen series hydrogels show a good electrical conductivity. It was found that, both increasing the pH, as well as increasing the concentration of fibrinogen in the hydrogel led to a significant increase in the ionic conductivity of the formulation. In the case of hydrogels at pH 3.0, with the same protein content, there are no significant differences in conductivities through the temperature range. However, in the case of pH 8.0 a significant enhancement in the ionic conductivity of the hydrogel can be observed with increasing temperature, mainly at lower temperatures.

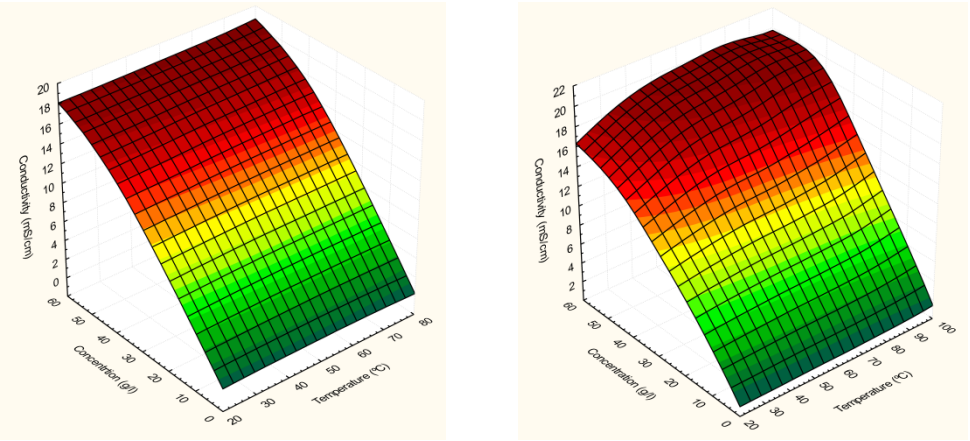

Figure 4.2: Plots of electrical conductivity of fibrinogen hydrogels against temperature and concentration at pH 3.0 (left) and pH 8.0 (right).

Protein solutions at pH 3.0 was used to form hydrogels due to pH 8.0 the protein coagulates and is not possible to obtain rheological results.

The conductivity of fibrinogen suspensions vary with de temperature and with the amount of the protein, as represent in Fig.1. We can observe the gelation curves at different pH (pH 3.0 and pH 8.0). At low protein concentration (10g/L) the gel formation begin at 30^{o}C, at higher protein concentration (50g/L) begin around 40^{o}C, due to a great change in the slope.

Figure 4.2 shows elastic modulus (G') obtained in oscillatory strain deformation sweeps measures as a function of fibrinogen concentration (C). Experiments were made at a frequency (ω) of 10 rad/s and at a temperature of 25°C, for gels obtained at 37°C (a) and at 70 °C (b). These experiments were performed in order to measure the linear viscoelastic region (LVR). The LVR is the deformation range where G' is independent of deformation (%γ)[109]. Breakdown of hydrogel structure, denoted by a rapid decline of G' marked the end of the LVR at the critical strain deformation.

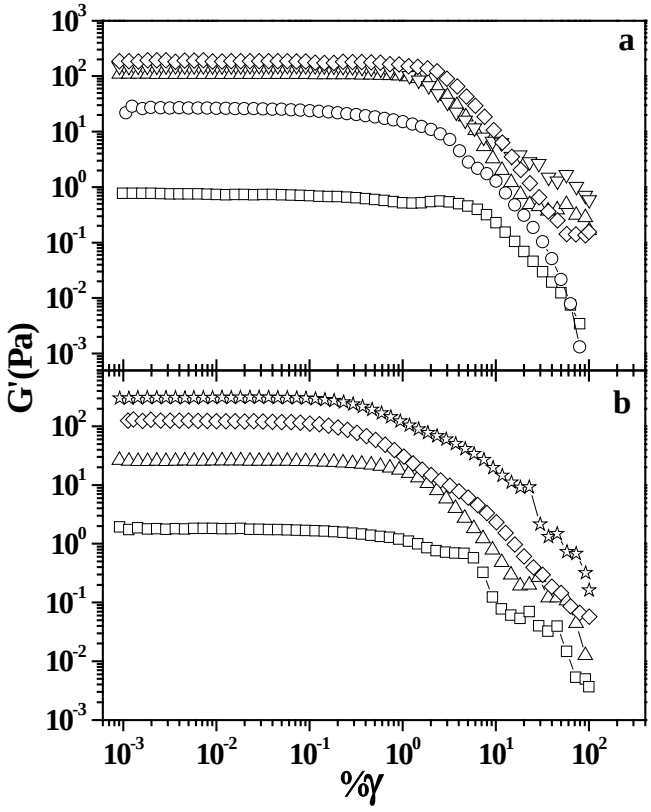

Figure 4.2. Strain sweeps made at 10 rad/s and 25 ºC as a function of fibrinogen concentration (g/L): (□), 10; (○), 15; (△), 20; (▽), 25; (◇), 30 and (☆), 40. Synthesized at (a) 37 ºC and (b) 70°C.

For hydrogels samples obtained at 37°C (Fig. 4.2.a), it is evident that the LVR is fibrinogen concentration dependent. For concentrations between 10 and 15 g/L, the linear viscoelastic region spans up to deformations around 0.1%. When the fibrinogen concentration is

increased, the strain-independent region goes at higher deformation values (1%). This augments in the LVR is due the increasing in the cross-linking density of the hydrogel samples. G'' developed similar tendency than that exhibited by elastic modulus (not shown), but G' values becomes considerably greater in magnitude than G'' values, with increasing concentration consequently the gel strength is dependent of the protein concentration, accordingly the cross-linking density. On the other hand, hydrogels obtained at 70°C (Fig. 4.2.b), exhibited a similar behavior than that depicted by samples obtained at 37°C. However, the strain-dependence region spans up to deformations up to around 0.1% for all the concentrations studied. This means that the hydrogels obtained at 37°C are more deformation-resistant than those obtained at 70°C.

Figure 4.3, a and b, depicts the elastic and viscous moduli obtained in frequency sweeps experiments for different concentrations at a deformation of 0.025% and at 25°C synthesized at 37 and 70°C respectively. For sample with concentration of 10 g/L obtained at 37°C (Fig. 4.3a), both G' and G" are almost independent with frequency. This behavior is similar to that observed in weak-gels of lamellar liquid crystals formed by anionic surfactants in water e.g., didodecyldimethylammonium bromide (DDAB) and aerosol OT (AOT) [110, 111]. At higher concentrations (Fig.4.3a), samples exhibited a gel-like behavior since both, the G' and G" moduli are frequency independent. It is evident in this figure that, the dynamic moduli values increase as the concentration augments, but G' values become greater in magnitude than that G'' values. The G' increasing causes that the gel strength enhancing stronger and harder due the relative increasing of G'/G". This may be due the augment in the cross-linking density with protein concentration augments. On the other hand, samples made at 70°C (Fig. 4.3.b) are almost frequency independent in all fibrinogen concentration studied. This means that for protein concentrations higher than 10 g/L, hydrogels made at temperature of 70°C are weaker than that obtained at 37°C.

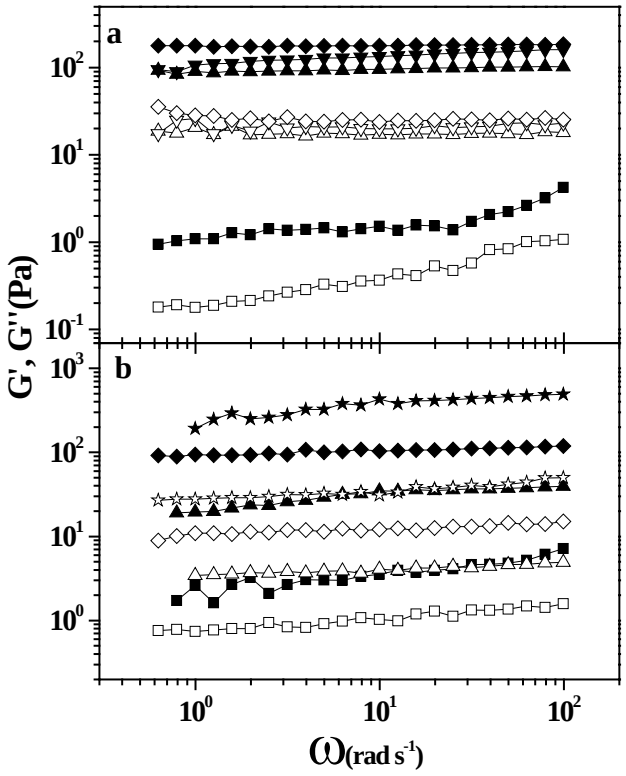

Figure 4.3. Elastic G' (closed symbols) and loss G" (open symbols) moduli as a function of frequency for different fibrinogen concentrations (g/L): (□), 10; (○), 15; (△), 20; (▽), 25; (◇), 30 and (☆), 40. Synthesized at (a) 37°C and (b) 70 ºC. Experiments were performed at a deformation of 0.02% and 25 °C.

The log-log plot variation of elastic modulus as a function of fibrinogen concentration and the preparation temperature is shown in Figure 4.4.a for 37 (squares) and 70°C (circles). Data were obtained at ω = 10 rad/s, at deformation value of 0.025% and at 25°C from the frequency sweeps experiments. It is seen in this figure that hydrogels prepared at 37°C show G' larger values than that prepared at 70°C, since samples prepared at 37°C are more cross-linked than that prepared at 70°C. In the other hand for both data sets, the slopes are almost the same, m ~ 3.5. Clark et al.[112], reported a power law relation between G' and concentration of protein and polysaccharide gels according to C^2 at high C/C_0 ratios, where C_0 is the critical concentration, below this concentration macroscopic gel are not formed.

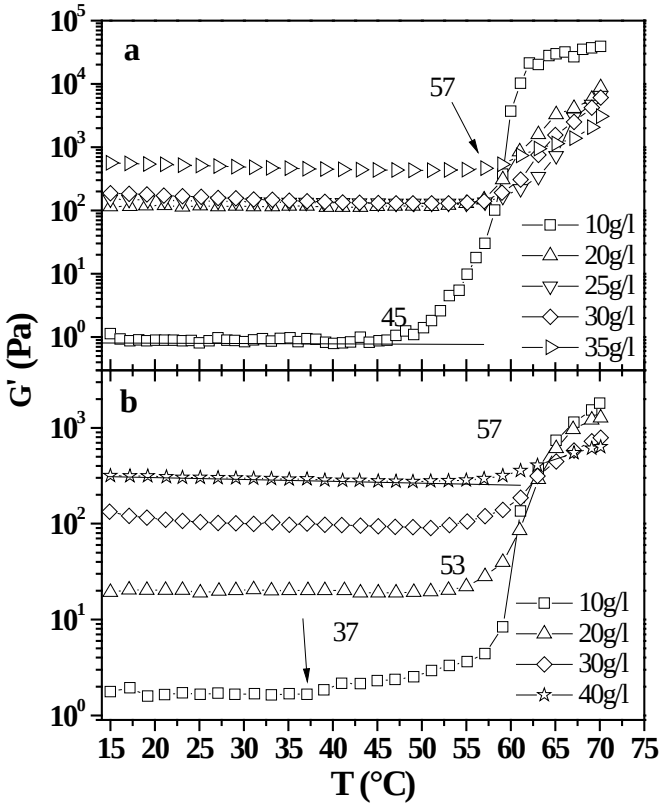

Figure 4.4. Temperature dependence of elastic modulus G' for samples made at 37 ºC (a) and 70 ºC (b) for different fibrinogen concentrations (g/L): (□), 10; (△), 20; (▽), 25; (◇), 30; (▷), 35 and (☆), 40. Experiments were performed at a deformation of 0.025% and at ω = 10 rad/s.

They reported that higher power law dependence is usually found in others gelling biopolymers for C/C_0 values lower than 10. A model for density cross-linked actin proteins and entangled solutions was proposed by MacKintosh et al. [113]. They showed that for an entangled solution the elastic modulus scaled with concentration as

$$G' \propto C^A \tag{4.1}$$

with A = 2.2. Similar power law exponents value were reported for hydrogels based on F-actin [113], oligopeptide [114]. The slope of 3.5 obtained for our system is higher than that predicted by equation X but lower than that reported for hydrogel based on oligomeric electrolyte [115]. In figure 4.43.b, log-log plot of variation of tan δ (G"/G') values with fibrinogen concentration and the preparation temperature at 37 (squares) and 70°C (circles), is shown in Figure 4.4.a. For both samples prepared at 37 and 70°C, tan δ values decrease as protein concentration increase, this diminishing indicates that hydrogel strength becoming harder. The slope value for samples prepared at 37°C is smaller than that for samples prepared at 70°C. This means that for concentrations higher than 10 g/L, the rigidity of 70°C samples becomes greater in magnitude than that for samples synthesed at 37°C with concentration augment.

Fibrinogen Sorption Kinetic on SiO_2 Nanofibers

1. Introduction

The adsorption of proteins from solution onto solid surfaces has attracted much attention due to its scientific importance and applications. An area of considerable interest where interfacial interactions are exceedingly important is in biomedical applications of artificial devices. The adsorption of proteins from body fluids is the first biological response to the implantation of a biomaterial, and this process will guide the future cell adhesion. Materials used in medical devices perform differently depending on their chemistry of solid surface and especially on their morphology and topology. Nowadays, specifically designed implantable materials that are used or that being proposed have constituent grains or particles with rough topographies at micron scale yet smooth at the nanoscale. It was in 2001, owing to their outstanding adsorptive properties, when silica materials with high surface areas were proposed for the first time as drug delivery system. Since then, this research field has experienced a significant growth and much effort has been devoted to tailor their nanostructure and their textural properties. In addition, the discovery of bioactive behaviour added an extra value to SiO_2 sieves as excellent candidates to be used as starting materials for the manufacture of 3D-scaffolds for tissue engineering.

In a previous work, we have report the use of a reverse microemulsion system to control the morphology of SiO_2 nanofibers during hydrothermal synthesis at 100^{o}C. Here, we have evaluate the interaction of the third most abundant blood plasma protein, fibrinogen (FB), on the synthesized SiO_2 nanofibers in simulated biological conditions as a previous step to test the future use of such materials in the construction of implantable units. The adsorption process of FB on solid surfaces has been extensively studied during the last decade. The interest in this protein originates from its special importance in blood coagulation and it contacts with artificial surface of foreign materials. Because of their complex chemical constitution, FB may adsorb by different mechanisms on different surfaces. Although it is well-known that physicochemical surface properties strongly affect the protein adsorption, such studies on chemically and morphologically well-characterized surfaces are scarce. We are interested in studying in detail the different FB-SiO_2 adsorption dynamic regimes and the effect of pore and intraparticle diffusion rates at different FB concentration.

2. Experimental

2.1 Materials

Fibrinogen from bovine plasma (F8630) was obtained from Sigma (CAS Number: 9001-32-5). The properly amount of FB was dissolved in buffer phosphate to pH = 7.00, to approach physiological conditions. Phosphate was preferred than tris(hydroxymethyl)aminomethane buffer because it was confirmed the co-adsorption of the small organic molecule and it interference on the experiments. The fibrinogen solution was prepared, stored at -20^{o}C and diluted as required. Before the beginning of an experiment FB solutions were stored at room temperature for a maximum of 1 h.

The SiO_2 nanofibers were synthesized by a microemulsion templated route following a previous descript procedure. Two different materials were prepared: M1 and M2 in which water/AOT/n-hexane and water/AOT/cicloxane microemulsions were used as a template.

2.2 Protein Adsorption

Adsorption experiment (in darkness to avoid protein photodegradation) were carried out *in situ* in an UV-vis-NIR scanning spectrophotometer (Beckman, model DU 640) provided with a thermostatic bath. For this 20 mg of adsorbent were contacting with 3mL of FB buffer solution of different concentrations at 37^{o}C. The supernatant concentration before and after adsorption was analyzed at λ = 280 nm following the emission of Tryptophan group. A mass balance was applied to calculate the protein adsorbed on SiO_2 fibrils.

2.3 Characterization

To evaluate the morphology of the materials before and after protein adsorption field emission scanning electron microscopy (FE-SEM) was performed using a FE-SEM ULTRA PLUS microscope. This instrument operates in high vacuum, 0.8 nm at 30 kV resolution; accelerating voltage of 0.02V-30kV, continuously adjusted in steps of 10 volts; magnification range 12-1000000x; sizes of openings: 7.5 μm,10μm, 20μm, 30μm, 60μm and 120μm. Local compensation of charge, by injecting nitrogen gas.

3. Results and discussion

3.1 Protein adsorption

The adsorption of proteins occurs at different types of interfaces, and the initial layers of proteins adsorbed significantly affect the process occurring at these interfaces. In order to determine the mechanism of FB adsorption, experimental data were fitted to Langmuir, Freundlich and Sips equations. The mathematical expressions are given by eqs (2-4), respectively as follows:

Langmuir model $$q_e = \frac{q_m K_L C_e}{1 + K_L C_e} \quad (4.2)$$

Freundlich model $$q_e = K_F C_e^{1/n} \quad (4.3)$$

Sips model $$q_e = \frac{b_s q_s C_e^{1/n}}{1 + b_s C_e^{1/n}} \quad (4.4)$$

The equilibrium adsorption capacity, q_e (mg mg^{-1}) was calculated with the equation:

$$q_e = \frac{(C_0 - C_e)V}{m} \quad (4.5)$$

where C_0 is the initial concentration (mg dm^{-3}), C_e the residual concentration at equilibrium (mg dm^{-3}), V the solution volume (dm^{-3}) and m is the adsorbent mass (mg). q_m (mg mg^{-1}), is the maximum amount of sorbate per unit weight of adsorbent to form a complete monolayer on the surface bound at high C_e, and K_L (L mg^{-1}) is Langmuir constant related to the affinity of the binding sites. K_F and n are Freundlich´s constants related to adsorption capacity and the heterogeneity factor, respectively. q_s, b_s and $1/n$ are Sips maximum adsorption capacity (mg mg^{-1}), equilibrium constant related to adsorption capacity (mg L^{-1}) and surface heterogeneity respectively. For a highly heterogeneous system, the deviation of $1/n$ value from unity will be higher. The Langmuir model is an ideal model for homogeneous monolayer adsorption while Freundlich isotherm is more flexible and assumes that the energy of adsorption decreases logarithmically as the fractional coverage increases. However, the

Freundlich isotherm does not tend to a limiting coverage as the concentration tends to infinity. Sips model is obtained by introducing a power law expression of the Freundlich model into the Langmuir model. At low sorbate concentrations it effectively reduces to a Freundlich isotherm, while at high sorbate concentration it predicts a monolayer adsorption capacity characteristic of the Langmuir isotherm.

As it was expected FB adsorption behaviour on both materials was badly predicted by the individual Langmuir or Freundlich equations. The reason may be found in the irreversible nature of FB adsorption and more generally, macromolecular adsorption which is now a well-established a heterogeneous phenomena. This complex phenomenon involves at least three different steps, namely: (i) transport of the molecules from the bulk to the surface by diffusion or diffusion/convection; (ii) adsorption, at a given rate, of dissolved macromolecules interacting with the solid surface; (iii) conformational / orientational changes of the molecule adsorbed on the surface, which may affect their structural, energetic and kinetic properties. This cannot be analyzed in a simple way.

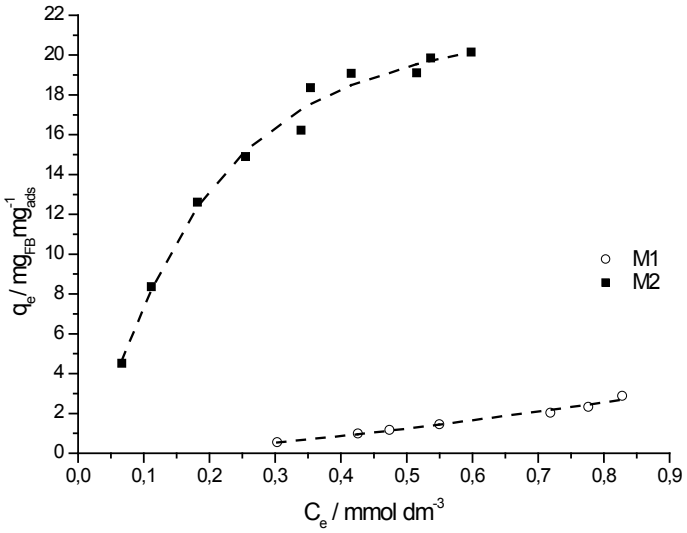

Figure 4.5: Isotermas de adsorción de Sips para FB sobre M1 y M2

This surface heterogeneity of the adsorbed protein molecule may arise either due to the energetic heterogeneity of the surface sites, to heterogeneity of the molecule in the solution,

or to a combination of the above reasons. Rudzinski et al. indicate that the protein adsorption model is complicated by surface heterogeneity or energetic heterogeneity of the surface sites.

If molecules of liquid mixtures may have similar cross-sectional areas (or homogeneity) on the solid surface, the sorption process can be analysed by Stieltjes transform. This equation was utilized earlier by Sips to describe the gaseous adsorption on actual heterogeneous solid surfaces and modified to solution adsorption by a simple transformation of variables.

Protein kinetics

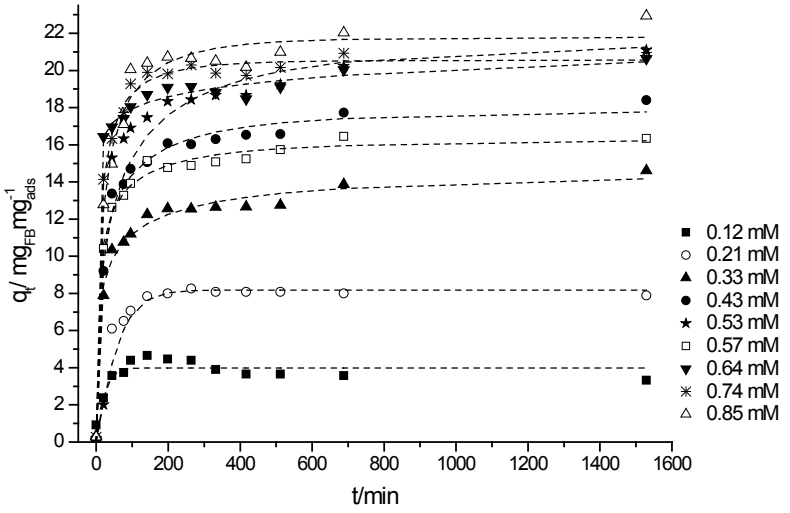

Figure 4.6: Avrami kinetic, FB on M2

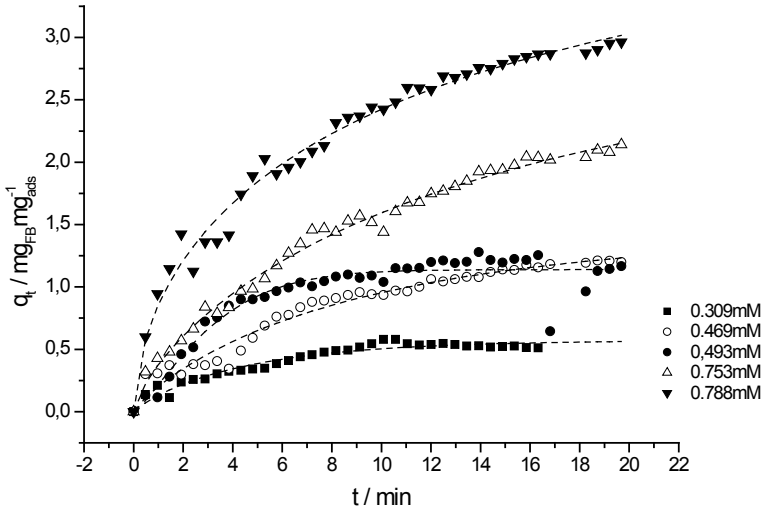

Figure 4.7: Avrami kinetic, FB on M1

Traditionally, the adsorption kinetics is described following the expressions originally given by Lagergren, which are special cases for the general Langmuir rate equation. A simple kinetic analysis of adsorption is the pseudo –first order equation in the form:

$$\frac{dq_t}{dt} = k_{1,s}\left(q_e - q_t\right) \tag{4.6}$$

where $k_{1,s}$ is the pseudo-first-order rate constant and q_e denote de amount of adsorption at equilibrium. Integrating equation (6) for the boundary conditions t=0 to t and q_t =0 to q_t gives:

$$\ln\left(q_e - q_t\right) = \ln\left(q_e\right) - k_{1,s}t \tag{4.7}$$

In addition, a pseudo-second-order equation based on adsorption equilibrium capacity may be expressed in the form:

$$\frac{dq_t}{dt} = k_{2,s}\left(q_e - q_t\right)^2 \tag{4.8}$$

where $k_{2,s}$ is the pseudo-second-order rate constant. Integrating and applying the initial conditions, we have:

$$\frac{1}{q_e - q_t} = \frac{1}{q_e} + k_{2,s}t \tag{4.9}$$

rearranged to obtain a linear form:

$$\frac{t}{q_t} = \frac{1}{k_{2,s}q_e^2} + \frac{1}{q_e}t \tag{4.10}$$

The fitting validity of these models is traditionally checked by the linear plots of ln (q_e-q_t) vs. t and t/q_t vs. t respectively. The slope and Y-intersection of the straight line obtained provide the respective kinetic constant and the q_e parameters.

Despite the Lagergren kinetic equations has been used for the most adsorption kinetic works, determination of some specific kinetic parameters, as possible changes of the adsorption rates in function of the contact time and temperature represent still lacks and a change in the kinetic adsorption model.

Experimental data were further treated with both above mentioned models; the obtained results indicated that those models do not agree with experimental values. In this way, an alternative kinetic equation was used, Avrami kinetic equation:

$$q_t = q_e\left(1 - \exp^{-[K_{av}t]^n}\right) \tag{4.11}$$

where k_{av} is the Avrami kinetic rate constant and n is the reaction order.

In order to quantitatively compare the applicability of the applied kinetic model, the normalized standard deviation (Δq_t) were calculated as follows [117]:

$$\Delta q_t(\%) = 100 \times \sqrt{\frac{\sum\left[\left(q_{t,\exp} - q_{t,calc}\right)/q_{t,\exp}\right]^2}{(a-1)}} \quad (4.12)$$

where $q_{t,calc}$ are the adsorption capacity calculated values from both the Lagergren and the Avrami models and *a* is the number of experimental points of the kinetic curve (Figures 4.6 and 4.7).

These figures show that fibrinogen adsorb much faster and more onto M2 than M1. These materials are quite similar; they were synthesized and characterized in our previous work[118].

It has been concluded in previous results, that adsorption capacity is dependent on the pore size of the adsorbent relative to that of the protein, and a pore size slightly larger than the hydrodynamic radius is sufficient to obtain high capacity. In our case, the materials present an unusual fibrous microstructure with a surface morphology with a BET specific surface area of 0.8 and 0.93 $m^2\ g^{-1}$ for M1 and M2 respectively. These materials have not a large surface area compared to other materials because it is not porous, however interact strongly with the protein due to adsorb large quantities (q_{mon}= 22.9 mgFB/mgM2 and 1.7 mgFB/mgM1). It is related to the shape of the material.

It is important to note that the interaction between proteins and biological materials is one of the top priorities in the design and synthesis of orthopedic and dental biomaterials, due to simulate properties of bone in synthetic implant formulations. Specifically, bone is a bioceramic composite that has long held the attention of the materials engineer who seeks to duplicate its enviable mechanical properties, in which both high strength and fracture toughness can be achieved due to the unique architecture of this organic-inorganic composite. Its most basic level of organization is constituted by nanostructured array of hydroxyapatite (HA) crystals embedded within the collagen matrix. This level of structure is created by intrafibrillar mineralization of collagen, and it is the intimate relationship between the self-assembled fibrillar collagen matrix and the uniaxially oriented, nanometer sized, platy HA crystals, that provides bone with its remarkable mechanical properties and remodeling capabilities. From materials science perspective, the interpenetrating nature of the organic-inorganic phases makes it difficult to classify bone as one specific type of composite. For

example, the high degree of loading of mineral phase which encases the collagen fibrils suggests that bone is a fiber-reinforced ceramic-matrix composite. It is the nanostructured architecture that is the essence of bone, both in terms of mechanical properties and bioresorbability[119].

The synthetic material applied to bone tissue reconstruction should not only have the right dimensions but also its appearance is a key in order to optimize the response of bone cells. Sufficient bonding between an orthopedic/dental implant and juxtaposed bone is necessary to minimize motion-induced damage to surrounding tissue in situ, to support physiological loading conditions, and to ensure overall implant efficacy. Carbon fibers with conventional dimensions in the micron scale have long been considered for hard and soft tissue implants due to exceptional mechanical properties[120]. For example, an in vivo study showed successful integration of interconnecting collagen fibrils parallel to carbon fibers implanted into the calcaneous tendon of rabbit after 4 weeks. In contrast, severe granulomatous foreign-body reactions were observed around carbon fibers implanted into the right knee of patients after 6 months[121-122]. For this reasons, it is clear that conventional carbon formulations may not be the optimal implant material. Carbon nanotubes and nanofibers have several properties that suggest these materials may be of value in the development of novel devices for bone reconstruction. Since they are organic particles, issues related to metal ions released from implants will not arise. The aspect ratio and physical shape of these fibers mimic the crystalline hydroxyapatite structures of natural bone. In previous results was observed that carbon nanofibers increased functions of osteoblasts with decreased carbon fibers dimensions, concluding that represent a class of material formulations that promise enhanced bonding of orthopedic implants[123-124]. Thus, osteoblasts have a favourable response on substrates made from fibrous ceramic nanophase.

In this work we can conclude that the protein adsorbed onto these nanofibrils will be suitable for the fabrication of scaffolds for a range of novel applications for cell growth, tissue engineering, and regenerative medicine.

5. Chapter 5: Concluding Remarks

The conclusions obtained in this thesis are summarized as follow:

- The association process of BTS seems to be an entropically driven. The size of the self-associated nanoparticles was estimated about 2.5-3.0 nms with aggregation number of ~30 molecules. It has been proposed that a BTS arrangement result with the aromatic rings toward the core of the structure. The aggregation process could be explained by the intramicellar repulsion, in presence of salt, due to the shield of the ionic interactions, and also can be explained by the presence of steric interactions.

- Catanionic surfactants PFO/CTA in absence of counterions present a synergistic micellization due to the dual lipophobic/hydrophobic character of perfluorinated chains, allowing the formation of a variety of structures. Experimental and computational molecular dynamic simulations indicate that a variety of structures of different sizes coexist in solution with vesicles of ~160nm diameter, self-assembling from a random distribution of monomers.

- The combination of drugs can form different kind of self-assembled structures. The combination of dicloxacillin and CTAB result in the formation of worm-like micelles, where It has been characterized proposing a new strategy to optimize conventional strategies in drug delivery.

- The effect of BTS on mioglobin, fibrinogen, ovalbumin and lysozyme promotes conformational changes in the proteins structures. BTS acts as a structure stabilizer at low concentration meanwhile it acts as a desestabilizer at higher concentrations in all the proteins studied, affecting mainly to mioglobin, the protein with the highest α-helical secondary structure.

- The interactions between fibrinogen and amphiphile betablockers modify the cluster formation of fibrinogen molecules, and results in changes in the secondary structure content. Acebutolol and propranolol, can act as structure stabilizer and desestabilizer at low and higher molar concentrations respectively. In absence of additives fibrinogen form dimmers, nevertheless the addition of small amounts of acebutolol results in aggregation of the dimmers to tetramers, increasing acebutolol concentrations tetramers dissociate to dimmers. However, complexation between fibrinogen and

-

- propranolol change the conformation of the protein leading to a more compact structure at the interface.

- The complexation between fibrinogen and hydrogenated/fluorinated surfactants results in a decrease of a-helix content. Depending on the hydrophobicity of the surfactant the configuration of the protein changes. In the bulk C8HONa did not promotes any significant change in fibrinogen, C8FONa monomer interact without promoting dissociation, nevertheless C12HONa interacts with fibrinogen forming a complex promoting the surfactant self-assembling at hydrophobic moieties. The behavior of fibrinogen with these surfactants at the air/water interface suggests complex formation. Specifically fluorinated surfactants cause a strong cooperativity or synergistic effect, however fibrinogen/hydrogenated mixtures no clusters formation is seen.

- Regarding on the aggregation and self-assembly of proteins, the strength of the ovalbumin gel increase with increasing surfactant concentration. Unfolded ovalbumin molecules tend to form a fibrillar structure of the gel and a fractal dimension dependent of the surfactant network at high concentrations. The different nature of the fluorinated surfactant provokes a disruption of the gel network at high concentrations.

- Formation of fibrinogen hydrogels depends on the pH value. Change in the pH induced the self-assembly of FB molecules and the subsequence formation of FB fibrils to form a three dimensional network. The cross-linking density of the hydrogel samples depends on protein concentration.

- The microcrystalline structure of opals and consequently their optoelectronic properties are a result of particular combination of all relevant microemulsion parameter, hydrothermal treatment time, and calcinations temperature. These materials present a fibrous microstructure but permit to adsorb large quantities of protein concluding that the protein adsorbed onto these nanofibrils will be suitable for the fabrication of scaffolds for a range of novel applications for cell growth, tissue engineering and regenerative medicine.

- These fibrous microstructures have not a large surface area compared to other materials because it is not porous, however interact strongly with the protein due to adsorb large quantities (q_{mon}= 22.9 mgFB/mgM2 and 1.7 mgFB/mgM1). It is related to the shape of the material. For fibrinogen concentrations higher than 10 g/L, the rigidity of 70^{o}C samples becomes greater in magnitude than that for samples synthesized at 37^{o}C with concentration augment.

6. Bibliography

1. Alexandridis, P.; Olsson, U. and Lindman, B. ***A record nine different phases (four cubic, two hexagonal, and one lamellar lyotropic liquid crystalline and two micellar solutions) in a ternary isothermal system of an amphiphilic block copolymer and selective solvents (water and oil)***, Langmuir, 1998, 14, 2627–2638.

2. Holmberg, K.; Jönsson, B.; Kronberg, B.; Lindman, B. (Eds.), ***Surfactants and Polymers in Aqueous Solution***, 2nd edn., Wiley, London, U.K., 2002.

3. Alexandridis, P. and Lindman, B. (Eds.), ***Amphiphilic Block Copolymers. Self-Assembly and Applications***. Elsevier, Amsterdam, the Netherlands, 2000.

4. Rajan R. and Balaram P. ***A model for the interaction of Trifluoroethanol with peptides and Proteins***. Int J. Pept. Protein Res., 1996, 48, 328-336.1

5. Aloy, P.; Russell, R. B. ***Structural systems biology: modelling protein interactions***. *Nat Rev Mol Cell Biol* 2006**,** *7* (3), 188-197.

6. Liu, K.; Jiang, L. ***Bio-inspired design of multiscale structures for function integration***. *Nano Today* **2011,** *6* (2), 155-175.

7. Zhang, S.; Marini, D. M.; Hwang, W.; Santoso, S. **Design of nanostructured biological materials through self-assembly of peptides and proteins.** ***Current Opinion in Chemical Biology*** 2002**,** 6 (6), 865-871.

8. Fratzl, P. ***Biomimetic materials research: what can we really learn from nature's structural materials?***. Journal of The Royal Society Interface 2007**,** 4 (15), 637-642.

9. Hamley I.W. ***Introduction to Soft Matter***. John Wiley and Sons, 2000. 13, 111.

10. Myers D. ***Surfaces, Interfaces and Colloids***. John Willey and Sons, 1999. 15, 32.

11. Burgess C. and Knowles A. ***Practical Adsorption Spectrometry, Techniques in Visible and Ultraviolet Spectrometry***. Volume 3. EDS. Chapman and Hall. London, 1984. 18.

12. Lakowicz, J. R. ***Principles of Fluorescence Spectroscopy***, 3rd ed.; Springer: New York, 2006.

13. Shulz, P.C. ***DSC analysis of the state of water in surfactants-based microstructures***. Journal of Thermal Analysis, 1998, 51, 135-149.

14. Chernik,G.G. ***A differential scanning calorimetry study of a binary system: I. Interpretation of DSC curves for isothermal and isothermal phase transitions in binary systems***. J. Colloid Interface Sci., 1991, 141, 400-408.

15. Chernik, G.G. and Sokolova, E.P. ***A differential scanning calorimetry study of a binary system: II. Phase diagram and transition enthalpies for the lyotropic liquid crystal dimethyldecylphosphine oxide-water system.*** J. Colloid Interface Sci., 1991, 141, 409-414.

16. Bellot, M. and Bouteiller, L. ***Thermodynamic Description of Bis-urea Self-Assembly: Competition between Two Supramolecular Polymers*** Langmuir, 2008, 24, 14176-14182.

17. ***DCS Data Analysis in Origin***, tutorial guide, versión 7.0 (2004) microcal.

18. A.Méndez-Vilas and J. Díaz ***Modern Research and Educational Topics in Microscopy Formatex*** 2007.

19. Ananthapadmanabham, K.P. ***Interactions of Surfactants with Polymers and Proteins***. CRC Press, Boca Raton, 1993. 137, 140, 141.

20. Hunter, R.J. ***Foundations of Colloids Science*** Oxford University Press, 2nd Edition, New York, 2001.

21. Goodwin J.W. ***Colloids and Interfaces with Surfactants and Polymers***. John Wiley and Sons, 2004.

22. Rosen, M.J. ***Surfactant and Interfacial Phenomena***, 2nd Ed. John Wiley and Sons, 1989, 113.

23. Stigter, D., ***Micelle Formation in ionic surfactants. II. Specificity of head groups, micelle structure***, J.Phys.Chem., 78, 24, 1974.

24. Ananthapadmanabham, K.P. ***Interactions of Surfactants with Polymers and Proteins***. CRC Press, Boca Raton, 1993. 137, 140, 141.

25. Chen, L.-J.; Lin, S.-Y.; Huang, C.-C. ***Effect of Hydrophobic chain length of surfactants on enthalpy-entropy compensation of micellization***. J. Phys. Chem. B, 1998, 102, 4350-4356.

26. Kahlweit, M.; Lessner, E.; Strey, R. J. ***Phase behavior of quaternary systemas of the type water-oil-nonionic surfactant-inorganic electrolyte***. Phys. Chem., 1984, 88, 1937-1944.

27. Chen, L.-J.; Hsu, M.-C.; Lin, S.-T.; Yang, S.-Y. ***Salt effect on wetting/nonwetting behaviors.*** J. Phys. Chem. 1995, 99, 4687-4697.

28. Moren A.K. and Khan A. ***Surfactant Hydrophobic Effect on the Phase Behavior of Opppositely Charged Protein and Surfactant Mixtures: Lysozyme and Sodium Alkyl Sulfates***. *Langmuir*, 14:6818, **1998**.148

29. Aloy, P; Russel, R.B., ***Structural systems biology: modeling protein interactions***. *Nat Rev Mol Cell Biol* 2006, 7 (3), 188-197.

30. Böhm, H.J. and Schneider, G. ***Protein-Ligand interactions: From Molecular Recognition to Drug Design*** WILEY-VCH Verlag GmbH & Co. KGaA,: Weinheim, 2003.

31. Jones M.N. ***A theoretical Approach to the Binding of Amphipatic Molecules to Globular Proteins***. Biochem J., 1975, 151:109-114, 148.

32. Shargel, L.; Wu-Pong, S.; Yu, A. B. C., ***Applied Biopharmaceutics & Pharmacokinetics***. McGraw-Hill: USA, 2005.

33. Jambhekar, S. S.; Breen, P. J., ***Basic Pharmacokinetics***. Pharmaceutical Press: Cornwall, UK, 2009.

34. Lee, K.-B.; Park, S.-J.; Mirkin, C. A.; Smith, J. C.; Mrksich, M., ***Protein Nanoarrays Generated By Dip-Pen Nanolithography***. *Science* 2002, *295* (5560), 1702-1705.

35. Lundahl P.; Greijer E.; Sandberg M.; Cardell S. and Ericksson K. ***A Model for Ionic and Hydrophobic Interactions and Hydrogen-Bonding in Sodium Dodecyl Sulfate-Protein Complexes***. Biochim. Biophys. Acta-Protein Structure and Molecular, 1986, 873, 20-26. 140

36. Coke, M.; Wilde, P.J.; Russell, E.J. and Clark, D.C., ***The Influence of Surface Composition and Molecular Diffusion on the Stability of Foams Formed from Protein-Surfactant Mixtures***, J. Colloid Interface Sci., 1990, 138, 489-504.

37. Sukow, W.W.; Sandberg, H.E.; Lewis, E.A.; Eatough, D.J. and Hansen, L.D., ***Binding of the Triton X Series of Non-Ionic Surfactants to Bovine Serum Albumin***, Biochemistry, 1980, 19, 912-917.

38. S. Van Vlierberghe, P. Dubruel, and E. Schacht. ***Biopolymer-based hydrogels as scaffolds for tissue engineering applications: A Review.*** Biomacromolecules 2011, 12, 1387-1408.

39. Yan, H.; Saiani, A.; Gough, J.E.; Miller, A.F. ***Thermoreversible protein hydrogel as cell scaffold.*** Biomacromolecules 2006, 7, 2776-27782.

40. Pochan, D.J; Pakstis, L.; Ozbas, B. ***SANS and Cryo-TEM study of self-assembled diblock copolypeptide hydrogels with rich nano- through microscale morphology***. Macromolecules 2002, 35, 5358–5360.

41. Kopecek, J. ***Hydrogels: From soft contact lenses and implants to self-assembled nanomaterials***. Journal of Polymer Science: Part A: Polymer Chemistry, 2009, 47, 5929–5946.

42. Halstenberg, S.;Panitch, A.;Rizzi, S.; Hall, H.; Hubbell, J.A. ***Biologically engineered protein-graft-poly(ethylene glycol) hydrogels:A cell adhesive and plasmin-degradable biosynthetic material for tissue repair***. Biomacromolecules 2002, 3, 710-723.

43. Hirano, Y.; Mooney, D.J. ***Peptide and protein presenting materials for tissue engineering***. Adv Mater, 2004, 16, 17-25.

44. Hersel, U.;Dahmen, C.; Kessler, H. ***RGD modified polymer: Biomaterials for stimulated cell adhesion and beyond***. Biomaterials 2003, 24, 4385–4415.

45. Zhu, J.M.; Beamsih, J.A.; Tang, C.; Kottke-Marchant, K.; Marchant, R.E. ***Extracellular matrix-like cell-adhesive hydrogels from RGD-containing poly(ethylene glycol) diacrylate***. Macromolecules 2006, 39, 1305-1307.

46. Lin, C.C.; Metters, A.T. ***Bifunctional monolithic affinity hydrogels for dual-protein delivery***. Biomacromolecules 2008, 9, 789-795.

47. Williams, C.G.; Malik, A.N.; Kim, T.K.; Manson, P.N.; Elisseeff, J.H. ***Variable cytocompatibility of six cell lines with photoinitiators used for polymerizinf hydrogels and cell encapsulation***. Biomaterials 2005, 26, 1211–1218

48. Lee, K.Y.; Rowley, J.A.; Eiselt, P.; Moy, E.M.; Bouhadir, K.H.; Mooney, D.J. ***Controlling mechanical and swelling properties of alginate hydrogels independently by cross linker type and cross linking density***. Macromolecules 2000, 33, 4291-4294.

49. Vermonden, T.; Besseling, N.A.M.; van Steenbergen, M.J.; Hennink, W.E. ***Rheological studies of thermosensitive triblock copolymer hydrogels***. Langmuir 2006, 22, 10180-10184.

50. Haglund, B.O.; Josi, R.; Himmelstein, K.J. ***An in situ gelling system for parental delivery***. J. Controlled Release 1996, 41, 229-235.

51. Nagahara, S.; Matsuda, T. ***Hydrogel formation via hybridization of oligonucleotides derivatized in water-soluble vinyl polymers***. Polym. Gels Networks 1996, 4, 111-127.

52. Peppas, N.A.;Hilt, J.Z.;Khademhosseini, A.;Langer, R. ***Hydrogels in biology and medicine: From moleculas principles to bionanotechnology***. Adv.Mater. 2006, 18, 1345-1360.

53. Bordi,F.; Paradossi, G.;Rinaldi, C.; Ruzicka, B. ***Chemical and physical hydrogels: two casesystems studied by quasi elastic light scattering***. Physica A: Statistical mechanical and its applications, 2002, 304, 119-128.

54. Bromberg, L.E., Ron, E.S. ***Temperature-responsive gels and thermogelling polymer matrices for protein and peptide delivery*.** Adv. Drug Delivery Rev. 1998, 31, 197-221.

55. Donhowe, I.G.; Fennema, O. ***The effects of solution composition and drying temperature on crystallinity, permeability and mechanical properties of methylcellulose films***. J.Food Process. Preserv. 1993, 17, 231-246.

56. Jiang, L.Y.; Li, Y.B.; Xiong, C.D. ***Preparation and biological properties of a novel composite scaffold of nano-hydroxyapatite/chitosan/carboxymethyl cellulose for bone tissue engineering***. J.Biomed.Sci., 2009, 16, 65.

57. Wang, Z., P. Deurenberg, W. Wang, A. Pietrobelli, R.N. Baumgartner, and S.B. Heymsfield. ***Hydration of fat-free body mass: review and critique of a classic body-composition constant.*** The American Journal of Clinical Nutrition 1999;69:833-841.

58. Greve, T.M., K.B. Andersen, and O.F. Nielsen, ***ATR-FTIR, FT-NIR and near-FT-Raman spectroscopic studies of molecular composition in human skin in vivo and pig ear skin in vitro*, in Spectroscop**y: An International Journal. 2008, IOS Press. p. 437-457.

59. Doolittle, R.F. ***Fibrinogen and Fibrin.*** Annual Review of Biochemistry 1984, 53, 195-229.

60. Xu, C.; Joss, L.;Wang, C.;Pechar, M.; Kopecek, J. ***The influence of fusion sequences on the thermal stabilities of coiled-coil proteins***. Macromol Biosci. 2002, 2, 395-401.

61. G.J. de A.A.Soler-Illia; Sanchez, C.; Lebeau, B.; Patarin, J. ***Chemical strategies to design textured materials: from microporous and mesoporous oxides to nanonetworks and hierarchical structures***. Chem Rev. 2002, 102, 4093-4138.

62. Yang, P.; Deng, T.; Zhao, D.; Feng, P.; Pine, D.; Chmelka, B.F.; Whitesides, G.M.; Stucky, G.D. Science, 1998, 282, 2244-2246.

63. Yuan, Z.-Y.: Su, B.-L. ***Insigths into hierarchically meso-macroporous structured materials***. J.Mater. Chem. 2006, 16, 663-667.

64. Mann, S.; Burkett, S.L.; Davis, S.A.; Fowler, C.E.; Mendelson, N.H.; Sims, S.D.; Walsh, D.; Whilton, N.T. ***Sol-gel synthesis of organized matter***. *Chem. Mater*.1997, 9, 2300-2310.

65. Corma, A. ***From microporous to mesoporous molecular sieve materials and their use in catalysis***. Chem. Rev.1997, 97, 2373-2419.

66. Handbook of Zeolite Science and Technology (Eds.:S.M.Auerbach, K.A.Carrado, P.K.Duta), Marcel Dekker, Inc., New York, 2003.

67. Antonietti, M. ***Surfactant for novel templating applications***. Curr.Opin. Colloid Interf. Sci. 2001, 6, 244-248.

68. Galliot, C.; Larre, C.; Caminade, A.-M.; Majoral, J.-P. Science, 1997, 277, 1981-1984.

69. G.J. de A.A. Soler-Illia; Crepaldi, E.L.; Grosso, D.; Sanchez, C. ***Block copolymer-templated mesoporous oxides***. Curr. Opin. Colloid Interf. Sci. 2003, 8, 109-126.

70. Stein, A. ***Sphere templating methods for periodic porous solids***. Micropor.Mesopor.Mat.2001, 44-45, 227-239.

71. Imhof; A.; Pine, D.J.Nature 1997, 389, 948-951.

72. Mertig, M.; Ciacchi, L.C.; Seidel, R.; Pompe, W.; De Vita, A. ***DNA as a selective metallization template.*** Nano Lett. 2002, 2, 841-844.

73. Douglas, T.; Strable, E.; Willits, D.; Aitouchen, A.; Libera, M. ***Protein engineering of a viral cage for cage for constrained nanomaterials synthesis***. Adv. Mater.2002, 14, 415-418.

74. Ying, J.Y.; Mehnert, C.P.; Wong, M.S. ***Synthesis and applications of supramolecular-templated mesoporous materials.*** Angew.Chem Int.Ed. 1999, 38, 56-77.

75. Ozin G. A. ***Nanochemistry: Synthesis in dimishing dimensions***. Adv. Mater. 1992, 4, 612-649.

76. Capek, I. ***Preparation of metal nanoparticles in water-in-oil (w/o) microemulsions.*** Adv. Colloid Interface Sci. 2004, 110, 49-74.

77. Mann, S.; Burkett, S. L.; Davis, S. A.; Fowler, C. E.; Mendelson, N. H.; Sims, S. D.; Walsh, D.; Whilton, N.T. ***Sol-gel synthesis of organized matter.*** Chem. Mat. 1997, 9, 2300-2310.

78. Limin, Q. ***Synthesis of inorganic nanostructures in reverse micelles***. Encycl.Surf. Colloidal Sci. 2006, 6183-6207 and references therein.

79. Zana, R.; Lang, J. ***In Microemulsions: Structure and Dynamics***; Friberg, S.E., Bothorel, P., Eds; CRC: Boca Raton, FL, 1998.

80. Lindman, B.;Stilbs, P. ***In Microemulsions: Structure and Dynamics***; Friberg, S.E., Bothorel, P., Eds.; CRC: Boca Raton, FL, 1998.

81. Ollson, U.; Wennerstrom, H. ***Globular and bicontinuous phases of nonionic surfcatnts films***. Adv. Colloid Interface Sci. 1994, 49, 113-146.

82. Adhyapak, P.V.; Karandikar, P.; Vijayamohanan, K. ; Athawale, A.A.; Chandwadkar, A.J. ***Synthesis of silver nanowires inside mesoporous*** MCM-41 host. Mater.Lett. 2004, 58, 1168-1171.

83. Lu, A.-H.; Schuth, F.; C.R. ***Nanocasting pathways to create ordered mesoporous solids***. Chimie 2005, 8, 609-620.

84. Shuguang, Z.; Marini, D.M.; Hwang, W.; Santoso, S. ***Design of nanostructured biological materials through self-assembly of peptides and proteins.*** Current Opinion in Chemical Biology 2002, 6, 865-871.

85. Petka W.A.; Harden, J.L.; McGranth, K.P.; Wirtz, D.; Tirrell, D.A. ***Reversible hydrogels from self-assembling artificial proteins***. Science 1998, 281, 389-392.

86. Caplan, M.; Moore, P.N.; Zhang, S.; Kamn, R.D.; Lauffenburger, D.A. ***Self Assembly of a -sheet protein governed by relief of electrostic repulsion relative to van de Waals attraction***. Biomacromlecules 200, 1, 627-631.

87. Hartgerink J.D.; Beniash, E.; Stupp, S.I. ***Peptide-amphiphile nanofibers: A versatile scaffold for the preparation of self-assembling materials.*** *Proc. Natl. Acad. Sci.* USA 2002, 99, 5133-5138.

88. Gaygadzhiev, Z.; Hill, A.; Corredig, M. ***Influence of the emulsion droplet type on the rheological characteristic and microemulsions of rennet gels from reconstituted milk***. Journal of Dairy Research 2009, 76, 349-355.

89. Weigandt, K.M., D.C. Pozzo, and L. Porcar. ***Structure of high density fibrin networks probed with neutron scattering and rheology***. Soft Matter 2009;5:4321-4330.

90. Dobrynin, A.V. and Carrillo. J.M.Y. ***Universality in Nonlinear Elasticity of Biological and Polymeric Networks and Gels***. Macromolecules 2011;44:140-146.

91. Djabourov, M., J.P. Lechaire, and F. Gaill. ***Structure and Rheology of Gelatin and Collagen Gels***. Biorheology 1993;30:191-205.

92. Greenfield, M.A., J.R. Hoffman, M.O. de la Cruz, and S.I. Stupp. ***Tunable Mechanics of Peptide Nanofiber Gels***. Langmuir2010;26:3641-3647.

93. Brown, A.E.X. et. al. Science 2009;325:741-744.

94. Fowler, W. E.; Hantgan, R. R.; Hermans, J.; Erickson, H. P. ***Structure of the fibrin protofibril***. *Proc.Natl. Acad. Sci. U.S.A.* **1981**, *78*, 4872–4876.

95. Mosesson, M. W. ***Fibrinogen function and fibrin assembly***. Fibrinolysis & Proteolysis **2000**, 14, 182–186.

96. Areva, S.; Peltola, T.; Sa¨ilynoja, E.; Laajalehto, K.; Linde´n, M.;Rosenholm, J. B. ***Effect of albumin and fibrinogen on calcium phosphate formation on sol-gel derived titania coatings in vitro.*** Chem. Mater. **2002**, *14*, 1614–1621.

97. Regañon, E. ; Vila, V.; Aznar, J. ***Gelation of fibrinogen in plasma***. Haemostasis 1984, 14, 170-178.

98. Kita, R., Takahashi, A.; Kaibara, M.; Kubota, K. ***Formation of fibrin gel in fibrinogen-thrombin system: Static and dynamic light scattering study***. BioMacromolecules, 2002, 3, 1013.

99. Mališauskas, M.; Zamotin, V.; Jass, J.; Noppe, W.; Dobson, C. M.; Morozova-Roche, L. A. ***Amyloid protofilaments from the calcium-binding protein equine lysozyme: Formation of ring and linear structure depends on pH and metal ion concentration***. J. Mol. Biol. **2003**, *330*, 879–890.

100. Arnaudov, L. N.; de Vries, R. ***Thermally induced fibrillar aggregation of hen egg White lysozyme***. *Biophys. J.* **2005**, *88*, 515–526.

101. Arnaudov, L. N.; de Vries, R. ***Thermally induced fibrillar aggregation of hen egg White lysozyme***. *Biophys. J.* **2005**, *88*, 515–526.

102. **Chen,Y.; Mao,H.; Zhang, X.; Gong, Y.; Zhao, N. *Thermal conformational changes of bovine fibrinogen by differential scanning calorimetry and circular dichroism*. International Journal of Biological Macromolecules, 1999, 26, 129-134.**

103. Hassan, N.; Barbosa, L.R.S.; Itri, R. ; Ruso, J. M. Fibrinogen Stability Under Surfactants Interactions. Journal of Colloid and Interface Science, 2011, 362, 118–12.

104. Privalov, P. L.; Medev, L. V. ***Domains in the fibrinogen molecule***. J. Mol. Biol., 1982, 159, 665-.

105. Donovan, J. W.; Mihalyi, E. ***Conformation of fibrinogen: Calorimetric evidence for a three-nodular structure***. Proc. Natl. Acad. Sci. USA, 1974, 71, 4125-4128.

106. Foegenig, E.A.; Allen, C.E.; Dayton, W.R. ***Effect of heating rate on thermally formed myosin, fibrinogen and albumin gels***. Journal of Food Science, 1986, 51, 104-108.

107. Ferry, J.D. 1948. ***Protein gels***. A v. Protein Chem. 1948, 4, 1.

108. Hermansson, A.M. ***Physico-chemical aspects of soy proteins structure formation***. J. Texture Stud. 1978, 9, 33.

109. Ferry, J.D. ***The viscoelastic properties of polymers***; Wiley: New York, 1980.

110. Robles-Vásquez, O.; Corona-Galvan, S.; Soltero, J.F.A.; Puig, J.E.; Tripodi, S.B.; Valles, E.; Manero, O. ***Rheology of lyotropic liquid crystals of aerosol OT: II. High concentration regime***. Journal of Colloid and Interface Science, 1993, 160, 65-71.

111. Soltero J.F.A.; Bautista, F.; Pecina, E.; Puig, J.E.; Manero, O. ***Rheological behavior in the didodecyldimethylammonium bromide/water system***. Coll. Polym Sci. 2000, 278, 37-47.

112. Clark, A.H. and Ross-Murphy, S.B. Adv. Polym. Sci, 1987, 83, 57.

113. MacKintosh, F.C.; Käs, J.; Janmey, P.A. ***Elasticity of semiflexible biopolymer networks.*** Phys. Rev. Lett. 1995, 75, 4425-4428.

114. Ozbas, B.; Rajagopal, K.; Schneider, J.P.; Pochan, D.J. ***Semiflexible chain networks formed via self-aseembly of β-hairpin molecules.*** J. Phys. Rev. Lett. 2004, 93, 268106-268110.

115. Kumar, S.; Yoshida, M.; Shibayama, M. ***Effect of salt content on the rheological properties of hydrogel based on oligomeric electrolyte***. J. Phys. Chem. B 2010, 114, 1541-1547.

116. Ho, Y.S.; Mc Kay, G. ***Sorption of dyes and cooper ions onto biosorbents***. Process Biochem, 2003, 38, 1047-1061.

117. Wu, F.C.; Tseng, R.L.; Juang, R.S. ***Preparation of highly microporous carbon from fir wood by KOH activation for adsorption of dyes and phenols from water***. Separ. Purif. Technol, 2005, 47, 10-19.

118. Hassan, N.; Verdinelli, V.; Ruso, J.M. and Messina, P.V. ***Mimicking natural fibrous structures of opals by means of a microemulsion-mediated hydrothermal method.*** Langmuir, 2011, 27, 8905-8912.

119. Olszta, M. J.; Cheng, X.; Jee, S.S.; Kumar, R.; Kim, Y-Y.; Kaufman, M.J.; Douglas, E. P; Gower. L.B. ***Materials science and engineering R***, 2007, 58, 77-116.

120. Morris, D.M.; Hindman, J.; Marino, A.A. ***Repair of fascial defects in dogs using carbon fibers***. J. Surg Res. 1998 , 80, 300-303.

121. Zhang, Q.; Yang, Z.; Peng, W. Chin J Rep Reconstr Surg 11 (1997) 168-71.

122. Mortier, J.; Engelhardt M.; Zeits fur Orth Ihre Grenz 138 (2000) 390-4.

123. Price, R.L.; Waid, M.C.; Haberstrom, K.M.; Webster, T.J. Selective ***bone cell adhesion on formulation containing carbon nanofibers***. Biomaterials, 2003, 24, 1877-1887.

124. Elias, K.L.; Price, R.L.; Webster, T.J. ***Enhanced functions of osteoblasts on nanometer diameter carbon fibers***. Biomaterials, 2002, 23, 3279-3287.

6. Resumen

Las diferentes aplicaciones y usos de las proteínas han crecido durante los últimos 50 años de forma continua. Sin embargo, en los últimos años hemos sido testigos de una irrefrenable aparición de aplicaciones más vanguardistas: materiales biomiméticos, ingeniería para tejidos, liberación de fármacos, bioelectrónica o modelos para nanopartículas. En este sentido, las interacciones entre moléculas pequeñas en solución de proteínas afectan su respectiva función bilógica y determina la estabilidad de las soluciones con respecto a la agregación, licuefacción, y otras transformaciones de fases. Además, la agregación de proteínas, formación de cristales, plegamiento o desnaturalización, están definidas en gran parte por las fuerzas que actúan sobre las moléculas.

Las proteínas juegan un rol fundamental en la estructura y función de las células biológicas y organismos. Están organizadas estructuralmente por la unión de diferentes aminoácidos que poseen grupos ya sea hidrofílicos o hidrofóbicos, por esta razón, las proteínas están consideradas como surfactantes macromoleculares debido a esta propiedad anfotérica que poseen.

Las proteínas están compuestas de cuatro niveles estructurales, estructura primaria, secundaria, terciaria y cuaternaria. La estructura primaria está basada en la unión de cientos de L-α-aminoácidos de diferente tipo (grupos polares y no-polares) a través de enlaces peptídicos formando cadenas lineales o ramificadas, y formando entre ellas enlaces covalentes inter-cadena a través de puentes disulfuro. Su estructura variará enormemente dependiendo de la secuencia de residuos de aminoácidos presentes en la cadena, clasificándolas en proteínas globulares, fibrosas o desordenadas. La estructura secundaria se genera a través de un arreglo específico de los enlaces polipeptídicos, es decir, a través del efecto estérico que exista entre los residuos que se encuentran uno cercano al otro. Las dos formas principales de estructura secundaria que existen son hélice α y hoja plegada β. La estructura hélice a se genera por la formación de un enlace de hidrogeno entre el oxigeno del residuo del péptido con el nitrógeno del otro residuo. En el caso de la hoja plegada β se forma por un estiramiento de la cadena principal adoptando esta configuración llamada hojas β. En esta estructura las cadenas laterales de los aminoácidos se sitúan de forma alternante a la derecha y a la izquierda del esqueleto de la cadena polipeptídica. Las estructuras β de distintas cadenas polipeptídicas o bien las estructuras β de distintas zonas de una misma cadena polipeptidica

pueden interaccionar entre sí mediante puentes de hidrógeno, dando lugar a estructuras laminares llamadas por su forma hojas plegadas u hojas β.

La estructura secundaria posee unidades estructurales llamadas dominios, que están constituidas por el plegamiento de ciertos elementos de la proteína del cual se compone la estructura terciaria. Muchas proteínas están compuestas por varios dominios, el cual a menudo están conectados únicamente por un segmento de la cadena polipeptidica. La estructura terciaria está estabilizada por cuatro tipos de interacciones entre los grupos de las cadenas laterales de los residuos de aminoácidos: enlaces de hidrógeno, interacciones iónicas entre los grupos de carga opuesta, interacciones hidrofóbicas y puentes disulfuros. Los puentes disulfuros incrementan la estabilidad del estado nativo de la proteína reduciendo el número de conformaciones desnaturalizadas.

Las proteínas contienen más de una cadena polipeptidica (subunidades) las cuales están catalogadas como parte de la estructura cuaternaria debido a su arreglo espacial.

Una amplia gama de sistemas biológicos de importancia industrial, farmacéutica, cosmetológica, etc. están contenidos por mezclas de proteínas y surfactantes de bajo peso molecular. Las proteínas en solución contiene una mezcla de diferentes tipos de grupos químicos no-polares, polares, y cargados eléctricamente, por esta razón no es sorprendente que estas pequeñas moléculas anfifílicas de bajo peso molecular puedan interactuar fuertemente con proteínas.

La asociación de moléculas de surfactante para la posterior formación de micelas y vesículas, como vimos anteriormente, está impulsada por una fuerza que permite la reducción del área de contacto hidrocarbonos-agua de la cadena alquílica del tensioactivo y, de esta misma manera, será favorecida la asociación de la cadena alquílica del surfactante con la parte hidrofóbica de la molécula de proteína, mientras que las cabezas cargadas de surfactantes iónicos tenderán a interactuar de forma atractiva con los grupos de carga opuesta que contiene la proteína. Cuando una proteína se encuentra en su estado nativo, posee un arreglo tridimensional que la caracteriza, sin embargo, ene l momento que las condiciones del medio son cambiadas, ya sea variación de la temperatura, pH o la adición de ciertos surfactantes, puede provocar la desnaturalización de tal proteína.

Tanto proteínas como surfactantes poseen la cualidad de adsorber en un extenso rango de superficies, ya sean hidrofílicas o hidrofóbicas, y la mezcla de ambos provocará una adsorción competitiva entre ambas especies que dependerá de la naturaleza y la fuerza de interacción entre proteína-surfactante. En el seno de la solución la mezcla (proteína-surfactante) reduce la cantidad de surfactante libre para competir con la proteína en la interface, además cabe

destacar que la carga neta o la hidrofobicidad macromolecular total se puede ver afectada debido a esta unión proteína-surfactante.

Las interacciones entre surfactantes y proteínas poseen una amplia importancia como estabilizadores funcionales en sistemas naturales tales como: procesadores de alimentos (usados para estabilizar emulsiones) en farmacia, también como estabilizadores para partículas orgánicas en pinturas o películas fotográficas. Cabe destacar que las moléculas de proteínas cumplen únicamente su función biológica cuando se pliegan para formar estructuras tridimensionales particulares. El conocimiento de esta estructura tridimensional provee por lo tanto la mayoría de los detalles de punto de partida para poder entender como las proteínas trabajan. El enlace proteína-surfactante es predominantemente electrostático, el grupo principal de los surfactantes enlazan a los grupos de carga opuesta de las proteínas. Por ejemplo, un cambio en el pH causa un cambio en la carga neta de la proteína y consecuentemente en el proceso del enlace.

Un modelo general explica como surfactantes aniónicos interactúan con proteínas globulares. El modelo se compone de tres etapas: enlaces específicos, enlaces no cooperativos y cooperativos. En la primera etapa el surfactante enlaza con un sitio específico sobre la superficie de la proteína. Se forman enlaces iónicos entre los grupos cargados de los surfactantes iónicos con los residuos de aminoácidos de carga opuesta, y además se observan interacciones hidrofóbicas entre la cadena alquílica de los surfactantes y la superficie no polar de la proteína, que son adyacentes a sitios cargados. Por otro lado, existen modelos que no solo toman en cuenta interacciones iónicas o hidrófobas, sino que también los enlaces de hidrógeno entre los grupos oxigeno de los surfactantes y los grupos nitrógeno de los enlaces peptídicos. En la segunda etapa, la estructura terciaria de la proteína es desplegada, debido a la repulsión electrostática que existe entre las cargas del surfactante con las cargas de la proteína o debido a que las cadenas hidrofóbicas del surfactante penetran en la región apolar de la proteína. Las interacciones hidrofóbicas entonces toman lugar entre las cadenas de las moléculas de surfactante y, los residuos no polares de la proteína, son expuestos como resultado de la desnaturalización. Esto acontece cuando la concentración de surfactante se aproxima a la concentración micelar crítica.

Interacciones proteína-surfactante son enormemente influenciadas por la naturaleza del grupo hidrofóbico del surfactante y el largo de la cadena. El pH también tiene un efecto sobre la carga neta de la proteína, el cual depende de su punto isoeléctrico (pI). Bajo el punto isoeléctrico (cuando la carga neta de la solución acuosa es cero) la proteína tiene una carga neta positiva, y las interacciones de los surfactantes aniónicos generalmente resultan de la precipitación del complejo, debido a la neutralización de las cargas. Sobre el pI, la proteína

cargada negativamente forma complejos solubles estables. La solubilidad de al proteína en agua incrementa con la proporción de grupos polares cargados, y decrece con el incremento del peso molecular. Muchas proteínas muestran un mínimo en la solubilidad en el punto isoeléctrico donde las interacciones electrostáticas son mínimas.

Es interesante hacer notar que las proteínas plegadas únicamente pueden realizar su función biológica. Este estado de plegamiento puede usualmente ser desplegado por los desnaturalizantes, incrementando la temperatura o variando el pH. El rol del surfactante como desnaturalizante de proteínas ha llevado a investigaciones dentro del área debido a sus importantes aplicaciones en la industria.

Las interacciones no covalentes (hidrofóbicas, electrostáticas, Van der waals y puentes de hidrógeno) gobiernan los procesos de enlace de los ligandos. Dilucidar el rol de estas interacciones y la escala de tiempo involucrada nos proporciona el mecanismo molecular y el rol de los enlaces cooperativos en la dinámica de proteínas.

La utilización de transportes o vectores para la liberación local de antibióticos es un tema importante e interesante tanto en terapéutica como en el campo de cirugía ortopédica, ya que ni la meticulosidad ni una precisión quirúrgica han demostrado ser suficientes para el tratamiento de situaciones clínicas donde se detecto la presencia de microorganismos infecciosos. En la bibliografía científica se describe una amplia variedad de sistemas de libración controlada de fármacos, generalmente constituidas por una matriz polimérica o por diversos sustratos a los que se le agrega el fármaco por impregnación. Existe una necesidad de encontrar procedimientos de incorporación de fármacos a los biomateriales implantables, ya que en cualquier tipo de intervención quirúrgica el riesgo de infección es muy elevado. Si el antibiótico y/o antiinflamatorio puede situarse en el propio implante, no cabe duda que actuará mayoritariamente de forma local, aprovechando su acción donde haga falta sin perjudicar otras partes del organismo.

Por otra parte, la adsorción de proteínas sobre una superficie de biomateriales, y consecuentemente, la naturaleza de la capa proteica adsorbida, es un elemento crucial de respuesta biológica. El estudio de las interacciones de las proteínas de la sangre con los biomateriales implantados ha sido reconocido recientemente como uno de los puntos más desafiantes para las nuevas generaciones de materiales biocompatibles.

La adsorción sobre una superficie de sustratos sintéticos esta mediada por proteínas presentes en la matriz extracelular (fibrinógeno, albumina) las cuales se adsorben cuando son expuestas o bien a los fluidos fisiológicos (in vivo), o provenientes de un medio de cultivo (in vitro). Una respuesta biológica está condicionada a la concentración de proteínas adsorbidas, así como a la conformación que estas adquieran y a la fuerza de adhesión entre sustrato-proteína. Es bien

sabido la existencia de secuencias peptídicas que fomentan la adhesión celular que, dependiendo de la conformación que la proteína adquiera al adsorberse sobre el sustrato, están disponibles o no para la interacción celular. El proceso de adsorción proteína-material es un proceso fisicoquímico complejo que depende en gran medida de las características superficiales, así como de la naturaleza de la proteína y el ambiente donde tiene lugar la adsorción. Algunas proteínas tales como fibrinógeno o albumina pueden llegar a competir con los tensioactivos pulmonares reduciendo la capacidad de estos en los alveolos pulmonares (síndrome de distrés respiratorio agudo ARDS). Las proteínas también pueden ser desorbidas de la interface debido a cambios en el pH de la disolución o por la presencia de ciertos tensioactivos.

Una posibilidad es el uso de matrices cerámicas con textura abierta, elevada superficie específica y porosidad. Esto puede conseguirse con cerámicas tradicionales tales como fosfatos, vidrios, cementos o cualquiera de sus combinaciones bifásicas, utilizando procedimientos adecuados, o sintetizando materiales mesoporosos ordenados que tienen una distribución ordenada de cavidades y canales de distinta geometría y constituyen una nueva generación de materiales cuyo armazón puede estar formado exclusivamente por sílice, poseen un elevado volumen de poro en el rango de los mesoporosos, con tamaño muy homogéneo y controlable dentro de un rango relativamente amplio. A su vez pueden funcionalizarse sus paredes tanto por medio de técnicas in situ (durante la síntesis) como ex situ (estrategias post síntesis).

El principio esencial para la formación de poros a cualquier escala, es acomodar una red inorgánica y continua alrededor de bloques orgánicos ensamblados por tensioactivos o polímeros y que son los computadores de estructura final. Los métodos empleados para el desenvolvimiento de estos materiales que principalmente fueron silicatos, se extendieron a los titanatos y aluminosilicatos. La ruta más patente para preparar materiales mesoporosos ordenados en tres dimensiones espaciales es usar una matriz determinada.

Debido a todo lo anteriormente expuesto, el presente trabajo se ha desarrollado y vertebrado de la manera como a continuación se describe.

1. **Estudio y Caracterización de diferentes moléculas anfifílicas.**

En primer lugar, se ha estudiado y caracterizado diferentes moléculas anfifílicas, así también como la caracterización de mezclas de moléculas heterogéneas. Hemos hecho este estudio mediante diversas técnicas experimentales tales como: Conductividad eléctrica, densidades, ultrasonidos, difusión de luz laser dinámica, resonancia magnética nuclear (NMR H1),

simulaciones de dinámica molecular, microscopia y crio-microscopia de trasmisión electrónica (TEM y Crio-TEM) microscopia de laser confocal, y espectroscopia UV-Vis. A partir de estas diferentes técnicas tanto teóricas como experimentales hemos estudiado el proceso de auto-agregación de BTS del cual el proceso de asociación parece ser conducido entrópicamente, como indicaron los análisis termodinámicos. Los resultaron indicaron que el logaritmo de la CAC como una función de la temperatura presentó una forma de U, similar a muchos fármacos anfifílicos. La formación del agregado en ausencia de sal está relacionada probablemente a un grado de ionización mayor y a una mejor habilidad para formar enlaces de hidrógeno. Sin embargo, en presencia de sal un grado mayor de iones de sal enlazando a la superficie de los agregados reduce las interacciones repulsivas entre las cabezas de los grupos cargados, promoviendo el crecimiento del agregado. Coeficientes de expansibilidad aparentes, así como compresibilidades, indicaron que el proceso de agregación tiende a disminuir la repulsión intramicelar, en presencia de sal, debido al apantallamiento de la interacción iónica. Este proceso podría ser explicado por la presencia de interacciones estéricas produciendo valores de compresibilidades adiabáticas molares aparentes. El tamaño de las nanopartículas asociadas fue estimado en 2.5-3.0 nm con un número de agregación de aproximadamente 30 moléculas de BTS.

A su vez, es importante destacar que a través de las técnicas experimentales y teóricas expuestas anteriormente hemos podido estudiar mezclas binarias de tensioactivos, así como el sinergismo establecido entre dichas mezclas.

Nuestros resultados muestran que mezclas equimolares de una molécula de cadena corta como el perfluorooctanoato (PFO^-) con una molécula con el doble de largo de cadena como el cetiltrimetilamonio (CTA^-) en ausencia de contraiones puede formar diferentes estructuras a diferentes concentraciones en solución acuosa. Se ha demostrado que cuanto mayor sea la concentración de surfactante cataniónico mayor es la densidad de la solución y menor la compresibilidad, la disponibilidad del volumen por moléculas de soluto, el área expuesta al solvente, y el coeficiente de difusión de ambas moléculas, PFO^- y CTA^-. Específicamente, experimentos de difusión de luz dinámica (DLS) indican que al menos dos diferentes tamaños existen en el rango de concentración estudiado. Las estructuras presentes en la primera población presentan un crecimiento con la concentración de surfactante, mientras que el tamaño de las estructuras en la segunda población, las cuales fueron identificadas como vesículas, es prácticamente constante, con un radio de 80 nm aproximadamente. A altas concentraciones de surfactante ambas poblaciones tienden a formar estas vesículas, las cuales fueron observadas por TEM, Crio-SEM, y microscopia confocal en el mismo rango de concentración. La formación espontanea de estas vesículas unilamelares homodispersadas han sido observadas en la literatura por similares sistemas. Los estudios de simulación de dinámica

molecular nos permitió observar como mezclas equimolares de moléculas de PFO^- y CTA^- inicialmente localizadas en posiciones al azar en agua también forman diferentes estructuras, incluyendo vesículas, dentro del tiempo de escalas más cortas que 20 ns. La variedad de estructuras observadas esta atribuido al balance entre las diferentes interacciones que ocurren entre PFO^- y CTA^- así como con las moléculas de solvente. El hecho que las moléculas de fluorocarbono presenten un carácter dual lipofóbico/hidrofóbico puede ser una importante contribución a la agregación de los surfactantes cataniónicos. Usando un parámetro similar de campo de fuerza para dibloques no iónicos fluorocarbono-hidrocarbono se observó recientemente a través de simulaciones de dinámica molecular la formación espontánea de dominios de fluoro e hidrocarbono en la interface solución/aire. La ausencia de dominios fluorinados/hidrocarbonados en las nanoestructuras obtenidas en este estudio indica que las interacciones electrostáticas son dominantes en estos sistemas. El incremento en el área de contacto de PFO^-/CTA^- cuando la concentración de surfactante aumenta, soporta esta conclusión. Interesantemente, ya que la longitud de las moléculas de CTA^- es el doble que las moléculas de PFO^-, la primera no se ajusta bien en la estructura y el final de su cadena forma el centro hidrogenado en el agregado. Desafortunadamente, nuestras simulaciones atómicas MD no permiten observar la formación de la vesícula entera.

En su totalidad, este trabajo muestra la versatilidad de estas moléculas para formar una variedad de estructuras debido al balance entre sus diferentes longitudes, las interacciones electrostáticas entre sus cabezas con carga de signo opuesto, y las particulares interacciones que ocurren entre las cadenas de fluorinados e hidrogenados.

En esta tesis además hemos definido el concepto de auto-agregación de fármacos a través de una combinación de dos fármacos individuales con efectos terapéuticos específicos. La combinación de ambos compuestos cumple la función tanto de agregado como de vector.

La caracterización completa de la agregación de esta mezcla de fármacos se realizó usando técnicas bastante definidas tales como densidad y velocidad de sonido, dispersión de luz dinámica, y crio-microscopia electrónica. La investigación de la estabilidad y el tiempo de evolución fue hecho usando experimentos de UV-Vis. Este es un primer paso para una fuerte investigación acerca de su actividad terapéutica y de la eficiencia comparada con otros métodos clásicos de liberación usando los fármacos incorporados en los vectores. Muchos otros agregados de fármacos tipo vesículas y cristales líquidos pueden ser obtenidos por una apropiada combinación de compuestos terapéuticos individuales. Nosotros esperamos que nuestro trabajo estimule a la comunidad científica a investigar nuevos agregados de fármacos y sus ventajas sobre muchas estrategias convencionales en liberación de fármacos.

2. Estudio energético de las interacciones proteína-fármaco y análisis estructural del complejo formado.

Como segunda parte de esta tesis, se han analizado los complejos formados entre proteínas y tensioactivos. Para este tipo de estudio además de algunas técnicas ya citadas hemos usado dicroísmo circular, calorimetría diferencial de barrido (DSC), tensión superficial, microscopia de fuerza atómica (AFM), reología. Con este propósito se han obtenido resultados relevantes a través de este estudio.

Como anteriormente estudiamos la auto-agregación de *3-(2-benzothiazolylthio)-1-propanesulfonic acid* (BTS), hemos investigado el efecto de esta molécula anfifílica en la estabilidad térmica de lisozima, mioglobina, ovalbumina, y fibrinógeno. Resultados demostraron que todas las proteínas tuvieron diferentes temperaturas de desnaturalización, indicando diferencias en la estabilidad térmica. El BTS enlaza a través de interacciones electrostáticas a la mioglobina y lisozima, y a través de interacciones hidrofóbicas a la ovalbumina y fibrinógeno. A altas concentraciones de BTS decrece la temperatura de transición y favorece la desnaturalización de la proteína. Un mayor efecto es observado en el caso de la mioglobina, la proteína que posee una mayor cantidad de a-hélices en su estructura secundaria (75%). Esto podría estar relacionado con el hecho de que los enlaces de hidrogeno de la cadena principal de α-hélice son en general ligeramente más débiles que los encontrados en hojas β. Por lo tanto, están rodeados fácilmente por moléculas de BTS.

Resultados relevantes también fueron obtenidos al estudiar el efecto de betabloqueantes (acebutolol, propranolol) sobre fibrinógeno. Acebutolol y propranolol juegan dos roles opuestos en el plegamiento y estabilidad de los fragmentos finales D de fibrinógeno: Estabiliza a la proteína a bajas concentraciones de betabloqueantes y la despliega a altas concentraciones. Con los otros dominios de la estructura de la proteína, ambos actúa como un potente desnaturalizante de los C-terminales de la cadena Aα y como desnaturalizante a altas concentraciones para el dominio central E. Las transiciones del estado nativo al estado desplegado de fibrinógeno inducido por estos compuestos ha sido encontrado ser un proceso de múltiples pasos y muchos estados intermediarios. Se observo también que la presencia de estos betabloqueantes causa un incremento en el contenido de hojas β y la pérdida de estructura de α-hélice a bajas temperaturas. Mientras que este efecto es atenuado cuando la temperatura incrementa. Es postulado que fibrinógeno forma dímeros en ausencia de aditivos debido a las interacciones electrostáticas entre los dominios negativos (D y E) de una molécula y los dominios positivos C de otra molécula. Específicamente, la adición de pequeñas moléculas de acebutolol resulta en la agregación de estos dímeros para formar tetrámeros. Sin embargo, cuando la concentración de acebutolol es alta, los tetrámeros se disocian a dímeros.

Estos resultados podrían ser útiles para aplicaciones en la ciencia de biomateriales donde los dispositivos deberían ser creados con mejor hemocompatibilidad.

Se estudio también la agregación supramolecular entre fibrinógeno y perfluorooctanoato, octanoato y dodecanoato de sodio en una solución de buffer. Como primer paso, se estudió la estabilidad térmica de fibrinógeno en presencia de los surfactantes. A través de las medidas de calorimetría diferencial de barrido pudimos observar que la adición de surfactantes hidrogenados provocó la disminución de la temperatura de transición. El surfactante fluorinado juega dos roles opuestos en el plegamiento y estabilidad de la proteína, asi como acebutolol y propranolol: actúa como estabilizador a concentraciones molares bajas (aumenta T_m) y como desestabilizador a concentraciones bajas (disminuye T_m). El proceso de despliegue de la proteína no es un proceso que conlleva solo dos estados, sino que también involucra estados intermediarios para todos los sistemas bajo estudio. Aumentando la temperatura y/o la concentración de surfactante resulta en una disminución del contenido de α-hélices y un aumento en el contenido de hojas β. Sin embargo, la estructura terciaria y cuaternaria no presenta grandes variaciones, que han sido verificadas a través de UV-Vis y espectroscopia Raman. Se observó a través de las medidas de SAXS que fibrinógeno puro existe como un par de dímeros en el medio que ha sido estudiado. En presencia de surfactante esto cambia, dependiendo de la hidrofobicidad del surfactante. La presencia de C_8HONa (con menos hidrofobicidad) no promueve un cambio significante en fibrinógeno. Monómeros de C_8FONa interactúan con el par de dímeros de fibrinógeno sin promover una disociación o cambios conformacionales significantes. Por otro lado, la interacción entre C_{12}HONa (de más alta hidrofobicidad) y la proteína promueve la auto-agregación en fracciones hidrófobas. Este sistema fluorocarbono/hidrocarbono mas fibrinógeno reportado aquí podría proveer una clave importante para el futuro en aplicaciones biomédicas y bioquímicas, por ejemplo, en la recuperación de proteínas y la conformación de proteínas para soporte como materiales para terapias regenerativas.

Por esta razón se ha realizó la caracterización superficial de mezclas de fibrinógeno con C_8FONa, C_8HONa y C_{12}HONa. Las medidas de tensión superficial sugieren la formación de un complejo de fibrinógeno con el surfactante fluorinado, debido al leve desplazamiento a bajas concentraciones de la cac con respecto a los valores de los surfactantes puros. Para las mezclas de fibrinógeno/surfactante hidrogenado, la cac coincide con la cmc del surfactante puro. Las interacciones entre fibrinógeno y el surfactante fluorinado causan una fuerte cooperatividad o efecto sinérgico debido a un incremento en la actividad superficial del sistema mezclado relativo a fibrinógeno. Fibrinógeno parece prevenir la formación de una estructura cohesiva en la adsorción con un bajo modulo dilatacional, y en todos los casos, la adición de surfactante resulta en una reducción de la elasticidad de la capa superficial debido al incremento de la presión superficial. Sin embargo, en el caso de la mezcla de fibrinógeno/surfactante

hidrogenado, la elasticidad de las capas de la superficie únicamente disminuye sobre una cierta concentración de surfactante. Así, basados en este hecho, y sobre la ausencia de interacción entre la mezcla fibrinógeno/surfactante hidrogenado, puede ser esperado una compactación en la capa superficial. Las imágenes de AFM son consistentes con los estudios de caracterización superficial. La formación de *clusters* en el caso de fibrinógeno/surfactante fluorinado es consistente con los resultados provenientes de la caracterización superficial. En el caso de la mezcla fibrinógeno/surfactante hidrogenado, no hay formación de clusters, de hecho, el tamaño de las moléculas individuales es similar a los de FB puro. Estas observaciones son consistentes con los resultados reportados de los datos de modulo dilatacional.

Con el fin de estudiar las posibles matrices que se puede utilizar para la formación de materiales mesoporosos hemos estudiado las propiedades reologicas de hydrogeles de ovalbumina y cómo afecta a su estructura la adición de diferentes surfactantes.

Las principales características de este estudio estas resumidas de la siguiente manera: Primeramente, se estudió la formación de geles del sistema ovoalbúmina-surfactante para los tres diferentes surfactantes (C_8HONa, C_8FONa y C_{12}HONa) a distintas concentraciones de mezclas de radios en el rango 0-10 mM, y también fue observado que la fuerza del gel incrementó con el aumento de la concentración de surfactante. Para los tres surfactantes bajo estudio la fuerza del gel sigue la siguiente secuencia C_8FONa> C_{12}HONa> C_8HONa. Segundo, la dependencia de la concentración de surfactante del modulo de pérdida puede ser descrito por “power laws”. Los resultados sugieren una estructura fibrilar de los geles y una dimensión fractal dependiente de la naturaleza del surfactante. Finalmente, basados en la medidas de viscosidad, la diferente naturaleza del surfactante fluorinado provoca una ruptura de la red del gel a altas concentraciones.

3. **Caracterización estructural y energética de las plantillas obtenidas. Adsorción de principios activos y proteínas.**

En este estudio nosotros hemos diseñado una simple y controlable ruta para la síntesis de materiales ópalos-CT con inusual microestructura de fibras similares a las existentes en la naturaleza, utilizando un sistema “bottom up” de gotas de microemulsión como microreactor químico. La estructura microcristalina de los ópalos y consecuentemente sus propiedades optoelectrónicas son un resultado de una particular combinación de todos los parámetros relevantes de una microemulsión, tiempo en el tratamiento hidrotérmico, y temperatura de calcinación.

Las fibras obtenidas son de un tamaño mayor que 20 μm con un diámetro de 30-50 nm y están agrupadas formando paquetes de 100-200 nm distribuidas en diferentes orientaciones. Las

fibras están compuestas por esferas poliedras de α-SiO_2 que tienen una tamaño monodisperso ($d \approx 2\text{Å}$), como es usual en cristales fotonicos. Debido a su inusual microestructura, exhiben emisiones de fotoluminiscencia a longitudes de onda largas y cortas del cual difiere con los apilados de cristobalita-tridimita. El material con alto contenido en fallas de apilamiento de tridimita muestra una alta intensidad ultravioleta A y B con menor intensidad en la emisión roja y amarilla, mientras el material que presenta gran ordenamiento de cristobalita emite luz ultravioleta A, naranjo y radiaciones verdes. Es creído que una combinación de un mecanismo cuántico y la presencia de capas de oxido de Si defectuosas son las responsables de las emisiones simultáneas de las bandas de S- y F-.

Adicionalmente, los valores computarizados de la banda del gap (5.50 y 4.41 eV) para ambos materiales sintetizados son similares a los obtenidos por semiconductores de óxidos metálicos basados en silicio y altamente inferiores al gap obtenido experimentalmente para polimorfos cristalinos de SiO_2 (8.9 eV).

De estos materiales se escogieron los obtenidos a través de las microemulsiones agua/AOT/n-hexano (M1) y agua/AOT/ciclohexano (M2) para adsorber fibrinógeno. Los resultados indicaron que fibrinógeno se adsorbió mucho más rápido y en mayor cantidad sobre el material M2 (q_{mon}= 22.9 mgFB/mgM1). Estos materiales no poseen mucha área superficial, ambos materiales son químicamente similares. Fibrinógeno altera notablemente la morfología de los materiales, lo cual está relacionado con la forma de estos materiales. Se ha comprobado que esto es muy importante para la interacción de materiales es medios biológicos. Por ejemplo, el hueso puede definirse como una matriz orgánica-inorgánica compuesta por distintos niveles de organización nano-estructurada creada por la mineralización intra-fibrilar del colágeno. El material sintético aplicable a la reconstrucción de tejido óseo no solo debe contar con las dimensiones adecuadas sino también su aspecto es clave en orden de optimizar la respuesta de las células óseas. Es así que los osteoblastos presentan una respuesta muy favorable sobre sustratos formulados a partir de nanofases cerámicas fibrosas. Un comportamiento similar ha sido obtenido sobre nano-fibras de carbono.